DOCTOR OF PHILOSOPHY

Development of Photocatalytic Reactor Technology for the Production of Fermentable Sugars

Nagarajan, Sanjay

Award date:
2017

Awarding institution:
Queen's University Belfast

Development of Photocatalytic Reactor Technology for the Production of Fermentable Sugars

by

Sanjay Nagarajan B.Tech; M.Sc

Being a thesis submitted for the degree of

Doctor of Philosophy

to the

School of Chemistry and Chemical Engineering

of

Queen's University Belfast

Based on research conducted under the direction of

Professor Peter Robertson and

Professor A Prasanna de Silva

February 2017

திருக்குறள் (Thirukural):

“சென்ற இடத்தால் செலவிடா தீதொரீஇ
நன்றின்பால் உய்ப்ப தறிவு”.

- அறிவுடைமை, குறள் 422
- (from chapter: Wisdom, phrase 422)

குறள் விளக்கம் (Meaning):

மனத்தை சென்ற இடத்தில் செல்ல விடாமல், தீமையானதிலிருந்து நீக்கிக் காத்து நன்மையானதில் செல்ல விடுவதே அறிவாகும்.

(Not letting the mind to wander on its own will, but to steer it towards good is wisdom.)

DEDICATION

To all people who have inspired me, especially to the people of Tamil Nadu (India) who have shown their humanitarian side during the floods and cyclone during 2015 and 2016 and to the unity of Tamilians who have protested peacefully and setting an example during January 2017 to revive Tamil culture.

DECLARATION

I hereby declare that this thesis is my original work and no part of it has been submitted for an award of another degree from any institution.

ACKNOWLEDGEMENTS

I would firstly like to thank my primary supervisor, Professor Peter Robertson for his guidance, advice and support throughout the PhD. I would also like to thank my supervisor Professor A. Prasanna de Silva for his encouraging and enlightening words during the progress meetings.

I would like to thank Dr. Nathan Skillen for providing his advice and expertise when required. I would also like to thank Professor Linda Lawton (Robert Gordon University, Aberdeen), Professor John Irvine (University of St. Andrews, Fife), Dr. Aakash Welgamage (Robert Gordon University, Aberdeen) and Dr. Guan Zhang (University of St. Andrews, Fife) for their support during collaboration. I would also like to thank the technicians in the glass blowing workshop and the mechanical engineering workshop for their help and support in fabricating the reactor. I would also like to thank the clerical and administrative staff of the school of chemistry and chemical engineering, Queen's University Belfast for their support in terms or ordering and logistics.

I am fortunate to have great parents in Mr. T. Nagarajan and Mrs. N. Meyyammai. I would like to thank them for their belief in me. I would also like to thank my brother, Mr. N. Sathappan for his encouraging words. I would also like to thank my wife Mrs. AR. Eswarimeena for being a pillar of support during my PhD.

I was privileged to have a mentor in Dr. KP. Gopinath (SSN College of Engineering, India) who impacted and influenced me and my view on research since I joined my undergraduate degree. Sir, you are a true inspiration. I would also like to extend my thanks to Dr. Zhou Zhi George (Purdue University, USA) for his support during my tough times in Singapore.

I would also like to thank all my friends for their continuous support throughout the course of my PhD.

Finally, I would also like to thank the Robert Gordon University's IDEAS for providing me a full fee scholarship and studentship for the 1st year of my PhD and Queen's University Belfast for providing me with a full fee scholarship and studentship for the 2nd and 3rd year of my PhD.

Abstract

Rapid depletion of fossil fuel stock with a simultaneous rise in greenhouse gas emissions has led to an increase in the need for alternative energy. Cellulose based biofuels, especially bioethanol is a form of alternative energy that has the potential to replace petrol. The first step in cellulosic bioethanol production is the release of fermentable sugars via pre-treatment. Conventionally, physico-chemical and biological pre-treatment methods are energy intensive, environmentally unfavourable and expensive. This study, however reports on the use of a less energy consuming, cheap and environmental friendly alternative; photocatalysis, to produce fermentable sugars from cellulose. To achieve this, a range of photocatalysts were first screened based on their OH radical production rates using coumarin as a probe. TiO_2 P25 was the photocatalyst that was found to have the highest OH radical production rate of 35.6 µM/hr, followed by Pt-C_3N_4 (0.88 µM/hr) and WO_3 (0.28 µM/hr). LaCr-$SrTiO_3$, Cr-$SrTiO_3$ and yellow TiO_2 did not produce any OH radicals due to their unsuitable electronic structure. P25 was further used for photocatalytic fermentable sugar production from cellulose. Photocatalytic cellulose I breakdown produced 0.04 % fermentable sugars whereas, with cellulose II feedstock the yield increased to 0.2 %. To further improve the yield, membrane bags were deployed which improved the sugar yields to 0.43 % and 0.71 % respectively from cellulose and cellulose II feedstocks. Photonic efficiencies followed the same trends as the sugar yields. Engineering design was further opted to enhance the sugar yields and hence a stacked frame photocatalytic reactor (SFPR) was designed. Various mixer

configurations were designed and their mixing regime was determined using COMSOL Multiphysics 5.1 simulations. Amongst the mixers simulated, an 8-blade Rushton impeller was found to be the best configuration due its superior radial mixing profile and higher fluid velocity. The SFPR was then fabricated and operated with the impeller or a plus shaped magnetic bar as the mixer and the sugar yields were determined. Highest sugar yield and photonic efficiency was obtained from the cellulose II-impeller setup and was calculated to be 2.61 % and 9.45 % respectively. Respective lowest yields were obtained with cellulose I-stirrer bar setup and calculated to be 1.71 % and 5.64 %. Furthermore, the effect of H_2O_2 on fermentable sugar production was also tested. The cellulose II-stirrer bar configuration yielded 3.15 % fermentable sugars with the addition of 0.01 wt% H_2O_2 to the reaction mixture. The yield improved significantly to 14.1 % when the concentration of H_2O_2 was increased to 0.1 wt%.

TABLE OF CONTENTS

LIST OF FIGURES

Chapter 1

Chapter 2

Chapter 3

Chapter 4

Chapter 5

LIST OF TABLES

Chapter 1

Chapter 2

Chapter 3

Chapter 4

-

Chapter 5

GLOSSARY

µl – microliters

µm – micrometres

µM/g/h – micromoles per gram per hour

µM/hr – micromoles per hour

µM/min – micromoles per minute

Å – angstroms

ATR-FTIR – Attenuated total reflectance – Fourier transform infrared spectroscopy

BMIM-Ac - 1-butyl-3-methylimidazolium acetate

CB – conduction band

CDH – cellobiose dehydrogenase

cm - centimetre

CPI – controlled periodic illumination

CrI – crystallinity index

CSTR – continuous stirred tank reactor

dcV – direct current volts

DI – deionised water

DMF – dimethyl furan

DMSO – dimethyl sulfoxide

DSC – differential scanning calorimetry

E_{bg} – band gap energy

e_{cb}^- - conduction band electrons

EMIM-Ac - 1-ethyl-3-methylimidazolium acetate

eV – electron volt

FPU – filter paper unit

g/dm^3 – grams per cubic decimetre

g/L – grams per litre

gt – gauche trans

h – hour

HMF – hydroxymethyl furfural

HPLC – high performance liquid chromatography

h_{vb}^{+} - valence band holes

IEA- International energy agency

ISO – international standardisation organisation

IU – international unit

Kg/m^3 – kilogram per cubic metre

kV – kilovolts

kW – kilowatts

L – litre

LED – Light emitting diode

M – moles/litre

m/s – metre per second

M6 – 6 millimetre diameter

mA – milliampere

MCC – Microcrystalline Cellulose

mg – milligrams

mins – minutes

ml – millilitres

ml/min – millilitres per minute

mm – millimetre

mM – millimoles

mmHg – millimetre mercury

MPC - N-methyl-2-pyrrolidonium chloride

MPDS - N-methyl-2-pyrrolidonium dihydrogen phosphate

MPHS - N-methyl-2-pyrrolidonium hydrogen sulfate

MPMS - N-methyl-2-pyrrolidonium methane sulfonate

mW – milliwatts

NHE – normal hydrogen electrode

nm – nanometres

nm/min – nanometres per minute

NMMO - N-methylmorpholine-N-oxide

^{O}C – degree Celsius

^{O}C/min degree Celsius per minutes

OECD – Organisation for economic co-operation and development

Pas – pascal seconds

PMMA – polymethyl methacrylate

PSTY – photocatalytic space time yield

RANS – Reynolds averaged Navier Stoke

RC – regenerated Cellulose

RI – refractive index

RPM – revolutions per minute

s – seconds

SFPR – stacked frame photocatalytic reactor

TBAH – tetrabutyl ammonium hydroxide

TBPH – tetrabutyl phosphonium hydroxide

TCI – total crystallinity index

tg – trans gauche

TGA – thermogravimetry

TMA – tetramethyl ammonium

UV- ultraviolet

V – volts

VB – valence band

W – watts

wt% - weight percentage

XRD – X-ray diffraction

Θ – theta

PUBLICATIONS

Published

1. **Nagarajan, S*.**, Stella, L., Lawton, L. A., Irvine, J. T. S., and Robertson, P. K. J*. (2017). “Mixing Regime Simulation and Cellulose Particle Tracing in a Stacked Frame Photocatalytic Reactor.” Chemical Engineering Journal, http://dx.doi.org/10.1016/j.cej.2016.12.016.

2. **Nagarajan, S*.**, Skillen, N. C., Fina, F., Zhang, G., Randhorn, C., Lawton, L. A., Irvine, J. T. S., and Robertson, P. K. J*. (2017). “Comparative assessment of visible light and UV active photocatalysts by hydroxyl radical quantification.” Journal of Photochemistry and Photobiology A: Chemistry, http://dx.doi.org/10.1016/j.jphotochem.2016.10.034.

3. **Nagarajan, S*.**, Skillen, N. C., Irvine, J. T. S., Lawton, L. A., and Robertson, P. K. J*. (2017). “Cellulose II as bioethanol feedstock and its advantages over native cellulose.” Renewable and Sustainable Energy Reviews journal, https://doi.org/10.1016/j.rser.2017.03.118.

To be submitted

1. **Nagarajan, S.**, Lawton, L. A., Irvine, J. T. S., and Robertson, P. K. J*. (2017). “Photocatalytic Fermentable Sugar Production from Native and Regenerated Cellulose – A Comparison” to be submitted to Green Chemistry journal.
2. **Nagarajan, S.**, McCurdy, C., Lawton, L. A., Irvine, J. T. S., and Robertson, P. K. J*. (2017). “Photocatalytic Fermentable Sugar Production in a Stacked Frame Photocatalytic Reactor” to be submitted to Energy and Environmental Science journal.

* corresponding author

CONFERENCES ATTENDED

1. **Nagarajan, S.**, (2016). Poster on “Photocatalytic fermentable sugar production” at The IChemE Young Researcher’s meeting held at the Royal Dublin Society, Dublin, Republic of Ireland.

2. **Nagarajan, S.**, Skillen, N. C., Lawton, L. A., Irvine, J. T. S., and Robertson, P. K. J. (2016). Presentation on “Development of a photocatalytic reactor for the production of fermentable sugars” at the UKISPC network meeting held at University College London, UK.

3. **Nagarajan, S.**, Skillen, N. C., Lawton, L. A., Irvine, J. T. S., and Robertson, P. K. J. (2016). Poster on “Photocatalytic fermentable sugar production from microcrystalline and regenerated cellulose – a comparison” at Solar Chemistry and Photocatalysis: Environmental Applications (SPEA) conference held in Strasbourg, France.

4. **Nagarajan, S.**, Skillen, N. C., Lawton, L. A., Irvine, J. T. S., and Robertson, P. K. J. (2016). Poster on “Simulation of mixing regime in a stacked frame photocatalytic cell for cellulose breakdown” at Solar Chemistry and Photocatalysis: Environmental Applications (SPEA) conference held in Strasbourg, France.

5. **Nagarajan, S.**, Skillen, N. C., Lawton, L. A., Irvine, J. T. S., and Robertson, P. K. J. (2015). Presentation on “Quantification of OH radicals on novel photocatalysts” at The UK and Ireland Semiconductor Photocatalytic Network Meeting (UKISPC) held at Queen’s university Belfast, UK.

Chapter 1: Introduction

1.1 Global energy scenario and the need for alternative energy

Enhanced global utilisation of the existing fossil fuel stock along with the simultaneous increase in greenhouse gas emissions due to increasing anthropogenic activities has been continuously debated. Additionally, global politics also influences the movement of fossil fuel stocks. It was assessed around two decades ago that the seriousness of fossil fuel depletion will be experienced by the start of 2030 (1). Furthermore, the International Energy Agency's (IEA), World Energy Outlook report from 2013 estimated that, globally for the fossil fuel dependence to drop from the present 82 % to 76 % by 2035, up to 18 % of the total consumed energy has to be supplied from renewable energy resources (2). Therefore, there is a need to increase the possibility of alternative energy production and accordingly, investments are now being made globally to expand the possibilities of alternative energy (Figure 1.1).

Sustainable development in the field of energy production has been continuously expanding over the past few years. Sustainable development according to Brundtland commission's report submitted to the United Nations quotes "Meeting the needs of the present without compromising the needs for the future" (3). Such sustainable renewable energy production could be achieved by the production of biofuels mediated by photocatalysis from cellulose and its wastes.

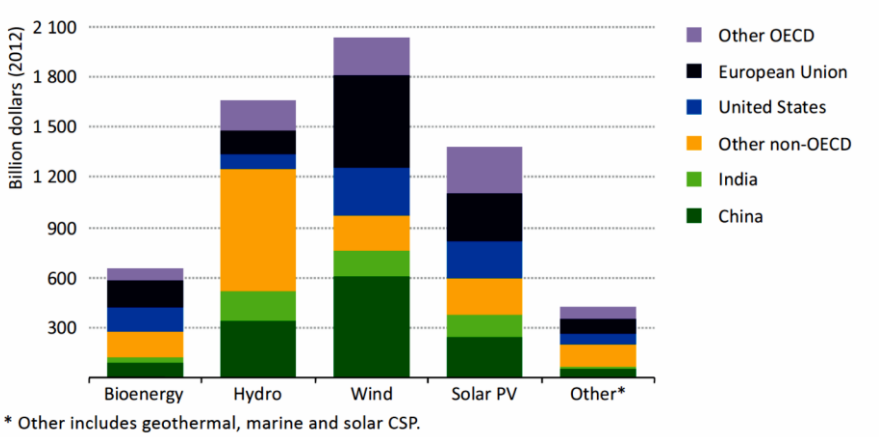

Figure 1.1: Cumulative investment in renewables-based power generation, 2013-2035 (2), where OECD stands for Organisation for Economic Co-operation and Development, reproduced with permission. © OECD/IEA 2013 *World Energy Outlook*, IEA Publishing. Licence: www.iea.org/t&c.

1.2 Current alternative energy sources

There are a lot of energy sources proving to be competent alternatives to fossil fuels, including biodiesel, bio alcohols (such as bioethanol and bio butanol), (bio) hydrogen, biogas, electricity produced from solar and wind farms, geothermal and tidal energy (4). Considering the possibilities mentioned above, biodiesel and bio alcohols are potential substitutes for current transportation fuels. Feedstocks essential to produce biodiesel include algae, waste vegetable oils, animal fats, palm oil and non-edible oils (5). The feedstock required to produce bio alcohols could be classified into two generations; first generation feedstock including food crops such as sugarcane and corn and second generation including ligno-cellulosic materials and cellulosic wastes (6,7).

1.2.1 Cellulose and cellulosic wastes

Second generation bio alcohol production focussed entirely on cellulose and cellulosic wastes for the fact that cellulose is one of the most

abundant naturally available organic materials on earth (8). Shown below in Table 1.1 is the cellulose content of various potential biofuel feedstock materials. All the feedstock detailed in Table 1.1 have varying amounts of lignin in them. Lignin is an aromatic hydrophobic compound which forms interlinking complexes with cellulose and reduces freely available cellulose, hence giving plants their structural stability (9). It is expensive, both from an energy and cost point of view to breakdown lignin and release cellulose. This would subsequently have to be followed by cellulose degradation to release fermentable sugars for biofuel production. In order to utilise cellulose to the fullest extent it is better to use freely available cellulose in the form of processed cellulose waste rather than lignocelluloses as the latter is interlocked between strands of lignin.

Material	**% cellulose content (w/w)**	**Reference**
Green algae	20-40	(10)
Cotton, flax, etc.	80-95	
Grasses	25-40	
Hardwoods	45±2	
Hardwood barks	22-40	
Softwoods	18-38	
Softwood barks	42±2	
Corn stalks	39-47	
Wheat straw	37-41	
Newspapers	40-55	
Chemical pulps	60-80	
Rice straw	46.5±1.5	(11)
Wheat straw	35-37	(12)
Rice husk	25-35	(13)
Bagasse	32-43	(14)
Coconut coir	59	

Table 1.1: Cellulose content of various biofuel feedstocks.

1.3 Structure of cellulose

Cellulose is an amphiphillic homopolysaccharide compound (15). Individual β-D-glucose units joined by (1-4)-glycosidic bond as well as intermolecular and intramolecular hydrogen bonds give rise to a rigid cellulose structure (16). Cellulose molecules have both disordered amorphous and highly ordered crystalline regions along its chain (17). The structure of cellulose with chair confirmation and equatorial orientation of the glucose molecules, the β-(1-4)-glycosidic bond and the intramolecular and intermolecular hydrogen bonds, represented by the green dotted lines, is shown in Figure 1.2.

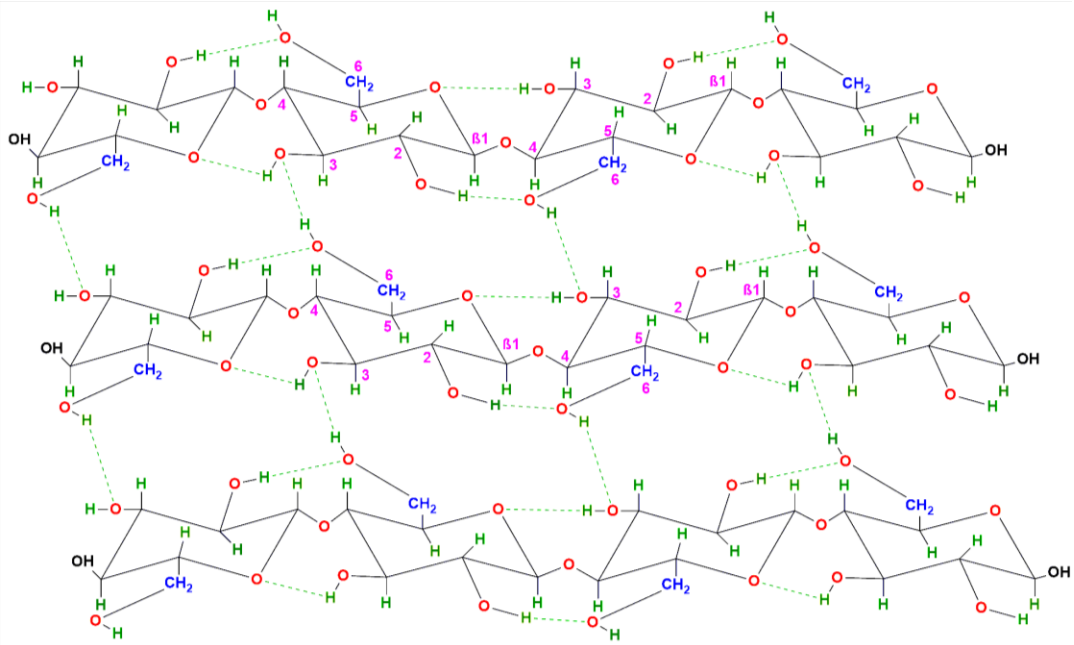

Figure 1.2: Structure of cellulose.

In nature, cellulose exists in its native form in higher plants as cellulose Iβ, however in some cases native cellulose Iα is produced by microbes. Although cellulose Iα and Iβ have parallel strands of cellulose, they differ in

their lattice arrangement with the former exhibiting triclinic arrangement and the latter having a monoclinic structure. In addition to the native polymorphs, cellulose can exist in different polymorphs as a result of physico-chemical treatments (18) (Figure 1.3). Cellulose II or regenerated cellulose (RC) can be produced from both cellulose Iα or Iβ via alkali treatment (mercerisation) or solubilising and recrystallizing (regeneration) respectively. In a few rare instances, naturally occurring cellulose II has been isolated from bacterial cultures (18-20). Unlike cellulose I, cellulose II has an antiparallel strand arrangement and monoclinic lattice arrangement. Another polymorph, cellulose III_I and III_{II} can be reversibly produced from cellulose I and II via NH_3 respectively. This polymorph exhibits parallel strand arrangement and monoclinic crystal structure (21). When these cellulose III_I and III_{II} materials are heat treated, cellulose IV_I and IV_{II} are formed.

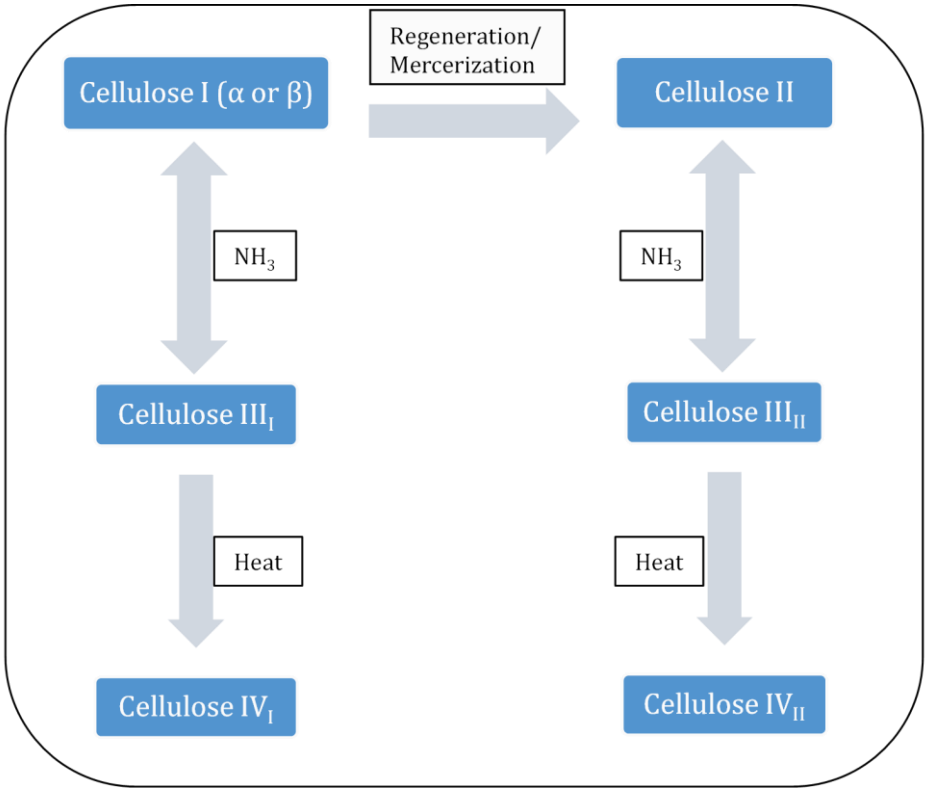

Figure 1.3: Cellulose polymorphs.

An in-depth understanding of the polymorph's characteristics is necessary for determining its end use. MCC (microcrystalline cellulose) is the naturally abundant cellulose whereas, RC is the most commonly used man made cellulose and for these reasons there is abundant information in the literature regarding the characterisation of these polymorphs (16-18,22). Of all the characterisation, the hydrogen bonding interactions play a governing role in the supramolecular structure of these polymorphs. The hydrogen bonding networks for cellulose I and II are shown along the a-c axis in Figure 1.4. As can be seen, the difference in hydrogen bonding between the two polymorphs is due to the irreversible transformation of cellulose I to cellulose II, thereby the latter forming anti-parallel chains affecting the hydrogen bonding patterns.

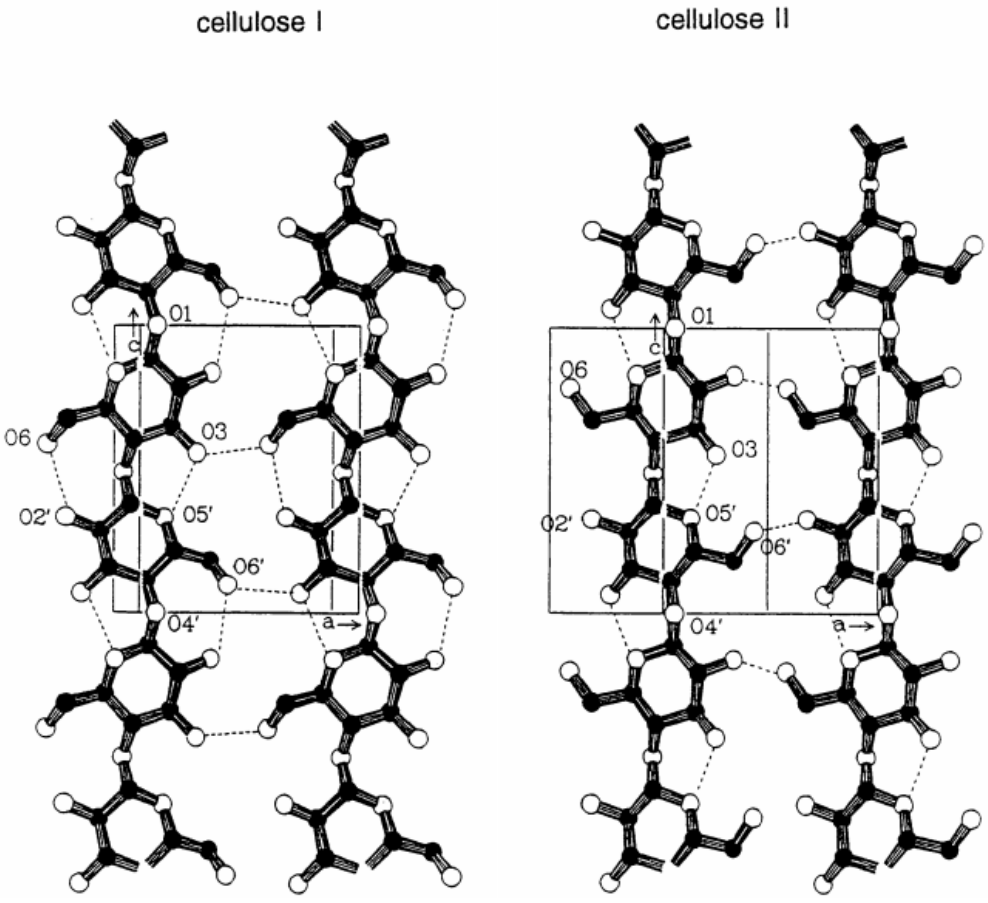

Figure 1.4: Hydrogen bonding in cellulose I and II, reprinted with permission from "John Wiley and Sons, Copyright 1998" (22).

The intermolecular hydrogen bonding is more complicated in cellulose II than MCC due to its antiparallel chain arrangement. For instance, in cellulose I, the O6-H-O3 intermolecular hydrogen bond is formed parallel to the a-axis as a result of trans-gauche (tg) conformation of the $–CH_2OH$ group. Whereas in cellulose II, the anti-parallel chains which has the $–CH_2OH$ group in the gauche-trans (gt) conformation forms two intermolecular hydrogen bonds, namely O6-H-O3 and OH6-O2' (22). The gt and tg conformations of the $–CH_2OH$ group not only determine the hydrogen bonding in the cellulose polymorphs but also the fate of chemical reactivity with various radical species and chemical compounds. In addition to the hydrogen bonds, glycosidic bonds are formed between the C1 of a glucose monomer and C4 of the subsequent monomer. During the transformation from cellulose I to II, it's the hydrogen bonding network that is reorganised whereas the glycosidic linkages remain unaffected. These glycosidic bonds need to be broken down in the cellulose polymorphs to gain access to the individual glucose monomers. For the efficient release of glucose monomers and other homo-oligosaacharides, the most easily digestible polymorph of cellulose has to be the starting material for sugar production and hence cellulose II has been considered as a better raw material than cellulose I due to the rearrangement in its supramolecular structure (23,24).

1.4 Releasing fermentable sugars

To facilitate bio alcohol production, fermentable sugars have to be released from cellulose. The procedure to breakdown cellulose, otherwise

known as a pre-treatment process, should fulfil the following requirements (16);

(i) Enable fermentable sugar release

(ii) Minimal loss of fermentable sugars

(iii) Minimal or no undesirable product formation

(iv) Cost effective

(v) Feasible scalability

(vi) Energy efficiency

Based on these factors there have been a lot of methods developed to pre-treat cellulose. The most frequently used method is steam explosion with dilute acid. During this process, the biomass is treated with high temperature and high pressure steam followed by a swift pressure decrease which releases the desired sugars. Although this is the preferred method, it has a few drawbacks including loss of fermentable sugars due to degradation and formation of undesirable inhibitory by-products (25). Additional methods of cellulose pre-treatment have been summarised and detailed in Table 1.2.

Pre-treatment Category	Method	Advantages	Disadvantages
Physical	Mechanical grinding	Ease of handling the raw materials	High energy requirement
	Pyrolysis	Rapid decomposition	High temperature requirement
Physico-chemical	Steam explosion along with dilute acids	Less energy requirement when compared to mechanical grinding, cost effective	Decomposition of monosaccharides
	Ammonia fibre explosion	Relatively higher yield of monosaccharides than steam explosion	Cost involved in ammonia recovery to make the process environmentally friendly
	CO_2 explosion	Cost effective	Low yield of monosaccharides when compared to steam or ammonia explosion
	Ozonolysis	Environmentally friendly, room temperature and pressure reactions	Large quantity of ozone required
Chemical	Acid hydrolysis	Higher yield of monosaccharides	Toxic and corrosive, cost involved in acid recovery to make the process environmentally friendly, downstream pH adjustment is required
	Alkaline hydrolysis	Works well to remove lignin and hemicellulose	Salt formation and downstream pH adjustment is required
Biological	White rot and brown rot fungi	Low energy requirements	Slow rate of hydrolysis
Enzymatic	Cellulases	High specificity for cellulose	Large quantity of enzyme required, expensive

Table 1.2: Cellulose pre-treatment methods (25).

1.5 Ionic liquids and onium hydroxides

Apart from directly releasing fermentable sugars from cellulose using the harsh methods mentioned above, MCC can be converted to a relatively easily digestible cellulose II form using molten salts or other organic solvents. These are either ionic liquids or aqueous organic solvents such as onium hydroxides. MCC could be completely dissolved in these non-derivatising solvents and precipitated out as cellulose II by mixing with suitable anti-solvents such as water, ethanol, methanol or acetone (26-28).

Ionic liquids are molten salts with melting points lower than 100 ^{O}C. Most common ionic liquids to date are air and moisture stable imidazolium based salts (29). Currently, ionic liquids are of prime interest due to their versatility as solvents in various applications. They are highly flexible as a number of cation and anion combinations can be fabricated based on the potential end use of the solvent. Methylimidazolium and methylpyridinium based cations, and chloride, acetate and formate anions are the most commonly used species for designing cellulose dissolving ionic liquids (28), however, other anions such as SCN, BF_4, PF_6 and many more have been used (27-29). It is believed that the OH groups of the neighbouring C6 and C3 cellulose chains form an electron donor-acceptor complex with ionic liquids to result in the dissolution of cellulose (28). Despite the high versatility for fabrication, its high viscosity, negligible vapour pressure, inability to dissolve wet cellulose and the requirement of temperatures higher than room temperature to dissolve cellulose does not make it completely “environmental friendly”.

To overcome this drawback, aqueous organic solvents such as onium hydroxides could be used to dissolve cellulose. Examples of onium hydroxides are Tetra-n-butylphosphonium hydroxide (TBPH) and tetra-n-butylammonium hydroxide (TBAH). These solvents primarily have a similar cellulose dissolution mechanism to ionic liquids (26), however operate at room temperature, making it a more energy favourable solvent. Furthermore, since onium hydroxides are available as aqueous solutions, they are comparatively less viscous than ionic liquids and can dissolve high concentrations of cellulose (up to 20 wt%) (26). Additionally, it has been reported that, onium hydroxides with a water content of 30–50 wt% can completely dissolve cellulose at room temperature (26).

1.6 Breakdown mechanism of cellulose and similar model compounds

Cellulose (native and regenerated forms) has to be broken down into fermentable sugars so that it can be further fermented to produce biofuels. All the known cellulose degradation mechanisms involve the attack of OH radicals on the cellulose molecule to produce fermentable sugars. The breakdown mechanisms of various cellulose, cellulose derivatives and similar compounds focusing on fermentable sugar release, apart from the methods mentioned in Table 1.2 are discussed in the following sections.

1.6.1 Polysaccharide degradation by cellobiose dehydrogenase

Cellobiose dehydrogenase (CDH) is an enzyme that binds specifically to a single cellulose chain to cleave the glycosidic bonds. The mechanism of

cellulose breakdown by CDH proceeds via a Fenton's reaction where OH radicals are produced locally at the site of cleavage.

Figure 1.5 shows the detailed mechanism of cellulose breakdown by OH radicals generated by CDH. The breakdown proceeds via hydrogen abstraction at C4 by the OH radical followed by the removal of water. In addition, oxidation takes place, which is followed by the release of a superoxide ion. The products of this reaction are an equimolar proportion of carbonyl radical and carbanion. This anion will undergo a deprotonation leading to ring opening (30).

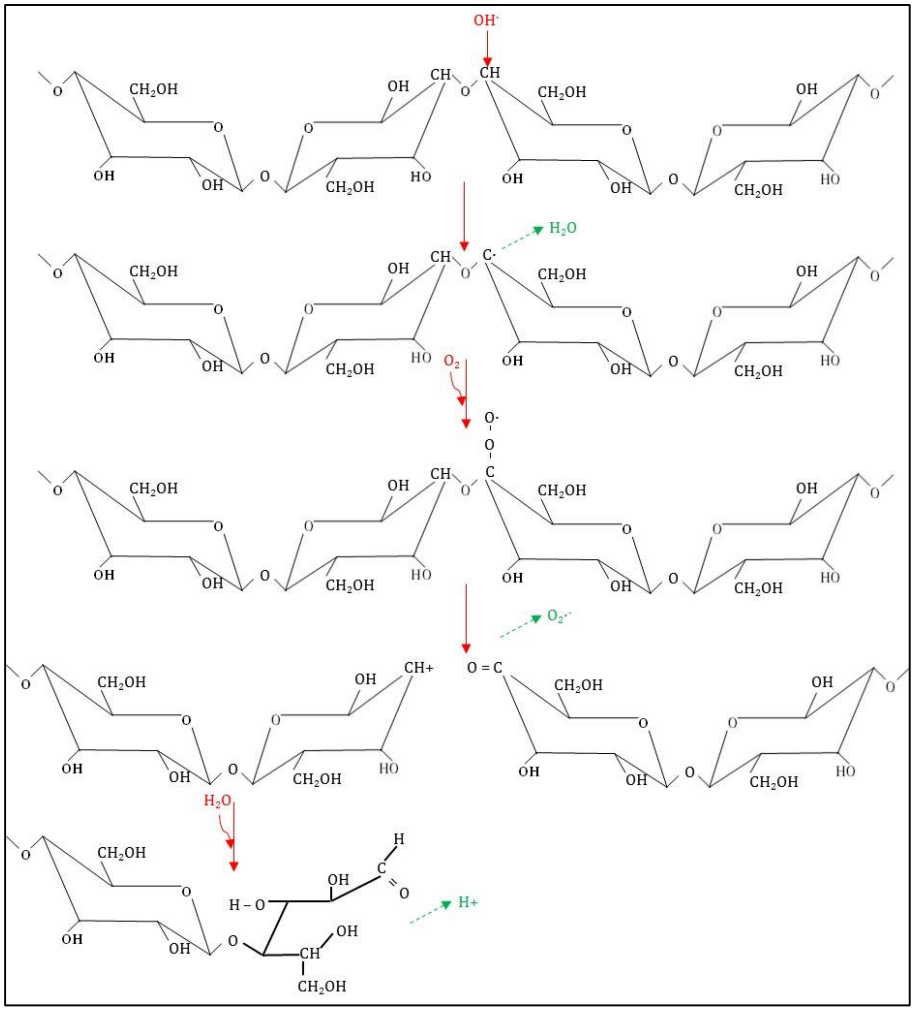

Figure 1.5: Cellulose breakdown mechanism by CDH.

1.6.2 Cellobiose degradation under ionising radiation

Cellobiose is a dimer of glucose, formed by a β-(1-4)-glycosidic bond. The bonding of these cellobiose chains along with interlinking intermolecular and intramolecular hydrogen bonds will result in the formation of cellulose. Since, cellobiose is the precursor of cellulose; it has been used as a model compound to study its interaction with OH radicals (31). Figure 1.6 shows the mechanism of cellobiose breakdown when the OH radical generated by the ionising radiation in aqueous solution attacks C1 of cellobiose. Figure 1.7 and Figure 1.8 shows the mechanism of OH radical attack on cellobiose at C4 and C5 respectively. Regardless of the site of attack of OH radicals on cellobiose, glucose and carbonyl radicals are produced in equal proportions.

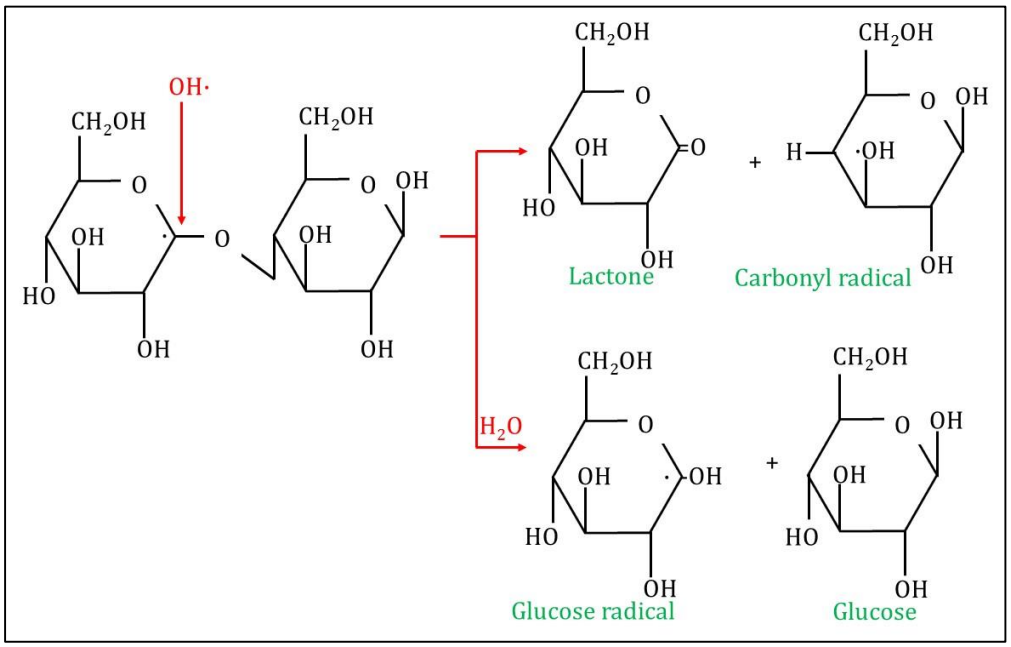

Figure 1.6: OH radical attack at C1 (31).

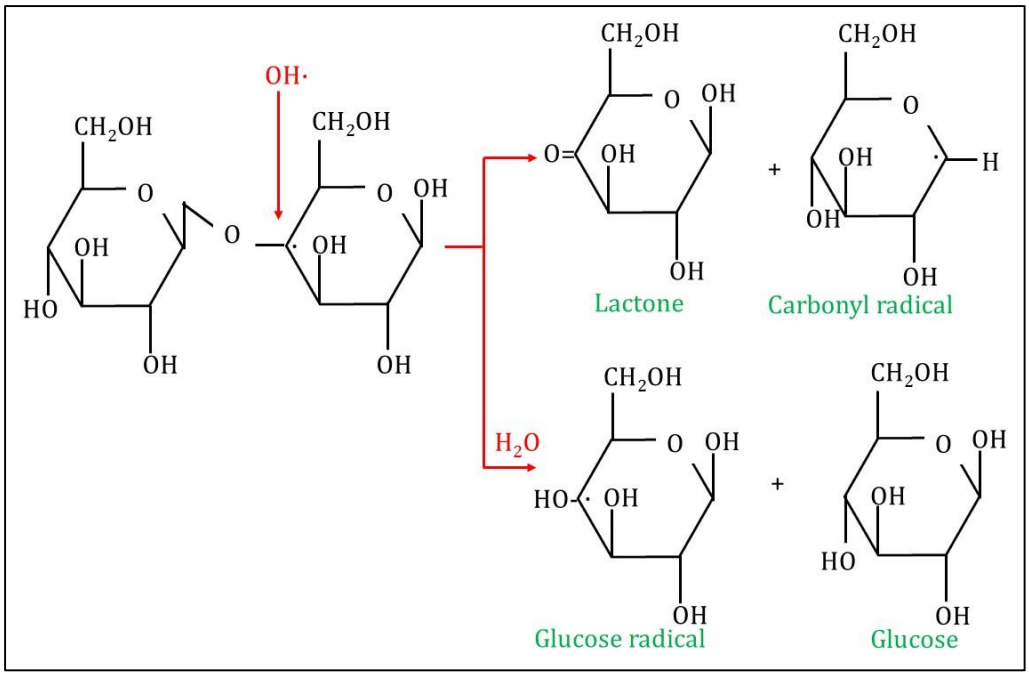

Figure 1.7: OH radical attack at C4 (31).

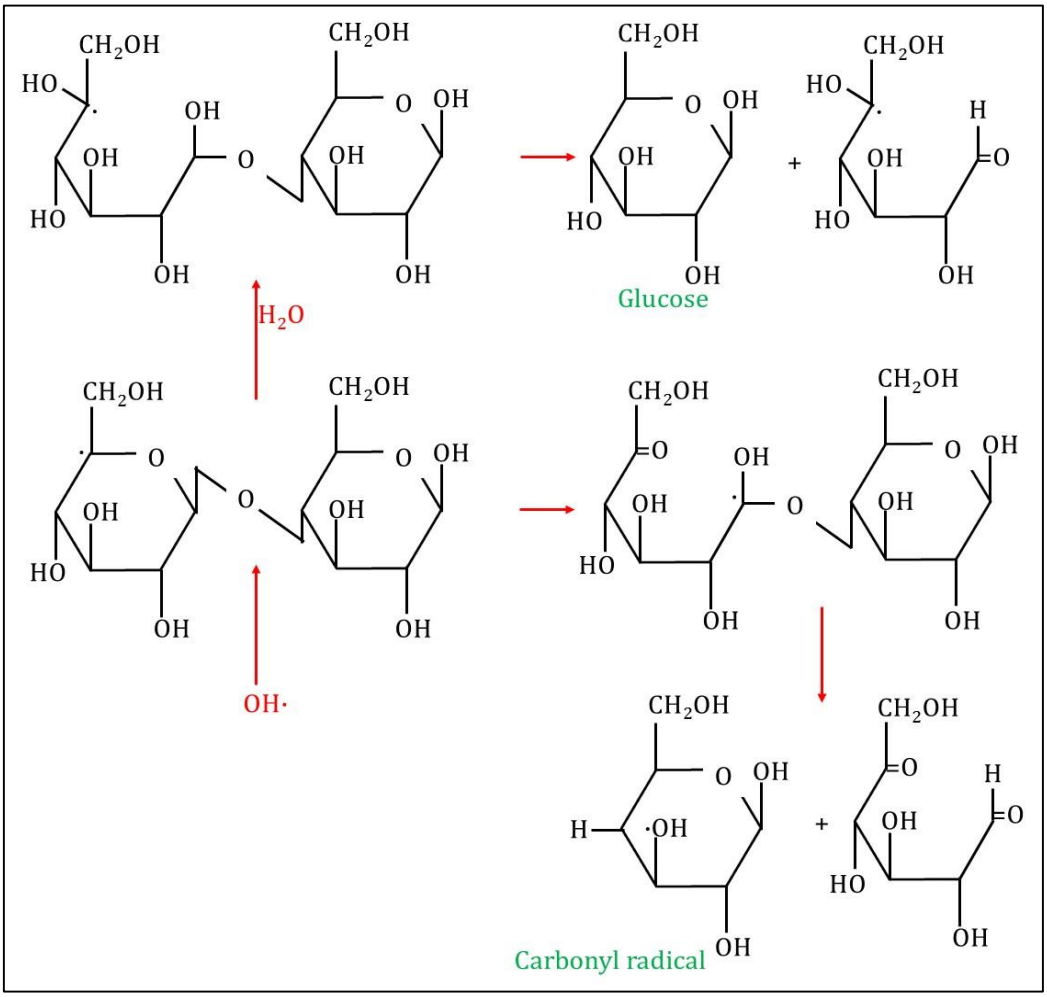

Figure 1.8: OH radical attack at C5 (31).

1.6.3 Electrochemical cellulose degradation

Cellulose degradation by electrochemical means has also been studied in the past (32). Meng *et al.* dispersed cotton cellulose in sulphuric acid and degraded it to 5-hydroxy methyl furfural (5-HMF) with the intermediate product being glucose in an electrochemical system with a Pb/PbO_2 anode (32). The mechanism proceeded via the production of OH radicals from the anode as shown in Figure 1.9. With the removal of water upon OH radical attack, a carbon radical at the C4 position is formed. Molecular oxygen then reacts with this radical for form a superoxide radical of cellulose leading to the cleavage of the glycosidic bond. Upon this breakdown, a C1 radical of glucose and an oxygen atom radical of cellulose is formed, further leading to the formation of 5-HMF, glucose and oligosaccharides.

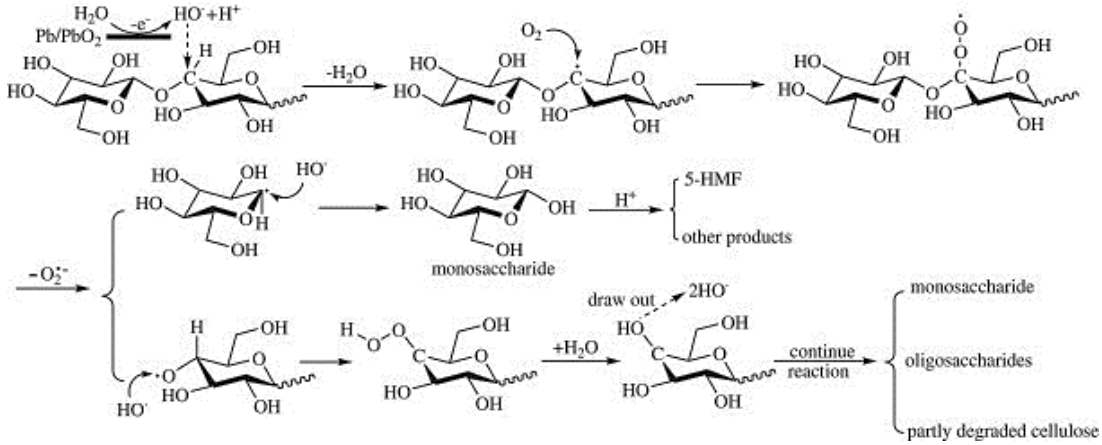

Figure 1.9: Electrochemical degradation of cotton, reprinted with permission from “Elsevier, Polymer Degradation and Stability, Copyright 2011” (32).

1.6.4 Autoxidation of cellulose

When a volume of cellulose is soaked in twice the volume of alkali and dried, it undergoes a slow reaction with atmospheric oxygen leading to degradation known as alkali autoxidation of cellulose (33). This mechanism is

shown below and has three steps; initiation, propagation and termination (34). Initiation reactions are the slowest of all the steps and start by the reaction of cellulose with oxygen to form intermediate radicals (R 1.1 and R 1.2). During propagation reactions, the cellulose radicals further react with oxygen to form peroxyl radicals thereby leading to a hydrogen abstraction from another cellulose molecule hence continuing the autoxidation (R 1.3-R 1.7). Finally, a termination reaction occurs where two radicals undergo reactions to form lower sugars or cellulose anions (R 1.8- R 1.10).

Initiation

$RH + O_2 \rightarrow R^{\cdot} + HOO^{\cdot}$ ..... R 1.1

$R^{-} + O_2 \rightarrow R^{\cdot} + O_{2}^{\cdot -}$ ..... R 1.2

Propagation

$R^{\cdot} + O_2 \rightarrow ROO^{\cdot}$ ..... R 1.3

$ROO^{\cdot} + R'H \rightarrow ROOH + R'^{\cdot}$ ..... R 1.4

$ROO^{\cdot} \rightarrow R^{+} + O_{2}^{\cdot -}$ ..... R 1.5

$R^{\cdot} + R'H \rightarrow RH + R'^{\cdot}$ ..... R 1.6

$RH + OH^{\cdot} \rightarrow R^{\cdot} + HOH$ ..... R 1.7

Termination

$R^{\cdot} + OH^{\cdot} \rightarrow ROH$ ..... R 1.8

$R^{\cdot} + O_{2}^{\cdot -} \rightarrow ROO^{-}$ ..... R 1.9

$R^{\cdot} + R^{\cdot} \rightarrow RR$ ..... R 1.10

1.6.5 Degradation of cotton cellulose in H_2O_2 based systems

To demonstrate the effect of H_2O_2 (and Fenton's reagent) on cellulose depolymerisation, Hastrup *et al*. performed experiments using cotton cellulose and treated it with H_2O_2 and Fenton's reagent (H_2O_2 + Iron) (35). To 6.67 g/L cotton cellulose suspended in water, 0.8-80 mM H_2O_2 was added and incubated for 24 hours. Cellulose degree of polymerisation reduced to half after 2 hours treatment with the addition of 80 mM H_2O_2 whereas it took 24 hours to achieve similar degree of polymerisation with 0.8 mM H_2O_2. Additionally, when the degradation was performed with the addition of $FeSO_4$, the rate of decrease in degree of depolymerisation of cellulose was enhanced. This increase in rate was attributed to Fenton's reactions (R 1.11). In addition to iron, manganese was also used and found to be an alternative metal to perform Fenton's reactions. Although cellulose degradation was reported in this study, no reduction in cellulose crystallinity was observed.

$$M^{n+} + H_2O_2 \rightarrow M^{(n+1)+} + OH^{\cdot} + OH^{-} \quad \text{..... R 1.11}$$

where M^{n+} is a metal with an oxidation state of 'n' and supports Fenton's (or Fenton's like) decomposition of H_2O_2 and $M^{(n+1)+}$ is the oxidised metal ion.

As discussed in this section, all the mechanisms of cellulose degradation involve OH radicals mediated breakdown. An advanced oxidation process, namely photocatalysis that has the capability to produce OH radicals could hence be used (36-38).

1.7 Photocatalysis

Fujishima and Honda reported the mechanism of photocatalysis when investigating the water splitting reaction which occurred over a TiO_2 electrode (39). Ever since this striking observation, photocatalysis with TiO_2 and other photocatalysts have been reported for various applications Table 1.3.

Area of application	Photocatalyst used	Region of light used for photoexcitation	Reference
Microcystin-LR destruction	TiO_2 P25	UV	(40)
Microcystin-LR destruction	N-TiO_2	Visible	(41)
Bactericidal application (*Escherichia coli*)	TiO_2 P25	UV	(42)
Virus disinfection	TiO_2	UV	(43)
Fungal disinfection	TiO_2	Visible	(44)
Water splitting for H_2 production	LaNaTaO3	Visible	(45)
Wastewater treatment and dye degradation	TiO_2 P25	UV	(46)
Organics degradation	g-C_3N_4/TiO_2 composite	UV-visible	(47)

Table 1.3: Application of photocatalysis in various fields

Photocatalysis is a light driven chemical reaction that involves the movement of an electron from the valence band (VB) to the conduction band (CB) upon excitation by light of a specific wavelength (48). In order for the process to proceed, the energy absorbed by the semiconductor photocatalyst must be higher than or equal to the band gap energy (E_{bg}) (48). Figure 1.10 shows the mechanism of photocatalysis, demonstrating the excitation of electrons from VB to CB as a result of energy absorption.

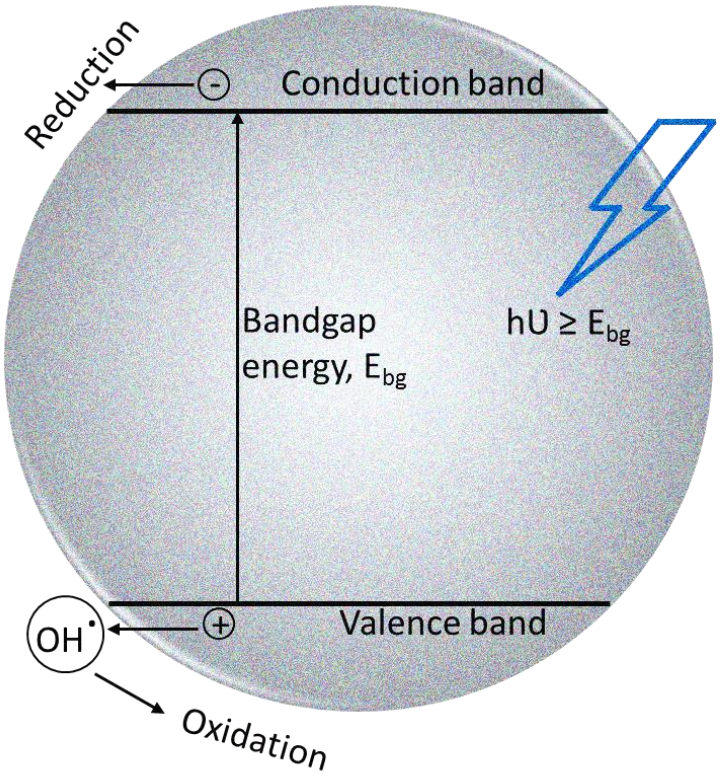

Figure 1.10: Mechanism of photocatalysis.

Upon illumination, photons are absorbed by the semiconductor photocatalyst particle which initiates the photoexcitation of an electron from VB to the CB leaving behind a photogenerated hole (h_{vb}^{+}) in the VB and an electron, e_{cb}^{-} at the top of the CB (R 1.12). This reaction occurs in the range of femtoseconds (49).

$$Photocatalyst \quad + h\nu \rightarrow \quad h_{vb^+} + e_{cb^-} \quad \text{..... R 1.12}$$

Both these photogenerated holes and CB bound electrons can participate in oxidation or reduction reactions directly (50). Additionally, the VB holes can react with water/OH^- to form $OH^{\cdot}$. These hydroxyl radicals are highly oxidising species and can degrade various organic compounds (R 1.13–R 1.14). The

CB electrons on the other hand are reducing and hence can react with molecular oxygen to produce superoxide radicals (R 1.15). These superoxide radicals can in turn play a role in the degradation of substrates (R 1.16). Furthermore, $O_2^{-\cdot}$ can contribute to the indirect production of $OH^{\cdot}$ via reactions R 1.17-R 1.19 (51,52). CB electrons can also react with the produced hydroxyl radicals to form hydroxyl ions (R 1.20).

$h_{vb^+} + OH^-(or\ H_2O) \rightarrow OH^{\cdot}$ .....R 1.13

$substrates + \cdot OH \rightarrow products$ .....R 1.14

$e_{cb^-} + O_2 \rightarrow O_2^{-\cdot}$ .....R 1.15

$O_2^{-\cdot} + reactants \rightarrow products$ .....R 1.16

$O_2^{-\cdot} + H^+ \rightarrow HO_2^{\cdot}$ .....R 1.17

$HO_2^{\cdot} + HO_2^{\cdot} \rightarrow H_2O_2 + O_2$ .....R 1.18

$H_2O_2 + e_{cb^-} \rightarrow OH^{\cdot} + OH^-$ .....R 1.19

$e_{cb^-} + OH^{\cdot} \rightarrow OH^-$ .....R 1.20

In addition to $OH^{\cdot}$/holes and $O_2^{-\cdot}$/electrons produced during photocatalysis, H_2O_2 and $HO_2^{\cdot}$ produced during the course of the reaction may also play important roles during photocatalysis depending on the area of application (R 1.17 and R 1.18). Finally, in addition to all the reactions occurring upon photoexcitation, a possible recombination reaction can also occur (R 1.21). Recombination reactions greatly reduce the photocatalytic efficiency because the photogenerated holes and CB electrons react and generate heat before participating in essential redox reactions. Hence, semiconductor particles with lesser defects (crystalline particles), smaller

particle size (in the nm range) and heterojunctions are usually chosen by researchers for photocatalysis to prevent recombination (53-55).

$h_{vb^+} + e_{cb^-} \rightarrow heat\ (recombination)$ .....R 1.21

In literature, however the use of electron acceptors has also been reported to reduce recombination (56). H_2O_2 is the most commonly used electron acceptor in photocatalysis to reduce recombination, because it generates OH radicals upon photolysis (R 1.22) (56-60). In addition to the production of OH radicals, H_2O_2 addition to a photocatalysis reaction mixture helps to reduce recombination by acting as an electron acceptor as seen from reaction R 1.23 (56,60). In addition to R 1.22 and R1.23, H_2O_2 also react with superoxide radicals according to R 1.24 to form OH radicals (56,60).

$H_2O_2 + h\nu \rightarrow 2OH^{\cdot}$ .....R 1.22

$H_2O_2 + e_{cb^-} \rightarrow OH^{\cdot} + OH^{-}$ .....R 1.23

$H_2O_2 + O_2^{-\cdot} \rightarrow OH^{\cdot} + OH^{-} + O_2$ .....R 1.24

The addition of H_2O_2 to the reaction mixture increases the overall quantity of OH radicals in solution. Due to the enhanced amount of OH radicals in solution, photocatalytic oxidation would be increased. It has however been reported that an increase in initial concentration of H_2O_2 does not always accompany an increase in the rate of photocatalytic oxidation. This could be due to the competition between substrates and H_2O_2 for the surface sites on the photocatalyst (57) or due to the scavenging of h_{vb}^+ and OH radicals by the excess H_2O_2 present in solution (56,58-62) (R 1.25-R 1.28).

$H_2O_2 + h_{vb^+} \rightarrow HO_2^{\cdot} + H^+$ .....R 1.25

$H_2O_2 + 2h_{vb^+} \rightarrow O_2 + 2H^+$ .....R 1.26

$H_2O_2 + OH^{\cdot} \rightarrow H_2O + HO_2^{\cdot}$ .....R 1.27

$HO_2^{\cdot} + OH^{\cdot} \rightarrow H_2O + O_2$ .....R 1.28

1.7.1 Photocatalysts

Photocatalysts absorb light based on their electronic structures and hence they can be classified into the following categories based on their band gap energies (63),

(i) highly photoactive,

(ii) weakly active (due to less negative conduction band),

(iii) weakly active (due to less positive valence band),

(iv) not active (due to narrow band gap) and

(v) not active (due to a large bang gap)

The wavelength required for photoexcitation is inversely proportional to the band gap energy of a photocatalyst. The wavelength required for photoexcitation can be determined by Planck's equation which is as follows,

$E_{bg} = \frac{hc}{\lambda}$ .....Equation 1.1

where, E_{bg} is the band gap energy (Joules), h is Planck's constant (6.626×10^{-34} Joules second), c is the speed of light (2.998×10^8 metre/second) and λ is the wavelength (metre). The conversion factor for 1 eV is 1.602×10^{-19} Joules. The band gap energies of various photocatalysts, along with the potentials required for $OH^{\cdot}$ and $O_2^{-\cdot}$ are shown in Figure 1.11 (64-66).

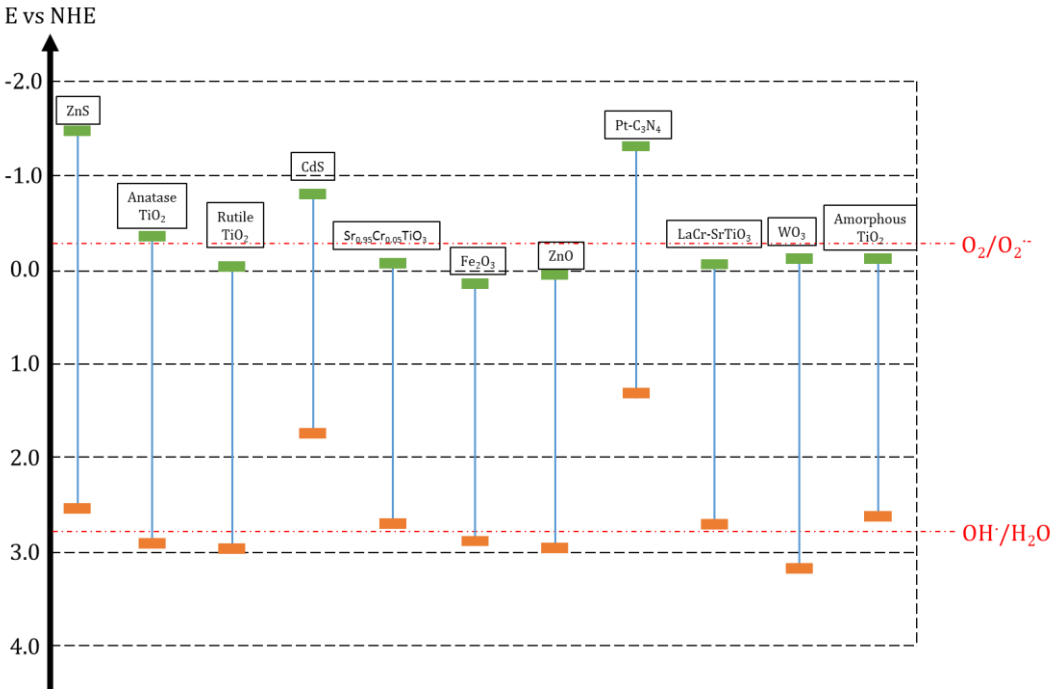

Figure 1.11: Band gap energies of various photocatalysts (64-66).

There are a range of materials that could be photoexcited and used as photocatalysts, however TiO_2 is the most commonly used photocatalyst. TiO_2 photocatalyst particles are water insoluble white odourless transition metal oxide powders that are non-toxic, cheap, inert and photostable. Three crystal phases of TiO_2 exists, namely; anatase, rutile and brookite. As can be seen from Figure 1.11, anatase form of TiO_2 with a band gap of 3.2 eV is a photocatalyst that falls under the 'highly photoactive' category. Band gap of 3.2 eV corresponds to an excitation wavelength of 387 nm (as calculated from Equation 1.1), which is in the near UV light region of the spectrum. The most commonly used form of TiO_2 is the P25 which is a mixture of 70 % anatase and 30 % rutile crystal phases. This combination is commercially preferred to avoid photocatalytic losses due to recombination (63).

TiO_2 has its particle size in the range of 25-65 nm (67), however it can increase to a few microns in size due to agglomeration. Surface charge is an allied phenomenon to particle size and can affect the particle aggregation (68). At a pH higher than its iso-electric point (>pH 6.25), TiO_2 has a negative surface charge (R 1.29).

$$Ti - OH \rightarrow Ti - O^- + H^+ \quad \text{.....R 1.29}$$

When the pH is however lower than its iso-electric point, TiO_2 exhibits a positive surface charge (R 1.30). At a lower pH resulting in a positive surface charge and increased repulsive forces, self-aggregation of particles is suppressed (Figure 1.12).

$$Ti - OH + H^+ \rightarrow Ti - OH_2{}^+ \quad \text{.....R 1.30}$$

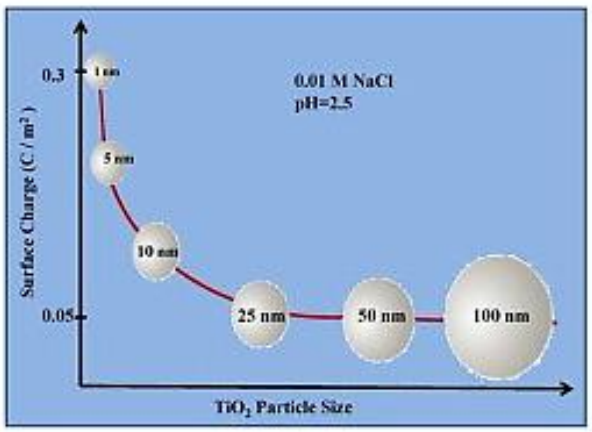

Figure 1.12: Relationship between TiO_2 particle size and surface charge, reprinted with permission from “Elsevier, Journal of Colloid and Interface Science, Copyright 2013” (69).

When a TiO_2 particle is illuminated, a series of reactions (R 1.13-R 1.21) occur. The timescale of these reactions occurring upon photoexcitation of TiO_2 is shown in Figure 1.13.

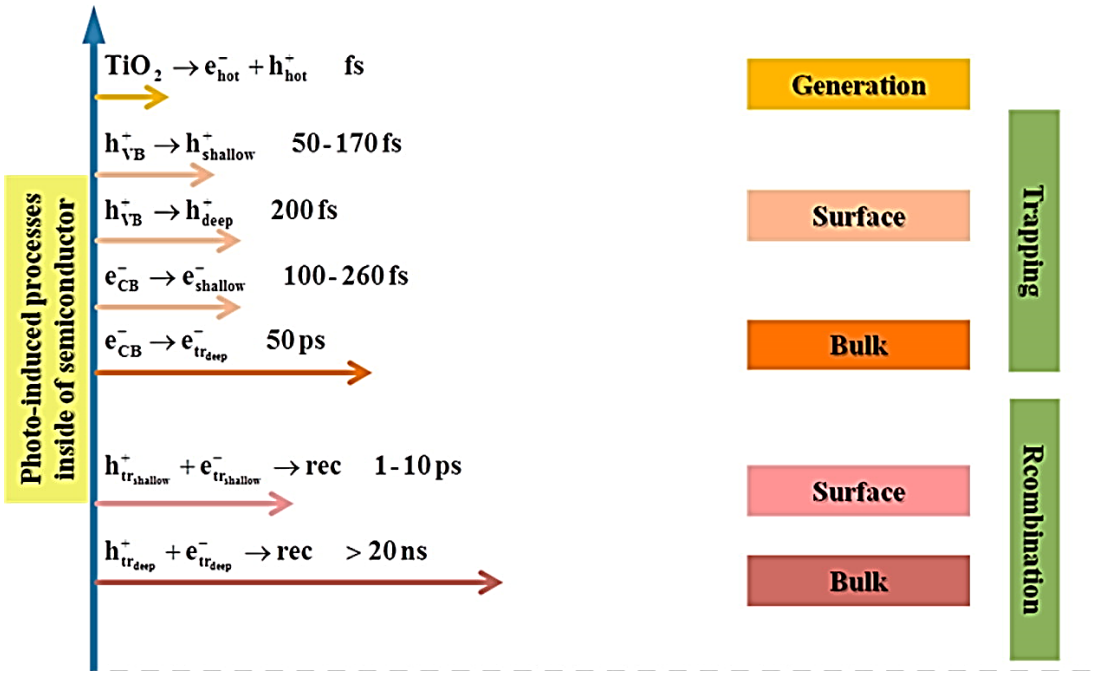

Figure 1.13: Timescale of reactions occurring upon photoexcitation, reprinted with permission from "ACS publications, Chemical Reviews, Copyright 2014" (70).

In addition to TiO_2, a range of materials such as ZnO (E_{bg}=3.2 eV), $SrTiO_3$ (E_{bg}=3.2 eV), WO_3 (E_{bg}=2.8 eV), ZnO (E_{bg}=3.6 eV), CdS (E_{bg}=2.4 eV) and Pt-C_3N_4 (E_{bg}=2.8 eV) have also been used for photocatalysis (37,71,72). When E_{bg} is between 3.1-3.9 eV, the photocatalyst can be photoexcited in the near UV region, whereas when E_{bg} is less than 3.1 eV, the photocatalyst can be photoinduced using visible light. Since only 4-5 % of the solar spectrum correspond to UV light, considerable interest has now shifted towards the production of visible light activated photocatalysts.

1.7.2 Illumination

Illumination is a critical parameter for any photocatalytic process because, a suitable light source has to be made available for the photocatalyst to remain active in the reaction mixture. The photon flux from the illumination source affects the rate of photocatalysis. A low photon flux, is linearly linked to the rate, whereas the rate is proportional to the square root of flux at a higher photon flux (73). In addition to flux, emission spectra of the illumination source is also an important factor affecting the photocatalytic process. The spectral range of some common illumination sources are shown in Table 1.4.

Type of illumination source	**Spectral range**	**Power**	**Reference**
Mercury arc lamp	UV and visible (265 – 580 nm)	300 W	(74)
Medium pressure mercury arc lamp	UV (peak at 365 nm)	700 W	(75)
Incandescent lamps	UV and visible (200 – 600 nm)	200 W	(76)
Mercury vapour fluorescent lamp	UV (peak at 254 nm)	6 - 10 W	(77-79)
PL-L-40 Philips UV lamps	UV (peak at 365 nm)	40 W	(80)
Blacklight blue Panasonic Fluorescent lamps	UV (300 – 400 nm)	4 W	(81)
Light emitting diodes (FoxUV™)	UV (peak at 360 nm)	454 µW	(82,83)
InGaN Light emitting diodes	UV (390 – 410 nm)	10 – 20 mW	(84)
TG Purple Hi LED E1L5M-4P0A2-01 Light emitting diodes	UV (peak at 383 nm)	20 mW	(85)

Table 1.4: Potential illumination sources used in photocatalysis and their emission spectra

The wavelength suitable for photoexcitation of a photocatalyst is determined by its band gap energy and therefore illumination source selection

is a key parameter in system design. Various illumination sources that have been used for photocatalysis are discussed below.

1.7.2.1 Arc lamps

Arc lamps are the most commonly used irradiation sources for photocatalysis. In arc lamps, radiation is emitted when atoms are excited due to an electrical discharge between a cathode and an anode (86). Elements such as sodium, krypton, xenon and mercury are used for such purposes. Xenon and mercury arc lamps are the most frequently used lamps for photocatalysis due to their emission spectra (74,75,87,88). The spectra of the mercury lamps depend on the pressure of the element in the lamp and based on this medium pressure (500-1500 mmHg pressure) mercury lamps are the regularly used lamps in photocatalysis for their spectral emission in the range of 190 – 600 nm (74,86). In typical experiments, Tian *et al*. used Hg arc lamp (UV light source) as the light source with a range of TiO_2 materials as photocatalysts for methyl orange degradation (74). The initial concentration of methyl orange in this reaction was 0.02 g/L and the concentration of photocatalyst used was 1 g/L. Upon photocatalysis for 25 minutes, more than 90 % of methyl orange was found to be degraded when reduced TiO_2 nanobelts were used as photocatalysts. When P25 or pristine TiO_2 nanobelts were used as photocatalysts, the degradation observed was however only 65.5 % and 63 % respectively.

1.7.2.2 Incandescent lamps

Incandescent lamps are those where tungsten filaments are heated using electrical current to radiate light. Tungsten filament lamps emit light in the visible region and therefore are suitable for visible light photocatalytic processes (89). Incandescent lamps generate immense heat while operating and hence are less frequently reported for photocatalytic processes (76,89). Yadav *et al*. performed methylene blue degradation experiments under visible light generated by a 200 W incandescent lamp on a Cr doped TiO_2 photocatalyst (76). They reported that a 10-hour degradation time is required to completely mineralise methylene blue under the above-mentioned conditions for a dye starting concentration of 1.6×10^{-5} M.

1.7.2.3 Fluorescent lamps

Fluorescent lamps operate based on the principle of luminescence at a lower temperature when compared to incandescent and arc lamps. The commonly used germicidal lamps are fluorescent lamps and hence can be used for photocatlaysis. These lamps span over a wide spectral range from UV-C or far UV (ultra violet) (190 nm) to the visible range. Due to the broad wavelength ranges of these lamps, they are being used commonly in photocatalysis as a relatively cheap and efficient light source (41,77-81).

For instance, Adams *et al*. used UV fluorescent lamps to illuminate a novel drum reactor consisting of TiO_2 pellets to degrade methylene blue dye (46). They looked at the effect of light source distance on the degradation of methylene blue in addition to other parameters. The lamps were positioned at

4 cm, 8 cm, 16 cm and 32 cm away from the drums. They determined that when the distance between the lamp and the drum was doubled, the light intensity illuminating the photocatalyst decreased by four folds according to inverse square law (Equation 1.2) (90). Due to a decrease in light intensity, the amount of active photocatalysts in the drum were relatively less and hence a lower degradation of methylene blue was achieved with increasing lamp distance.

$$E = \frac{I}{d^2}$$ ..... Equation 1.2

where E is the light intensity per unit area, I is the light intensity and d is the distance between the light source and point of measurement.

1.7.2.4 Light emitting diodes

A light emitting diode (LED) is a p-n junction diode which emits light when the electrons combine with the holes in the semiconductor with an applied voltage. LED's use relatively low energy (in terms of milli and micro watts) when compared to other light sources such as arc lamps, incandescent and fluorescent lamps which are in the range of hundreds to tens of watts of energy. Due to this low energy input and a range of available wavelengths, LED's are an attractive illumination source for photocatalysis (82-85,91).

Shie and Pai performed photocatalytic degradation of toluene with Ag/TiO_2 under LEDs and compared the rates of degradation to different UV light sources (85). Their reactor set up consisted of a Pyrex vessel of 1 L capacity with a light source installed in it. The light source used was a 16 W

UV-C lamp (peak wavelength at 254 nm) or a 12 W UV-A lamp (peak wavelength at 365 nm) or an array of 40 LEDs (20 mW, peak wavelength at 383 nm). After 30 minutes of passing dry air, toluene was introduced into the reactor and then the change in concentration of toluene over time was monitored. Their results indicated that the UV LED photoreactor system for the degradation of toluene was 7.4 times energy efficient than the UV-C system.

1.7.2.5 Solar light

Considerable interest is also given to solar light photocatalysis as it is a sustainable source of light. Solar light's spectrum consists of both UV (approximately 4-5 %) and visible light and hence could be utilised for photocatalysis to perform degradation and energy production (45,92). Due to the lack of a range of commercial visible light photocatalysts, however, maximum exploitation of solar light is not possible.

Skillen *et al*. performed H_2 production experiments over $LaNaTaO_3$ from water with oxalic acid as the sacrificial electron donor under solar light and UV-visible lamps (45). They performed H_2 evolution experiments in a novel propeller fluidised photocatalytic reactor illuminated by either 4 × 36 W UV-visible lamps in an illumination chamber or concentrated solar light. Results revealed that 6 hours' illumination from the lamps yielded 20.6 µM H_2 whereas 4.6 µM H_2 was generated when illuminated for the same time with concentrated solar light. The production rate in the former case was found to be 14 µM/g/h whereas in the latter case was 5 µM/g/h. The lower production

rate and amounts were attributed to the presence of contaminants in the solar light path and the weather dependent nature of the solar light.

1.7.2.6 Controlled periodic illumination

Controlled periodic illumination (CPI) is an illumination source operating condition during which the light source is switched on (T_{ON}) and off (T_{OFF}) alternatively to increase the efficiency of semiconductor photocatalysis (Figure 1.14). The concept of CPI was first suggested by Sczechowski *et al*. in the early 1990's where they used alternating light and dark times to decompose formate (93). The efficiency of the photocatalysis upon CPI was reported to be increased by 500 %.

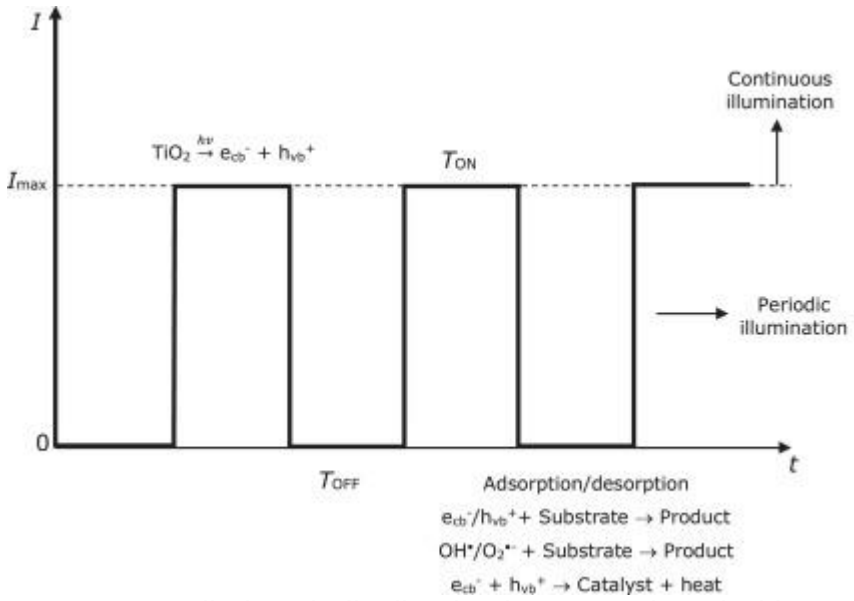

Figure 1.14: Controlled Periodic Illumination, reproduced with permission from "Elsevier, Journal of Photochemistry and Photobiology A: Chemistry, Copyright 2015" (49).

During CPI, upon illumination of the photocatalyst particle, electron-hole pairs are generated. These electron-hole pairs further react with water/OH^- or O_2 to form $OH^{\cdot}$ and $O_2^{-\cdot}$ respectively. Illumination is essential for

this initial photoexcitation step for the generation of electron-hole pairs whereas the subsequent steps for the formation of reactive oxygen species does not require light and hence can occur in the dark. This alternating T_{ON} and T_{OFF} periods will avoid the accumulation of charge carriers on the photocatalyst which may lead to recombination or unnecessary reactions that may lower the overall efficiency of the process (49).

For instance, Tokode *et al*. monitored the change in photonic efficiencies for the photocatalytic degradation of methyl orange under CPI using UV LED's as the illumination source (82). In a typical experiment, T_{ON} was kept constant at 1 s and T_{OFF} was varied from a minimum of 0.1 s to 1.1 s to determine the photonic efficiencies for photocatalytic methyl orange degradation. In addition, another set of experiments with a constant T_{OFF} at 1.1 s and varying T_{ON} from a minimum of 0.1 s to 1.1 s was also conducted. It was reported that with a constant T_{ON} and varying T_{OFF}, the photonic efficiencies increased with an increase in T_{OFF}. This was attributed to the O_2 re-adsorption to the photocatalyst particle during T_{OFF} thereby reducing recombination. Furthermore, it was also reported that when T_{OFF} was kept constant, the photonic efficiencies decreased with increasing T_{ON} which was due to the accumulation of charge carriers with increasing T_{ON}. It was also concluded that increasing the T_{OFF} increased the photonic efficiency by 38 % and decreasing the T_{ON} increased the photonic efficiency by 89 %.

1.7.3 Photocatalysis kinetics

Photocatalysis kinetics, like any other chemical reactions kinetics can be determined by monitoring the degradation of reactants or formation of products over time. One of the most commonly observed models in photocatalysis kinetics is of first order (94). First order kinetics is usually represented by Equations 1.3 and 1.4.

$$\frac{d[C]}{[C]} = \int -K_r . dt \quad \text{.....Equation 1.3}$$

where [C] is the concentration of the reactant, K_r is the reaction rate constant and t is time. Integrating Equation 1.3 between the limits t = 0 to t = t for time and [C] = $[C]_0$ to [C] = $[C]_t$ at time t for concentration, Equation 1.4 is obtained.

$$\ln[C]_t = \ln[C]_0 - kt \quad \text{.....Equation 1.4}$$

In photocatalysis, however due to the effect of initial reactant concentration on the rate of product accumulation, rate kinetics has been described using Langmuir-Hinshelwood model (95). For instance, in the case of a heterogeneous catalytic reaction as shown in Equation 1.5, the rate is given as r (Equation 1.6).

$$S1 + S2 \rightarrow P1 + P2 \quad \text{.....Equation 1.5}$$

$$r = k\Theta_{S1}\Theta_{S2} \quad \text{.....Equation 1.6}$$

where S1 and S2 are substrates 1 and 2, P1 and P2 are products 1 and 2, k is the rate constant and Θ_{S1} and Θ_{S2} are given as follows,

$$\Theta_{S1} = \frac{K_{S1}X_{S1}}{(1+K_{S1}X_{S1})} \quad \text{.....Equation 1.7}$$

$$\Theta_{S2} = \frac{K_{S2}X_{S2}}{(1+K_{S2}X_{S2})}$$ ……Equation 1.8

where K_{S1} and K_{S2} are the adsorption constants of S1 and S2 respectively and X_{S1} and X_{S2} are the concentration of the reactants S1 and S2 in the liquid phase respectively.

Now, substituting the values of Θ_{S1} and Θ_{S2} from Equations 1.7 and 1.8 in Equation 1.6 gives Equation 1.9.

$$r = k\frac{K_{S1}X_{S1}K_{S2}X_{S2}}{(1+K_{S1}X_{S1})(1+K_{S2}X_{S2})}$$ .....Equation 1.9

During photocatalysis, when one of the substrates, S2 is present in excess or is constant, for instance, when a photocatalytic reaction mixture is aerated continuously with ambient air, the amount of oxygen is constant and hence Θ_{S2} becomes a constant, or in the case of S2 being present in excess, Θ_{S2} equals 1 (96,97). Hence, Equation 1.9 can be re-written as Equation 1.10.

$$r = k'\frac{K_{S1}X_{S1}}{(1+K_{S1}X_{S1})}$$ .....Equation 1.10

where k' = k Θ_{S2}.

Equation 1.10 can be rewritten as follows,

$$r = k'\frac{K_{S1}X_{S1}}{(1+K_{S1}X_{S1})} = k_{app}X_{S1}$$ .....Equation 1.11

where k_{app} is known as the apparent rate constant. Taking the reciprocal of Equation 1.11 and rearranging it gives Equation 1.12

$$\frac{1}{k_{app}} = \frac{1}{k'K_{S1}} + \frac{X_{S1}}{k'}$$ .....Equation 1.12

In addition to the influence of reactant concentration, the effect of incident light also influences the rate of the reaction in photocatalysis. The relationship incorporates light intensity to Equation 1.11 and is given by a modified Langmuir Hinshelwood as shown in Equation 1.13 (98,99).

$$r = \frac{k\prime(\gamma.I_{max})^{m}K_{S1}X_{S1}}{(1+K_{S1}X_{S1})} \quad \text{.....Equation 1.13}$$

$$\gamma = \frac{T_{ON}}{T_{ON}+T_{OFF}} \quad \text{.....Equation 1.14}$$

where, γ is the ratio of light time to the total operated time in a CPI process, I_{max} is maximum intensity and m is order of light intensity. As can be seen from the equation, γ is proportional to the rate of the reaction. Same is the case with the I_{max} at low intensities, however at higher intensities the rate tends to be independent of light intensity (99).

1.8 Hydroxyl radicals

1.8.1 OH radical diffusion

OH radicals produced during semiconductor photocatalysis is one of the most important reactive oxygen species generated during the process. These radicals produced at the surface of the photocatalyst particles react with surface adsorbed reactants and oxidise them to products, however there is also a possibility that these species can diffuse into the bulk and still perform oxidation as shown in Figure 1.15 (100).

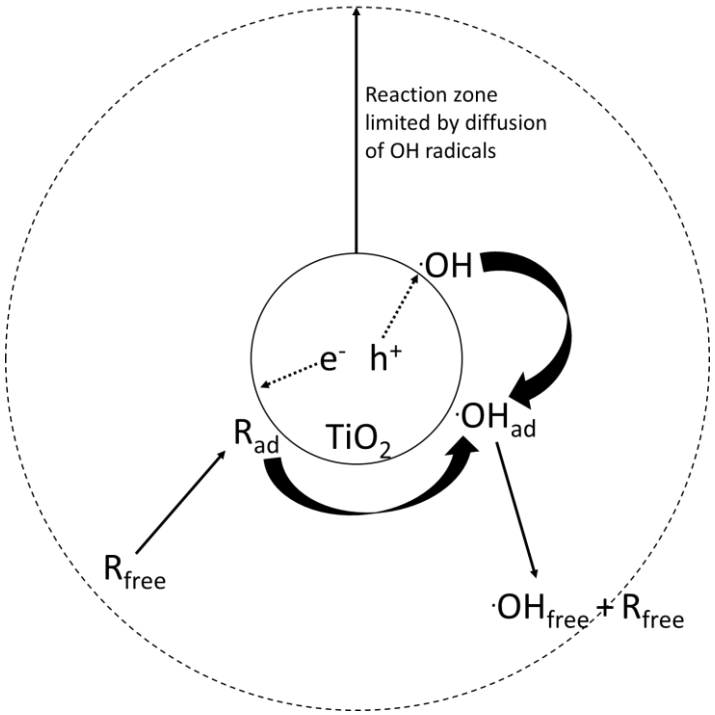

Figure 1.15: Schematic illustrating the diffusion of OH radicals, adapted from Choi *et al*. (100) where R_{free} is the reactant in bulk, R_{ad} is the reactant adsorbed onto the photocatalyst surface, $\cdot OH_{ad}$ is the surface bound hydroxyl radical and $\cdot OH_{free}$ is the hydroxyl radical that diffused into the bulk.

The diffusion of OH radicals in bulk was verified by a series of simple experiments performed by Choi *et al.* (100). They used tetramethylammonium (TMA) as the model compound to illustrate OH radical diffusion. A suspension of TMA and 0.5 g/L TiO_2 photocatalyst was prepared and maintained at pH 3 and pH 11 (2 sets). Then t-butanol was added to one of the sets as a bulk OH radical scavenger. Upon irradiation for 6 hours for suspensions without scavengers, the highest TMA degradation was observed for the suspension with pH 11 followed by pH 3. At pH 3, TMA does not adsorb onto the surface of TiO_2 as it carries a positive charge (isoelectric point of TiO_2 is 6.25) whereas at pH 11 TMA, hosting a negative charge adsorbed onto the photocatalyst. Due to these reasons TMA was oxidised by the OH radicals present in bulk in the former case and by a combination of surface adsorbed and bulk radicals in the latter case. During the presence of a scavenger however, TMA

degradation was only observed at pH 11 but not at pH 3. This was because, at an acidic pH when only the surface radicals prevail and when the radicals in bulk were scavenged, TMA could not be degraded, whereas at an alkaline pH TMA adsorbed onto the surface of the photocatalyst particle and hence the surface bound OH radicals oxidised the adsorbed TMA.

As seen from the example, it is necessary for the reactant to be in contact with the reactive oxygen species to undergo the desirable reaction. This could either be facilitated via varying the pH of the suspension so that the reactant can adsorb onto the surface of the photocatalyst for photodegradation or improve mass transfer so that the OH radicals in the bulk can come in contact with the reactant and form desirable products. The latter case is of important consideration when the reactant is pH sensitive. Mass transfer limitations in photocatalysis can be overcome by appropriate reactor designs which will be discussed in the subsequent section (Section 1.9).

1.8.2 OH radical quantification

To get a better understanding of photocatalysis, total OH radicals produced by the photocatalyst have to be quantified. OH radicals have a short lifetime of approximately one nanosecond and hence it is highly unlikely to quantify it directly (63). Therefore, a range of methods have been developed in the past such as emission spectroscopy, laser induced fluorescence, electron spin resonance, spin trap and chemical probes or quencher based methods to quantify OH radicals (63,101-115). Methods using chemical probes capture OH radicals as a product of a chemical reaction and based on

its stoichiometry, the amount of OH radicals can then be calculated. A common approach for chemical probe based quantification is either through fluorimetric or colourmetric analysis. A selection of the OH radical quantification methodologies found in literature based on fluorescence and colourimetry are shown in Table 1.5.

Reaction	Product quantified	Stoichiometry	Measurement	References
Dimethyl sulfoxide (DMSO) added to a Fenton's or Photo Fenton's reaction mixture and monitored for formaldehyde production	Formaldehyde	2 moles of OH radical gives 1 mole of formaldehyde	Colourimetric measurement at 580 nm	(106-109)
Monitoring the amount of H_2O_2 present in the mixture after every reaction of Fenton's or photo Fenton's	H_2O_2	1 mole of H_2O_2 gives 1 mole of OH radical	Colourimetric measurement at 410 nm	(108)
Coumarin + 2OH radicals = 7-hydroxycoumarin + H_2O	7-hydroxy coumarin	1 mole of OH radical yields 1 mole of 7-hydroxycoumarin	Measurement of fluorescence intensity at 456 nm	(63,104,105,114,116)
Terepthalic acid + OH radical = 2-hydroxyerepthalic acid	2-hydroxy terepthalic acid	1 mole of OH radical gives 1 mole of 2-hydroxyereptha lic acid	Measurement of fluorescence intensity at 425 nm	(101-103,106)

Table 1.5: Chemical probe based OH radical quantification methods.

In the past, OH radical quantification have been carried out for various commercially available photocatalysts, photo-Fenton's reaction and other modified TiO_2 based visible light photocatalysts with coumarin as the reactant (63,104,105,114,116). The photocatalytic degradation of coumarin yields a number of products such as 7-hydroxycoumarin, 3-hydroxycoumarin, 4-hydroxycoumarin, 6-hydroxycoumarin, 8-hydroxycoumarin and ortho coumaric acid (117). 7-hydroxycoumarin is the only fluorescent product of the reaction that could be quantified using its fluorescence intensity, and hence based on the stoichiometry of 7-hydroxycoumarin produced, the amount of OH radicals can be calculated. In this work, one of the objectives was to quantify the OH radical produced by novel visible light photocatalysts synthesised in the collaborator's laboratory and compare it to the OH radical production from TiO_2 photocatalysis. The efficiency of OH radical production in photocatalysis depends on the band gap of the photocatalysts and illumination source as mentioned in the previous sections. Apart from these parameters, reactor design is also vital to enhance the production of OH radicals.

1.9 Reactor design

Reactors are vessels designed to perform chemical reactions. Photocatalytic reactors are vessels that incorporate light distribution as a design parameter in addition to conventional reactor design parameters. A typical photocatalytic reactor has to facilitate ample light distribution via reflection and scattering, provide suitable mixing if required and enhance mass

transfer. Some important parameters to be taken into account while designing a photocatalytic reactor are as follows (86,118),

(i) total irradiated catalyst surface area,

(ii) light distribution,

(iii) ease of product recovery

(iv) mass transfer

(v) construction material

There has been a number of reactor configurations mentioned in the literature, which can be broadly divided into suspended or immobilised catalyst photoreactors. A review by McCullagh *et al.* covered a variety of these available designs such as the annular photoreactor, packed bed photoreactor, Taylor vortex photoreactor, fluidised bed reactor, coated fibre optic cable reactor, falling film reactor and fixed bed reactor (52). It is not feasible to compare the current reactor designs on a common scale as they have their own advantages and disadvantages based on their area of application (52).

Recently 12 different photocatalytic reactors for wastewater treatment were compared by using a benchmark ratio proposed as the photocatalytic space time yield (PSTY) (119). According to Leblebici *et al*. PSTY is defined as the “volume of water treated for each kW lamp power per volume of reactor per unit of time” (119). They concluded that among the compared designs, a pilot scale slurry reactor obtained the highest score. Additionally, it was also observed that an immobilised microreactor had high area to volume geometry. Furthermore, with an effective scale up of the microreactor using LED’s as the

light source, it was determined that the microreactors can perform better than slurry reactors.

1.9.1 Suspended photoreactor

Suspended photoreactors are those in which the reaction mixture comprises of the photocatalysts suspended in solution (reactant). Suspended photocatalytic reactors are used when an increased surface area of the photocatalyst is required to carry out photocatalysis. Increased surface area of the photocatalysts will enhance the interaction between the photocatalysts and reactant, improve mass transfer and enhances the overall photonic efficiency. Although a high surface area is achieved in suspended photoreactors, the separation of photocatalyst from the reaction mixture is extremely difficult making it a major disadvantage. Light penetration issues also have to be considered in such systems while using photocatalysts of higher concentrations.

Shon *et al.* performed photocatalytic wastewater degradation using TiO_2 P25 photocatalyst material in a suspended photocatalytic reactor with the light source inserted into the reactor (120). The system was designed to be a batch reactor which can support up to three 8 W UV lamps as the illumination source (Figure 1.16). The reaction vessel containing wastewater had a magnetic stirrer bar to facilitate mixing. An air blower was also fixed to the bottom vessel to enable air (O_2) bubbling. The vessel was jacketed to allow water to pass through for cooling purposes. For the photocatalytic reaction to begin, 1 g/L P25 was suspended in the wastewater solution and either one,

two or three lamps were switched on and the degradation of wastewater was monitored in terms of dissolved organic carbon. With the increase in number of lamps, the light intensity reaching the photocatalyst increased thereby increasing the rate of photocatalytic degradation. It was determined that compared to one lamp, when three lamps were switched on to illuminate the reactor, the rate constant was 27.6 times higher.

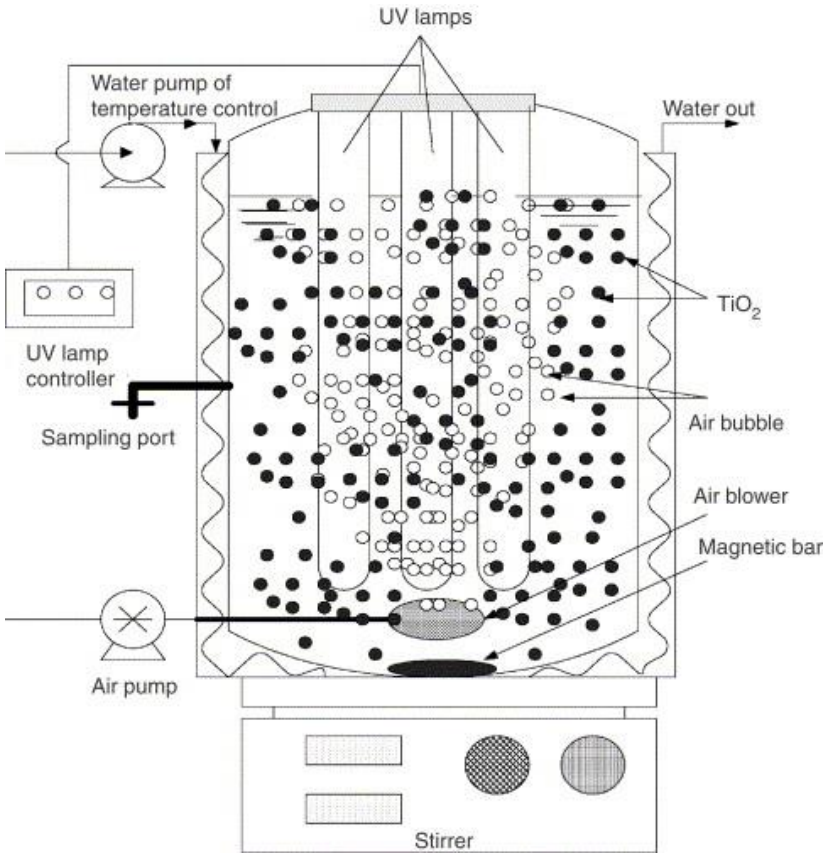

Figure 1.16: Suspended photocatalytic reactor for wastewater treatment, reproduced with permission from “Elsevier, Water Research, Copyright 2005” (120).

Increased photocatalyst loading will increase the total available surface area for photocatalysis but will also gradually decrease the light penetration into the reactor leading to decreasing efficiency. This was demonstrated by Nan Chong *et al.* when they increased the concentration of

the H-titanate nanofibers from 0.5 to 4 g/dm^3 to degrade congo red dye in an annular slurry reactor (121) (Figure 1.17). When the concentration of the photocatalyst was increased from 0.5 to 3 g/dm^3 they noticed a linear increase in the dye degradation efficiency, however, when the concentration increased to 4 g/dm^3 the efficiency dropped. This suggested that the increase in photocatalyst concentration decreased light penetration due to a 'light shielding effect'.

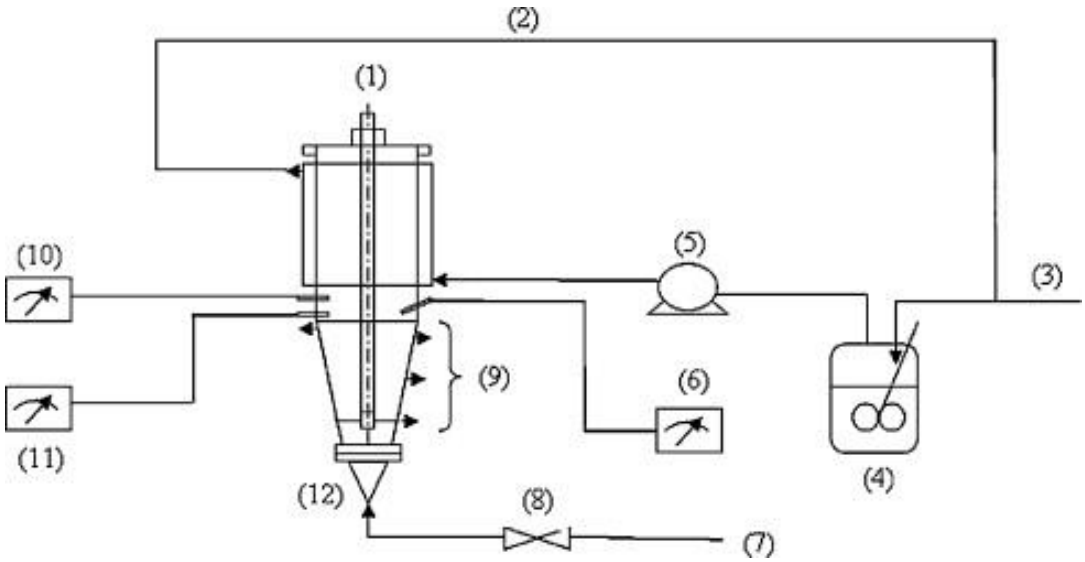

Figure 1.17: Experimental setup for the annular slurry photoreactor system: 1 - UV light, 2 - recirculation water line, 3 - fresh cool water line, 4 - cooling water vessel, 5 - cooling water pump, 6 - temperature meter, 7 - compressed air supply line, 8 - compressed air regulation valve, 9 - sampling ports, 10 - pH meter, 11 - dissolved oxygen meter and 12 – photoreactor, reproduced with permission from "Elsevier, Chemical Engineering Journal, Copyright 2008" (121).

To elucidate the importance of mass transfer, Skillen *et al*. performed H_2 production experiments in a propeller fluidised photocatalytic reactor, by varying the speeds of the propeller from 0 – 1730 rpm (Figure 1.18) (45). The photocatalytic reaction mixture was composed of 0.025 M oxalic acid solution in water and 1 g/L Pt-C_3N_4 photocatalyst. A 144 W UV-visible lamp was used

as the light source. At a propeller speed of 0 rpm, the total H_2 production was 15.9 µM, however, when the speed was increased to 289 rpm it increased to 42.4 µM and further increased to 65.7 µM at 1035 rpm. This experiment demonstrated that mass transfer limitations can be eliminated when the photocatalyst slurry is fluidised. When the propeller speeds were however increased beyond 1035 rpm to 1384 and 1730 rpm, the total H_2 production declined to 65.2 and 61.9 µM respectively. Since maximum photon penetration depth was achieved with 1035 rpm, increasing the speeds beyond this did not yield a higher amount of H_2.

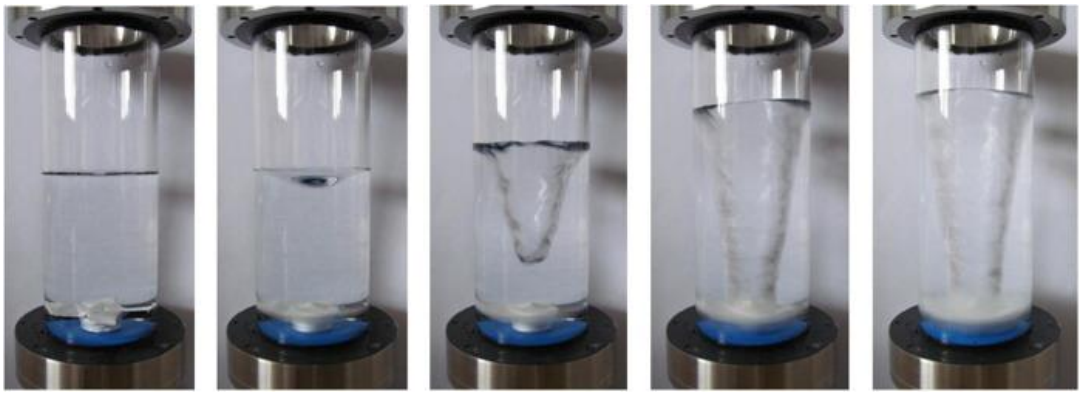

Figure 1.18: Propeller fluidised photocatalytic reactor operating over a range of 0 – 8 dcV (0 – 1730 rpm) designed to overcome mass transport limitations, reproduced with permission from “Elsevier, Chemical Engineering Journal, Copyright 2016” (45).

1.9.2 Immobilised photoreactor

Immobilised photoreactors are those that have the photocatalysts immobilised (coated) on to a support in the photoreactor. The support could be glass beads, foams, stainless steel meshes, walls of the reactor and optical fibres (52). Immobilised photoreactors overcome the disadvantage of light penetration and photocatalyst separation posed by the slurry systems, however a high surface area of the photocatalysts cannot be achieved with

immobilised systems. Immobilised reactors are also mass transport limited (52,119).

To overcome mass transport limitations in immobilised systems, McMurray *et al*. performed photocatalytic degradation of formic acid and oxalic acid in a CSTR (continuous stirred tank reactor) with TiO_2 immobilised on borosilicate glass sheets (122) (Figure 1.19). They performed the degradation experiments under different stirring speeds ranging from 1000 – 2000 rpm and determined that the rates of degradation were similar for speeds above 1000 rpm and hence concluded that mass transport limitations could be overcome with mixing speeds of higher than 1000 rpm. Mass transport limitations could also be overcome in fixed bed systems when they are aerated (52).

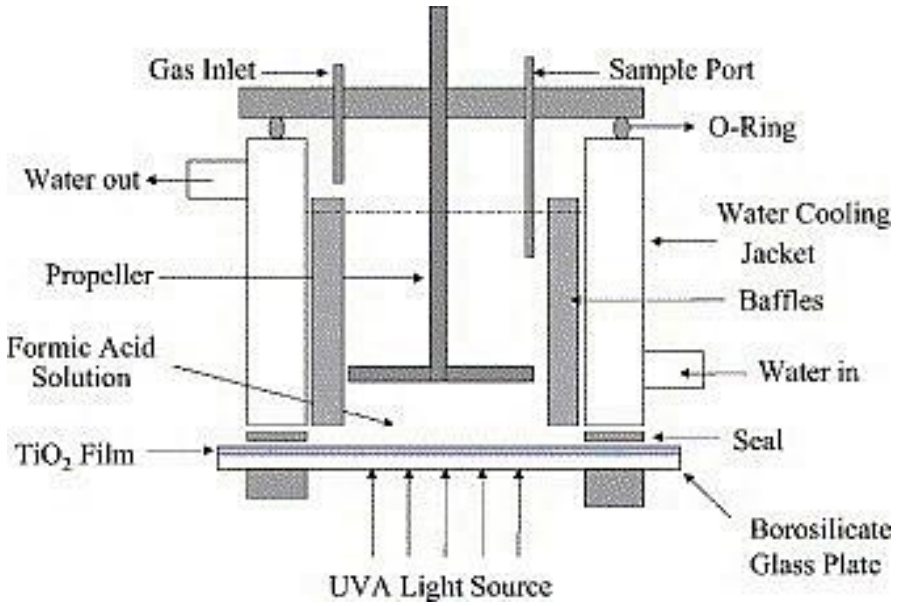

Figure 1.19: Stirred tank reactor with immobilised photocatalyst, reproduced with permission from “Elsevier, Applied Catalysis A: General, Copyright 2003” (122).

To demonstrate the photocatalytic capability of an immobilised photocatalyst, TiO_2 P25 was coated on to optical fibres to degrade 4-

chlorophenol under UV light by Peill and Hoffmann (123) (Figure 1.20). A part of the cladding and the outer core of the optical fibre buddle (20 cm length) was stripped and coated with P25 and dried. The bundle had 72 quartz optical fibres of 1 mm diameter each. An optical fibre reactor was then built with the P25 coated fibre end dipped in the Pyrex vessel to degrade 0.1 mM solution of 4-chlorophenol. Light from a xenon arc lamp was focussed on to the non-coated end of the optical fibre bundle at various incident angles close to 90 degrees. A gas bubbling system was also included at the bottom to enhance mass transfer. A light absorption higher than 95 % was recorded for this system and it was found that 4-chlorophenol could be completely degraded within 13 hours. They also compared the performance of this reactor with a conventional slurry reactor and found the quantum efficiencies to be similar. It was further concluded that this comparable performance of the optical fibre reactor was due to the increased light absorption (minimal light loss) and elimination of mass transfer limitations.

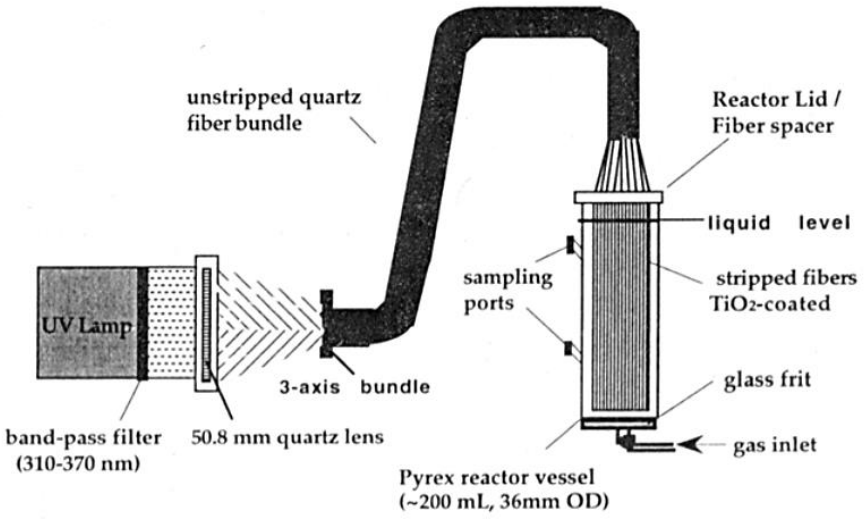

Figure 1.20: Optical fiber reactor with coated photocatalyst for 4-Chlorophenol degradation, reproduced with permission from “American Chemical Society, Environmental Science and Technology, Copyright 1995” (123).

1.10 Photocatalytic cellulose breakdown

As discussed in the previous sections, in addition to various available photocatalysts and illumination sources, an effective reactor design is also necessary to obtain the desired output from the photocatalytic process. A synergy of photocatalysts, light sources and photoreactor design has been successfully used as an advanced oxidation process to address various environmental problems such as pollutant decontamination, wastewater treatment and degradation of organic compounds (37,38,124-126). This advanced oxidation process has now been extended to degrade polysaccharides, especially cellulose (127,128).

The photocatalytic breakdown of cellulose has not been extensively reported but there have been a small number of reports in the literature, earliest of which was performed by Kawai and Sakata in 1980 (128). They dispersed cellulose in water or NaOH and used it as a sacrificial agent for hydrogen generation over a $RuO_2/TiO_2/Pt$ photocatalyst under UV light. Filter paper cut into pieces was used as the source of cellulose. This experiment yielded 70 µM H_2 in 20 hours, whereas the control experiment with no sacrificial agent yielded only 4 µM.

Another study also discussed the breakdown of the cellulose via TiO_2 photocatalysis under UV (127). Fan *et al* published their work featuring the photodegradation of cellulose dissolved in 66% $ZnCl_2$ under UV light with TiO_2 as a photocatalyst (127). The final product of this process was 5-HMF, whereas the intermediate product was glucose. The fact that cellulose

undergoes degradation under strong acidic conditions as well as from photocatalysis could also contribute to the production of glucose and 5-HMF. Figure 1.21 shows their suggested mechanism for the above-mentioned process.

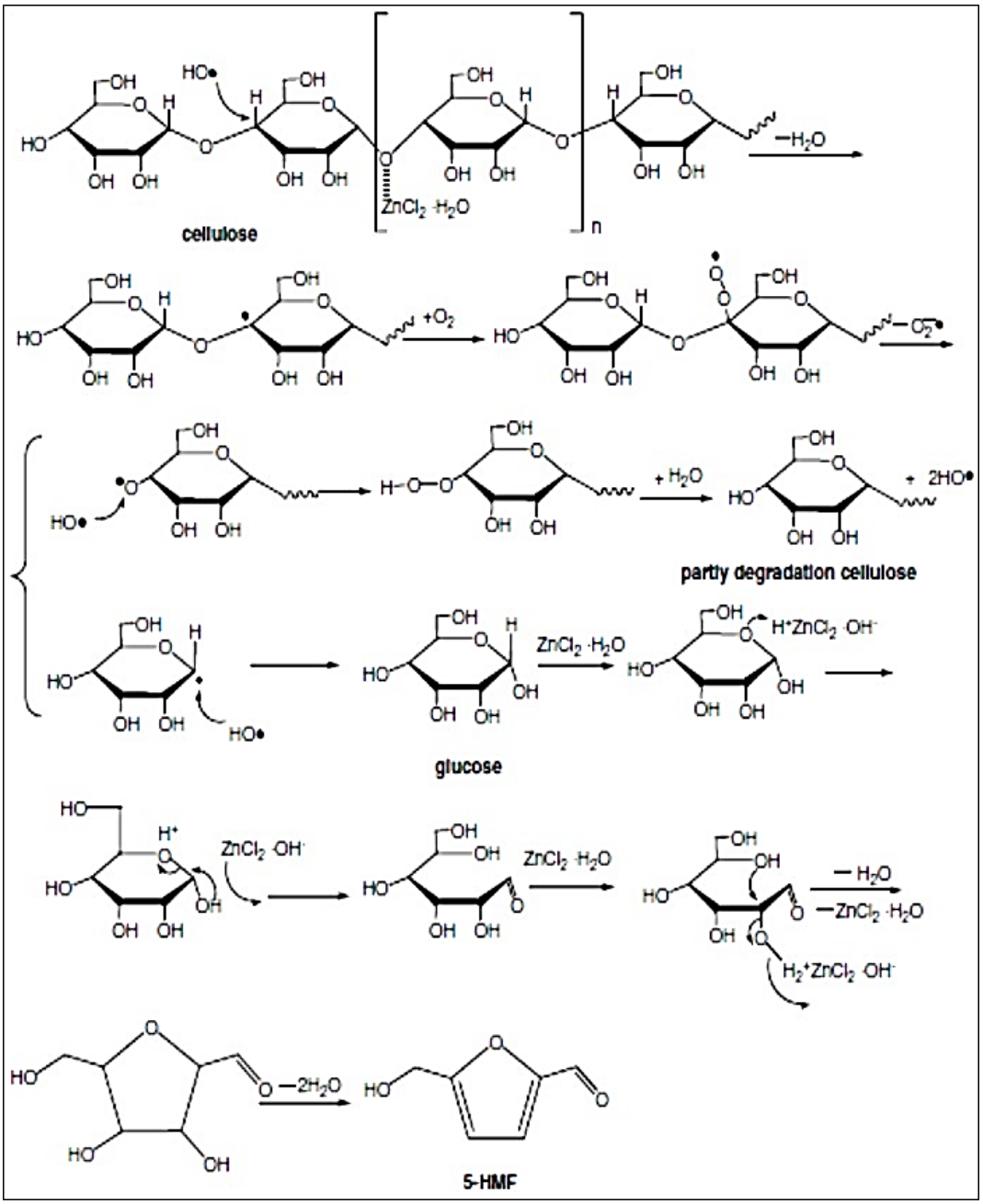

Figure 1.21: Photodegradation of $ZnCl_2$ dissolved cellulose, reproduced with permission from “John Wiley and Sons, Journal of Chemical Technology and Biotechnology, Copyright 2011” (127).

1.11 Summary

This chapter discussed in detail about the potential of cellulose photocatalysis for biofuel production. Firstly, the need for alternative energy was emphasised by discussing about the demand for energy and the current investments made in the field of renewable energy. Next, the possibility of using the world's most abundant organic material - cellulose as a raw material for biofuel production was highlighted. Cellulose biorefineries are a possibility when they are environmentally sustainable, but currently to produce biofuels from cellulose, environmentally unfavourable harsh physico-chemical pre-treatment methods are used. These harsh pre-treatment methods not only release fermentable sugars, but also degrade them in addition to releasing harmful chemicals into the environment. The need for these harsh methods could be attributed to the amphiphilic structure of cellulose. Hence, the conversion of native cellulose to cellulose II (a relatively easier form of cellulose to digest) could be a possibility. This conversion occurs due to the rearrangement of H bonds as a result of mercerisation or regeneration. Instead of using adverse solvents such as aqueous NaOH to produce cellulose II, green solvents in the form of ionic liquids or onium hydroxides can be used.

To effectively exploit cellulose for the production of biofuels, the compound has to be broken down. All the known cellulose degradation mechanisms utilise OH radicals to breakdown cellulose via the disruption of glycosidic bonds. This paves the way for the use of photocatalysis, an environmental friendly method which can effectively generate OH radicals to breakdown cellulose. OH radical production from photocatalysis is based on

the band gap energy of the photocatalyst. The band gap also dictates the selection of the illumination source for photocatalysis. The electrons from VB has to be excited to the CB using a suitable source of illumination so that a hole is left behind in the VB thereby forming OH radicals. In addition to the illumination source and the photocatalyst material, an effective reactor design can enhance the production of OH radicals.

Overall, this chapter has discussed the current position of renewable energy, cellulose conversion and the role photocatalysis can play. It is evident that an energy efficient method is required to breakdown cellulose in order to harvest fermentable sugars for biofuel production.

1.12 Research aims and objectives

The aim of this research was to develop a photocatalysis assisted method to release fermentable sugars from cellulose and cellulosic wastes for biofuel production.

The objectives of this project are:

- To asses and select photocatalysts via OH radical quantification and study its interaction with cellulose molecules.
- To determine the efficiency on the preceding photocatalytic process based on fermentable sugar formation.
- To design, simulate and fabricate a photocatalytic reactor to investigate fermentable sugar release.

The results of these studies are detailed in the subsequent chapters.

Chapter 2: Comparative assessment of visible light and UV active photocatalysts by hydroxyl radical quantification

2.1 Introduction

Photocatalysis has gained significant interest since the early publication by Fujishima and Honda in 1972, demonstrating the potential of splitting water over TiO_2 (39). Since this publication, photocatalysis has been applied to a broad range of fields including waste water treatment, microbe destruction, toxin removal, energy production and air treatment. (37,46,48,129-132). The general mechanism of photocatalysis is shown in Figure 1.10. The mechanism of photocatalysis has been well documented and can be generally represented by the equations shown in reactions R 1.11 – R 1.20. The formation of surface radical species such as superoxide ($O_2^{-\cdot}$) and hydroxyl radicals (OH·) play a key role in a number of photocatalytic pathways and as such their identification and quantification is a key consideration. As shown in reaction R1.14, OH radicals are primarily generated from the reaction between valence band holes and hydroxyl ions on the catalyst surface. An indirect pathway, via $O_2^{-\cdot}$, also results in OH radical formation, as shown in reactions R 1.15-1.18 (51,52). OH radicals being strong oxidants have an oxidation potential of 2.8 V (vs NHE) (normal hydrogen electrode) (124,133) and are highly non-specific and break any bonds that are within close proximity. The non-selective nature of these reactive oxygen species also aids rapid degradation of various pollutants and organic contaminants (37,38,48,124,127,134-136).

Newly developed photocatalytic technologies and materials have often utilised model compounds and screening methods to assess their performance (137-140). Common evaluation methods reported in the literature include the decomposition of dyes such as methylene blue (ISO test 10678:2010), or degradation of organic pollutants such as 4-chlorophenol or toluene (137-140). These procedures are often coupled with the corresponding calculated photonic efficiencies and quantum yields to evaluate overall efficiency. While these methods can be effective in identifying the specific photocatalytic performance of a material in relation to a fingerprint compound, they provide little information regarding the production of OH radicals involved within the mechanism. Therefore, the requirement for a simple and robust method of radical quantification for screening the oxidative potential of catalysts has significantly increased. The challenge in OH radical quantification lies in both the non-selective nature and short lifetime (~ 1 nanosecond) of the radical, which restricts the possibility of direct quantification (63). Consequently, a range of methods have been developed such as emission spectroscopy, laser induced fluorescence, electron spin resonance, spin trap and chemical probes or quencher based methods to quantify OH radicals (63,101-115,141).

The use of a chemical probe to capture OH radicals presents a potentially efficient way to measure the radical due to the low cost, rapid analysis time and reproducibility of the method. Monitoring a probe compound through spectroscopy allows the concentration of OH radicals to be calculated based on stoichiometric ratios of products formed. A recently reported *in vivo*

technique utilised a nanoprobe comprising of a nanoparticle and azo dye in order to quantify OH radicals in the femtomolar range (141). Here the nanoparticle was used as an energy donor and the modified orange was used as an OH radical capturing ligand molecule (and the energy acceptor).

DMSO based methods for OH radical capture have also been utilised in the past to quantify these species via the formation of formaldehyde based on reactions R2.1-R2.4 (106,108,109). The formation of CH_4 in a closed system coupled with O_2 bubbling however reduces the suitability of utilising DMSO as a probe molecule.

$(CH_3)_2SO_3 + OH^{\cdot} \rightarrow CH_3SOOH + CH_3^{\cdot}$ ..... R 2.1

$O_2 + CH_3^{\cdot} \rightarrow CH_3OO^{\cdot}$ ..... R 2.2

$2CH_3OO^{\cdot} \rightarrow HCHO + CH_3OH + O_2$ ..... R 2.3

$CH_3^{\cdot} + RH \rightarrow CH_4 + R^{\cdot}$ ..... R 2.4

In the past, OH radical quantification has been carried out for various commercially available photocatalysts, photo-Fenton's reaction and other modified TiO_2 based visible light photocatalysts with either coumarin or terepthalic acid as probe molecules (63,101-106,114,116,142). Both compounds are capable of acting as OH radical traps by forming fluorescent products as result of reacting with the radical species. Terepthalic acid has been investigated in a study by Ishibashi *et al*. which achieved an OH radical concentration of 7×10^{-5} M based on the measurement of 2-hydroxyterepthalic acid (102). In addition to the use of terepthalic acid as a probe molecule,

coumarin has been used in a number of studies to determine the concentration of OH radicals produced from TiO_2 at relatively high loadings of 1 to 5 g/L (63,114,143). For instance, Czili *et al*. used 100 µM coumarin as the probe molecule to capture OH radicals under a 40 W UV lamp. They determined a maximum OH radical production rate of 23.39 µM/g/hr (calculated from their reported 7-hydroxycoumarin rates) with 1 g/L TiO_2 P25 photocatalyst.

This chapter discusses the utilisation of coumarin as a hydroxyl radical trap and reports the screening of a selection of visible light responsive photocatalysts under low power illumination based on their OH radical producing capability. In contrast to previous reports, which concentrated on quantifying the OH radicals produced from TiO_2, other commercially available and a few synthesised photocatalysts (63,106,114,143), this work focusses on assessing the oxidative strength of visible light photocatalytsts Pt-C_3N_4, 5% LaCr doped $SrTiO_3$, $Sr_{0.95}Cr_{0.05}TiO_3$ (referred to as Cr-$SrTiO_3$ from here on) and yellow TiO_2 and compares them against commercial TiO_2 P25 and WO_3 for evaluation. In addition, a low catalyst loading was used to highlight efficient OH radical formation can be achieved without requiring large quantities of powdered catalyst.

2.2 Experimental Procedure

2.2.1 Materials

Coumarin and 7-hydroxycoumarin were purchased from Tokyo Chemical Industry UK Ltd, while TiO_2 P25 was purchased from Degussa (now Evonik industries) and WO_3 nano powders were purchased from Sigma

Aldrich. All commercial chemicals were used as received. The catalysts Pt-C_3N_4 (65), 5% LaCr doped $SrTiO_3$, Cr-$SrTiO_3$ and yellow TiO_2 (144) were synthesised and characterised by collaborators at the school of chemistry, University of St. Andrews, using methods cited in the literature (65,66,144) (Appendix A).

2.2.2 Standard curves

A stock solution of coumarin was prepared by dissolving 21.9 mg coumarin in 200 ml deionised (DI) water at 80˚C. This solution was left to cool to room temperature and then made up to a volume of 300 ml by adding DI water to achieve a final concentration of 500 µM. From this stock solution, a range of concentrations from 0 – 100 µM were prepared by diluting with the required amount of DI water. A volume of 1.5 ml from each concentration was taken and the absorbance was measured using a Cary 300 Scan, UV-Visible Spectrophotometer at a wavelength of 277 nm. DI water was used as the blank solution for absorbance measurements. The standard curve was plotted as absorbance at 277 nm against coumarin concentration.

A stock solution of 10 µM 7-hydroxycoumarin was prepared by dissolving 0.162 mg 7-hydroxycoumarin in 100 ml DI water. From the stock solution, two sets of concentration ranges were prepared; 0-1 µM and 0-10 µM. Both sets were prepared by diluting a set volume of the stock solution with DI water. A volume of 3 ml of the working solution was placed in a Kartell disposable Poly methyl methacrylate (PMMA) UV grade fluorimetric analysis cuvette and analysed using a PerkinElmer LS 50B luminescence

spectrophotometer. The excitation wavelength was set at 332 nm and the emission wavelength was set at 456 nm (63). The excitation and emission slit width was 4 mm and the scan rate was 200 nm/min. Two standard curves (one for each concentration range) were plotted as fluorescence intensity at 456 nm against concentration of 7-hydroxycoumarin.

2.2.3 Photocatalytic experiments

All photocatalytic experiments were performed in closed screw cap bottles. The reaction solution was composed of 100 ml of 100 μM coumarin along with 10 mg of photocatalyst (0.1 g/L). A magnetic stirrer bar was placed inside the bottle and the bottle was then placed on a magnetic stirrer at a distance of 11 cm from a 36 W compact fluorescent non-integrated visible lamp (Philips, colour code 830) or a 36 W UV lamp (Philips, Cleo lamps). The spectral outputs of the lamps were measured by a StellaNet spectrometer and the spectra are shown in Figure 2.1. Prior to illumination, the reaction solution was stirred in the dark to allow a state of equilibrium to be reached. The length of time required in the dark was calculated from the control experiments conducted in the absence of light. During irradiation, samples (3 mL) were taken at dedicated time intervals for a maximum of 120 mins. Samples were filtered through a 0.22 μm Millex syringe filter prior to analysis. Coumarin absorbance was monitored using a Cary 300 Scan, UV-Visible Spectrophotometer at 277 nm, with a scan rate of 400 nm/min. 7-hydroxycoumarin fluorescence was measured in a PerkinElmer LS 50B luminescence spectrophotometer, using an excitation wavelength of 332 nm and emission wavelength at 456 nm (63). The excitation and emission slit

width was 4 mm and the scan rate was 200 nm/min. A sample UV/Visible and fluorimeter spectrum, with peaks at 277 nm and 456 nm respectively, are shown in Figure 2.2 and Figure 2.3. All experiments were performed in triplicate.

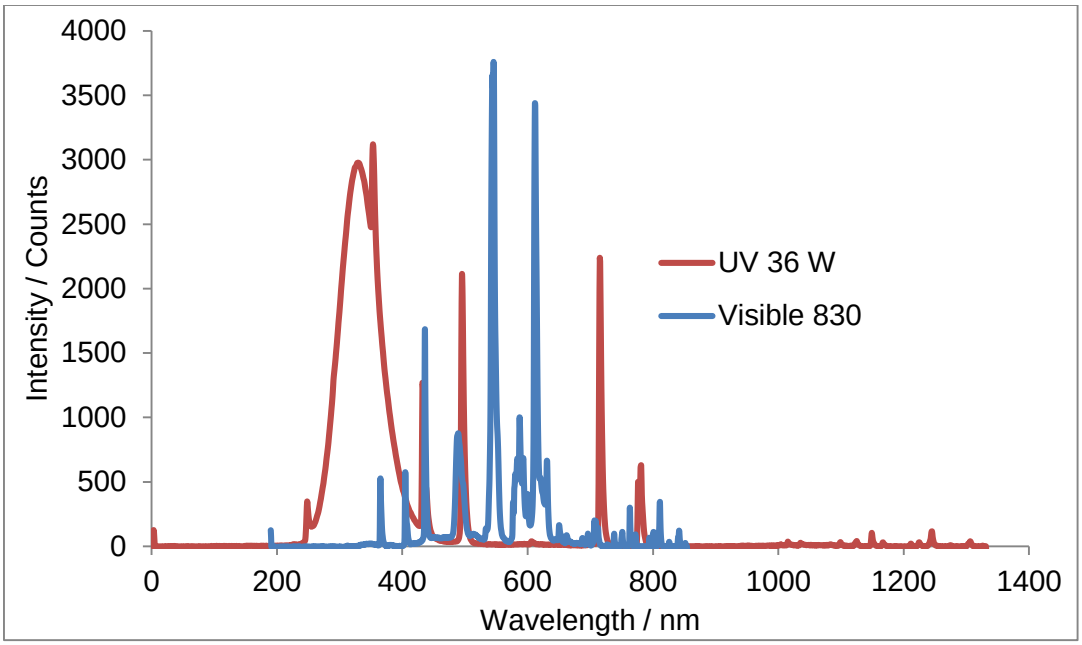

Figure 2.1: Lamp spectra for 36 W UV lamp and code 830 visible lamps

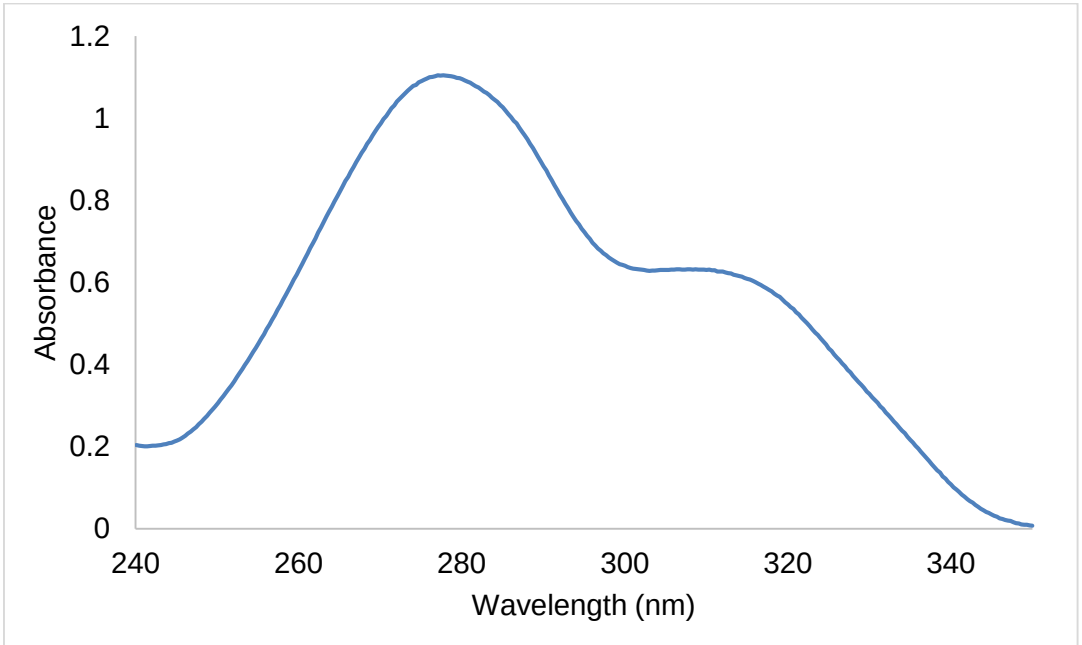

Figure 2.2: Sample UV/Visible absorbance spectra of coumarin with a peak at 277 nm

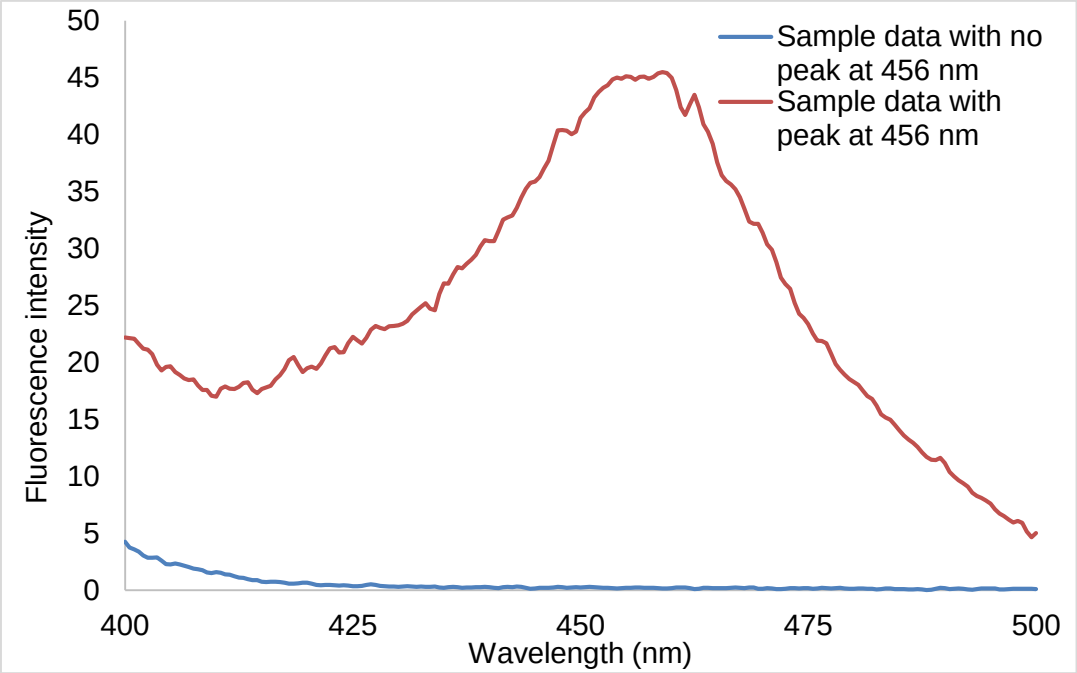

Figure 2.3: Sample fluorimeter spectra with and without a peak at 456 nm

2.2.4 Control experiments

To observe any significant effects on coumarin concentration over time, control experiments were performed in the absence of light and photocatalyst.

2.2.4.1 Dark adsorption experiments

Dark adsorption experiments were performed to determine the equilibration time for the adsorption, maximum possible amount of coumarin adsorbed onto the photocatalyst as well as to make sure that any degradation of coumarin occurring over time in the absence of light is accounted for. This helped to ensure that the amount of actual coumarin available for degradation is lower or equal to the initial amount. The experimental procedure for dark adsorption is as described in section 2.2.3 except that this experiment was performed under dark conditions.

2.2.4.2 Light control experiments without photocatalysts

Light control experiments without photocatalysts were performed to determine if any OH radicals were produced in the experiment when light was illuminated on to coumarin working solution. This experiment also ensured that any coumarin degradation in the absence of photocatalyst is monitored over time. Once quantified, this was useful to calculate the actual OH radicals produced from the photocatalytic experiments. The procedure to perform a light control experiment is as described in section 2.2.3 except that the experiment was performed without the addition of any photocatalyst.

2.2.5 OH radical quantification

OH radicals were quantified based on a modified method described by Zhang *et al.* (116) and according to Equation 2.1. The concentration of OH radicals was calculated by assuming that 6.1 % of total OH radicals were captured as 7-hydroxycoumarin. The stoichiometric ratio of one mole of OH radical consumed for the production of one mole of 7-hydroxycoumarin was used (Figure 2.4) (114).

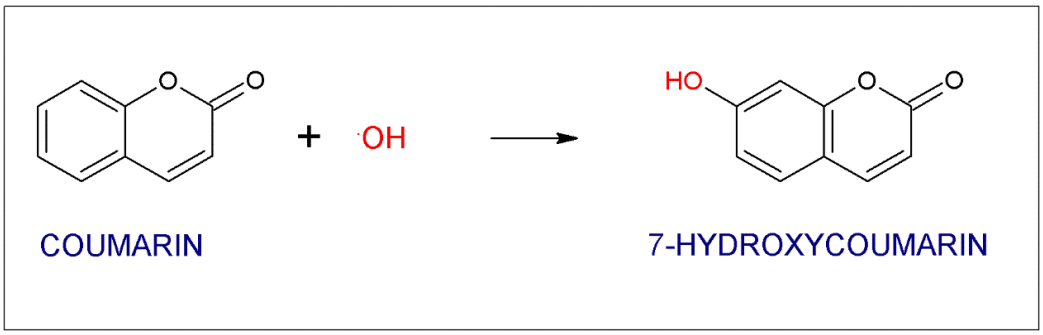

Figure 2.4: Coumarin hydroxylation

The total number of OH radicals produced over time during this photocatalytic process was calculated using the following equation.

$$X = \{\frac{A}{6.1\%} - B\}$$ ..... Equation 2.1

where, X is the total OH radical concentration (μM) produced during photocatalysis, A is the mean 7-hydroxycoumarin concentration (μM) and B is the amount of OH radicals (μM) produced during the light control experiments.

The assumption that 6.1 % of total OH radicals produced were captured as 7-hydroxycoumarin may not be accurate for a photocatalytic process. The potential inaccuracy with this assumption was because it was adopted from a gamma radiolysis experiment capturing OH radicals with the coumarin probe. Researchers however still tend to use this assumption because it could be used to relatively quantify OH radicals produced by various photocatalysts against P25. The actual percentage of 7-hydroxycourmain produced upon photocatalytic oxidation of coumarin possibly could be determined if individual products of coumarin hydroxylation were quantified. This was not performed in this work as this was beyond the scope of the project.

2.3 Results and discussion

2.3.1 Standard curves

2.3.1.1 Coumarin standard curves

Coumarin standard curve was obtained by plotting absorbance at 277 nm in the Y-axis and concentration of coumarin in the X-axis as shown in Figure 2.5. The values of absorbance were taken as average values from

triplicate readings. When the absorbance of an unknown coumarin sample is measured, its concentration can be determined by using the equation obtained from the standard curve.

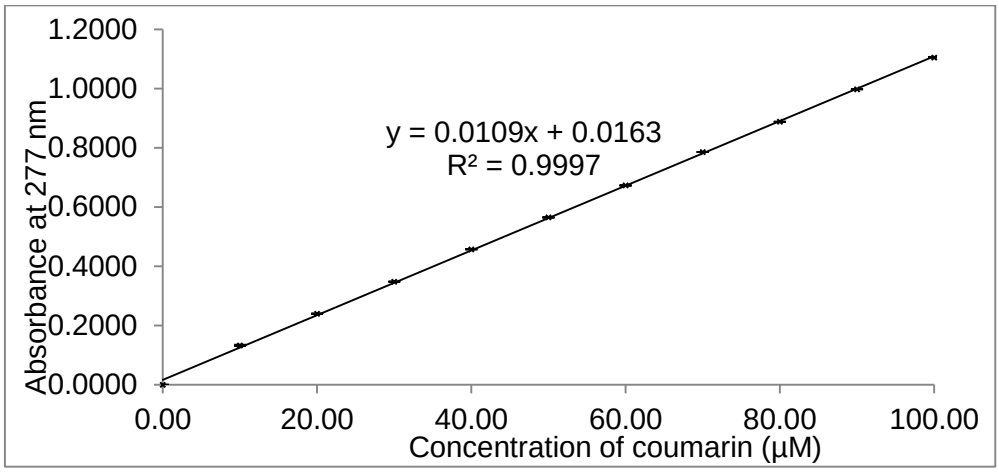

Figure 2.5: Coumarin standard curve

2.3.1.2 7-hydroxycoumarin standard curves

Two sets of 7-hydroxycoumarin standard curves were prepared. The first set from a 0-1 µM concentration and the second set from 0-10 µM as shown in Figure 2.6 and Figure 2.7 respectively. Both the curves were obtained by plotting the fluorescence intensity of 7-hydroxycoumarin at 456 nm on the Y-axis and concentration of 7-hydroxycoumarin on the X-axis. When the fluorescence of an unknown 7-hydroxycoumarin sample is measured, its concentration can be determined by using the appropriate equations obtained from the respective standard curve.

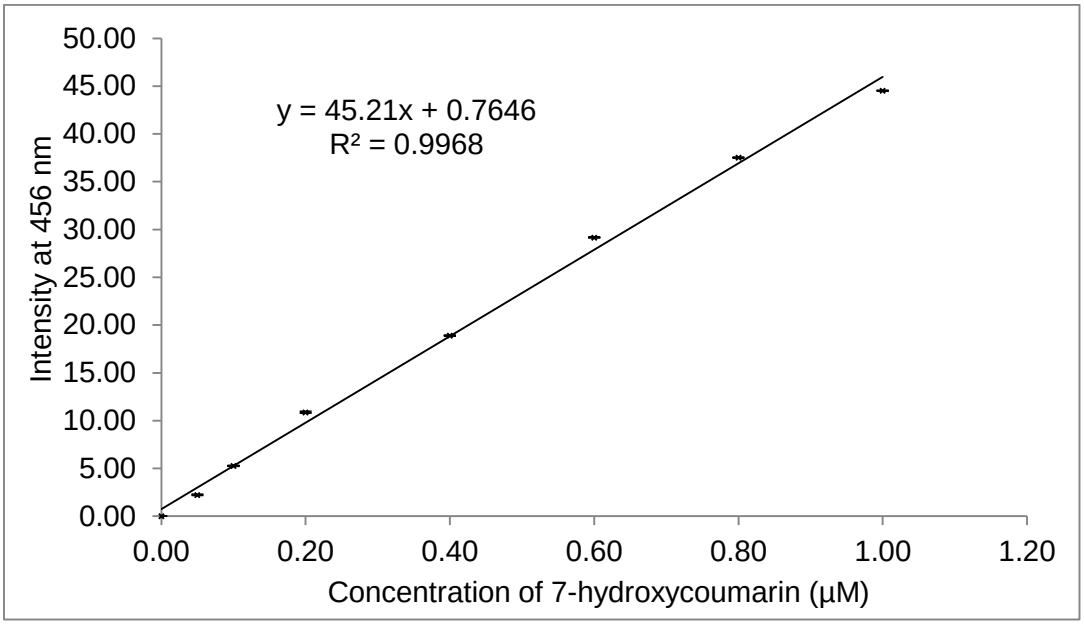

Figure 2.6: 7-hydroxycoumarin standard curve (0-1 µM)

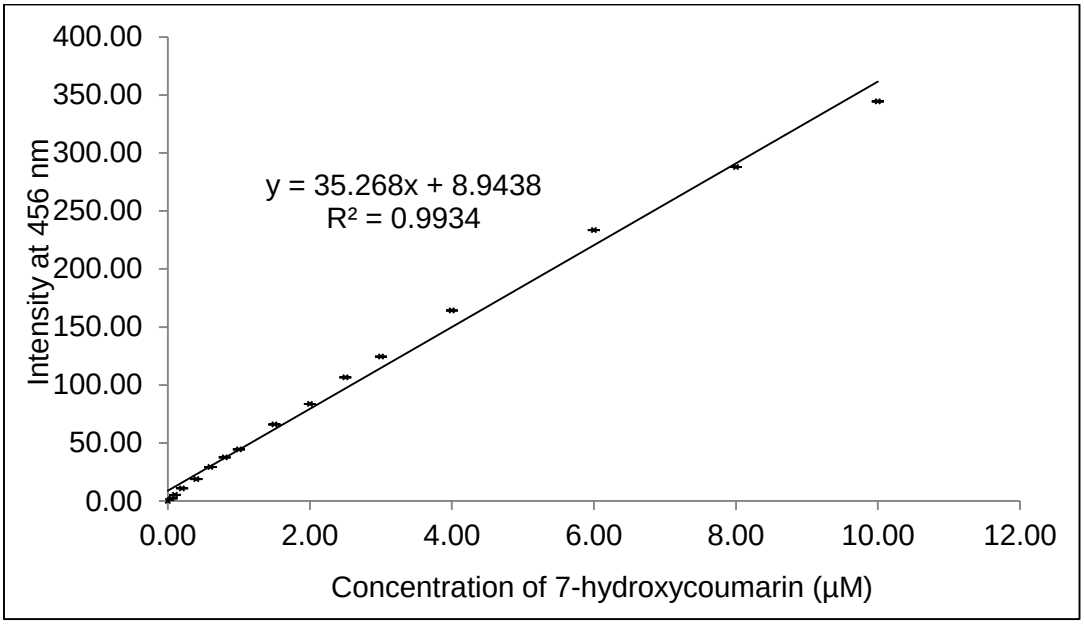

Figure 2.7: 7-hydroxycoumarin standard curve (0-10 µM)

2.3.2 Control experiments

Dark adsorption experiments were performed to ensure no OH radicals were formed in the absence of light. The results of the dark adsorption experiments are shown in Table 2.1. The results also indicate the difference in time at which equilibrium was reached between the photocatalyst surface

and coumarin solution and this could be ascribed to the particle size. Among the photocatalysts used in the experiments, P25 with the lowest particle size had the highest coumarin adsorption, while WO_3 with the highest particle size had the lowest coumarin adsorption thereby indicating the influence of particle size on coumarin adsorption.

The production of 7-hydroxycoumarin was also monitored during the experiment. The spectra of all the dark control samples showed no peaks at 456 nm, confirming that there was no formation of 7-hydroxycoumarin. A sample fluorimeter spectrum with no peak at 456 nm is shown in Figure 2.8. Therefore, it was concluded that there was no OH radical production on the catalyst surface during dark conditions. Furthermore, this confirms that any reduction in concentration of COU during the dark control experiments could be attributed to its adsorption onto the photocatalyst but not degradation.

Photocatalyst	**Percentage coumarin adsorbed (%)**	**Equilibration time (minutes)**	**Surface area (m^2/g)**	**Reference from which surface area data was taken**
TiO_2 P25	10.48	30	57.4	(145)
Pt-C_3N_4	1.66	30	23	(146)
WO_3	0.58	45	2.1	(147)
LaCr-$SrTiO_3$	3.04	15	16.6	(66)
Cr-$SrTiO_3$	2.76	45	54.3	(148)
yellow TiO_2	2.85	60	261	(144)

Table 2.1: Percentage adsorption and equilibration time of coumarin on photocatalysts

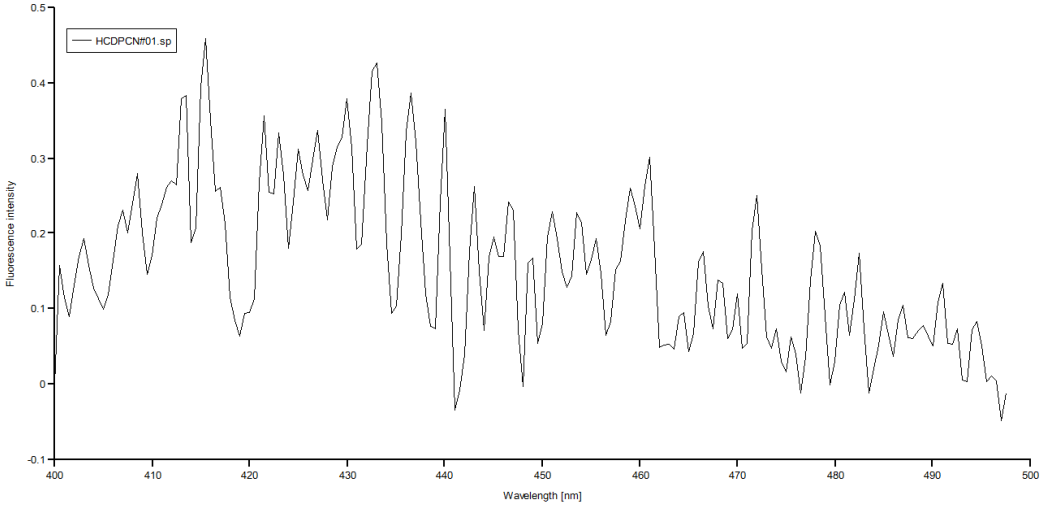

Figure 2.8: Sample fluorimeter spectra with no peak at 456 nm

Light control experiments in the absence of photocatalysts were performed to monitor the interaction between either UV or visible light and coumarin. This result from the light control experiments assisted in the precise calculation of the actual OH radicals produced during the coumarin degradation experiments. Figure 2.9 shows the effect of visible and UV illumination on coumarin degradation.

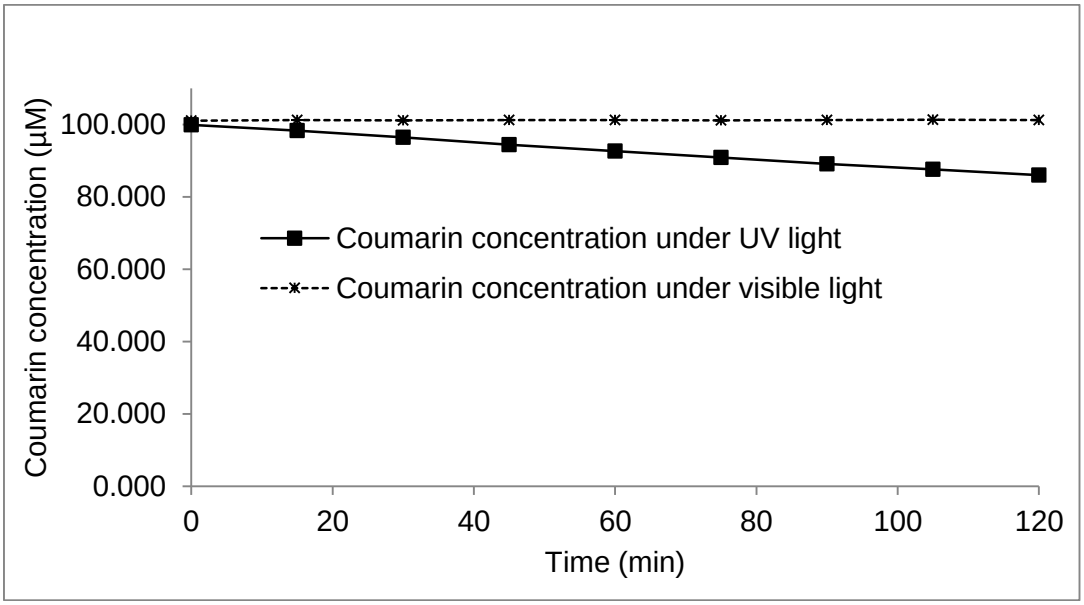

Figure 2.9: UV and Visible light control profiles

Under visible light, no degradation of coumarin was observed, whereas under UV light and no photocatalyst there was a slow and steady degradation of coumarin occurring over the time as shown in Figure 2.9. This degradation could be due to the photolysis effect under UV-A irradiation from the illumination source. Similar UV photolysis of aromatic compounds leading to their degradation have been reported in the past (149). Furthermore, no simultaneous 7-hydroxycoumarin was observed during the 120 minutes' experiment under either visible light or UV light, suggesting it was degradation of coumarin occurring and not its hydroxylation to 7-hydroxycoumarin. This suggested that in the absence of a photocatalyst, no OH radicals were produced from the light control experiments.

2.3.3 Photocatalytic OH radical production

2.3.3.1 UV light photocatalysis on TiO_2

P25 has been one of the most extensively investigated and most active commercially available photocatalysts under UV irradiation and therefore was used as a benchmark for comparison in this study. Although, recent studies have reported that nano-spherical $InCrO_4$-loaded TiO_2 and TiO_2 nanospheres deposited on graphene performed better than P25 for OH radical production and dye degradation upon UV irradiation (150,151), to date P25 is still regarded as the benchmark. The photocatalytic hydroxylation of coumarin over P25 under UV light and subsequent formation of 7-hydroxycoumarin is shown in Figure 2.10. The production of 7-hydroxycoumarin under these conditions equates to a peak OH radical concentration of 16.9 µM after 45 mins.

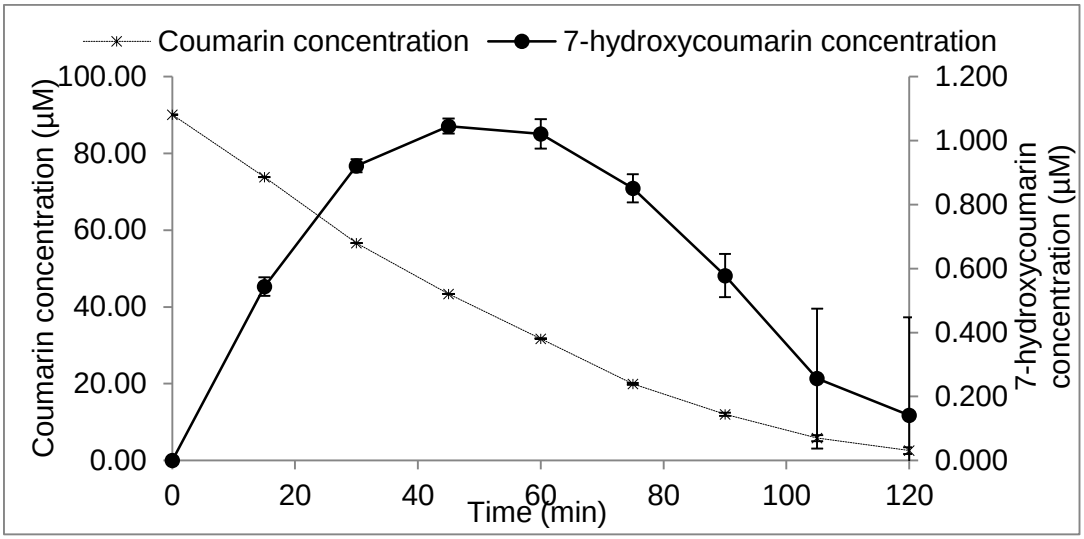

Figure 2.10: Coumarin and 7-hydroxycoumarin profiles with TiO_2 under UV light

As shown in the figure, near complete degradation (97 %) of coumarin was achieved after 120 minutes' irradiation. This level of degradation was likely to result from the increased adsorption of coumarin onto the catalyst, which facilitated the reaction with surface bound OH radicals. The role of surface bound radicals and those that are present in bulk has been highlighted in a previous publication by Li *et al.* (152), who investigated acid orange oxidation over TiO_2 P25 and AgBr. This group investigated the quenching of OH radicals at the catalyst surface and in bulk in order to demonstrate that surface bound species were the predominant radicals in the oxidation pathway. This observation confirmed that increased adsorption of the substrate on the catalyst surface can significantly increase the degradation efficiency.

When a mass balance was conducted with the maximum amount of 7-hydroxycoumarin produced at 45 minutes, it revealed that for 56.99 µM coumarin that was used up in the reaction (at 45 minutes), the total

hydroxylated product produced would have been 17.13 µM in addition to the by-product of 17.13 µM water. This adds up to 38.26 µM total products as a result of hyrdroxylation. Moreover, 5.44 % of the total initial coumarin at 45 minutes would have been degraded by UV light as observed from the UV light control experiments. This total accounts for 77 % of all products. This deviation in mass balance could be due to a number of reasons such as the assumption that 6.1 % of the total hydroxylated products produced was 7-hydroxycoumarin (obtained from a gamma radiolysis OH radical producing experiment) and the reactive oxygen species produced during photocatalysis playing a role in degrading the 7-hydroxycoumarin. The deviation due to the former assumption could be corrected if all the hydroxylated products produced upon coumarin photocatalysis were quantified.

Figure 2.10 also shows the profile of 7-hydroxycoumarin production and decomposition which indirectly indicates the quantity of OH radicals generated. 7-hydroxycoumarin concentration peaked at 45 minutes, with a maximum concentration of 1.045 µM, which was equivalent to 16.9 µM OH radicals (as calculated from equation 3). It was observed that an average production rate of 1.8 µM/hr was achieved during the first 45 mins, followed by an average degradation rate of 0.46 µM/hr during the latter stages of irradiation. The decrease in concentration of 7-hydroxycoumarin could also be attributed to the presence of superoxide radicals as reported by Czili and Horvath (114).

Several reports have suggested the kinetics for 7-hydroxycoumarin generation from coumarin with P25 under UV irradiation are zero order (63,114,116,153-155), however, a number of these investigations also used a high concentration of both catalyst and coumarin. Furthermore, it has been suggested that at higher concentrations of coumarin (>100 µM), more UV light is absorbed by this probe and not the catalyst, which results in a low 7-hydroxycoumarin and OH radical production rate (114). In the present study, K_{app} which is the rate constant for the formation of 7-hydroxycoumarin was calculated to be 0.0234 µM/min whereas K_{dis}, the rate constant for the disappearance of 7-hydroxycoumarin was calculated to be 0.0135 µM/min. In this study it was established that both, production and degradation of 7-hydroxycoumarin followed zero order kinetics, which is agreement with previous studies.

2.3.3.2 Visible light photocatalysis

A number of visible light catalysts were also selected for comparison to P25 TiO_2. While the synthesised catalysts all possessed energy band gaps that supported visible light activation, only WO_3 and Pt-C_3N_4 had energy band potentials (valence band at 3.2 V and 1.4 V respectively and conduction band at 0.2 V and -1.3 V respectively) that would facilitate OH radical formation either directly or indirectly as mentioned in reactions R 1.12 – R 1.16. Catalysts LaCr-$SrTiO_3$, Cr-$SrTiO_3$ and yellow TiO_2 (valence bands at 2.7 V, 2.7 V and 2.6 V respectively and conduction bands at -0.1 V for all the three photocatalysts) were selected to monitor if 7-hydroxycoumarin was formed

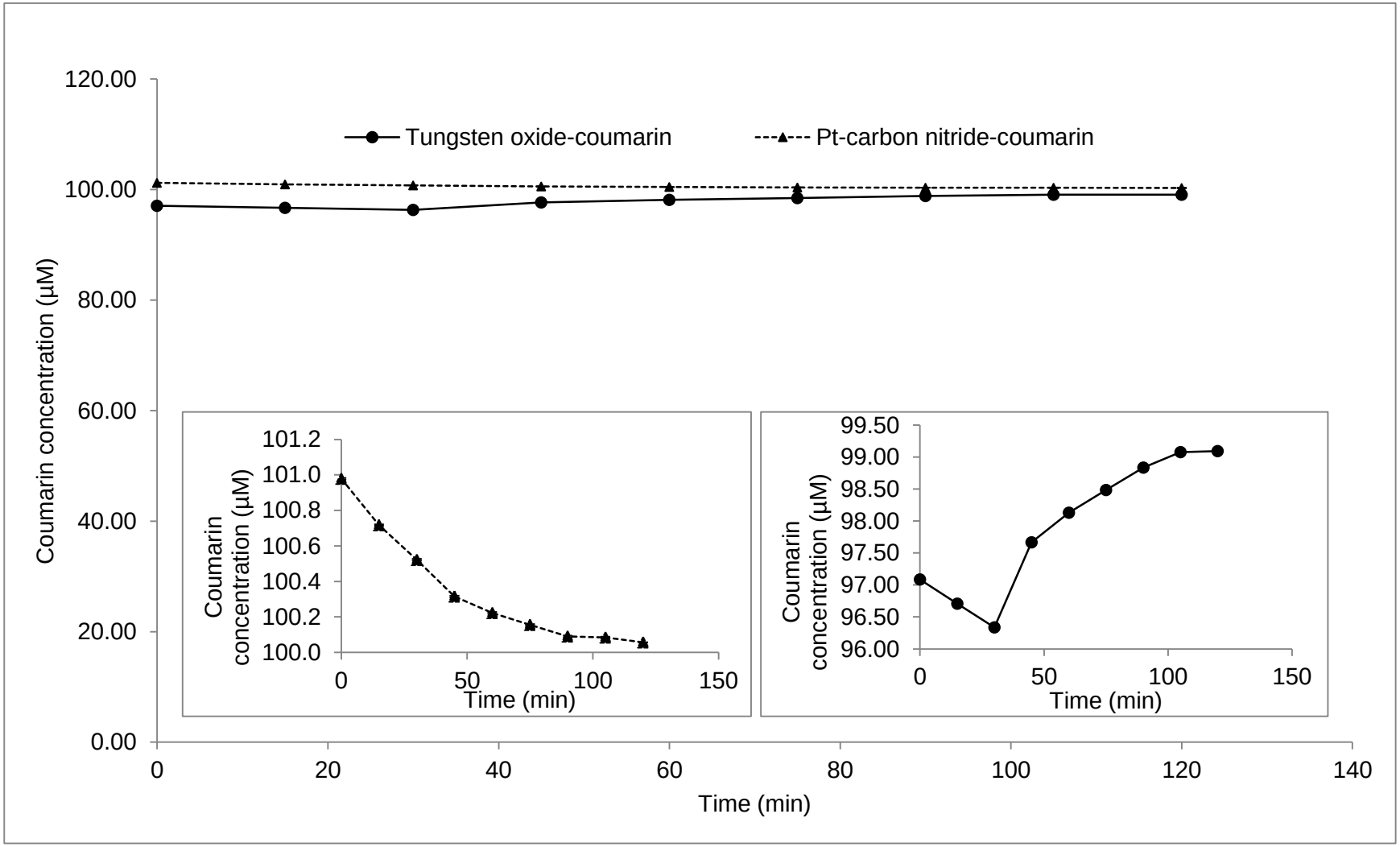

Figure 2.11: Coumarin degradation profiles on visible light photocatalysts. Inset: Coumarin degradation profiles of WO_3 and Pt-C_3N_4

even when the electronic structure of the catalyst was not suited to the redox potential of the reaction.

The photocatalytic hydroxylation of coumarin to 7-hydroxycoumarin over WO_3 and Pt-C_3N_4 under visible light is shown in Figure 2.11. As can be seen, minimal conversion of coumarin was observed over both Pt-C_3N_4 and WO_3, which was also supported by the low formation of 7-hydroxycoumarin (Figure 2.12). Pt-C_3N_4 displayed a slow yet steady conversion rate, reaching a 0.91 % drop in coumarin after 120 mins of irradiation whereas, a varying coumarin concentration pattern was seen over time on WO_3. It is interesting to note that there was an initial decrease in coumarin concentration followed by an increase which may be attributed to coumarin desorption from the surface of WO_3. This desorption could be a result of the alteration in equilibrium in the closed system due to the possible evolution of O_2 from water on WO_3 under visible light. If these photocatalysts were to be illuminated by the UV light source used for the P25 experiments (with minimal intensities in the visible region as seen from Figure 2.1), a similar activity as seen in Figure 2.11 and Figure 2.12 could be expected.

While the decrease in coumarin concentration is low, production of OH radicals over Pt-C_3N_4 and WO_3 was supported by the detection of 7-hydroxycoumarin upon photocatalysis Figure 2.12. When WO_3 was used as the photocatalyst, there was no 7-hydroxycoumarin production until 30 minutes of irradiation which could be due to the rapid recombination of the electrons and the photo generated holes. After 30 minutes, OH radical

production was steady with a gradual generation of 7-hydroxycoumarin being observed. In the case of Pt-C_3N_4 however, 7-hydroxycoumarin production was seen from 15 minutes. The initial increase in the 7-hydroxycoumarin concentration correlates to a rapid degradation of coumarin during the first 60 mins of irradiation. In contrast to Pt-C_3N_4 and WO_3, the catalysts LaCr-$SrTiO_3$, Cr-$SrTiO_3$ and yellow TiO_2 displayed no activity towards coumarin conversion to 7-hydroxycoumarin, which indicates no OH radical formation. Furthermore, under prolonged visible light irradiation no detectable 7-hydroxycoumarin was recorded.

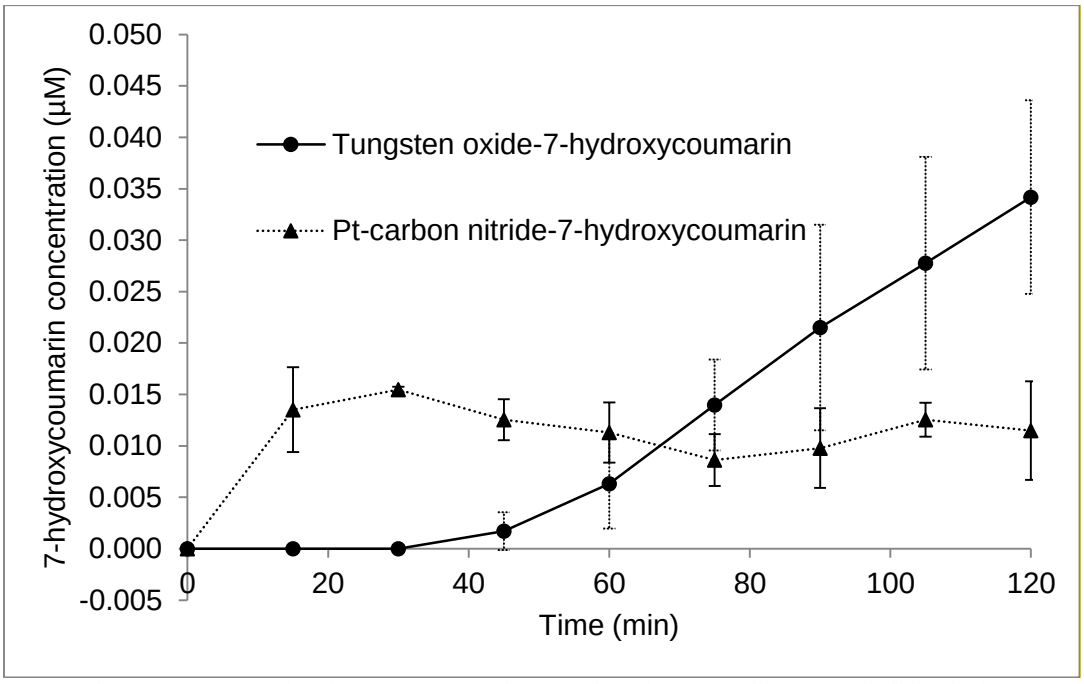

Figure 2.12: 7-hydroxycoumarin production profiles on visible light photocatalysts

2.3.3.3 Influence of photocatalysts' electronic structure and particle size on OH radical formation

In order to evaluate and discuss the performance of the catalysts, it is essential to consider the primary contributing factors; electronic structure and

particle size. The electronic structure of the catalysts dictates the initial photo-excitation of electrons to higher energy levels, while the particle size dictates the concentration of photons absorbed and surface reactions between coumarin and OH radicals. As shown in reactions R 1.14 – R 1.18, OH radicals can occur via two routes in photocatalysis. The direct formation at the valence band requires a redox potential of 2.8 V vs NHE, while the indirect method occurs via the intermediate radical, $O_2^{-\cdot}$ and requires a redox potential of -0.33 V vs NHE (156). The electronic structure of the catalysts tested in this study, in relation to the redox potentials required for radical formation, are shown in Figure 2.13.

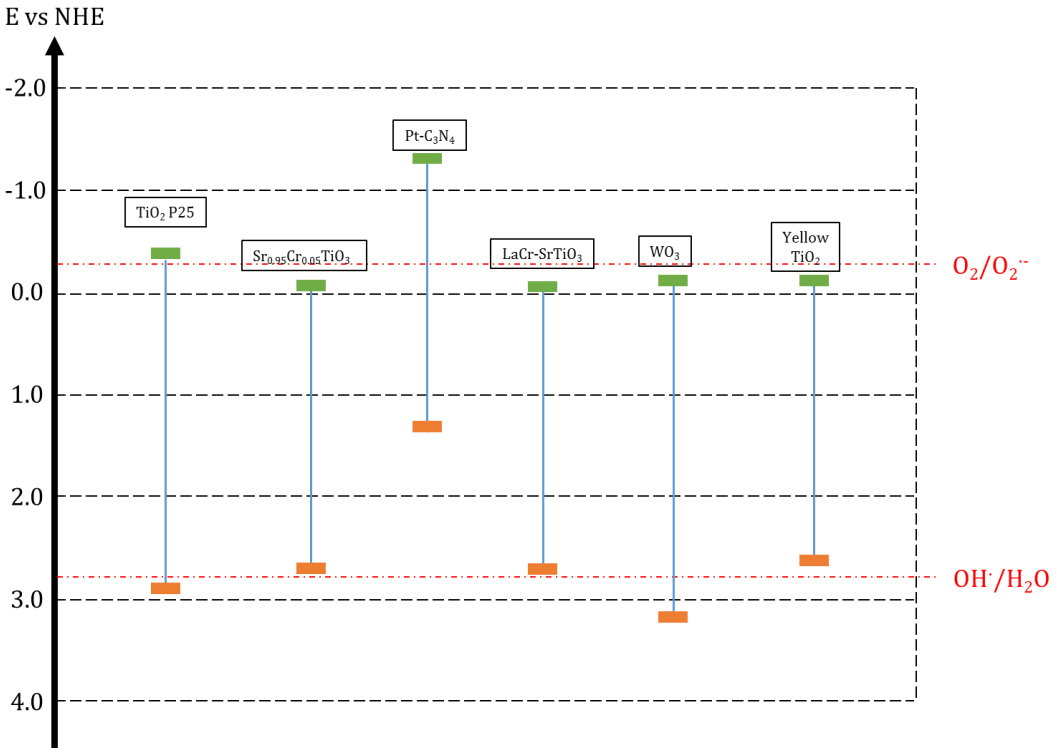

Figure 2.13: Electronic structure of the photocatalysts used

As shown in the figure, catalysts TiO_2 P25, Pt-C_3N_4 and WO_3 possess an electronic structure which corresponds to the redox potential of OH radical

formation via either direct or indirect mechanisms. The favourable electronic structure of TiO_2 for OH radical formation has been well documented and is evident from the results highlighted here. The performance of Pt-C_3N_4 and WO_3 for OH radical formation, however, has not been as well reported. The structure of WO_3 with a more positive valence band suggests it is capable of generating surface OH radicals, however, the results obtained indicate minimal 7-hydroxycoumarin production within 2 hours. Based on the structure, it was likely an increased rate of recombination preventing OH radical formation via the valence band hole, due to insufficient energy to initiate a reduction reaction at the conduction band (63). To prevent recombination and to increase the OH radical production, Kim *et al*. synthesised Pt-doped WO_3 and found that the OH radical production from Pt-WO_3 was significantly higher than un-doped WO_3 (140). Furthermore, the large particle size of approximately 100 nm for WO_3 indicates a smaller surface area, which leads to minimum absorption of light.

The electronic structure of Pt-C_3N_4 as seen from Figure 2.13 clearly indicates a reducing catalyst, which is also supported by its application in water reduction investigations (157). Therefore, the hydroxylation of coumarin and subsequent formation of 7-hydroxycoumarin, as indicated by the earlier results, is likely via the indirect $O_2^{\cdot -}$ pathway. Based upon this observation, it is likely the low yield of OH radicals is a result of competition for the conduction band electron between superoxide formation and H^+ reduction to form H_2 (0 V vs NHE). In addition, since all these experiments were performed in a closed system with limited O_2, a reducing catalyst such as Pt-C_3N_4 is expected to

produce less OH radicals than an open system. Furthermore, despite a favourable particle size of 20-40 nm, Pt-C_3N_4 was observed to agglomerate to form larger aggregates leading to a decrease in surface area and in turn light absorption.

In the case of LaCr-$SrTiO_3$, Cr-$SrTiO_3$ and yellow TiO_2, the electronic structures showed both the valence band and conduction band of all these catalysts to be lower than the redox potentials to facilitate radical formation as seen in Figure 2.13. These catalysts were primarily used as a control parameter to ensure no 7-hydroxycoumarin formation was observed.

The calculated OH radical concentrations and production rates produced over all catalysts screened are summarised in Table 2.2. The results show that the activity of the visible light activated photocatalysts studied were significantly lower than commercial P25 under UV light. This further emphasises that although there are numerous visible light absorbing photocatalysts, their ability to produce OH radicals is significantly lower than P25. In future, if any visible light absorbing photocatalysts are to be fabricated for the purpose of photocatalytic oxidation, their OH radical producing rates (and quantities) should be determined and compared to P25 as demonstrated here.

Photocatalyst	Light Source	Maximum OH radical concentration (μM)	Time at which maximum concentration of OH radical was produced (min)	Maximum OH radical production rate (μM/hr)
TiO_2	UV	16.9	45	35.654
WO_3	visible	0.560	120	0.280
Pt-C_3N_4	visible	0.254	30	0.886

Table 2.2: OH radical rates and quantities

2.4 Conclusion

The aim of screening UV and visible light absorbing photocatalysts to assess their oxidative strength was accomplished successfully by trapping OH radicals produced by the photocatalysts in 7-hydroxycoumarin. The OH radical production capabilities of various photocatalysts covering a range of band gaps and particle sizes were assessed by comparing and discussing their differences with the commercial UV light activated P25. To conclude, visible light activated photocatalysts such as LaCr-$SrTiO_3$, Cr-$SrTiO_3$ and yellow TiO_2 did not produce any OH radicals and this could be attributed to their electronic structure. Whereas, the (pseudo) maximum OH radical production rates of other visible light activated photocatalysts namely, WO_3 (0.28 μM/hr) and Pt-C_3N_4 (0.886 μM/hr) were found to be significantly lower when compared to the commercial UV light activated P25 photocatalyst (35.654 μM/hr). This method could be further exploited as novel photocatalysts are developed and to compare a range of P25 concentrations for OH radical production. This study further emphasises the challenges faced by the visible light photocatalysts for photocatalytic oxidation.

Chapter 3: Photocatalytic Fermentable Sugar Production from Native and Regenerated Cellulose – A Comparison

3.1 Introduction

Cellulose is a homopolysaccharide containing glucose units bonded together by (1-4)-glycosidic bond (Figure 1.2, Chapter 1). The characteristic feature of cellulose is the presence of inter and intramolecular hydrogen bonds connecting the cellulose chains thereby forming highly crystalline regions (and occasional amorphous regions). The arrangement of these hydrogen bonds are different in polymorphs as a result of various physico-chemical treatments. A detailed discussion on the different polymorphs of cellulose is available in section 1.3 in Chapter 1. In addition to the hydrogen bonds, recently it was also confirmed that cellulose consists of both hydrophilic and hydrophobic regions (158). Therefore, it was proposed that cellulose is an amphiphilic compound. Cellulose being amphiphilic has its hydroxyl groups oriented equatorially (making it hydrophilic) and the H atoms of its C-H bonds oriented axially (making it hydrophobic) (15,158-163) as shown in Figure 3.1.

The amphiphilic property of cellulose opens up new possibilities for cellulose pre-treatment. Cellulose I (native cellulose) is the most abundant and difficult to process polymorph without pre-treatment, whereas cellulose II is the most commonly used man-made form which is considered to be relatively easier to process (23,24,164). This easier digestibility of cellulose II could be due to the increased inter-planar spacing (d-spacing) as a result of weakening of the hydrophobic bonds (van der Waals interactions) upon regeneration from

solution (23,159,164,165). Cellulose II in contrast to cellulose I has an increased density of hydroxyl groups along the (1 -1 0) plane due to the stacking of its glucopyranose rings with each other by hydrophobic interactions, thereby resulting in increased hydrophilicity (159). Furthermore, a lower crystallinity index (CrI) and a higher surface area and porous volume of cellulose II when compared to cellulose I further supports the fact that cellulose II would be a better raw material for biofuel/fermentable sugar production than cellulose I (23,166,167).

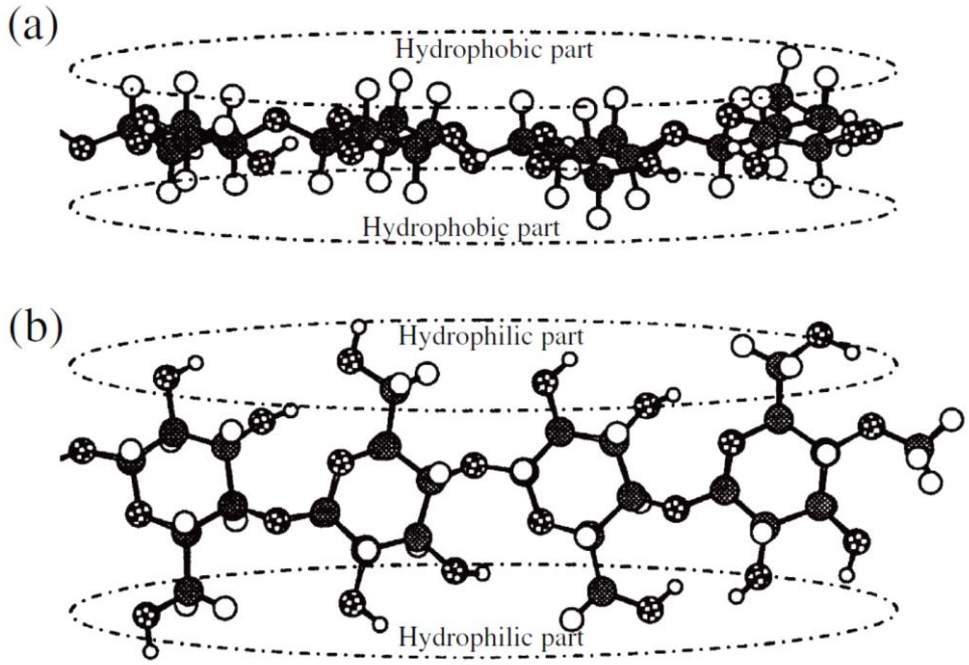

Figure 3.1: Hydrophillic and hydrophobic sides of Cellulose I: (a) end view of glucopyranose ring plane; (b), front view of glucopyranose ring plane, reproduced with permission from “Nature publishing group, Polymer Journal, Copyright 2006” (159).

To access the cellulose structure better for chemical processing, cellulose I has to be converted to cellulose II via an efficient pre-treatment process such as dissolution in an appropriate solvent and regeneration. Due

to its amphiphilic property, cellulose I is insoluble in water, however other solvents such as trifluoroacetic acid, ionic liquids, onium hydroxides, molten salts and alkalis (15,26,28,168,169) can be used to dissolve cellulose I. Unlike alkalis, ionic liquids and onium hydroxides are considered as green amphiphilic cellulose solvents due to their negligible volatility (28,169). Upon dissolution, cellulose II can be precipitated by the addition of anti-solvents. Some commonly used anti-solvents are (hot) water, ethanol, dilute acids or methanol (158).

Recently, Alves *et al*. demonstrated the amphiphilicity of onium hydroxides and cellulose (169). In their experiments, they dissolved 1 wt% cellulose in 8 wt% NaOH/H_2O and 40 wt% TBAH/H_2O solvent systems. Upon complete dissolution, the samples were subjected to dynamic light scattering. These measurements revealed an average particle size of 10-20 nm and 200 nm in the TBAH system and NaOH system respectively. Furthermore, images from a scanning electron microscope revealed that an aqueous solution of an onium hydroxide (TBAH) dissolved cellulose down to the molecular level whereas a NaOH/water system dissolved cellulose only macroscopically. This suggests that an amphiphilic solvent such as TBAH could be used to effectively dissolve cellulose I and regenerate cellulose II.

Currently, the most common method to produce fermentable sugars from cellulose II is via enzymatic hydrolysis (170-172). Enzymatic hydrolysis has been the preferred method over other methods such as microwave assisted hydrolysis, biological cellulose breakdown or acid hydrolysis due to

the high selectivity of enzymes for cellulose. Although the selectivity of enzymes is high, its high costs does not make it a suitable method to scale up. A potential low cost, environment friendly, low energy consuming method – photocatalysis was therefore tested in this work as an alternative to produce fermentable sugars from cellulose II. Photocatalysis produce OH radicals upon irradiation and these reactive oxygen species have been used for various applications such as wastewater treatment, dye degradation, microbe contamination control, toxin degradation and self-cleaning applications (37,46,48,129,130,132), in addition it has also been now extended for fermentable sugar production from cellulose II in this work.

Photocatalytic cellulose breakdown for renewable energy production has not been extensively studied but only occasionally (127,128,173). This is due to the high crystallinity, inter and intramolecular hydrogen bonding and the orientation of hydrophobic and hydrophilic regions of native cellulose. When cellulose II is used as a starting material, its relatively low crystallinity and high hydrophilicity favours hydrolysis. This hypothesis has been recently verified using enzymatic hydrolysis, acid hydrolysis and microwave assisted hydrolysis (166,170-172,174-178), but not with photocatalysis. Hence, this chapter will discuss the production of fermentable sugars from cellulose I and cellulose II mediated via photocatalysis.

3.2 Experimental procedure

3.2.1 Materials

MCC (cellulose I) was purchased from Acros organics, UK and 55 % wt/wt TBAH in water was purchased from Alfa Aesar. TiO_2 P25 was purchased from Degussa (now Evonik industries). All the chemicals were used as received without further purification. Fisher brand dialysis tubing with a wall thickness of 28 µm and a diameter of 29.3 mm and dialysis tubing clamps were purchased from Fisher scientific.

3.2.2 Dissolution of cellulose and regeneration

250 mg of cellulose I was added to a glass vial containing 5 ml of TBAH and a magnetic stirrer bar. The vial was then capped and placed on a magnetic stirrer plate at room temperature. The mixture was mixed until all the cellulose dissolved. After complete dissolution, excess deionised water (anti-solvent) was added to the cellulose-TBAH solution and stirred thoroughly. Upon stirring for 30 minutes, regenerated cellulose started to precipitate out from the solution. This mixture was filtered using a filter paper and then washed with DI water to remove all the bound TBAH and stored in its hydrate form for further experiments.

3.2.3 Characterisation of regenerated cellulose

A sample volume of this cellulose II hydrate was taken and its dry weight was determined so as to calculate the concentration of cellulose II in the mixture after filtration. Cellulose II was further characterised using XRD

(X-ray diffraction), attenuated total reflectance - Fourier transform infrared spectroscopy (ATR-FTIR) and thermogravimetry (TGA) as discussed below.

3.2.3.1 XRD profiles for cellulose

XRD patterns of cellulose I and cellulose II were obtained using a PANalytical PW3719 powder diffractometer. A spinner cell PW3064 was used to capture the pattern with a step size of 0.0167113^{O} and time per step of 29.845 seconds. The wavelength of the X-ray radiation was 1.54 Å. The generator voltage and current were set at 40 kV and 40 mA. The diffraction pattern was recorded between the 2Θ (2 Theta) range of 5 – 50^{O}. The diffraction patterns were recorded using an X'Pert data collector software. Once the diffraction patterns were obtained, percentage crystallinity was calculated as follows (167),

$$\text{CrI for cellulose I} = \frac{(I_{(200)} - I_{amI})}{I_{(200)}} \times 100 \quad \text{.....Equation 3.1}$$

$$\text{CrI for cellulose II} = \frac{(I_{(1-1\,0)} - I_{amII})}{I_{(1-1\,0)}} \times 100 \quad \text{.....Equation 3.2}$$

Where $I_{(200)}$ is the intensity of cellulose I at 2Θ = 22.5 ^{O}, I_{amI} is the intensity of cellulose I at 2Θ = 18 ^{O}, $I_{(1\,-1\,0)}$ is the intensity of cellulose II at 2Θ = 19.8 ^{O} and I_{amII} is the intensity of cellulose II at 2Θ = 16 ^{O}.

Bragg's law was used to calculate the inter-planar distance which is also known as d-spacing.

$\lambda = 2 . d . \sin \Theta$ ……..Equation 3.3

where λ is the wavelength of X-ray, d is the inter-planar distance (nm) and Θ is the angle between the plane and the incident X-ray which is calculated from 2Θ.

3.2.3.2 ATR-FTIR profiles for cellulose

FTIR spectra of cellulose I and cellulose II were taken with a Perkin Elmer Spectrum One spectrophotometer fitted with an ATR attachment. The spectra were recorded at room temperature in the wavenumber range of 4000 – 650 cm^{-1} in transmittance mode on a diamond/ZnSe crystal plate cell. An average of 16 scans was taken per sample with a resolution of 4 cm^{-1} and the spectra was recorded using Spectrum 6.3.4 software. The total crystallinity index (TCI) was calculated from the FTIR spectra using the following equation (179).

TCI = Intensity at 1364 cm^{-1}/Intensity at 2892 cm^{-1} ……..…Equation 3.4

It has to be noted that TCI does not represent the actual crystallinity of the samples but the relative crystallinity.

3.2.3.3 Thermogravimetric analysis

Thermal behaviour of the cellulose samples was recorded by a Mettler Toledo TGA/DSC 1 STAR^e system. Thermal profiles of 4–15 mg samples were recorded in the temperature range of 50 – 600 ^OC at a heating rate of 5 ^OC/min in air. The rate of weight loss due to temperature was determined from the

derivative thermogravimetric data (DTG). STAR^{e} software was used to record the thermal profiles of the samples.

3.2.4 Photocatalytic cellulose breakdown experiments

All photocatalytic experiments were performed in a 250 ml Pyrex glass beaker with a working volume of 200 ml. The reaction volume composed of 200 ml of 1 g/L cellulose (cellulose I or cellulose II) along with 150 mg photocatalyst to achieve a catalyst loading concentration of 0.75 g/L. A magnetic stirrer bar was placed inside the beaker and the beaker was then placed on a magnetic stirrer plate. A 36 W UV lamp (Philips, Cleo lamp) was then placed at a distance of 11 cm away from the centre of the beaker. The spectral output of the lamp was measured by a StellaNet spectrometer and the spectra is shown in Figure 2.1. The photon flux was determined to be 5.22 × 10^{-1} µEinstein L^{-1} min^{-1} as measured by ferrioxalate actinometry (Appendix B) (180). The contents of the beaker were allowed to mix in the dark for 30 minutes to attain equilibrium prior to illumination. 3 ml samples were collected every 30 minutes for 3 hours using a disposable syringe, filtered through Millex syringe filters with a pore diameter of 0.22 µm, accumulated, concentrated by freeze drying or air stripping and analysed for fermentable sugars using a high-performance liquid chromatography (HPLC) system coupled with a refractive index (RI) detector. Furthermore, it should be noted that only products in the liquid phase was monitored and no gaseous products were captured for quantification.

Another set of experiments with a similar arrangement as above was performed but with dialysis membrane bags immersed inside the beaker to instantaneously capture the fermentable sugars. In this set up, a 5 cm dialysis membrane bag was filled with 3 ml deionised water and immersed inside the beaker. After every 30 minutes for 3 hours, samples in the bags were collected and the bag was filled with deionised water and replaced. The experimental setup used for photocatalytic fermentable sugar production is depicted in Figure 3.2. All the experiments mentioned were performed in triplicate.

Control experiments were performed in the dark with the same arrangement as above but in the absence of illumination. Light control experiments were also performed with the same arrangement but without the addition of a photocatalyst to the reaction mixture.

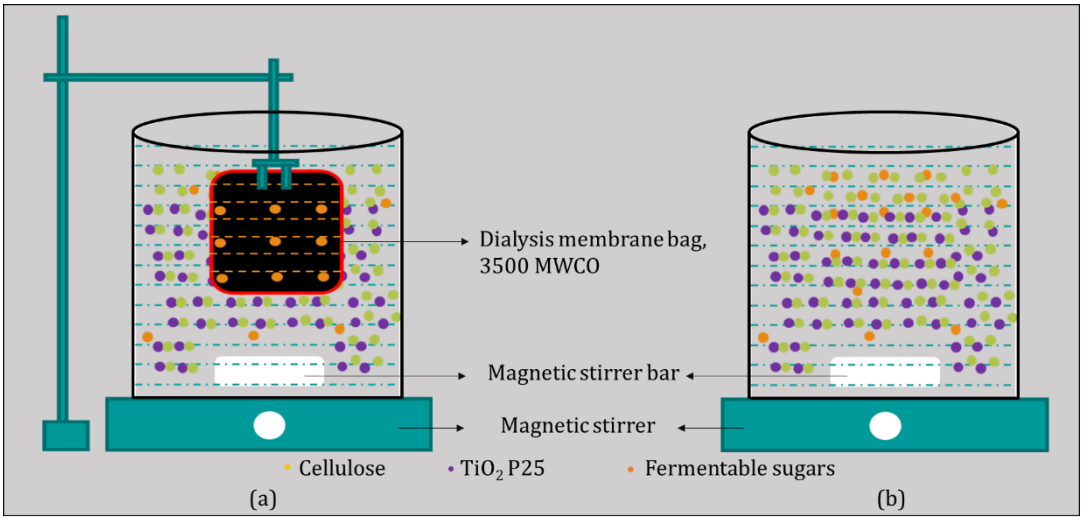

Figure 3.2: Experimental set up photocatalytic fermentable sugar production (a) with dialysis bags and (b) without dialysis bags. The UV lamp was placed 11 cm from the centre of the beakers.

3.2.5 Fermentable sugar monitoring

The concentrated products from cellulose photocatalysis were re-suspended to a final volume of 1 ml using deionised water and stored for further analysis. 0.2 ml of this sample was mixed with 0.2 ml mobile phase (5 mM H_2SO_4) and analysed in a HPLC-RI system. An Agilent 1260 infinity HPLC equipped with a Rezex ROA-Organic acid H+ column (300 × 7.8 mm) was used for analysis. The mobile phase flow rate was set at 0.5 ml/min and a sample volume of 10 µl was withdrawn to analyse for products. HPLC profiles of the respective commercial products were used as standards, which the unknown samples were measured against.

Furthermore, the yield of fermentable sugars from the cellulose feedstock was calculated according to Equation 3.5.

$$\text{Fermentable sugar yield} = \frac{total\ fermentable\ sugars\ produced}{Initial\ cellulose\ used} \times 100 \quad \ldots \text{Equation 3.5}$$

where total fermentable sugars produced is the sum of all glucose, cellobiose, galactose, fructose and anhydroglucose produced upon photocatalysis (in mg) and initial cellulose used was 200 mg.

3.3 Results and discussion

3.3.1 Dissolution and regeneration of cellulose

Extraction of cellulose II from cellulose I via dissolution in TBAH and regeneration with DI water is shown in Figure 3.3. Upon complete dissolution of cellulose I, excess DI water was added to the solution and mixed for 30 minutes. Due to mixing with excess DI water, the cellulose solution was diluted

and cellulose II precipitated out. Precipitation of cellulose from solution could be attributed to the displacement of cellulose-TBAH hydrogen bonds by water-TBAH hydrogen bonds. Regenerated cellulose obtained from this process was further washed to remove the bound TBAH and further characterised using various techniques as discussed in the subsequent sections.

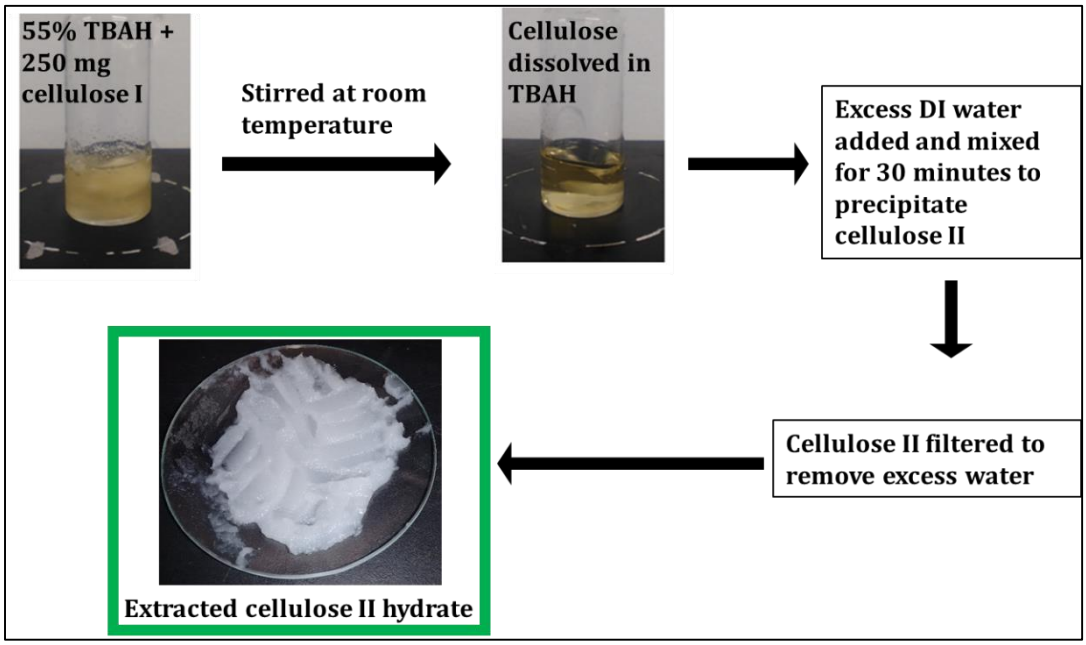

Figure 3.3: Cellulose I dissolution and cellulose II regeneration

3.3.2 XRD profiles for cellulose

XRD profiles of cellulose I and regenerated cellulose are shown in Figure 3.4. The XRD profiles of cellulose II and cellulose I obtained here are consistent with the results reported in literature (26,169) with the significant peaks for cellulose I being close to ~ 22.5^{O}, ~16^{O} and ~ 34.5^{O} and the peaks for cellulose II close to ~19.8^{O}, ~21^{O} and ~12.1^{O}. The CrI for cellulose I was found to be 85.4 % and that of cellulose II was found to be 52.8 % as calculated from Equation 3.1 and 3.2. This decrease in crystallinity of cellulose II when compared to cellulose I was a result of the rearranged hydrogen bond network

which occurred due to the TBAH pre-treatment step. In addition to the CrI, inter-planar spacing was also calculated for the (2 0 0) planes for cellulose I and cellulose II. It was found that the inter-planar spacing for cellulose II was 0.402 nm and that of cellulose I was 0.387 nm as calculated from equation 3.3. Increased d-spacing means that the hydrophobic interactions (van der Waals forces) are weakened between the adjacent planes in the lattice (164,165). Hence it can be concluded that TBAH dissolution is an effective pre-treatment step to produce cellulose II from cellulose I.

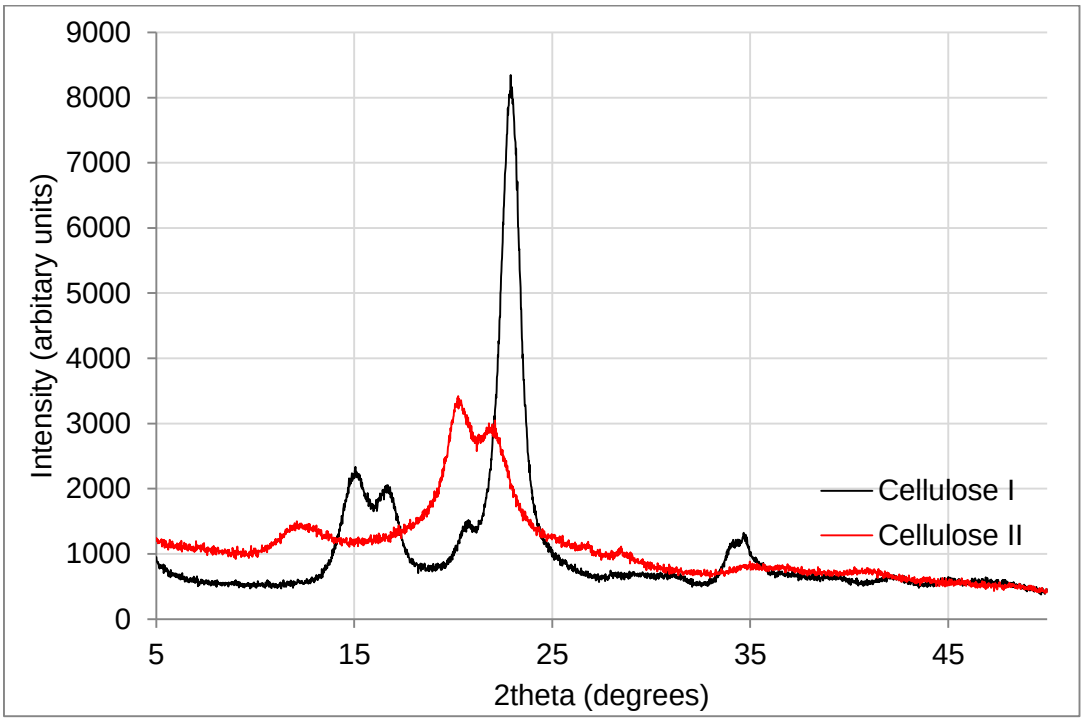

Figure 3.4: Typical XRD profiles of cellulose I (black line) and cellulose II (red line).

3.3.3 ATR-FTIR profiles for cellulose

The ATR-FTIR profiles of cellulose I and cellulose II are shown in Figure 3.5. As can be seen from the figure, the intensity of cellulose I at 3330 cm^{-1} and 3270 cm^{-1} correspond to the O(3)-H-O(5) intramolecular hydrogen bond

and the O(6)-H-O(3) intermolecular hydrogen bond respectively (181,182). These bands were not seen in cellulose II. The bands between 2800 cm^{-1} and 3000 cm^{-1} correspond to the -CH stretching and the bands between 1200 cm^{-1} to 1400 cm^{-1} correspond to $–CH_2$ bending at C6 (181,183). Furthermore, the bands for –CO stretching at C6 and the C-O-C vibration (glycosidic bond) for cellulose I is at 1030 cm^{-1} and 897 cm^{-1} whereas for cellulose II they were shifted to 1021 cm^{-1} and 890 cm^{-1} respectively (181).

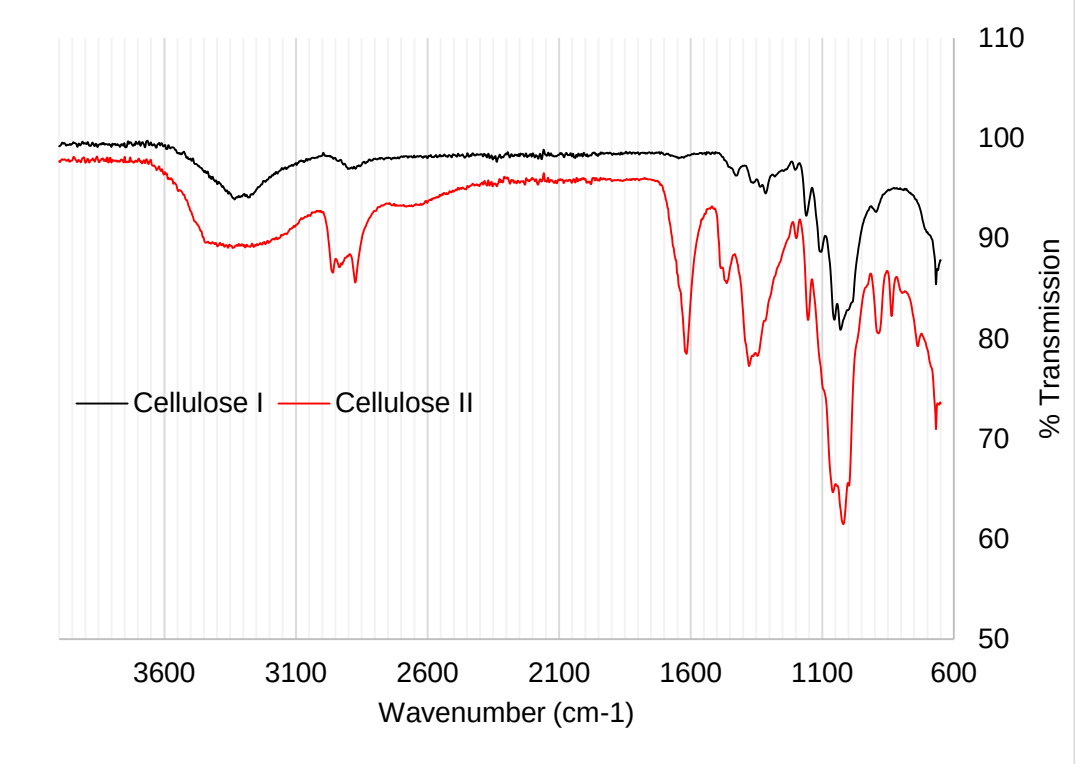

Figure 3.5: ATR-FTIR profiles for cellulose

In addition to the shifts in bands, TCI ratios for cellulose I and cellulose II were also calculated using equation 3.4 and were found to be 0.98 and 0.88 respectively. A lower TCI of cellulose means that the crystallinity of the cellulose II sample had reduced after the TBAH pre-treatment step as a result of rearranged hydrogen bond network and the weakened van der Waals

interaction. This trend obtained was consistent with the CrI calculated from the XRD data.

3.3.4 TGA profiles for cellulose

TGA patterns were recorded for native cellulose and cellulose II and shown in Figure 3.6. The thermal degradation of cellulose I was observed within the narrow region of 290 – 330 ^{O}C, whereas for cellulose II, the degradation occurred over a broad range of 160 – 350 ^{O}C. Degradation occurring from 100 – 160 ^{O}C in the cellulose II sample could be attributed to the evaporation of water. The onset temperature for thermal degradation of cellulose I was found to be 294 ^{O}C and that of cellulose II was found to be 168 ^{O}C. The temperature at which maximum thermal decomposition was achieved for cellulose I was 318 ^{O}C and for cellulose II was 197 ^{O}C. Similar observations of lower onset temperature for cellulose II than cellulose I was also observed by Pang *et al* when they characterised the regenerated cellulose obtained from various ionic liquid treatments (184). The reason for a lower onset temperature and a lower maximum thermal decomposition temperature of cellulose II when compared to cellulose I could be due to its lower CrI (185). In addition, due to the higher available surface area of cellulose II as discussed earlier, more area is exposed for the thermal degradation to proceed (181). These distinct differences between the thermal degradation profiles reveal that the TBAH treatment was successful in converting cellulose I to cellulose II.

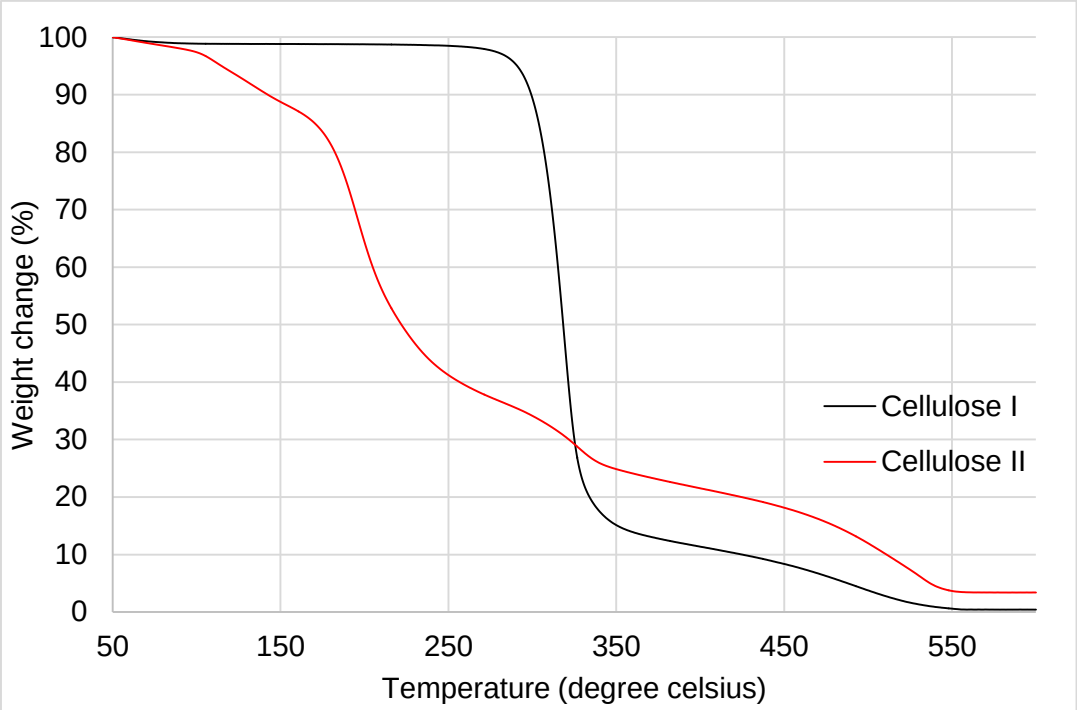

Figure 3.6: TGA profiles for cellulose I and cellulose II

3.3.5 Photocatalytic fermentable sugar production

Photocatalytic fermentable sugar production results are summarised in Figure 3.7. The dark and light control experiments did not yield any sugars or products and hence all the products produced during the subsequent experiments was due to photocatalysis. It is evident from Figure 3.7 that the amount of fermentable sugars produced from cellulose II (2.10 µM) upon photocatalysis is higher than that from cellulose I (0.44 µM). The yields were further calculated using Equation 3.5 which equates to a 0.21 % fermentable sugar yield from cellulose II when compared to only 0.04 % produced from cellulose I. This increase in fermentable sugar production could be attributed to the reduced crystallinity of cellulose II, rearranged inter and intramolecular hydrogen bonding network, increased porous volume and increase lattice distance (170-172). In the case as described, where both cellulose and P25 photocatalyst are in suspension under continuous mixing and illumination,

limitations due to mass transfer are eliminated. Hence, when P25 comes in contact with cellulose particles, especially cellulose II which has an increased lattice distance and higher porous volume, the possibility of OH radicals penetrating its lattice is higher than that of cellulose I thereby producing an increased quantity of fermentable sugars. In addition to this, all products including the fermentable sugars were always present in solution throughout the experiment and hence a part of the sugars and products could have been oxidised or completely mineralised.

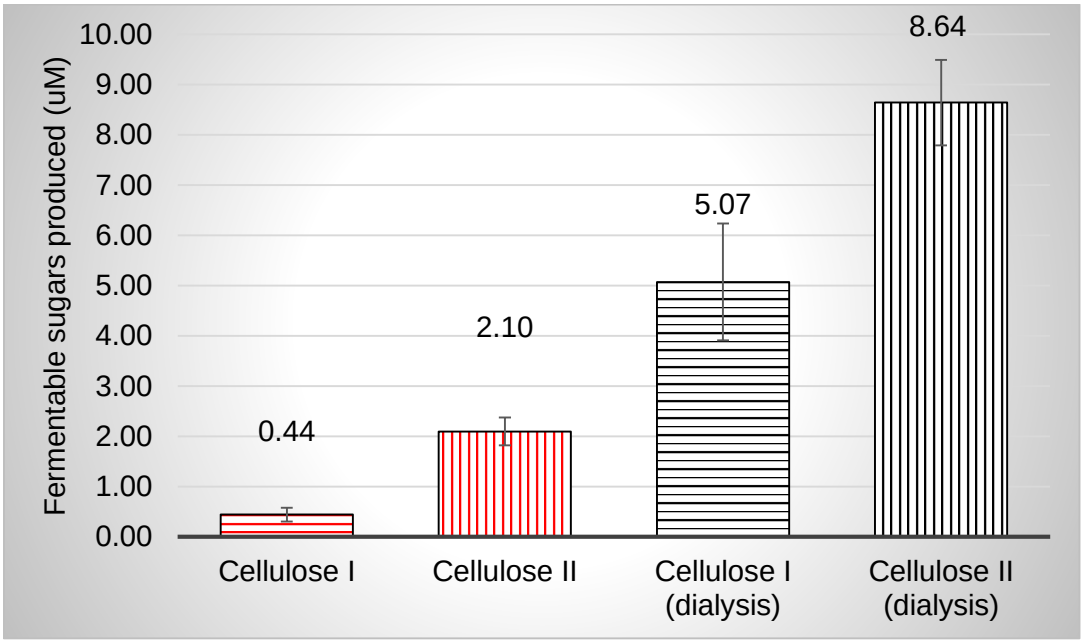

Figure 3.7: Fermentable sugars produced upon photocatalysis

A part of the losses could also be attributed to the selectivity of the photocatalyst. The photocatalyst used in this process is P25, which is a commercially available photocatalyst often used as the benchmark amongst photocatalysts which is capable of producing highly oxidising OH radicals in addition to producing reduced superoxide radicals (Chapter 2). Superoxide radicals can combine with H^+ to form hydroperoxyl radicals which in turn can

self-combine to form H_2O_2. Apart from producing these radicals, the photocatalytically produced electron could also combine with H^+ to form hydrogen. In a reaction mixture containing sugars and hydrogen, there is a possibility of hydrogenation reaction occurring to produce sugar alcohols such as sorbitol from glucose. On the other hand, OH radicals produced are non-specific and oxidise any compound in its vicinity. Therefore, the sugars produced could be further oxidised to other products such as acetic acid, formic acid, glycolaldehyde, arabinose, erythrose, dihydroxyacetone, dimethylfuran (DMF) and CO_2 further decreasing the yield of desirable sugars.

To avoid the loss of sugars, dialysis membrane bags were placed inside the beaker. These bags were immersed in an attempt to capture the sugars instantaneously upon production. Dialysis works on the principle of a concentration difference on either side of the membrane; i.e. when fermentable sugars are produced in solution in the beaker upon photocatalysis, due to the difference in concentration of the sugars/products between the beaker and the membrane bags, sugars diffuse through the membrane into the bag to attain equilibrium. This mechanism was utilised to capture the fermentable sugars and enhance their yield. Accordingly, when the membrane bags were installed, the fermentable sugar quantities produced from cellulose I and cellulose II increased to 5.07 µM and 8.64 µM which equates to a fermentable sugar yield of 0.43 % and 0.71 % respectively. These fermentable sugar yields for cellulose I increased by 91 % and for cellulose II increased by 70 % respectively when compared to their membraneless counterparts. Hence it could be concluded that installation of dialysis

membrane bags could effectively capture sugars and reduce the loss of sugars formed.

There have been examples in literature where cellulose II was proven to be a better starting material for biofuel/fermentable sugar production than cellulose I as mentioned in Table 3.1. For instance, Ma *et al*. used aqueous pyrrolidonium based ionic liquids such as N-methyl-2-pyrrolidonium hydrogen sulfate (MPHS), N-methyl-2-pyrrolidonium dihydrogen phosphate (MPDP), N-methyl-2-pyrrolidonium chloride (MPC) and N-methyl-2-pyrrolidonium methane sulfonate (MPMS) to extract regenerated cellulose from corn stalk for fermentable sugar production via enzymatic hydrolysis (171). Upon ionic liquid treatment, reduced crystallinity of cellulose II samples were confirmed using FTIR. Furthermore, this regenerated cellulose was subjected to enzymatic hydrolysis by commercial *Aspergillus niger* cellulase at 50 ^{O}C for 72 hours at a pH 4.8, maintained using 0.1 M sodium citrate buffer. Fermentable sugars in the range of 39 - 92 % were obtained in this process. The hydrogen bonding capability and acidity of the ionic liquids which successfully removed the bound hemicelluloses and lignin in the corn stalk and the reduced crystallinity of the regenerated cellulose were quoted as reasons for the high sugar yields. In yet another example, Shafiei *et al*. dissolved either spruce wood chips or powder (5 %) in imidazolium based ionic liquids at 120 ^{O}C in an oil bath for varied experiment times (172). To precipitate cellulose II from solution, 20 ml of boiling water was added to the solution. Furthermore, a mixture of cellulase and β-glucosidase enzymes was used to perform enzymatic hydrolysis of the regenerated cellulose and untreated wood

chips/powder samples at 45 ^{O}C for 72 h in citrate buffer. A fermentable sugar yield in the range of 57 – 66 % was reported from cellulose II samples whereas the untreated wood samples yielded only 2 % sugars. The reason for a higher yield of fermentable sugars was ascribed towards the lower crystallinity of the raw material, cellulose II.

Although the fermentable sugar yields reported in literature are multiple folds higher than the quantities produced in this work, it should be noted that the process used in this work to produce fermentable sugars was photocatalysis. Reported data of fermentable sugar production in Table 3.1 have utilised highly cellulose specific, expensive enzymes, whereas the results reported here exploited OH radicals produced from photocatalysis. Since these radicals are non-specific, they also tend to breakdown the fermentable sugars that were produced. With continuous mixing, this loss was inevitable and hence this led to the installation of dialysis membrane bags to capture sugars. To further reduce the sugar losses, in addition to instantaneous removal of sugars using membrane bags, simultaneous alcohol fermentation could also be carried out in a one pot system.

Type of cellulose I	**Method for cellulose II production**	**Anti-solvent used**	**Fermentable sugar production method**	**Comments**	**Reference**
Avicel PH-101 α-cellulose Cotton linters Cellulose extracted from corn stover	Dissolved in 16.5 wt% aqueous NaOH at 25 ^{O}C under a nitrogen atmosphere	Water	Enzymatic hydrolysis using Genencor GC220 cellulase	Enzymatic hydrolysis rate of cellulose II was found to be two times faster than cellulose I	(170)
Corn stalk	0.05 wt% corn stalk was added to a range of aqueous pyrrolidonium based ionic liquids and the mixture was heated to 90 ^{O}C and stirred for 30 minutes	1:1 acetone/deionised water solution	Enzymatic hydrolysis using commercial *Aspergillus niger* cellulase	Highest yield of fermentable sugars of 91.81% was obtained from cellulose II regenerated from N-methyl-2-pyrrolidonium chloride	(171)
Spruce wood chips Spruce wood powder	5 % cellulose I was added to 1-ethyl-3-methylimidazolium acetate (EMIM-Ac), 1-butyl-3-methylimidazolium acetate (BMIM-Ac) or N-methylmorpholine-N-oxide (NMMO) and mixed at 120 ^{O}C	Boiling water	Enzymatic hydrolysis using 15 FPU cellulase and 30 IU β-glucosidase per g substrate	EMIM-Ac treated cellulose produced the highest fermentable sugar yield of 66 %	(172)

Type of cellulose I	Method for cellulose II production	Anti-solvent used	Fermentable sugar production method	Comments	Reference
Fibrous and microgranular cellulose	5 % cellulose dissolved in 1-butyl-3-methylimidazolium chloride (BMIM-Cl) in temperature range of 100-120 ^{O}C	Various acids with the pKa ranging from -14.9 to 4.8 and finally water to stop the reaction	Acid hydrolysis using various acids with the pKa ranging from -14.9 to 4.8	A maximum yield of 11-12 g/ml fermentable sugars was produced	(178)
α-Cellulose Avicel PH-101 Spruce cellulose Sigmacell cellulose Milled cellulose	5 % cellulose in BMIM-Cl at 100 ^{O}C.	Water	0.5 % HY zeolite catalyst added to the mixture and placed in a microwave reactor	Reducing sugar yields in the range of 12-48 % was reported	(177)

Table 3.1: A list of fermentable sugar yields obtained from literature

In addition to the fermentable sugar yields, photonic efficiencies were also calculated for the system. Photonic efficiency is defined as the “amount of products formed per litre per minute over the incident photon flux” (186). It has to be noted that the sugar production rate used here was calculated as an aggregated sugar production rate over 3 hours for each experiment. This was because, sugars were not quantifiable at each time point as they were below the detection limits of the HPLC and hence the products had to be accumulated and then concentrated down to measure the total sugars. The calculated photonic efficiencies for the production of fermentable sugar from cellulose I and cellulose II as feedstock in a setup without dialysis membrane bags was found to 0.39 % and 1.86 % respectively. Whereas, in the setup with dialysis membrane bags, the photonic efficiencies were found to be 4.5 % and 7.67 % for cellulose I and cellulose II feedstocks respectively. The drastic increase in photonic efficiencies from the latter setup was due to the installation of dialysis membranes which increased the amount of fermentable sugars captured.

A scheme of possible reactions leading to the formation of fermentable sugars and other products from the photocatalytic breakdown of cellulose is shown in Figure 3.8. Upon illumination of the cellulose – P25 suspension, OH radicals are produced and with the elimination of mass transfer limitations due to continuous mixing, these reactive oxygen species diffuse into the bulk from photocatalyst surface to breakdown cellulose. When the glycosidic bonds are broken at random lengths, higher saccharides or cellodextrins of different

chain lengths are obtained. These higher saccharides could further undergo scission and lead to the formation of cellobiose and glucose.

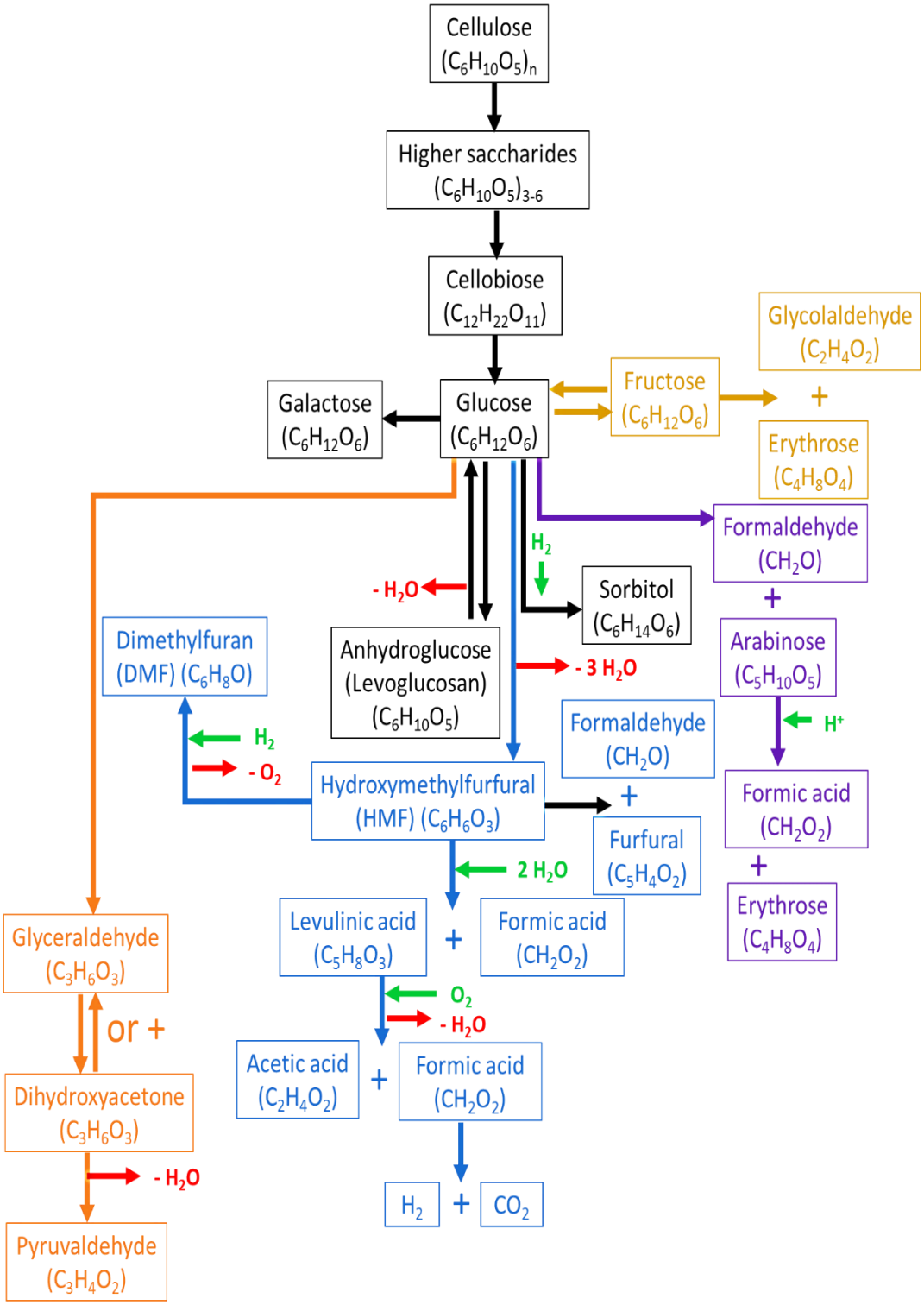

Figure 3.8: Possible route of product formation upon cellulose photocatalysis

In addition, there is also a possibility of a one-step glucose monomer formation upon OH radical attack on the cellulose molecule. Glucose can isomerise in solution to further form either fructose or galactose or undergo a dehydration reaction to form levoglucosan, also known as anhydroglucose. Additionally, glucose could also be degraded to form a five carbon sugar – arabinose, which could further be degraded to form erythrose. The by-products of these reactions are formaldehyde and formic acid respectively. Another possible route of glucose degradation yields glyceraldehyde or dihydroxyacetone which upon dehydration leads to the formation of pyruvaldehyde. Moreover, another possibility is the dehydration of glucose to form hydroxymethyl furfural (HMF) which could then be hydrolysed to levulinic acid and formic acid. Levulinic acid could be further oxidised to form acetic acid and formic acid which could then be completely mineralised to form H_2 and CO_2.

A range of products speculated in Figure 3.8 were produced during photocatalysis of the cellulose feedstocks. Total quantities of each product observed after the end of photocatalysis is shown in Figure 3.9. It can be seen from the figure that a wider range of products was produced from the experiments without dialysis membranes (both cellulose I and cellulose II). This suggests that since the sugars produced were always in solution, they came in contact with the illuminated P25, hence resulting in the production of smaller organic compounds. In the case of experiments conducted with the dialysis bags, however, a comparatively smaller range of products was seen. This could be attributed to the use of dialysis membrane bags which removed the sugars effectively, leaving behind only minimal sugars for further oxidation.

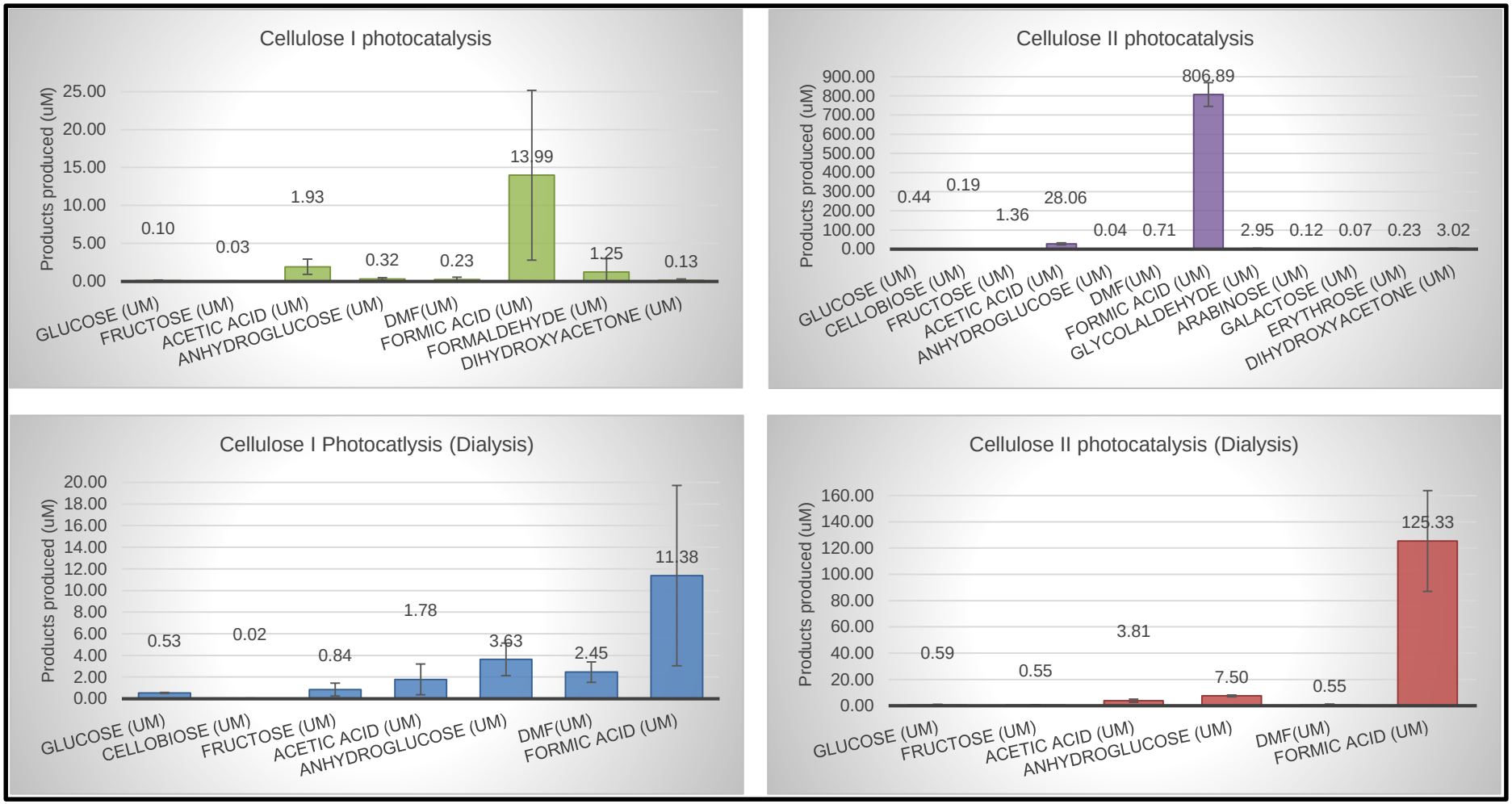

Figure 3.9: Accumulated quantities of products produced across different experiments

It has to be noted that the products produced were random and did not follow any trends and hence the kinetics of product formation could not be determined. To show the random product production pattern, the raw data determined from the experiments are enclosed in Appendix B. Furthermore, to clarify on whether the mobile phase used for the HPLC had any effect on the product formation, standard glucose samples were mixed with mobile phase and analysed in the HPLC-RI. No significant degradation of the sugars was seen nor were any products formed as a result, hence concluding that the mobile phase used for the analysis had minimal/negligible influence on the product formation.

Amongst the products formed, formic acid was produced in highest quantities. As seen from Figure 3.8, this was due to rapid oxidation of sugars under continuous illumination and multiple pathways leading to formic acid formation. For instance, in the case of cellulose II as the raw material and the system without dialysis bag, the total amount of formic acid produced was 807 µM whereas in the case of a similar set up with dialysis bags, the amount of formic acid produced was only 125 µM. In the former case, the produced sugars were present in solution along with the photocatalyst and hence instantaneous oxidation of sugars occur once they come in contact with the produced OH radicals leading to the formation of formic acid. In the latter case, however, the sugars produced diffuse into the membrane bags and are removed at continuous intervals, leaving behind a minimal quantity of sugars in the bulk (beaker) and hence less formic acid was observed in the set up with dialysis bags. Similar explanation could be given for the cases mentioned

above using cellulose I as the starting material where 11 µM and 14 µM formic acid were produced from set ups with and without dialysis membrane. It could hence be concluded that continuous removal of sugars is required to improve the sugar yield and avoid undesirable mineralisation.

3.4 Conclusion

The hypothesis of cellulose II being a better starting material than cellulose I for fermentable sugar production via photocatalysis has been verified in this work and presented in this chapter. Fermentable sugar yield from cellulose II was found to be 0.21 % whereas the yield from cellulose I was found to be only 0.04 %. When the native polymorph of cellulose was converted to cellulose II, the fermentable sugar yield increased by 81 %. This increase could be ascribed to the reduced crystallinity of cellulose II, rearranged inter and intramolecular hydrogen bonding network and increased lattice distance as seen from the XRD and FTIR results. Although the sugar yields improved with the conversion of cellulose I to cellulose II, it was still not significant when compared to enzymatic hydrolysis results from literature. This difference can be attributed to the non-specificity of OH radicals produced upon photocatalysis, which tend to oxidise the fermentable sugars in solution to produce undesirable products. Hence to improve the fermentable sugar yield, dialysis membrane bags were deployed. This increased the fermentable sugar yields from cellulose I and cellulose II to 0.43 % and 0.71 % respectively, which is an increase in yield by 91% and 70 % when compared to similar setups without membrane bags. Photonic efficiencies calculated for fermentable sugar production from cellulose II feedstock was found to be

higher when compared to cellulose I. In addition, the installation of membrane bags improved the sugar capture leading to a further increase in photonic efficiencies. Furthermore, it could also be concluded that to improve the yields of fermentable sugars, continuous removal of sugars is necessary which could be made possible by effective reactor engineering, which will be the focus of the next couple of chapters.

Chapter 4: Mixing Regime Simulation and Cellulose Particle Tracing in a Stacked Frame Photocatalytic Reactor

4.1 Introduction

Fossil fuel depletion and rising greenhouse gas emissions have increased the need for alternative renewable energy technologies. Along with solar energy, wind energy and tidal energy, biofuels could also contribute to global clean energy production. Biofuel production could be brought about from various sources such as waste vegetable oil, food waste, animal fats, algae and cellulose. Among these sources, cellulose is the most attractive raw material as it is the world's most abundant organic material (187), however, cellulose cannot be used directly as a fuel and has to be converted to fermentable sugars which can then lead to the production of bioalcohols via fermentation. Conventionally, cellulose hydrolysis has been achieved through environmentally unfavourable, high energy consuming physico-chemical methods such as steam explosion, pyrolysis or acid/alkali hydrolysis (25). A potential new route for cellulose breakdown using photocatalysis could be an alternative, more sustainable method to breakdown the cellulose molecule to smaller carbohydrate species (173).

Conventional reactors for chemical engineering are well established and classified, whereas photocatalytic reactor designs are still relatively new (52). In addition to the conventional reactor design parameters such as reactor geometry, mixer configuration, mode of operation (continuous or batch), separation efficiency, residence time, reaction selectivity, materials of

construction and cost, the following parameters with respect to illumination need to be considered while designing a photocatalytic reactor (188),

(i) Type of illumination source

(ii) Output power of the light source

(iii) Spectral distribution

(iv) Maintenance

(v) Inclusion of reflectors, mirrors and windows

(vi) Construction materials to facilitate light transmission

Furthermore, the illumination source also influences the choice of materials for reactor construction. When external UV light sources are used for photocatalysis, expensive fused silica (quartz) is the primary choice of material for the reactor vessel as standard glass is not fully transparent to UV radiation, especially at wavelengths less than 400 nm. Pyrex glass, which is a cheaper alternative may, however, be used under near UV illumination (350-400 nm) or for visible light photocatalysis. When illumination sources are deployed within the reactor, the unit is made of materials such as aluminium or stainless steel (for reflection and light distribution), however Pyrex or quartz lamp housing units will still be required.

As previously reported in the literature, photocatalytic reactor designs can potentially fulfil the following objectives (119):

(i) Improve the catalyst-to-reactant ratio and residence time,

(ii) Increase the catalyst illumination time,

(iii) Improve light penetration and distribution for the system,

(iv) Eliminate mass transfer limitations and

(v) Increase the product production and recovery.

Photocatalytic reactors can be broadly grouped under either suspended or immobilised photoreactors based on the platform of photocatalyst deployment. It is not feasible to compare the current reactor designs on a common scale as they have their own advantages and disadvantages based on their area of application (52).

Simulation is a useful tool to compare various reactor configurations or to compare different modifications done to the same reactor design without having to fabricate the actual unit thereby making it valuable in engineering design to reduce the time and costs. The rotating machinery turbulent flow k-ε model in COMSOL Multiphysics® 5.1 was used in this study (189). The reason for choosing k-ε model for the simulations are as follows,

(i) Offers a good trade-off between accuracy and the computational resource requirement,

(ii) Performs well when the pressure drop in the system is expected to be negligible,

(iii) Provides an approximation of the flow patterns for a new design, such as the SFPR (Stacked frame photocatalytic reactor).

Simulation and modelling has been reported for chemical reactions, multi-phase fluid flow, mixing, filtration, dialysis and other processes, (189-194) but only a limited number of applications in photocatalytic reactors have

been published. Simulations focussing especially on mixing regimes in a reactor using COMSOL Multiphysics® have been performed in the past for reactor design verification and bioethanol fermentation purposes (189,194). Patel *et al*. performed simulations to determine the best possible mixing profiles to understand the mass transfer for a combination of either ellipsoidal or flat base vessel with five different impeller blade configurations (189). Similarly, Rana performed simulations to determine the mixing profiles of marine and Rushton impellers for bioethanol fermentation (194). Furthermore, Rana reported that marine impellers were superior in performance and cost efficient over Rushton impellers for bioethanol fermentation in a stirred tank reactor. This chapter describes the design of a novel SFPR (slurry reactor design) along with its mixing regime simulations of a commercially available 'plus shaped' stirrer bar and an 8-blade Rushton impeller configuration for the SFPR.

4.2 Methodology

4.2.1 Stacked Frame Photocatalytic Reactor (SFPR) design

A novel SFPR was designed using FreeCAD 15.0. The SFPR design consists of the following parts,

(i) Perspex frames (with and without inlet/outlet ports)

(ii) Pyrex end plates

(iii) Acrylic inlet and outlet port tubes

(iv) Silicone rubber gaskets

(v) Nylon threaded rods, nuts and washers

(vi) ‘Plus’ shaped magnetic stirrer bar or a stainless steel 316 grade impeller (8-blade Rushton impeller)

Figure 4.1 shows the front view of the SFPR frames displaying the dimensions, M6 slots for inserting the threaded rods and the slots for holding the reaction mixture (cellulose + water + TiO_2). The thickness of each frame was 10 mm and the liquid holding volume of each frame was 12 ml. All the silicone gaskets were of the same dimensions as the Perspex frames, except that the thickness was 1.5 mm. Similarly, the Pyrex end-plates were also of the same dimensions as the Perspex frames, except that the thickness was 3.8 mm and there was no slot for the liquid holding volume.

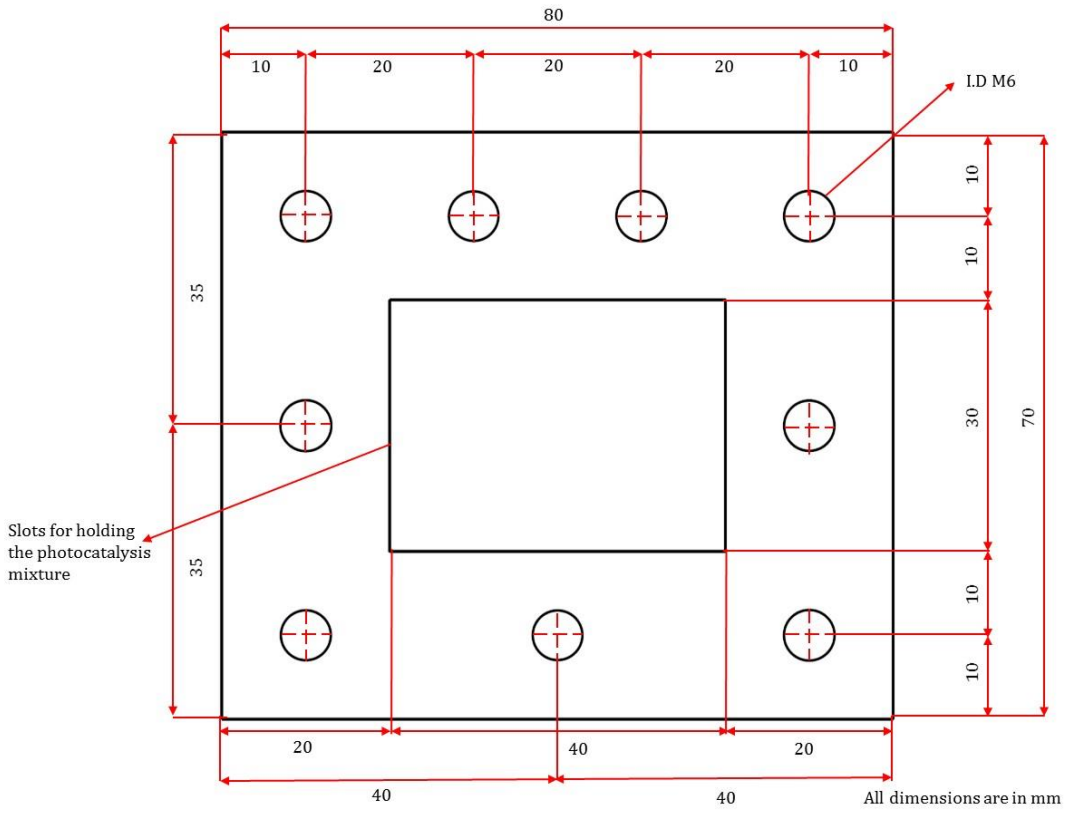

Figure 4.1: Front view of SFPR frames

Two Perspex frames were also designed to have inlet and outlet ports as shown in Figure 4.2. Multiple frames were stacked together with alternating gaskets and sandwiched between Pyrex end plates on either side to form the SFPR. Threaded ports (Figure 4.3) made of acrylic tubes were further fixed to the inlet and the outlet ports of the frames to facilitate inflow and outflow of the reaction mixture. A light source could be positioned in such a way so that it faces the end plate adjacent to the frame with the inlet port.

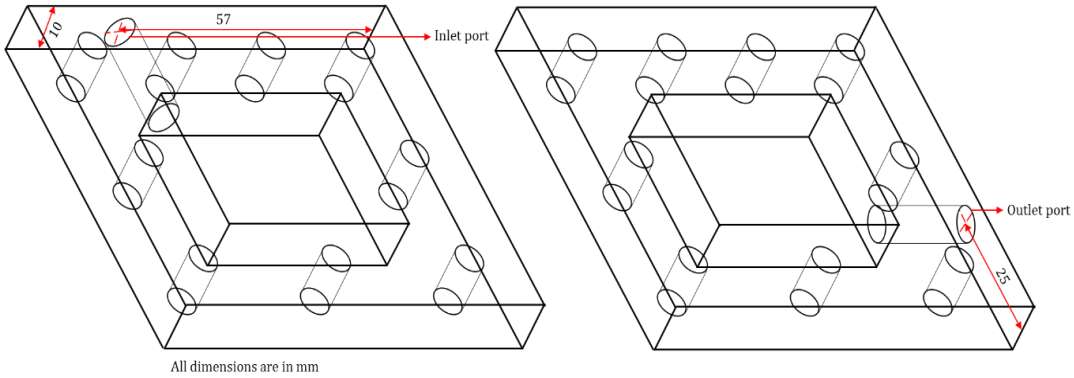

Figure 4.2: Isometric view of a frame with ports

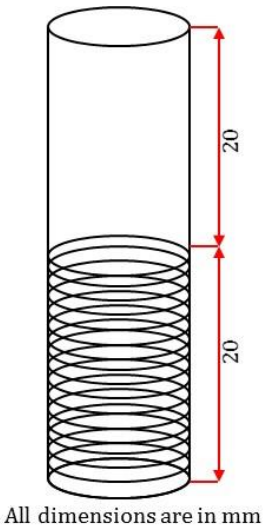

Figure 4.3: Ports for inlet and outlet with an outer diameter of M6

To facilitate mixing in the reactor, various commercially available magnetic stirrer bar configurations were designed to fit the liquid holding volume of the SFPR (Figure 4.4). Similarly, various impeller configurations were also designed to fit the SFPR liquid holding volume (Figure 4.5). Results, however from a plus shaped stirrer bar and an 8-blade Rushton impeller will only be discussed and hence their dimensions are as follows; the dimensions of the stirrer bar are 19.1 mm × 9.5 mm × 2 mm (width × height × thickness) and that of the Rushton impeller are 20 mm × 15 mm (total width × total height), 4 mm × 5 mm (blade height × blade width) and a shaft diameter of 1 mm.

Despite the extensive use of baffles in conventional chemical reactors, no baffles were installed in this assembled photocatalytic reactor. The reasons for this being that the baffles might block the light reaching the photocatalyst, avoid vortex formation thereby diminishing chances of forcing the reaction mixture towards the walls (and the illumination source), hence creating “dead layers” and decreasing the fluid-particle mass transfer (195).

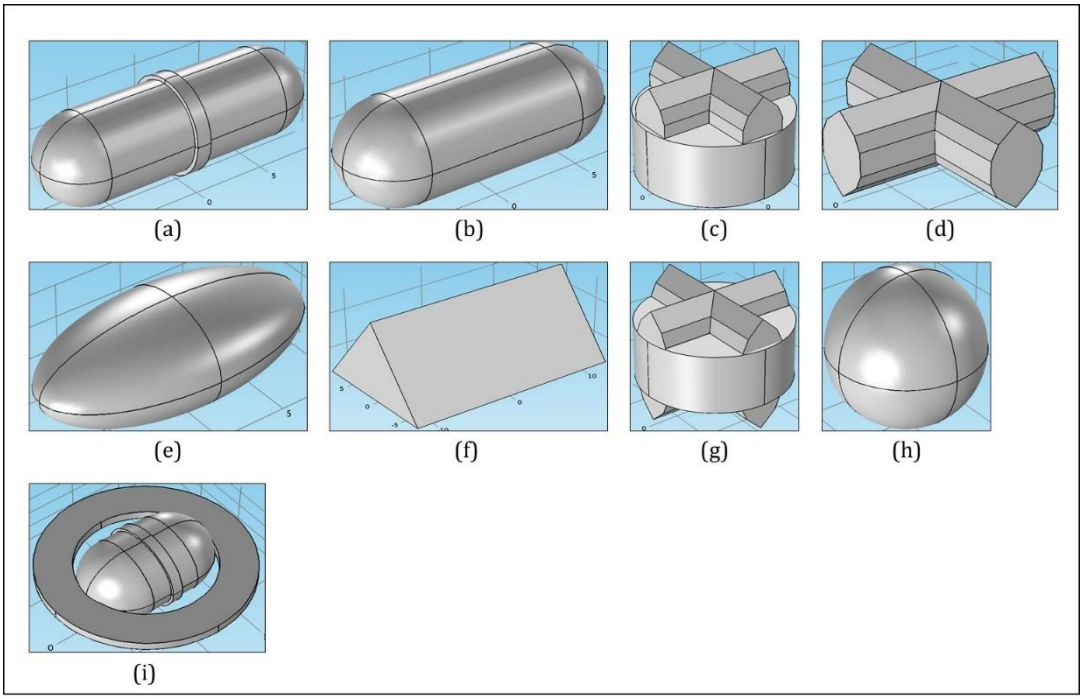

Figure 4.4: Stirrer bar configurations used (a) pivot cylinder, (b) cylinder, (C) single sided plus, (d) plus, (e) capsule, (f) triangular wedge, (g) cross head plus, (h) sphere and (i) spin ring

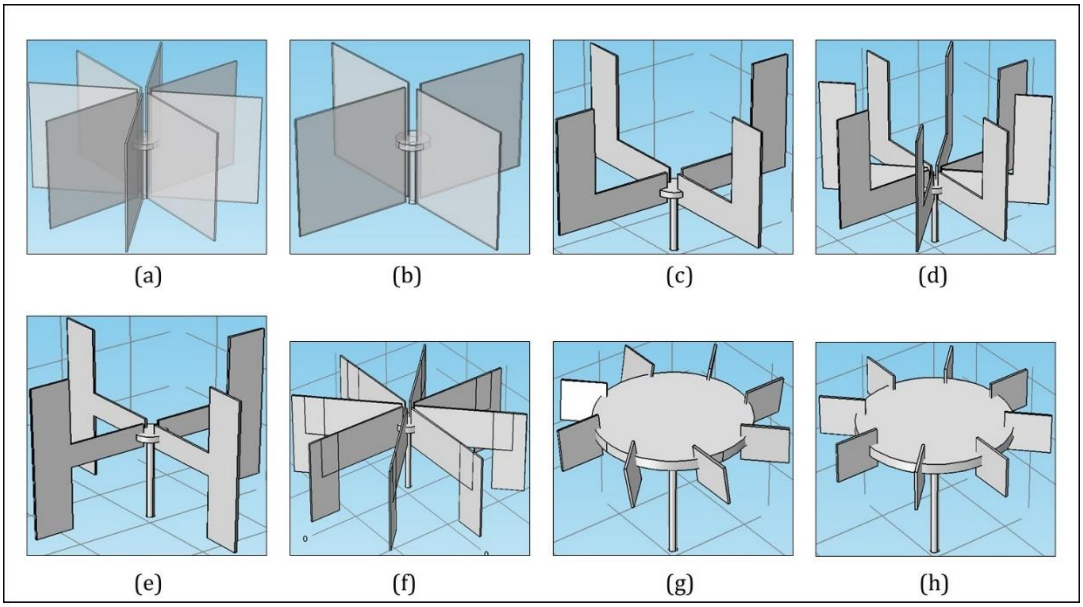

Figure 4.5: Impeller configurations (a) 8-broad blade, (b) 4 broad blade, (c) 2-anchors, (d) 4-anchors, (e) 2-H shaped, (f) 4-inverted anchors, (g) angled 8-blade Rushton and (h) 8-blade Rushton

4.2.2 Mixing simulation

A flow chart on the simulation procedure is given in Figure 4.6. Firstly, the geometry of the fluid domain (liquid holding domain) of the SFPR was created in the COMSOL Multiphysics® 5.1 workspace assuming that 4 frames were stacked together. When 4 frames are stacked together, the liquid holding domain measures 40 mm × 40 mm × 30 mm (thickness × width × height) and has a volume of 48 ml. The inlets and the outlet ports were also created. Secondly, the mixer (either the stirrer bar or the impeller) was created.

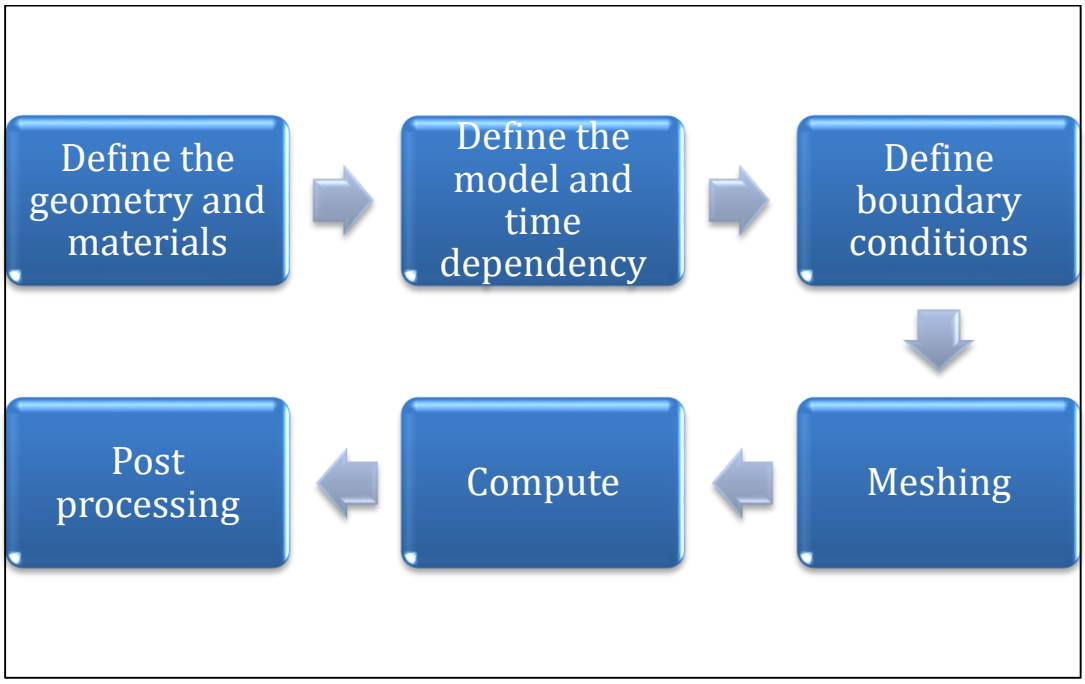

Figure 4.6: COMSOL simulation procedure

Once the geometry of the system was defined, rotating machinery turbulent flow k-ε model with a frozen rotor study (stationary with respect to the reactor) was selected in COMSOL Multiphysics®. This model uses incompressible fluid flow and assumes Reynolds-Averaged-Navier-Stokes (RANS) equation for the fluid flow (189). Next, the material in the fluid domain

was defined as water. Its fluid properties were defined with the density being 1000 kg/m^3 and the dynamic viscosity being 1.002 × 10^{-3} Pas. Then the rotating domains were allotted and the speed of rotation of the mixer was set at 1000 rpm. Subsequently, the inlet was assigned and the normal inflow velocity of the system was set at 0.01 m/s. The outlet for the system was then defined with the backflow suppressed. Finally, flow continuity was set up for the rotating and the fluid domains. All domains were meshed using the "physics controlled mesh" option provided by COMSOL Multiphysics® model builder and hence automatic (Figure 4.7).

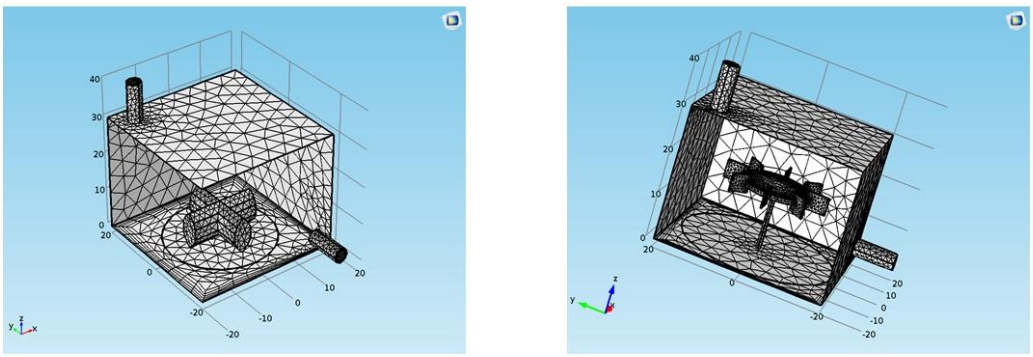

(a) (b)

Figure 4.7: Meshing of the SFPR fluid domain hosting (a) plus shaped stirrer bar and (b) 8-blade Rushton impeller

4.2.3 Particle tracing

Once mixing simulation was completed, particle tracing module was added to the model to simulate the motion of cellulose particles in the SFPR. Then a new time dependent study was included in the model for particle tracing. A drag force node was introduced to the module where the fluid domain defined in the mixing simulation was chosen as the domain where the particles will be present. The velocity field and the dynamic viscosity from the

mixing simulation results were used to compute the drag force on the cellulose particles. The inlet and the outlet for the cellulose particles were then defined. The number of particles per release was assumed to be 3000. From the mixing simulation results, the velocity field was chosen and defined as the initial velocity of the particles for particle tracing. In the particle properties section, the density of the cellulose particles was set as 1500 kg/m^3 (an average value obtained from literature) (196) and the particle diameter was set as 55 µm (obtained as an average diameter for cellulose particle from various suppliers). Furthermore, to use the results from the mixing simulation for the velocity field and to reduce the computation time for particle tracing, in the time dependent solver settings, the mixing simulation study was selected and included. The time range to compute the motion of the cellulose particles was chosen from 0 seconds to 1 second, with a step time of 0.1 seconds to visualise the mixing at the initial stages.

4.3 Results and discussion

4.3.1 Mixing simulation

Mixing simulation for the SFPR with various stirrer bar and impeller configurations were performed, with results in the form of slice plots, XY streamline plots and YZ streamline plots generated and summarised in the Appendix C. The results suggested that the plus shaped stirrer bar and the 8-blade Rushton impeller had superior mixing profiles when compared to the other mixers. Hence the mixing profiles and particle motions of the plus shaped stirrer and the Rushton impeller will be discussed from hereon.

Slice plots obtained from the mixing simulation for a plus shaped stirrer bar and the 8-blade Rushton impeller are shown in Figure 4.8. As seen from the figure, the arrows indicate the direction of fluid flow as a result of mixing where the size of the arrows is proportional to the fluid velocity at that point. It can be observed that the fluid velocity is higher (as seen from the proportional arrows) close to the blades of the Rushton impeller when compared to the walls of the stirrer bar. This observation is explained by the flat blade impeller exerting a relatively stronger force on the fluid than the convex walls of the stirrer bar. This explanation is further supported by the specific velocity magnitudes where the maximum fluid velocity close to the walls of the impeller blade and the stirrer bar is 1.2 m/s and 0.9 m/s respectively.

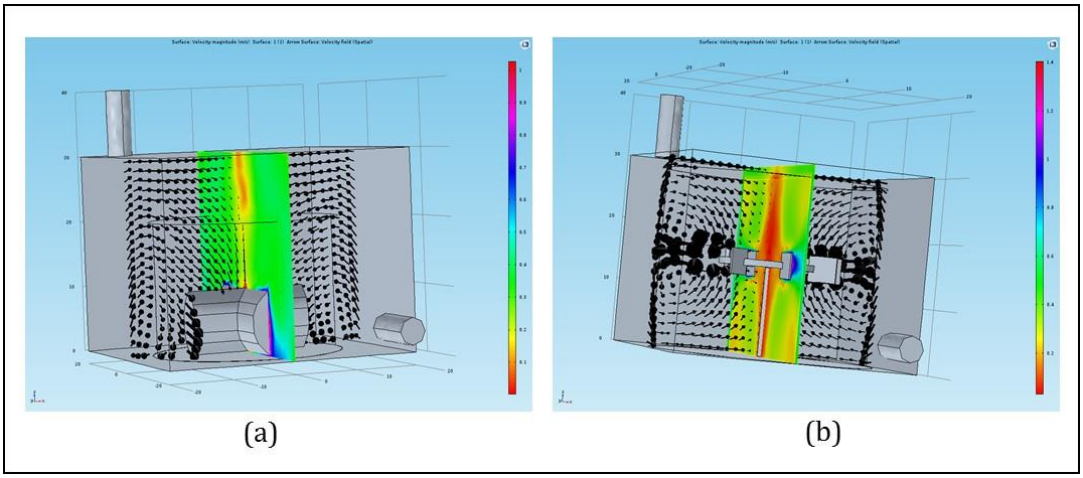

Figure 4.8: Mixing profile - Slice plot of SFPR with (a) plus shaped stirrer bar and (b) 8-blade Rushton impeller

Figure 4.9 and Figure 4.10 shows the XY and YZ streamline plots of the mixing profiles respectively in the SFPR with a plus shaped stirrer bar and the 8-blade Rushton impeller. As can be seen from the XY plot, a prominent circular flow is developed with the stirrer bar, however it is not the case with the Rushton impeller. The arrows indicate the direction of fluid flow during

mixing. The velocity magnitude spread across the XY plane for the stirrer bar is in the range of 0.2-0.4 m/s and that for the impeller is in the range of 0.1-1.2 m/s as seen from the streamlines and the special velocity fields.

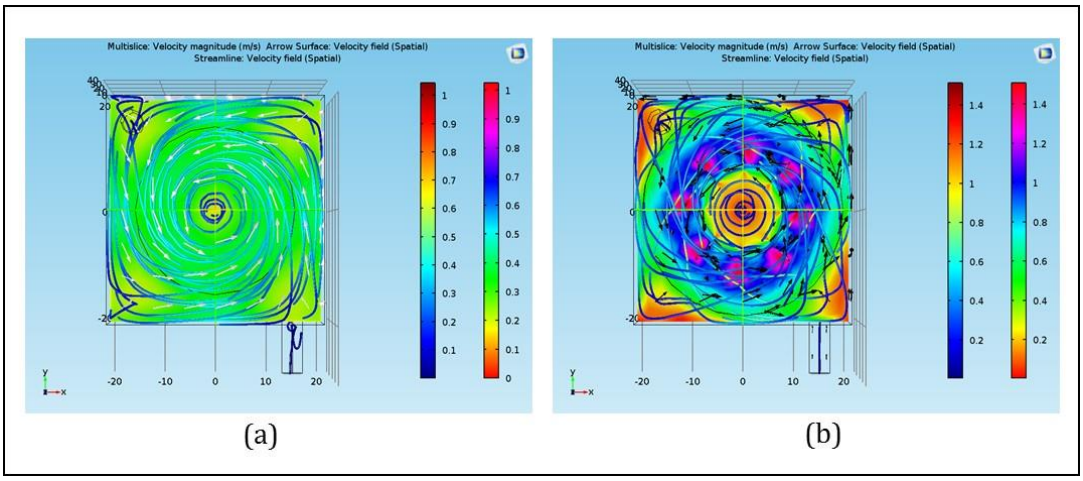

Figure 4.9: Mixing profiles - XY streamline plot for SFPR with (a) plus shaped stirrer bar and (b) 8-blade Rushton impeller

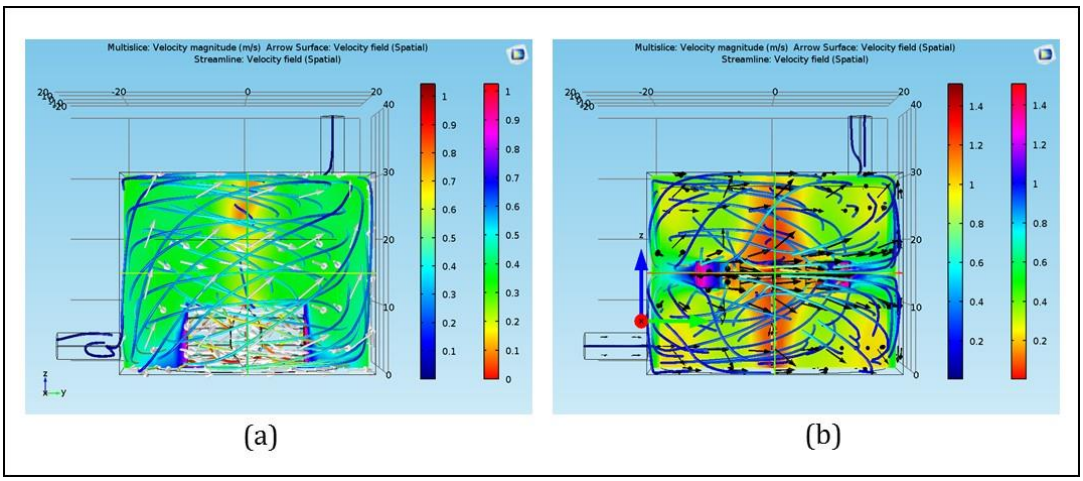

Figure 4.10: Mixing profiles - YZ streamline plot for SFPR with (a) plus shaped stirrer bar and (b) 8-blade Rushton impeller

Furthermore, Figure 4.10 also shows that there are no obvious “dead layers” in both the cases, which is an indication that when particles are introduced in the SFPR, they will stay in suspension. The maximum fluid velocity in both the cases is observed close to the walls of the impeller blades

and the stirrer bar. Once the fluid is pushed away from the stirrer bar, the fluid velocity drops to 0.4 m/s along the walls of the SFPR. Whereas in the case of the impeller, a fully developed radial mixing pattern is observed. This observation is consistent with the existing literature (197-199). The fluid velocity close to the top centre of the SFPR is small, indicating that a tiny vorticity is generated when the stirrer bar is used. This conclusion is also supported by the XY streamline plot. In the case of the impeller, a well-developed vorticity is seen in the middle thereby pushing the fluid towards the walls. In the case of a photocatalytic reactor (SFPR), when the liquid is forced towards the walls of the reactor, light penetration through the solution is significantly increased.

4.3.2 Particle tracing simulation

Particle tracing simulations for cellulose in the SFPR followed mixing simulations. The particle tracing simulations revealed that the motion of the cellulose particles in both the cases followed the fluid flow patterns initiated by the mixing. As a result of mixing, in both the cases, cellulose particles were well dispersed in the suspension. In the case of the impeller, as a result of a prominent vorticity developed due to agitation, the particles enter the vortex first along with the fluid flow and with the constant rotation of the impeller they are pulled closer to the blades and instantaneously pushed towards the walls.

The most commonly used form of TiO_2 is the P25 which has an average particle size of 25 nm (67), which can aggregate to form particles in the size range of microns or could adsorb on to the cellulose surface thereby

considerably increasing the combined particle size. In addition, since the motion of particles in the fluid domain are proportional to the fluid motion, these photocatalyst particles are expected to have a similar motion such as that of cellulose in the fluid domain. Since the particles are forced towards the walls, the chances of more photocatalyst particles being illuminated are higher than a system which offers no mixing. This mechanism also decreases the mass transfer limitations and will help to improve the cellulose-TiO_2 particle interaction, thereby producing desired products.

From literature, the scattering and absorption coefficients of P25 could be obtained which correspond to 54208 $cm^2\ g^{-1}$ and 887 $cm^2\ g^{-1}$ at 365 nm respectively (200). It should be noted that the scattering coefficient is multiple folds (60 times) higher than the absorption coefficient which means that the majority of the light extinction depends on scattering. This was also supported by Egerton and Tooley, who reported that when illuminated at 360 nm, TiO_2 particles of a mean size 50 nm contributed only 22% for extinction (201). They also reported that with the increase in particle size, scattering coefficient would increase. This increase could be possible in the case of cellulose-TiO_2 mix in a SFPR. With cellulose particles being poor light absorbers (202) and with the possibility of TiO_2-cellulose aggregate formation, the scattering coefficient for these particles (and aggregates) would tend to increase in the SFPR and would contribute to an uniform light distribution within the reactor. In addition, from the numbers reported in literature it is evident that minimal light absorption by TiO_2 particles occurs and therefore would have an effect on photocatalysis. Hence to avoid a negative effect of minimal absorption on

photocatalysis, proper mixing has to be established as reported in this study. It should be noted that more insight on the motion of particles and radiation scattering could be revealed when particle-particle interaction and the particle-radiation interaction studies are undertaken in the future.

4.4 Conclusion

Mixing profiles in the SFPR with various impeller and stirrer bar configurations were determined using the rotating machinery turbulent flow k-ε model in COMSOL Multiphysics® 5.1. Simulations were performed with water present in the fluid domain. The mixers were set to be operated at 1000 rpm. The results reveal that the plus shaped stirrer bar had a circular flow with the highest average fluid flow velocity around 0.9 m/s whereas, the 8-blade Rushton impeller had a superior performance than the stirrer bar and produced a radial mixing profile in addition to having higher fluid flow velocity of 1.2 m/s.

Further to the mixing profiles, particle tracing simulations were also performed in the SFPR using cellulose as the model particle. The drag force of the cellulose particles in the particle tracing were proportional to the fluid velocity obtained from the mixing simulations. In the cases with both the stirrer bar and the Rushton impeller, the particles were well dispersed, however the particle dispersion was superior in the case of the Rushton impeller where the vorticity generated during mixing pushed the particles towards the walls. A similar particle motion is expected with the TiO_2 P25 photocatalyst due to the

mixing regime generated by the Rushton impeller, thereby facilitating better illumination of the photocatalyst.

Chapter 5: Photocatalytic Fermentable Sugar Production in a Stacked Frame Photocatalytic Reactor

5.1 Introduction

The need for alternative energy production has already been outlined in Chapter 1. With a view towards alternative energy for transportation fuels, researchers have always focussed on producing bioethanol. Bioethanol production from cellulose conventionally proceeded via the release of fermentable sugars from various methods such as steam explosion, ammonia explosion, acid/base hydrolysis, microbes and enzymes (25). The advantages and disadvantages of these methods are detailed in Table 1.2, Chapter 1. Although there were a number of methods used earlier, there is no single process which can fulfil the criteria of fermentable sugar production from an environmentally friendly, sustainable and cheap method. To overcome these disadvantages a new route for fermentable sugar production via photocatalysis was proposed in the earlier chapters. As seen from the results in Chapter 3, the preliminary experiments for photocatalytic fermentable sugar production are positive and opens new doors for more work. The fermentable sugar yields obtained from the preliminary experiments can be further enhanced with proper reactor design.

Reactors for photocatalysis have been used in the past for various applications such as wastewater treatment, treatment of volatile organic compounds, toxin removal, dye degradation, killing microbes and pathogens, water splitting and hydrogen production (45,52,129,157,203-207).

Occasionally, however photocatalytic reactors have also been used to breakdown cellulose for the production of fermentable sugars, hydrogen and other value added products such as 5-HMF (127,173). Fan *et al*. for instance used a corrugated plate reactor where these plates coated with nanoporous TiO_2 were placed in a cylindrical tube (127). This photoreactor system was then irradiated with a 21 W UV lamp with a peak wavelength of 254 nm upon the addition of 100 ml of 100 g/L cellulose dissolved in 66 % $ZnCl_2$. Ambient air was bubbled into the reactor to supply oxygen. No mixer configuration was installed in this system. The primary product obtained from this process was HMF at a highest concentration of 3.8 g/L when the plates were placed at an angle of 42^O. Glucose was also produced in the process but only as an intermediate product. Zhang *et al*. on the other hand immobilised ball-milled cellulose onto the surface of TiO_2 and Pt-TiO_2 and dispersed the composites in water in a gas tight photoreactor (173). The 0.3 g/L composite was irradiated by a 250 W iron doped halide lamp and all the O_2 in the system was removed prior to photocatalysis. Glucose was the predominant product of the reaction, followed by formic acid and cellobiose.

It has to be noted that in both the reported cases of cellulose breakdown using photocatalysis, native cellulose (cellulose I) was used as the raw material. In this work, in addition to cellulose I, a polymorph of cellulose - cellulose II was also used as feedstock for photocatalytic fermentable sugar production. Photocatalysis of cellulose (cellulose I and cellulose II) dispersed in water with P25 TiO_2 was performed in a SFPR for fermentable sugar production. The design of the SFPR has already been discussed in Chapter

4. This chapter specifically discusses the production of fermentable sugars from cellulose in a SFPR to determine the effect of the installed mixer configurations on fermentable sugar production. A plus shaped magnetic stirrer bar or an 8-blade Rushton impeller was used for comparison purposes whose configuration, design and mixing profiles have already been discussed in Chapter 4. In addition, the effect of H_2O_2 addition on the production of fermentable sugars was also tested.

5.2 Experimental procedure

5.2.1 Materials

Microcrystalline cellulose (cellulose I) was purchased from Acros organics, UK. Cellulose II was prepared in the laboratory and characterised by procedures detailed in Chapter 3, section 3.2.2 and section 3.2.3. TiO_2 P25 was purchased from Degussa (now Evonik industries). 30 wt% H_2O_2 was purchased from SciChem. All the chemicals purchased were used as received without further purification. Fisher brand dialysis membrane (3500 molecular weight cut-off) tubing with a wall thickness of 28 µm and a diameter of 29.3 mm was purchased from Fisher scientific and cut to into membrane sheets prior use.

5.2.2 SFPR Assembly

Components of the SFPR were assembled as seen in Figure 5.1. The reaction chamber consisted of Perspex frames with the outer dimensions of 80 × 70 × 10 mm (width × height × thickness). Liquid holding slots were made in the centre of each frame with a volume of 12 ml and dimensions of 40 × 30

×10 mm. Five Perspex frames alternating with silicone gaskets were stacked together. The silicone gaskets had the same dimensions as that of the Perspex frames except that its thickness was 1.5 mm. One frame at the end of the stack had slots for inlet and outlet. Next to this frame was placed another gasket followed by a Pyrex glass end plate.

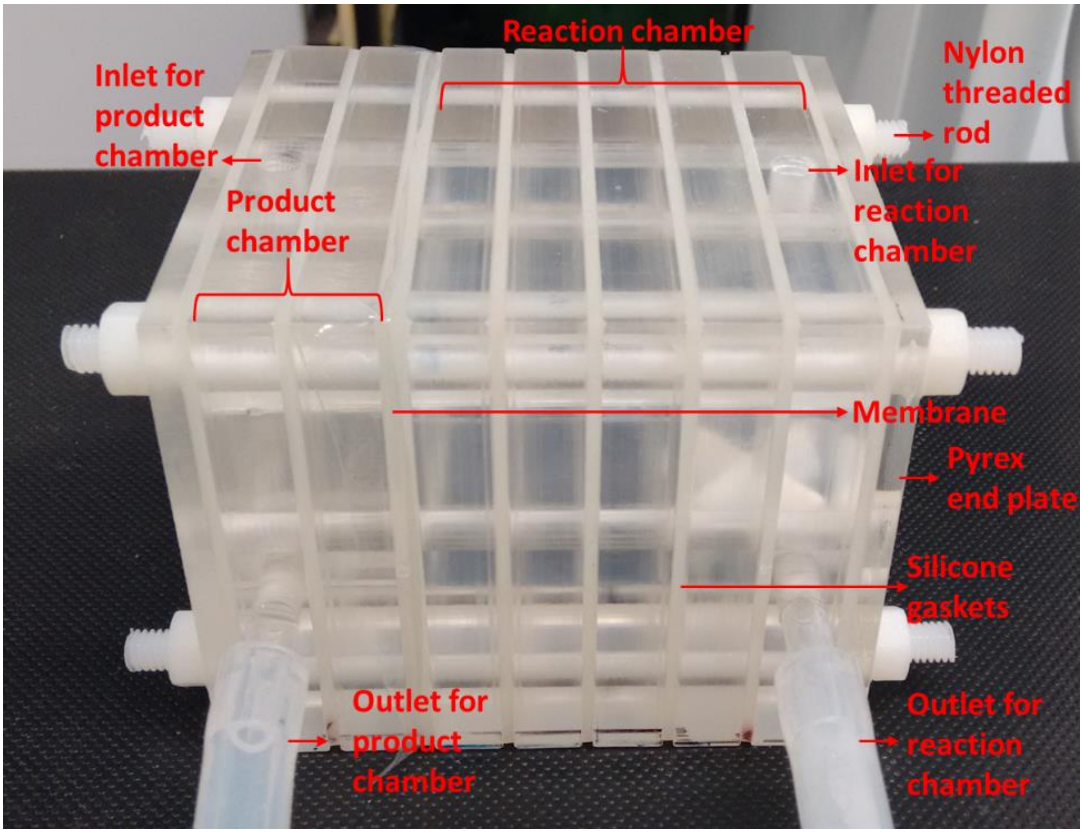

Figure 5.1: Components of the SFPR

This Pyrex glass plate had the dimensions same as the frames, but its thickness was 3.8 mm and it had no liquid holding volume in the centre. On the other side of the stack was placed the dialysis membrane sandwiched between two gaskets. The dialysis membrane was cut to the required dimensions to suit the SFPR and stored in DI water prior use. The product chamber, sandwiched between a Pyrex end plate and the membrane stack

immediately followed. The frame next to this end plate had slots for inlet and outlet. Once the SFPR was assembled, the stack was held together in place using nylon threaded rods, washers and nuts via the M6 slots made on the frames, gaskets and end plates.

5.2.3 Photocatalytic cellulose breakdown experiments

All photocatalytic cellulose breakdown experiments were performed in the SFPR with either a plus shaped magnetic stirrer bar or an 8-blade Rushton impeller as the mixer configuration (Figure 5.2). When the SFPR hosted a magnetic stirrer bar as the mixer, the reactor was placed on top of a magnetic stirrer plate. When the Rushton impeller was used as the mixer, the third frame from the membrane in the reaction chamber was replaced with a new frame having a 3 mm hole in the top to allow the shaft of the impeller to pass through. This shaft was then coupled with a Kitronik motor and operated at approximately 1000 rpm (no load speed). In both the cases, the reaction chamber composed of 55 ml of 1 g/L cellulose (cellulose I or cellulose II) and 0.75 g/L P25 TiO_2 in DI water. The product chamber which consisted of 25 ml DI water was separated from the reaction chamber by a dialysis membrane. 15 minutes' dark equilibration time was allowed before switching on the irradiation source. Upon dark adsorption, 20 ml of sample (marked as sample at time 0 minutes) from the product chamber was withdrawn and replaced with 20 ml DI water. A 36 W UV lamp (Philips, Cleo), placed 3 cm away from the reaction chamber end plate was then switched on. The spectra of the lamp used is shown in Figure 2.1. The photon flux reaching the SFPR was determined to be 5.1×10^{-1} µEinstein L^{-1} min^{-1} as measured by ferrioxalate

actinometry (Appendix D) (180). 20 ml sample was then taken from the product chamber and replaced with 20 ml DI water at various sampling times until 180 minutes. Samples from each sample time were air stripped to concentrate the products down to 1 ml. Dark control and light control experiments were also performed with the same set up as above, except that for the former, the reactor was operated in dark and for the latter, the reaction mixture devoid of P25 was illuminated. All the experiments were performed in triplicates unless mentioned otherwise.

Another set of dark, light and photocatalytic experiments were performed with both the mentioned mixer configurations with cellulose II as feedstock. 0.01 wt% or 0.1 wt% H_2O_2 was added to the reaction mixture to determine its effect on fermentable sugar production. Experiments involving H_2O_2 were performed in duplicates.

5.2.4 Fermentable sugar monitoring

0.2 ml of the concentrated sample was mixed with 0.2 ml of 5mM H_2SO_4 (mobile phase) and analysed in an Agilent 1260 infinity HPLC-RI system. A Rezex ROA-Organic acid H+ column (300 × 7.8 mm) was used for analysis. Flow rate of the mobile phase was set to 0.5 ml/min. Sample volume of 10 µl was withdrawn to analyse products in the mixture. The detector temperature was set at 40^{O}. Samples were measured against the HPLC profiles of respective commercial standards.

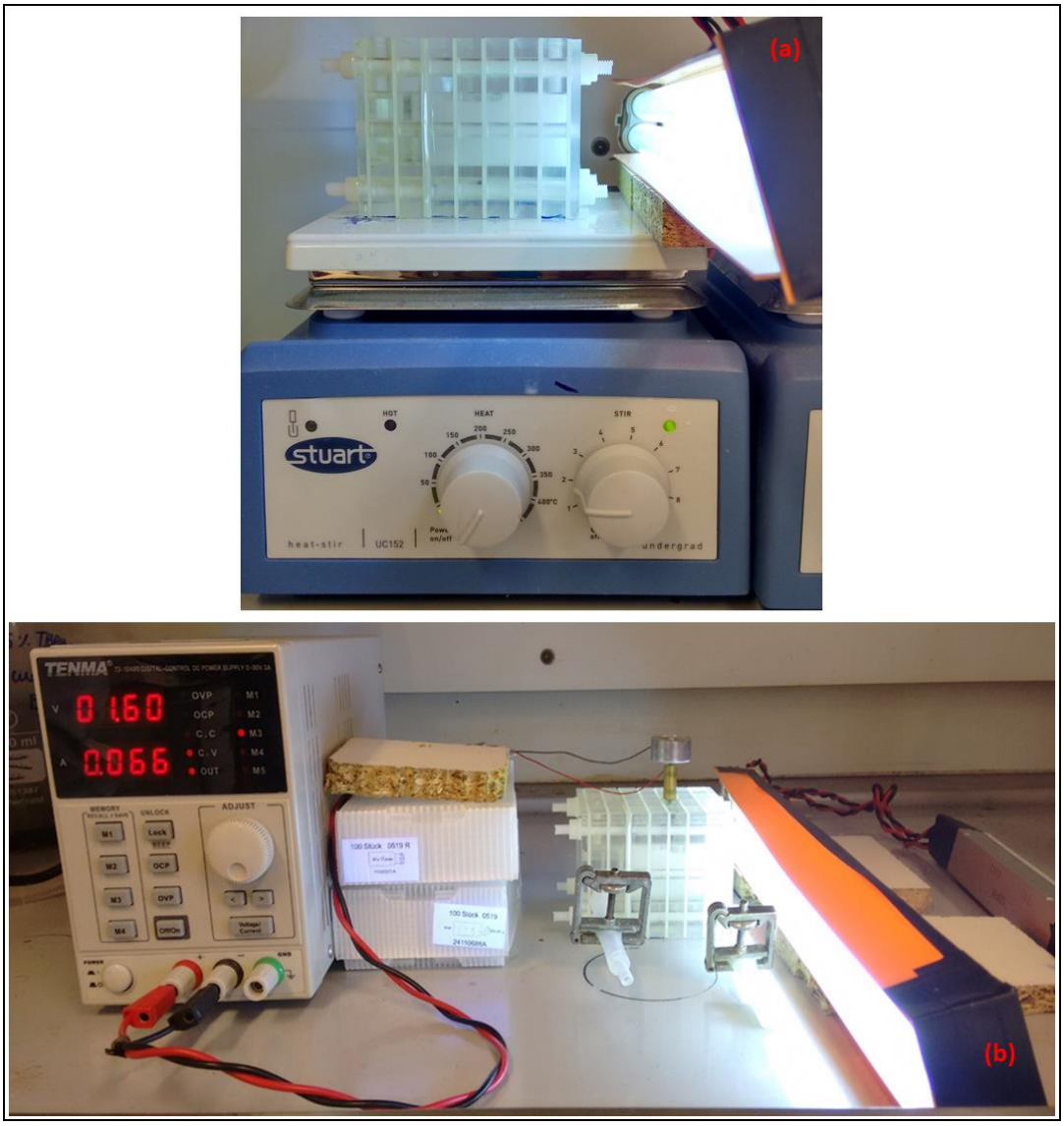

Figure 5.2: SFPR in operation with (a) plus shaped magnetic stirrer bar and (b) 8-blade Rushton impeller

5.3 Results and discussion

5.3.1 Photocatalytic cellulose breakdown

Preliminary results from Chapter 3 demonstrated that fermentable sugars could be produced photocatalytically from cellulose I and cellulose II. The highest fermentable sugar yield obtained with cellulose I feedstock (and dialysis membrane bags) was 0.43 % whereas with cellulose II feedstock the yield improved to 0.71 %. The increase in yields when compared to their

membraneless counterparts were 0.04 % and 0.20 % respectively. This enhanced yield could be attributed to the deployed dialysis membrane bags which were capable of capturing the fermentable sugars thereby reducing losses. These experiments showed the potential for photocatalytic fermentable sugar production from two different cellulose polymorphs, however the yields had to be improved.

In the beaker based experiments, membrane bags deployed in the centre of the beaker acted as a barrier and disturbed the mixing pattern. In addition, these bags also blocked the light path, and resulted in a decreased number of photons reaching the P25 particles. Hence, to avoid such losses and to achieve an enhanced fermentable sugar yield, reactor engineering was chosen and therefore a SFPR was designed and fabricated. The primary focus of the SFPR design was to overcome mass transfer limitations, followed by improved light penetration (and absorption by P25) and effective product separation. To attain this, an ideal mixer configuration had to be installed. On this basis, various mixing configurations were designed and mixing profiles were simulated using COMSOL Multiphysics as mentioned in chapter 4. Amongst the mixer configurations, a plus shaped magnetic stirrer bar and an 8-blade Rushton impeller were chosen as mixers due to their superior mixing regimes and higher achievable fluid velocity when compared to others (Appendix C). An increased fluid velocity would proportionally increase the velocity of particle in solution, which means that an improved light absorption by the photocatalyst could be achieved. In addition, with the presence of cellulose particles in suspension, increased light scattering would also occur,

thereby improving the light distribution in the SFPR. From a mass transfer perspective, short-lived photogenerated OH radicals need to diffuse into the bulk to perform cellulose oxidation. This could also be achieved with the use of proper mixers because, the cellulose particles in suspension are forced to come in contact with the OH radicals due to higher particle velocity generated as a result of mixing. Furthermore, upon proper mixing, constant contact between cellulose and P25 could be achieved, which would also favour the photocatalytic oxidation of cellulose. Finally, from the product separation viewpoint, instead of membrane bags, membrane sheets were used. Since, the assembly of the SFPR was by stacking frames, these dialysis membrane sheets were sandwiched between the reaction and product chambers of the SFPR. Since the membrane was packed between chambers, blocking of light or alteration of mixing profile as seen from the beaker experiments were not observed. This paved the way for effective product separation as can be seen from the enhanced results due to photocatalysis (Figure 5.3). Dark and light control experiments did not yield any fermentable sugars as there was no light or no catalyst to initiate cellulose breakdown.

Photocatalytic fermentable sugar production results (accumulated concentrations over a 3 hour time period) in a SFPR with two different mixer configurations is shown in Figure 5.3. The details on the individual quantities of various products produced at different sample times are shown in Appendix D. The photocatalytic fermentable sugar production from cellulose I and cellulose II with the impeller as the mixer were observed to be higher when compared to its magnetic stirrer bar counterparts. The corresponding

fermentable sugar yield with the stirrer bar configuration when cellulose I was used as the feedstock was found to be (5.12 µM) 1.71 %, however when cellulose II was used as the feedstock, the yield increased to (7.9 µM) 2.56 %. Similarly, when the impeller was used as the mixer configuration, the yields increased from (6.08 µM) 1.86 % to (8.58 µM) 2.61 %.

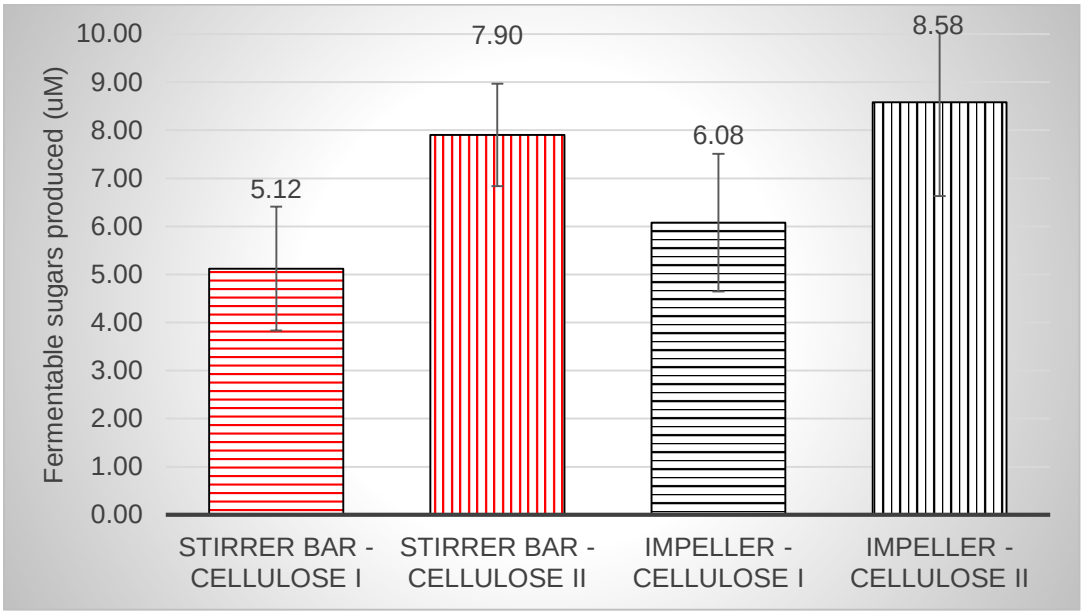

Figure 5.3: Photocatalytic fermentable sugar production in a SFPR with a plus shaped stirrer bar or an 8-blade Rushton impeller

In addition to the accumulated fermentable sugar production shown in Figure 5.3, other by-products produced during the process are shown in Figure 5.4 and Figure 5.5. As can be seen from the figures, formic acid was always the highest produced product. This reveals that some of the fermentable sugars that were produced were instantaneously oxidised to smaller products such as formic acid or there might have bee some back diffusion happening from the product chamber back into the reaction chamber. This back diffusion could introduce the captured sugars back in the reaction chamber (to attain equlibrium) thereby leading to the production of undesired products. It can be

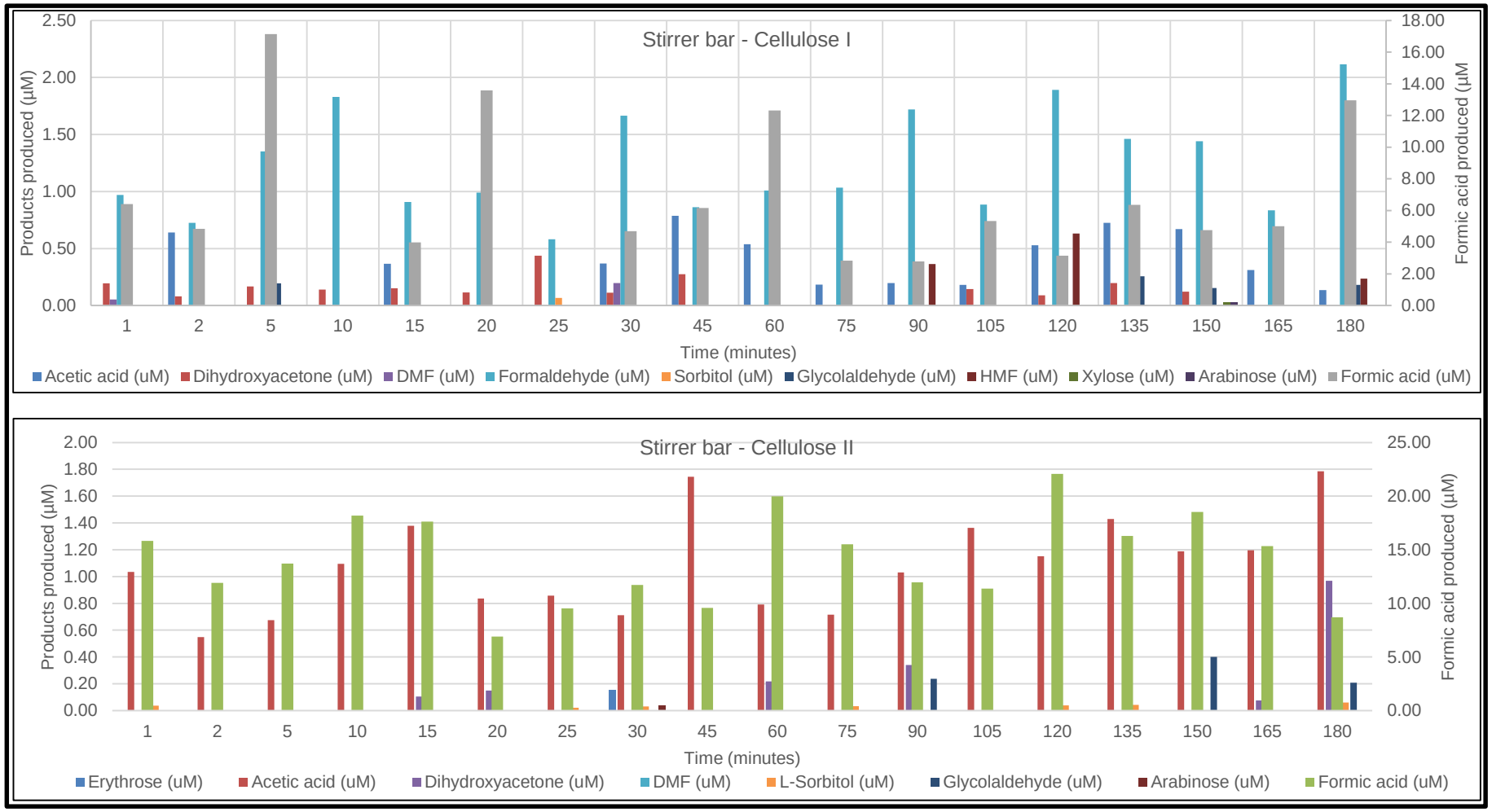

Figure 5.4: Various products produced during (top) cellulose I photocatalysis in a SFPR with the plus shaped stirrer bar and (bottom) cellulose II photocatalysis in a SFPR with the plus shaped stirrer bar.

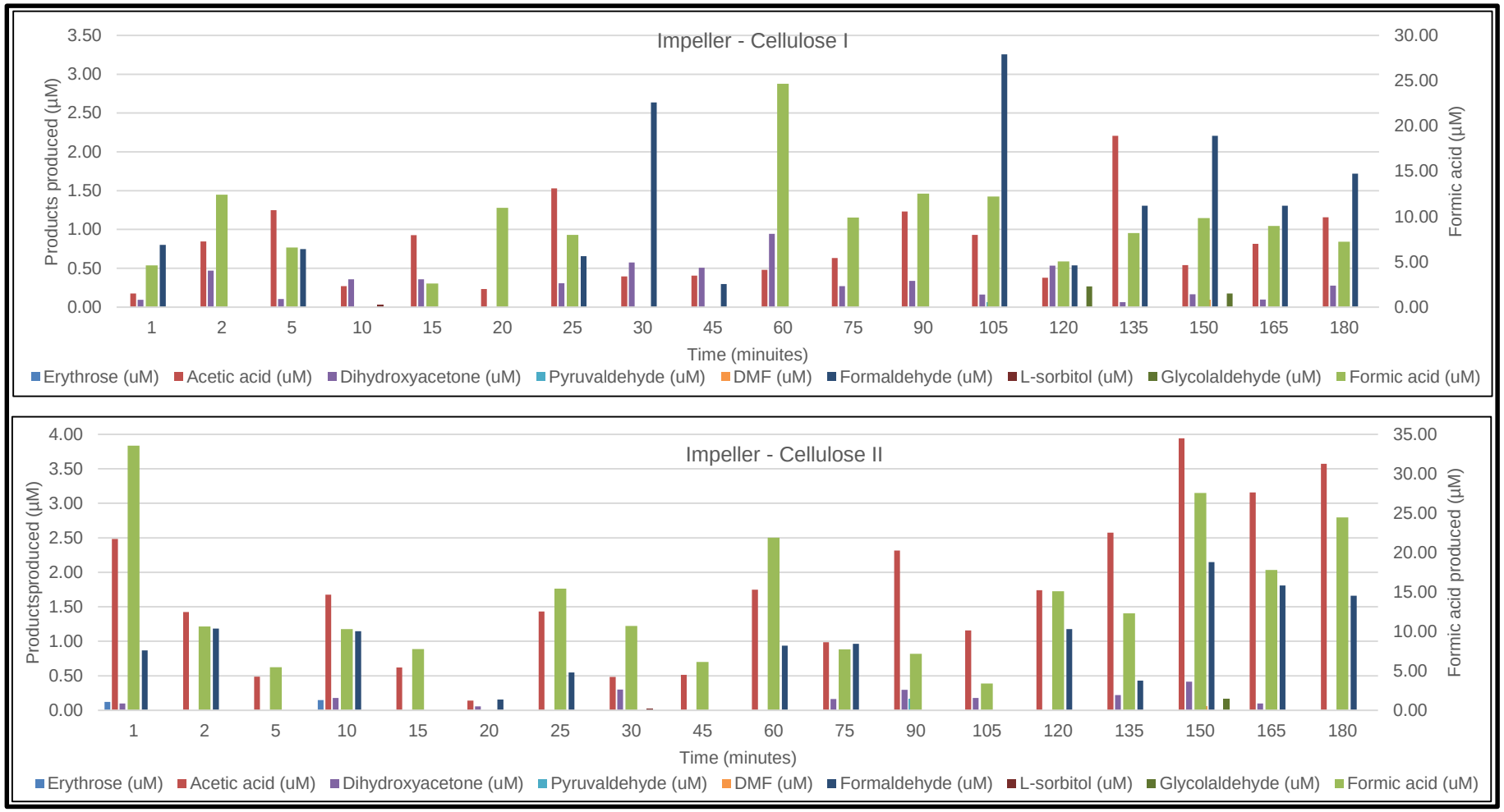

Figure 5.5: Various products produced during (top) cellulose I photocatalysis in a SFPR with the Rushton impeller and (bottom) cellulose II photocatalysis in a SFPR with the Rushton impeller.

further seen from the figures that the products produced do not follow a trend but is produced randomly. This randomness is dependent on the degree of polymerisation of cellulose to some extent and to the non-specific nature of the OH radicals to some extent. This can however be controlled by optimising the photocatalyst, loading rate, mode of photocatalyst deployment, pH or the removal rates of the product from the product chamber.

Particle size of cellulose II was measured before the experiments using a zetasizer. It was determined that the average particle size of cellulose II was 4.4 µm and that of cellulose I was 90 µm (obtained from the material specifications given by the vendor). Therefore, a higher fermentable sugar production with cellulose II could also be attributed to its lower particle size. With a lower particle size and an increased surface area, the possibility of more OH radicals attacking the cellulose II particles in bulk would prevail, thereby producing higher fermentable sugars. The increase in sugar yield upon the use of cellulose II as feed stock for both the mixer configurations could also be ascribed to factors such as increased lattice distance, rearranged hydrogen bonding, higher porous volume and relatively lower crystallinity (23,159,164-167).

Switching the mixer from a stirrer bar to the impeller also improved the sugar yield by 2 % with cellulose II feedstock. An increase in yield of 8 % upon switching mixers in the case of cellulose I was however observed. Cellulose I has amorphous regions packed at random sections along its chain. Upon switching to the impeller, due to improved mass transfer an increased number

of these amorphous regions would have come in contact with the OH radicals/P25 as an effect of mixing which has resulted in an increased amount of fermentable sugars. This demonstrates that mass transfer limitations could be overcome when proper mixing is offered in a photoreactor.

There have been a number of studies that utilised cellulosic biomass as sacrificial electron donors to photocatalytically produce hydrogen using modified TiO_2 photocatalysts (128,173,208-211). Although reported extensively for H_2 production, one paper has reported the simultaneous production of fermentable sugars and H_2 using Pt-TiO_2 as the photocatalyst (173). Zhang *et al.* reported a maximum fermentable sugar production of 0.7 µM in 6 hours with ball-milled native cellulose immobilised onto Pt-TiO_2. In the results reported here, however higher quantities (6.08 µM) were produced in 3 hours with P25 photocatalyst in the SFPR (with Rushton impeller) using cellulose I as the feedstock. With cellulose II polymorph, even more sugars were produced (8.58 µM). It has to be noted that an energy intensive ball-milling pre-treatment step has been avoided here and instead a green and sustainable onium hydroxide based pre-treatment was utilised to produce cellulose II which proved to be a better feedstock than native and ball-milled cellulose. Another reason for a higher production of fermentable sugars in this case can be attributed to mixing (and enhanced mass transfer). As pointed out by the simulation results in Chapter 4, with proper mixing an increased number of P25 particles could be irradiated as opposed to a system with no mixing.

A positive effect of mixer configuration on the production of fermentable sugars was earlier proposed in Chapter 4. Mixing simulation results from Chapter 4 revealed that an 8-blade Rushton impeller when used as the mixer configuration in the SFPR instead of the plus shaped stirrer bar had superior mixing profiles. As expected, the conclusion proposed in Chapter 4 was experimentally verified here. A higher fermentable sugar yield obtained upon switching the mixer configuration to an 8-blade Rushton impeller was due to the higher fluid velocity and a radial mixing profile created by the impeller. Mixing not only helps to maintain the particles in suspension but also eliminate mass transfer limitations by promoting contact between P25-cellulose particles and enhancing the OH radical diffusion in bulk. Diffusion of OH radicals in bulk meant that, in addition to cellulose particles adsorbed to the surface sites of P25, particles in bulk could also be oxidised to fermentable sugars. With continuous mixing and illumination, as new desired and undesired products were produced, the adsorption equilibrium between cellulose and P25 would have been altered. Due to this alteration, there are chances that the produced sugars could adsorb to the P25 surface sites leading to the inevitable formation of unwanted products. Similar to the oxidation of cellulose in bulk, fermentable sugar oxidation in bulk could also occur due to the diffusion of OH radicals favouring the formation of more undesired products. This was evident with the production of smaller molecular weight products, especially formic acid. For example, a higher amount of formic acid was always detected whenever the amount of fermentable sugars produced at a given sample time was lower than the preceding sample. This means that, the sugars produced were subjected to further photocatalytic

oxidation leading to production of undesirable products. Some of the products detected in solution in addition to formic acid were acetic acid, formaldehyde, arabinose, dihydroxyacetone, glycolaldehyde, pyruvaldehyde, erythrose and DMF. A possible route of formation of these products are detailed in Figure 3.8.

5.3.2 Photocatalytic cellulose breakdown with the addition of H_2O_2

Conventionally, H_2O_2 due to its oxidising potential (1.8 V) and non-toxic nature (212-214) have been used as a bleaching agent in pulp and paper industries to treat cellulosic (lignocellulose) biomass. This bleaching process, in addition to the degradation of a part of cellulose, mainly removes organic impurities such as lignin and hemicellulose and increases the whiteness of cellulose for paper manufacturing. In the field of photocatalysis a number of papers have reported an increase in efficiency of photocatalytic oxidation due to the addition of H_2O_2 to the reaction mixture (36,56-60,62,215). These reactions include the degradation of various organic contaminants, microbial toxins, dyes and wastewater.

The amount of fermentable sugars produced from the photocatalytic cellulose II breakdown with the addition of H_2O_2 is summarised in Table 5.1. When the initial H_2O_2 concentration was 0.01 %, the amount of fermentable sugars produced during the photocatalytic experiments were the highest, followed by the light control and finally the dark control experiments with the plus shaped stirrer bar as the mixer. Cellulose oxidation in the dark to fermentable sugars could be due the formation of OH radicals via the catalytic

decomposition of H_2O_2 on TiO_2 (216). During the light control experiments, however UV photolysis of H_2O_2 occurs (R 1.22) producing stronger oxidants in the form of OH radicals (60,62,215,217,218). These OH radicals tend to breakdown cellulose upon illumination to form fermentable sugars.

Concentration of H_2O_2	**Experiment type**	**Mixer configuration**	**Fermentable sugars produced (µM)**	**Fermentable sugar yield (%)**
0.01 %	Dark control	Plus shaped stirrer bar	0.69 ± 0.49	0.22
	Light control		1.9 ± 0.66	0.64
	Photocatalysis		9.56 ± 4.01	3.15
	Dark control	8-blade Rushton impeller	3.89 ± 1.23	1.27
	Light control		4.02 ± 0.95	1.32
	Photocatalysis		6.43 ± 1.76	1.98
0.1 %	Dark control	Plus shaped stirrer bar	74.6 ± 0.90	22.01
	Light control		82.46 ± 16.04	24.34
	Photocatalysis		47.81 ± 1.44	14.10
	Dark control	8-blade Rushton impeller	63.57 ± 22.70	19.10
	Light control		134.82 ± 86.74	39.74
	Photocatalysis		26.25 ± 1.98	8.84

Table 5.1: Fermentable sugar production in the SFPR from cellulose II with the addition of H_2O_2

During photocatalysis, in addition to photolysis (R 1.22), H_2O_2 also acts as an electron acceptor to improve the electron-hole charge separation thereby preventing recombination and producing OH radicals as shown in reaction R 1.23. Furthermore, H_2O_2 also reacts with the superoxide radical to form OH radicals (R 1.24). Besides photocatalytic OH radical production, H_2O_2 also contributes to an increased formation of OH radicals as mentioned (60,62,215,217,218) thereby producing the highest amount of fermentable sugars upon photocatalysis. Fermentable sugar yield from this process was

calculated to be 3.15 % which was found to be 18.7 % higher than sugars produced from a similar set up without any H_2O_2.

When the concentration of H_2O_2 was increased 10 times to 0.1 %, the amount of fermentable sugars produced during the light control was the highest followed by the dark control and photocatalytic experiments. Highest amount of fermentable sugars from light control experiments could be explained due to the enhanced OH radical production due to the photolysis of a higher concentration of H_2O_2 (R 1.22). During photocatalysis in the presence of a higher concentration of H_2O_2, however there are three possibilities that could lead to the loss of fermentable sugars, namely;

(i) oxidation of fermentable sugars to undesirable products

(ii) hole scavenging by H_2O_2 (R 1.25 and R 1.26) (56)

(iii) OH radical scavenging by H_2O_2 (R 1.27) (56)

Oxidation of fermentable sugars to undesirable products is a possible reason for a part of the sugar loss. This is because, a range of glucose degradation products such as anhydroglucose, formaldehyde, dihydroxyacetone, acetic acid and formic acid were detected in the product mixture. In a few instances DMF, glycolaldehyde, furfural, arabinose and erythrose were also witnessed.

A decrease in efficiency of photocatalytic oxidation have been reported in the presence of a higher concentration of H_2O_2 in solution (59,60). This could either be due to the scavenging of holes or OH radicals by H_2O_2 present

in a higher concentration in solution. Scavenging of holes by H_2O_2 can occur via two reactions (R 1.25 and R 1.26) which could lead to the production of a weaker oxidising species - the hydroperoxy radical, oxygen and protons (56,58-60,62). In addition, OH radical scavenging could also occur in solution as mentioned in reaction R 1.27 leading to the formation of water and hydroperoxy radical (oxidation potential of 1.06 V) (61). These $HO_{2\cdot}$ radicals further combine with hydroxyl radicals to form water and oxygen (R 1.28). Hence due to these reactions, the yield of fermentable sugars produced upon photocatalysis with the addition of H_2O_2 was 14.1 %, which was lower than the light control experiments (24.34 %). Although the yields were lower than the light control experiments, it was still higher than the yields obtained from setups with 0.01 % and no H_2O_2 by 77.65 % and 81.84 % respectively. The effect of an even higher concentration of H_2O_2 beyond 0.1 % was not tested, because a decrease in yield was already observed with increasing the H_2O_2 concentration from 0.01 % to 0.1 %. Similar trend of lower photocatalytic degradation rates with the increase in concentration of H_2O_2 was reported by Wong and Chu (60) who performed H_2O_2 assisted photocatalytic degradation of alachlor using TiO_2 under UV irradiation and Cornish *et al*. , who performed photocatalytic degradation of microcystin-LR over UV illuminated TiO_2 (57).

In the case of Rushton impeller as the mixer in the SFPR, with a concentration of 0.01 % H_2O_2 in solution, the amount of fermentable sugars produced in the dark was the lowest followed by the light control experiments and then the photocatalytic experiments. When the concentration of H_2O_2 was increased to 0.1 % the amount of fermentable sugar produced was lowest

photocatalytically, followed by the dark control and the light control. The sugar production trends observed were similar to that as the stirrer bar setups but the yields were multiple folds higher with the impeller. This could be attributed to better mixing profile and higher fluid velocity generated by the impeller to overcome the mass transport limitations when compared to the stirrer bar. In addition, the material of construction of the impeller – stainless steel grade 316 interfering with photocatalysis also play a role in enhanced sugar production. Stainless steel is an iron based alloy which also contains small amounts of manganese, chromium and nickel. All these metals are capable of catalysing the decomposition of H_2O_2 producing OH radicals (219) (R 1.11). Reaction R 1.11 represents a typical Fenton's or Fenton's like reaction where H_2O_2 is decomposed on transition metal leading to the formation of OH radicals. When reaction R 1.11 occurs in the presence of a suitable light source (UV light in this case), it is termed as photo-Fenton's reaction. Due to the interference of these metals with H_2O_2 during the dark control, light control and photocatalytic experiments, the yield of fermentable sugars was influenced by Fenton's and photo-Fenton's reactions.

5.3.3 Photonic efficiency

Photocatalytic photonic efficiencies for fermentable sugar production in the SFPR was calculated in addition to the fermentable sugar yields and the results are summarised in Table 5.2. Photonic efficiency is defined as the "amount of products formed per litre per minute over the incident photon flux". The photonic efficiencies for the production of fermentable sugar in the SFPR with cellulose I and cellulose II as feedstock and stirrer bar as the mixer

configuration was calculated to be 5.64 % and 8.7 % respectively. Whereas, switching the mixer configuration to the impeller enhanced the photonic efficiencies to 6.69 % and 9.45 % for cellulose I and cellulose II feedstocks respectively. As the photonic efficiencies calculated were based on the fermentable sugars produced, these efficiencies followed a similar trend as observed for the sugar yields.

Mixer configuration	**Experiment type**	**Photonic efficiency (%)**
Plus shaped stirrer bar	Cellulose I photocatalysis	5.64
	Cellulose II photocatalysis	8.70
8-blade Rushton impeller	Cellulose I photocatalysis	6.69
	Cellulose II photocatalysis	9.45

Table 5.2: Photonic efficiencies for fermentable sugar production from the SFPR

The increase in photonic efficiencies with cellulose II feedstock in general could be attributed to its rearranged structure as compared to cellulose I which favoured the higher production of fermentable sugars as detailed in chapter 1 and chapter 3. The increase in photonic efficiencies with the change in mixer configuration from the stirrer bar to the impeller could be attributed to the better mixing profile (radial mixing) and higher fluid (particle) velocity offered by the impeller. Photonic efficiencies could not be calculated for the H_2O_2 based systems because, the fermentable sugars produced were not a result of photocatalysis alone, but a combined result due to the photolysis of H_2O_2, photocatalysis, Fenton's reaction, photo-Fenton's reaction and oxidation of cellulose by H_2O_2.

5.3.4 Possible mechanism of fermentable sugar production from photocatalytic cellulose breakdown

A scheme of possible products formed as a result of photocatalytic cellulose breakdown is already mentioned in Figure 3.8. The possible mechanism of cellulose degradation specific to fermentable sugars produced is however mentioned here. The fermentable sugars produced during the process were cellobiose, glucose, fructose, galactose and anhydroglucose. Upon photoexcitation of P25, the produced OH radicals would attack the glycosidic bonds in cellulose leading to the release of oligosaccharides and cellulose radical. If the OH radical attack the glycosidic bonds of the end anhydroglucose unit, a glucose molecule is directly formed (Figure 5.6). The cellulose radical formed would further react with OH radicals and water subsequently to form cellulose with a lower degree of polymerisation than the initial cellulose. This cellulose would further be subjected to OH radical attack with continuous illumination forming more fermentable sugars.

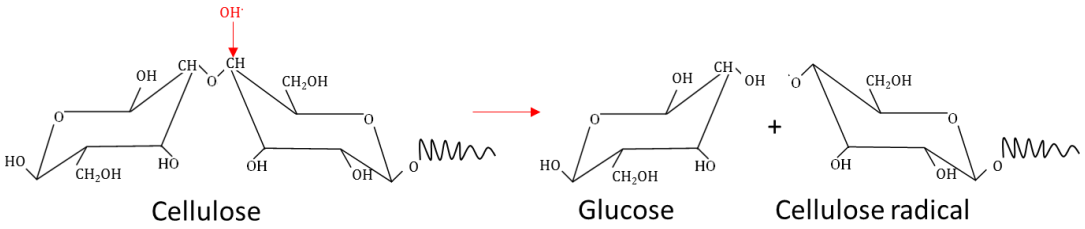

Figure 5.6: Photocatalytic cellulose breakdown for the production of glucose

Glucose produced in this reaction would be isomerised to fructose as reported by Marianou *et al*., who observed the isomerisation over TiO_2 and other heterogeneous catalysts (220). In addition, the produced glucose could also epimerise to form galactose. Epimerisation of glucose to galactose has

been reported earlier in biological systems by Topper and Stetten Jr in 1951 (221).

Additionally, glucose has a higher affinity towards P25 and adsorbs to its surface (222). Therefore, due to the presence of both basic and acidic surface sites on P25, isomerisation of glucose to fructose and dehydration of to HMF occurs (223), leading to the loss of glucose. Furthermore, OH radical attack on cellulose is random and could be on any position on the hexose ring. For example, Figure 1.6, Figure 1.7and Figure 1.8 in section 1.6.2 could be referred to see the products formed, when OH radical attacks C1, C4 and C5 of the ring respectively. Nevertheless, the position of OH radical attack, glucose is always formed. According to the mechanism speculated here, it seems like a large quantity of glucose could be produced from photocatalysis, however since OH radicals are non-specific, the oxidise everything that they come in contact with. Hence, a loss of valuable glucose is seen.

5.4 Conclusion

The effect of two mixer configurations, namely, the plus shaped stirrer bar and an 8-blade Rushton impeller on the production of fermentable sugars from cellulose I and cellulose II via photocatalysis was tested. Photocatalytic fermentable sugar production in the SFPR with the Rushton impeller was always higher when compared to the stirrer bar counterpart regardless of the cellulose polymorph used as the raw material. This could be attributed to the higher fluid velocity, radial mixing pattern and better mass transport achieved due the impeller. Amongst the feedstock used, cellulose II was found to be the

superior raw material for fermentable sugar production (2.61 %) due to its relatively lower crystallinity, higher porous volume, rearranged hydrogen bonding and increased lattice distance. To further improve the yield of fermentable sugars from cellulose II, photocatalytic experiments were conducted in the SFPR with the plus shaped stirrer bar as the mixer with the addition of H_2O_2 (0.01 % or 0.1 %). The addition of 0.01 % of H_2O_2 increased the sugar yield to 3.15 % and when the concentration of H_2O_2 was increased to 0.1 % the sugar yield drastically increased to 14.1 %. This could be ascribed to an improved charge carrier separation facilitated by H_2O_2 and an increased amount of OH radicals produced from the photolytic decomposition of H_2O_2 and it reactions with the conduction band electrons or superoxide radical. When these H_2O_2 based experiments were performed in the SFPR installed with the Rushton impeller as the mixer, the sugar yields were influenced by Fenton's and photo-Fenton's reactions in combination with photocatalysis. To avoid such interferences and determine the true fermentable sugar yields, a Teflon coated Rushton impeller could be used in place of the existing impeller. Calculated photonic efficiencies in the SFPR without the addition of H_2O_2 was higher with the impeller configuration when compared to the stirrer bar configuration. The calculated photonic efficiencies with the addition of H_2O_2, however followed inverse trends. An even higher yield of fermentable sugars production could be achieved when the effect of pH and the effect of loading concentration of P25 and cellulose II are optimised. From an engineering perspective, the effect of immobilised P25 on fermentable sugar production and the effect of continuous product removal has to be tested as measures to avoid losses.

Chapter 6: Conclusion

6.1 Conclusion

Globally, the need for alternate energy production is increasing due to the over utilisation of fossil fuels coupled with the emission of harmful greenhouse gases. This problem was introduced in Chapter 1 followed by the current alternatives to fossil fuels. These alternatives include electricity from solar, wind and hydroelectricity and biofuels. Biofuels are potential alternatives to the present transportation fuels. Biofuels, especially bioethanol could be produced by the fermentation of glucose. Glucose, however is not abundant but a glucose homopolysaccharide – cellulose is widely available. Native cellulose (cellulose I) has a complex structure due to its amphiphillicty and inter and intramolecular hydrogen bonding network. This complex structure hinders its chemical processing. To utilise cellulose to the fullest, cellulose II which is a superior polymorph could be utilised. Cellulose II could be produced by dissolving cellulose I in appropriate amphiphilic solvents such as ionic liquids, aqueous NaOH or onium hydroxides and regenerating cellulose II from solution with the addition of a range of antisolvents.

Cellulose breakdown for fermentable sugar release have always been conducted with energy intensive, expensive and environmentally harmful physico-chemical or biological methods, this work however used photocatalysis as an environmentally friendly, cheap alternative. Photocatalysis of cellulose has only been studied occasionally for the

production of hydrogen, HMF or rarely glucose. When the parameters influencing photocatalysis are optimised, glucose production could be focussed extensively. The factors affecting photocatalysis were also detailed in Chapter 1, which led to the research aims of this project.

The aim of this project was to produce fermentable sugars from cellulose using photocatalysis. This was achieved by first screening suitable photocatalyst materials based on their oxidising ability (OH radical producing capability). Secondly, the best photocatalyst was chosen to perform photocatalytic cellulose breakdown. Thirdly, to improve the yields a photocatalytic reactor was designed and fabricated for photocatalytic fermentable sugar production.

Chapter 2, exclusively focussed on screening various photocatalysts based on their OH radical producing capability. OH radicals produced upon illumination of the photocatalysts were quantified indirectly using a probe. The probe in this case was coumarin, which reacts with OH radicals and forms hydroxylated products. One of the hydroxylation products is 7-hydroxycoumarin, which could be quantified using a fluorimeter. Based on stoichiometry, amount of OH radicals produced was then calculated. Amongst the tested photocatalysts, LaCr-$SrTiO_3$, Cr-$SrTiO_3$ and yellow TiO_2 were incapable of producing OH radicals predominantly due to their band gap, VB and CB positions. Highest rate of OH radical production was achieved with TiO_2 P25 followed by Pt-C_3N_4 and WO_3. P25 was the only UV illuminated photocatalyst whereas the other materials were irradiated using visible light.

Chapter 3 discussed the use of highest OH radical producing photocatalyst (P25) for photocatalytic cellulose breakdown. A simple setup was utilised where the P25 particles were dispersed in DI water along with cellulose I in a Pyrex beaker and illuminated. The fermentable sugar yield and photonic efficiencies were calculated to be 0.04 % and 0.39 % respectively. When cellulose II was however used as the feedstock, the respective yields increased to 0.2 % and 1.86 %. The increase in yields could be attributed to the rearranged inter and intramolecular hydrogen bonding, increased lattice distance, reduced crystallinity and increased porous volume of cellulose II. To further enhance the yields and avoid fermentable sugar losses, dialysis membrane bags were installed. Installation of membrane bags improved the fermentable sugar yields from cellulose I and cellulose II to 0.43 % and 0.71 % respectively. Respective photonic efficiencies also enhanced and were calculated to be 4.5 % and 7.67 % respectively.

Chapter 4 focussed on the design of a photocatalytic reactor – the SFPR. In addition, a range of mixer configurations were also designed to suit the SFPR. Mixing profiles of these mixers in the SFPR were simulated using COMSOL Multiphysics 5.1. Upon the completion of mixing profile simulation, particle tracing simulations were also performed using the properties of cellulose particles. Finally, it was determined that an 8-blade Rushton impeller offered better mixing regimes (radial mixing) and higher fluid velocities when compared to the plus shaped magnetic stirrer bar. The conclusion of this chapter proposed that, upon illumination of cellulose-P25 mixture in a SFPR

with an appropriate mixer configuration would yield a higher amount of fermentable sugars when compared to a system that offers no mixing.

Based on the simulation results from Chapter 4, SFPR and an 8-blade Rushton impeller was fabricated and commercially available plus shaped magnetic stirrer bar was purchased. Assembly and operation of the SFPR for the production of fermentable sugars with various mixer configurations was discussed in Chapter 5. The SFPR when operated with the stirrer bar as the mixer and cellulose I as the feedstock yielded 1.71 % fermentable sugars at a photonic efficiency of 5.64 %. When the feedstock was switched to cellulose II, the respective yields increased to 2.56 % and 8.70 %. The SFPR when operated with the impeller as mixer and cellulose I as the feedstock produced 1.86 % sugar yield and 6.69 % photonic efficiency. With cellulose II as the feedstock in the same setup, the yields increased to 2.61 % and 9.45 % respectively. Higher sugar yield obtained from the SFPR using an impeller as the mixer was due to the radial mixing profile generated by the mixer. With such a mixing pattern, an increased number of P25 particles are illuminated. This chapter hence experimentally verified the simulation results reported in Chapter 4.

Furthermore, to improve the photonic efficiencies and sugar yields further, H_2O_2 was added to the photocatalytic mixture containing cellulose II and P25 with either the stirrer bar or the impeller as the mixer. Addition of 0.01 wt% H_2O_2 to the SFPR (with the stirrer bar) yielded 3.15 % fermentable sugars. When the concentration of H_2O_2 was increased 10 times, the yield

enhanced to 14.1 %. The respective photonic efficiencies were also calculated to be 10.53 % and 52.66 % respectively. With the impeller, however the sugar yields were influenced by the material of construction, stainless steel grade 316. Since stainless steel is an iron alloy, that also consists of Ni, Cr and Mn, which initiated Fenton's and photo-Fenton's reactions with the addition of H_2O_2. Hence the sugars produced was a combined result of photo-Fenton's and photocatalysis. The sugar yields and photonic efficiencies were also found to be lower in this case. This was due to the over production of OH radicals which were scavenged by the H_2O_2 present in solution.

6.2 Future work

6.2.1 Photocatalysts, illumination and OH radical production

A range of visible light photocatalysts were tested based on their OH radical producing capability and compared against the commercial P25 standard under UV illumination in Chapter 2. The results revealed that no photocatalyst could achieve OH radical production rates similar to P25. To make photocatalysis energy efficient, it would be better to utilise natural solar irradiation as the source of illumination. To accomplish this, effective visible light absorbing photocatalysts have to prepared and their OH radical production rates has to be determined and compared to P25. Only by comparing the rates against P25, the efficiency of a new photocatalyst and its suitability for photocatalytic oxidation could be determined. Addition of small quantities of H_2O_2 to the coumarin probe solution could also be conducted to determine its effect on OH radical generation.

In addition, from a process integration perspective, solar radiation could be harvested via solar panels as electricity and used to power an UV lamp to illuminate a P25 based reaction mixture. The use of low power UV light sources such as LED's could also be considered as an alternative to make photocatalysis less energy intensive.

6.2.2 COMSOL multiphysics simulation

Simulation is a useful tool which aids in understanding an engineering design. As discussed in Chapter 4, the mixing profiles and particle tracing profiles were determined from the simulation results. To further understand the photocatalytic process, scattering and absorption of light inside the reactor and its interaction with cellulose particles have to be studied. This could be accomplished using COMSOL's inbuilt ray optics module which helps in visualising the light path in the SFPR.

6.2.3 Improving fermentable sugar yield

From an illumination point of view, effect of CPI on the production of fermentable sugars has to be tested. CPI has been successfully used in the past to achieve enhanced oxidation rates. CPI could potentially improve the sugar yields because, the loss of valuable OH radicals upon its scavenging by H_2O_2 due to its overproduction could be avoided. Recombination of VB holes and CB electrons could also be greatly reduced upon CPI.

The use of a dialysis membrane to separate the reaction and product chambers in the SFPR improved the sugar yields and separated the

photocatalyst-cellulose mixture from the products. Due to the principle of osmosis, sugars could still diffuse back into the reaction chamber and get oxidised. To avoid these losses, solution from the product chamber has to be continuously removed instead of removal in batches at regular time intervals. The effect of P25 loading concentration, cellulose II concentration, pH and light intensity on fermentable sugar production also has to be tested to further optimise the sugar yields.

In terms of material of construction, the impeller has to be fabricated with Perspex and tested for fermentable sugar production in the presence of a range of H_2O_2 concentrations. This would reveal the sole effect of H_2O_2 on photocatalytic fermentable sugars without the interference from photo-Fenton's reactions. If the designs of the inlet and outlet for the reaction and product chambers are updated, a gas tight SFPR could be obtained. This would facilitate the monitoring of gases during the reaction, thus giving an overall picture.

REFERENCES

(1) Wigley TML, Richels R, Edmonds JA. Economic and environmental choices in the stabilization of atmospheric CO_2 concentrations. Nature 1996;379(6562):240-243.

(2) van der Hoeven M. World Energy Outlook Report. 2013.

(3) Brundtland GH. Our Common Future. 1987;United Nations World Commission on Environment and Development.

(4) Michaelides EES. Alternative Energy Sources. : Springer Berlin Heidelberg; 2012.

(5) Gui MM, Lee KT, Bhatia S. Feasibility of edible oil vs. non-edible oil vs. waste edible oil as biodiesel feedstock. Energy 2008;33(11):1646-1653.

(6) Nagarajan S, Chou SK, Cao S, Wu C, Zhou Z. An updated comprehensive techno-economic analysis of algae biodiesel. Bioresour Technol 2013;145(0):150-156.

(7) Linoj KN, Prabha D, Anandajit G, Sameer M. Liquid Biofuels in South Asia: Resources and Technologies. Asian Biotechnol Dev Rev 2006;8(2):31.

(8) Lavoine N, Desloges I, Dufresne A, Bras J. Microfibrillated cellulose – Its barrier properties and applications in cellulosic materials: A review. Carbohydr Polym 2012;90(2):735-764.

(9) Betts WB, Dart RK, Ball AS, Pedlar SL. Biosynthesis and Structure of Lignocellulose. In: Betts WB, editor. : Springer London; 1991. p. 139-155.

(10) Demirbas A. Bioethanol from Cellulosic Materials: A Renewable Motor Fuel from Biomass. Energy Sources 2005;27(4):327-337.

(11) Nasri-Nasrabadi B, Behzad T, Bagheri R. Extraction and characterization of rice straw cellulose nanofibers by an optimized chemomechanical method. J Appl Polym Sci 2014;131(7).

(12) Lindedam J, Bruun S, Jørgensen H, Felby C, Magid J. Cellulosic ethanol: interactions between cultivar and enzyme loading in wheat straw processing. Biotechnol Biofuels 2010;3(1):1-10.

(13) Mansaray KG, Ghaly AE. Thermal degradation of rice husks in nitrogen atmosphere. Bioresour Technol 1998;65(1–2):13-20.

(14) Jústiz-Smith NG, Virgo GJ, Buchanan VE. Potential of Jamaican banana, coconut coir and bagasse fibres as composite materials. Mater Charact 2008;59(9):1273-1278.

(15) Lindman B, Karlström G, Stigsson L. On the mechanism of dissolution of cellulose. J Mol Liq 2010;156(1):76-81.

(16) Silverstein RA. A Comparison of Chemical Pretreatment Methods for Converting Cotton Stalks to Ethanol.North Carolina State University; 2005.

(17) Sjöström E. Wood Chemistry: Fundamentals and Applications. : Academic Press; 1993.

(18) O'Sullivan A. Cellulose: the structure slowly unravels. Cellulose 1997;4(3):173-207.

(19) Shibazaki H, Saito M, Kuga S, Okano T. Native Cellulose II Production by *Acetobacter Xylinum* Under Physical Constraints. Cellulose 1998;5(3):165-173.

(20) Kuga S, Takagi S, Brown RM. Native folded-chain cellulose II. Polymer 1993;34(15):3293-3297.

(21) Wada M, Chanzy H, Nishiyama Y, Langan P. Cellulose IIII Crystal Structure and Hydrogen Bonding by Synchrotron X-ray and Neutron Fiber Diffraction. Macromolecules 2004;37(23):8548-8555.

(22) Klemm D, Philipp B, Heinze T, Heinze U, Wagenknecht W. General Considerations on Structure and Reactivity of Cellulose: Section 2.1-2.1.4. Comprehensive Cellulose Chemistry: Wiley-VCH Verlag GmbH & Co. KGaA; 1998. p. 9-29.

(23) Boissou F, Muhlbauer A, De OV, Leclercq L, Kunz W, Marinkovic S, Estrine B, Nardello-Rataj V, Jerome F. Transition of cellulose crystalline structure in biodegradable mixtures of renewably-sourced levulinate alkyl ammonium ionic liquids, γ-valerolactone and water. Green Chem 2014;16(5):2463-2471.

(24) Wahlstrom RM, Suurnakki A. Enzymatic hydrolysis of lignocellulosic polysaccharides in the presence of ionic liquids. Green Chem 2015;17(2):694-714.

(25) Sun Y, Cheng J. Hydrolysis of lignocellulosic materials for ethanol production: a review. Bioresour Technol 2002;83(1):1-11.

(26) Abe M, Fukaya Y, Ohno H. Fast and facile dissolution of cellulose with tetrabutylphosphonium hydroxide containing 40 wt% water. Chem Commun 2012;48(12):1808-1810.

(27) Swatloski RP, Spear SK, Holbrey JD, Rogers RD. Dissolution of Cellulose with Ionic Liquids. J Am Chem Soc 2002;124(18):4974-4975.

(28) Pinkert A, Marsh KN, Pang S, Staiger MP. Ionic Liquids and Their Interaction with Cellulose. Chem Rev 2009;109(12):6712-6728.

(29) Wilkes JS, Zaworotko MJ. Air and water stable 1-ethyl-3-methylimidazolium based ionic liquids. J Chem Soc , Chem Commun 1992;13(13):965-967.

(30) Henriksson G, Johansson G, Pettersson G. A critical review of cellobiose dehydrogenases. J Biotechnol 2000;78(2):93-113.

(31) von Sonntag C, Schuchmann HP. Carbohydrates. In: Charles D J, Madhava Rao BS, editors. Radiation Chemistry Present Status and Future Trends; 2001. p. 481-511.

(32) Meng D, Li G, Liu Z, Yang F. Study of depolymerization of cotton cellulose by Pb/PbO_2 anode electrochemical catalysis in sulfuric acid solution. Polym Degrad Stab 2011;96(7):1173-1178.

(33) Mattor JA. A Study of the Mechanism of Alkali Cellulose Autoxidation.The Institute of Paper Chemistry, Georgia Institute of Technology.; 1963.

(34) Kolar J. Mechanism of Autoxidative Degradation of Cellulose. Restaurator 1997;18(4):163.

(35) Hastrup,ACS, Jensen,B and Green III,F. Chemical mediated depolymerization of cotton cellulose for the understanding of non-enzymatic fungal decay. The International Research Group on Wood Protection; 9-13, May; Biarritz, France; 2010.

(36) Venkatadri R, Peters RW. Chemical Oxidation Technologies: Ultraviolet Light/Hydrogen Peroxide, Fenton's Reagent, and Titanium Dioxide-Assisted Photocatalysis. Hazard Waste Hazard Mater 1993;10(2):107-149.

(37) Hoffmann MR, Martin ST, Choi W, Bahnemann DW. Environmental Applications of Semiconductor Photocatalysis. Chem Rev 1995;95(1):69-96.

(38) Asghar A, Abdul Raman AA, Wan Daud WMA. Advanced oxidation processes for in-situ production of hydrogen peroxide/hydroxyl radical for textile wastewater treatment: a review. J Clean Prod 2015;87(0):826-838.

(39) Fujishima A, Honda K. Electrochemical Photolysis of Water at a Semiconductor Electrode. Nature 1972;238(5358):37-38.

(40) Robertson P,K.J., Lawton L,A., Munch B, Rouzade J. Destruction of cyanobacterial toxins by semiconductor photocatalysis. Chem Commun 1997(4):393-394.

(41) Choi H, Antoniou MG, Pelaez M, de lC, Shoemaker JA, Dionysiou DD. Mesoporous Nitrogen-Doped TiO_2 for the Photocatalytic Destruction of the Cyanobacterial Toxin Microcystin-LR under Visible Light Irradiation. Environ Sci Technol 2007;41(21):7530-7535.

(42) Robertson JMC, J. Robertson PK, Lawton LA. A comparison of the effectiveness of TiO_2 photocatalysis and UVA photolysis for the destruction of three pathogenic micro-organisms. J Photochem Photobiol A 2005;175(1):51-56.

(43) Zan L, Fa W, Peng T, Gong Z. Photocatalysis effect of nanometer TiO_2 and TiO_2-coated ceramic plate on Hepatitis B virus. Journal of Photochemistry and Photobiology B: Biology 2007;86(2):165-169.

(44) Sichel C, Tello J, de Cara M, Fernández-Ibáñez P. Effect of UV solar intensity and dose on the photocatalytic disinfection of bacteria and fungi. Catalysis Today 2007;129(1–2):152-160.

(45) Skillen N, Adams M, McCullagh C, Ryu SY, Fina F, Hoffmann MR, Irvine JTS, Robertson PKJ. The application of a novel fluidised photo reactor under UV–Visible and natural solar irradiation in the photocatalytic generation of hydrogen. Chem Eng J 2016;286:610-621.

(46) Adams M, Campbell I, McCullagh C, Russell D, Bahnemann DW, Robertson PKJ. From Ideal Reactor Concepts to Reality: The Novel Drum Reactor for Photocatalytic Wastewater Treatment. Int J Chem React Eng 2013;11:621-632.

(47) Tong Z, Yang D, Xiao T, Tian Y, Jiang Z. Biomimetic fabrication of g-C_3N_4/TiO_2 nanosheets with enhanced photocatalytic activity toward organic pollutant degradation. Chem Eng J 2015;260:117-125.

(48) Robertson PKJ. Semiconductor photocatalysis: an environmentally acceptable alternative production technique and effluent treatment process. J Clean Prod 1996;4(3-4):203-212.

(49) Tokode O, Prabhu R, Lawton LA, Robertson PKJ. Controlled periodic illumination in semiconductor photocatalysis. J Photochem Photobiol A 2016;319–320:96-106.

(50) Fujishima A, Rao TN, Tryk DA. Titanium dioxide photocatalysis. J Photochem Photobiol C 2000;1(1):1-21.

(51) Carp O, Huisman CL, Reller A. Photoinduced reactivity of titanium dioxide. Prog Solid State Chem 2004;32(1-2):33-177.

(52) McCullagh C, Skillen N, Adams M, Robertson PKJ. Photocatalytic reactors for environmental remediation: a review. J Chem Technol Biotechnol 2011;86(8):1002-1017.

(53) Park H, Kim H, Moon G, Choi W. Photoinduced charge transfer processes in solar photocatalysis based on modified TiO_2. Energy Environ Sci 2016;9(2):411-433.

(54) Zhang P, Wang T, Chang X, Gong J. Effective Charge Carrier Utilization in Photocatalytic Conversions. Acc Chem Res 2016;49(5):911-921.

(55) Jafari T, Moharreri E, Amin SA, Miao R, Song W, Suib LS. Photocatalytic Water Splitting - The Untamed Dream: A Review of Recent Advances. Molecules 2016;21(7):900.

(56) Zang Y, Farnood R. Effect of Hydrogen Peroxide on the Photocatalytic Degradation of Methyl tert-butyl Ether. Top Catal 2006;37(2):91-96.

(57) Cornish BJPA, Lawton LA, Robertson PKJ. Hydrogen peroxide enhanced photocatalytic oxidation of microcystin-LR using titanium dioxide. Appl Catal B 2000;25(1):59-67.

(58) Barakat MA, Tseng JM, Huang CP. Hydrogen peroxide-assisted photocatalytic oxidation of phenolic compounds. Appl Catal B 2005;59(1–2):99-104.

(59) Tseng D, Juang L, Huang H. Effect of Oxygen and Hydrogen Peroxide on the Photocatalytic Degradation of Monochlorobenzene in Aqueous Suspension. Int J Photoenergy 2012;2012:9.

(60) Wong CC, Chu W. The Hydrogen Peroxide-Assisted Photocatalytic Degradation of Alachlor in TiO2 Suspensions. Environ Sci Technol 2003;37(10):2310-2316.

(61) Buettner GR. The Pecking Order of Free Radicals and Antioxidants: Lipid Peroxidation, α-Tocopherol, and Ascorbate. Arch Biochem Biophys 1993;300(2):535-543.

(62) Guozheng,J, Guoxiang,W, Yong,Z and Linsheng,Z. Effects of Light Intensity and H_2O_2 on Photocatalytic Degradation of Phenol in Wastewater Using TiO_2/ACF. Proceedings of the 2010 International Conference on Digital Manufacturing \& Automation - Volume 01: IEEE Computer Society; 2010.

(63) Xiang Q, Yu J, Wong PK. Quantitative characterization of hydroxyl radicals produced by various photocatalysts. J Colloid Interface Sci 2011;357(1):163-167.

(64) Wu W, Jiang C, Roy VAL. Recent progress in magnetic iron oxide-semiconductor composite nanomaterials as promising photocatalysts. Nanoscale 2015;7(1):38-58.

(65) Fina F, Menard H, Irvine JTS. The effect of Pt NPs crystallinity and distribution on the photocatalytic activity of Pt-g-C_3N_4. Phys Chem Chem Phys 2015;17(21):13929-13936.

(66) Ouyang S, Tong H, Umezawa N, Cao J, Li P, Bi Y, Zhang Y, Ye J. Surface-Alkalinization-Induced Enhancement of Photocatalytic H_2 Evolution over $SrTiO_3$-Based Photocatalysts. J Am Chem Soc 2012;134(4):1974-1977.

(67) Gribb AA, Banfield JF. Particle size effects on transformation kinetics and phase stability in nanocrystalline TiO_2. Am Mineral 2015;82:717.

(68) Suttiponparnit K, Jiang J, Sahu M, Suvachittanont S, Charinpanitkul T, Biswas P. Role of Surface Area, Primary Particle Size, and Crystal Phase on Titanium Dioxide Nanoparticle Dispersion Properties. Nanoscale Res Lett 2010;6(1):27.

(69) Holmberg JP, Ahlberg E, Bergenholtz J, Hassellöv M, Abbas Z. Surface charge and interfacial potential of titanium dioxide nanoparticles: Experimental and theoretical investigations. J Colloid Interface Sci 2013;407:168-176.

(70) Schneider J, Matsuoka M, Takeuchi M, Zhang J, Horiuchi Y, Anpo M, Bahnemann DW. Understanding TiO_2 Photocatalysis: Mechanisms and Materials. Chem Rev 2014;114(19):9919-9986.

(71) Zhang G, Lan Z, Lin L, Lin S, Wang X. Overall water splitting by Pt/g-C3N4 photocatalysts without using sacrificial agents. Chem Sci 2016;7(5):3062-3066.

(72) Xiaoping C, Wenfeng S. Hydrogen production from water splitting on CdS-based photocatalysts using solar light. Front Energy 2013;7(1):111.

(73) Blake DM, Webb J, Turchi C, Magrini K. Kinetic and mechanistic overview of TiO_2-photocatalyzed oxidation reactions in aqueous solution. Sol Energ Mat 1991;24(1):584-593.

(74) Tian J, Hu X, Yang H, Zhou Y, Cui H, Liu H. High yield production of reduced TiO_2 with enhanced photocatalytic activity. Appl Surf Sci 2016;360, Part B:738-743.

(75) Raillard C, Héquet V, Le Cloirec P, Legrand J. Kinetic study of ketones photocatalytic oxidation in gas phase using TiO_2-containing paper: effect of water vapor. J Photochem Photobiol A 2004;163(3):425-431.

(76) Yadav HM, Kolekar TV, Barge AS, Thorat ND, Delekar SD, Kim BM, Kim BJ, Kim JS. Enhanced visible light photocatalytic activity of Cr^{3+}-doped anatase TiO_2 nanoparticles synthesized by sol--gel method. J Mater Sci : Mater Electron 2015;27(1):526-534.

(77) Zuo G, Cheng Z, Chen H, Li G, Miao T. Study on photocatalytic degradation of several volatile organic compounds. J Hazard Mater 2006;128(2–3):158-163.

(78) Zhong J, Wang J, Tao L, Gong M, Zhimin L, Chen Y. Photocatalytic degradation of gaseous benzene over TiO_2/Sr_2CeO_4: Kinetic model and degradation mechanisms. J Hazard Mater 2007;139(2):323-331.

(79) Kim SB, Hwang HT, Hong SC. Photocatalytic degradation of volatile organic compounds at the gas–solid interface of a TiO_2 photocatalyst. Chemosphere 2002;48(4):437-444.

(80) Ourrad H, Thevenet F, Gaudion V, Riffault V. Limonene photocatalytic oxidation at ppb levels: Assessment of gas phase reaction intermediates and secondary organic aerosol heterogeneous formation. Appl Catal B 2015;168–169:183-194.

(81) Miyawaki A, Taira S, Shiraishi F. Performance of continuous stirred-tank reactors connected in series as a photocatalytic reactor system. Chem Eng J 2016;286:594-601.

(82) Tokode OI, Prabhu R, Lawton LA, Robertson PKJ. Effect of controlled periodic-based illumination on the photonic efficiency of photocatalytic degradation of methyl orange. J Catal 2012;290(0):138-142.

(83) Tokode O, Prabhu R, Lawton LA, Robertson PKJ. The effect of pH on the photonic efficiency of the destruction of methyl orange under controlled periodic illumination with UV-LED sources. Chem Eng J 2014;246:337-342.

(84) Natarajan K, Natarajan TS, Bajaj HC, Tayade RJ. Photocatalytic reactor based on UV-LED/TiO_2 coated quartz tube for degradation of dyes. Chem Eng J 2011;178:40-49.

(85) Shie J, Pai C. Photodegradation Kinetics of Toluene in Indoor Air at Different Humidities Using UV-A, UV-C and UV-LED Light Sources in the Presence of Silver Titanium Dioxide. Indoor Built Environ 2010;19(5):503-512.

(86) Pareek V, Chong S, Tadé M, Adesina AA. Light intensity distribution in heterogenous photocatalytic reactors. Asia-Pac J Chem Eng 2008;3(2):171-201.

(87) García-López E, Marcì G, Megna B, Parisi F, Armelao L, Trovarelli A, Boaro M, Palmisano L. $SrTiO_3$-based perovskites: Preparation, characterization and photocatalytic activity in gas–solid regime under simulated solar irradiation. J Catal 2015;321:13-22.

(88) Yang Y, Zhang T, Le L, Ruan X, Fang P, Pan C, Xiong R, Shi J, Wei J. Quick and Facile Preparation of Visible light-Driven TiO_2 Photocatalyst with High Absorption and Photocatalytic Activity. Sci Rep 2014;4:7045.

(89) Wong M, Chu W, Sun D, Huang H, Chen J, Tsai P, Lin N, Yu M, Hsu S, Wang S, Chang H. Visible-Light-Induced Bactericidal Activity of a Nitrogen-

Doped Titanium Photocatalyst against Human Pathogens. Appl Environ Microbiol 2006;72(9):6111-6116.

(90) Ryer A. The light measurement handbook. 1997; Available at: https://www.intl-lighttech.com/sites/default/files/pdf/handbook/ILT-Light-Measurement-Handbook.pdf. Accessed Jan, 28, 2017.

(91) Izadifard M, Achari G, Langford CH. Application of Photocatalysts and LED Light Sources in Drinking Water Treatment. Catalysts 2013;3(3):726.

(92) Zhang L, Wang W, Sun S, Jiang D, Gao E. Solar light photocatalysis using Bi_2O_3/Bi_2SiO_5 nanoheterostructures formed in mesoporous SiO_2 microspheres. Cryst Eng Comm 2013;15(46):10043-10048.

(93) Sczechowski JG, Koval CA, Noble RD. Evidence of critical illumination and dark recovery times for increasing the photoefficiency of aqueous heterogeneous photocatalysis. J Photochem Photobiol A 1993;74(2):273-278.

(94) Gaya UI. Kinetic Concepts of Heterogeneous Photocatalysis. In: Gaya UI, editor. Heterogeneous Photocatalysis Using Inorganic Semiconductor Solids Dordrecht: Springer Netherlands; 2014. p. 43-71.

(95) Rabani J, Goldstein S. Mechanisms of Reactions Induced by Photocatalysis of Titanium Dioxide Nanoparticles. In: Bahnemann DW, Robertson PKJ, editors. Environmental Photochemistry Part III Berlin, Heidelberg: Springer Berlin Heidelberg; 2015. p. 115-157.

(96) Herrmann J. Photocatalysis fundamentals revisited to avoid several misconceptions. Applied Catalysis B: Environmental 2010;99(3–4):461-468.

(97) De Heredia JB, Torregrosa J, Dominguez JR, Peres JA. Oxidation of p-hydroxybenzoic acid by UV radiation and by TiO_2/UV radiation: comparison and modelling of reaction kinetic. J Hazard Mater 2001;83(3):255-264.

(98) Chen H, Ku Y, Irawan A. Photodecomposition of o-cresol by UV-LED/TiO_2 process with controlled periodic illumination. Chemosphere 2007;69(2):184-190.

(99) Tokode O, Prabhu R, Lawton LA, Robertson PKJ. Mathematical modelling of quantum yield enhancements of methyl orange photooxidation in aqueous TiO_2 suspensions under controlled periodic UV LED illumination. Appl Catal B 2014;156–157(0):398-403.

(100) Choi W, Kim S, Cho S, Yoo H, Kim M. Photocatalytic reactivity and diffusing OH radicals in the reaction medium containing TiO_2 particles. Korean J Chem Eng 2001;18(6):898-902.

(101) Hirakawa T, Nosaka Y. Properties of $O_2^{\cdot -}$ and $OH^{\cdot}$ Formed in TiO_2 Aqueous Suspensions by Photocatalytic Reaction and the Influence of H_2O_2 and Some Ions. Langmuir 2002;18(8):3247-3254.

(102) Ishibashi K, Fujishima A, Watanabe T, Hashimoto K. Quantum yields of active oxidative species formed on TiO_2 photocatalyst. J Photochem Photobiol A 2000;134(1–2):139-142.

(103) Kanazawa S, Furuki T, Nakaji T, Akamine S, Ichiki R. Measurement of OH Radicals in Aqueous Solution Produced by Atmospheric-pressure LF Plasma Jet. Int J Plasma Environ Sci Tech 2012;6(2):166-171.

(104) Tokumura M, Morito R, Hatayama R, Kawase Y. Iron redox cycling in hydroxyl radical generation during the photo-Fenton oxidative degradation: Dynamic change of hydroxyl radical concentration. Appl Catal B 2011;106(3–4):565-576.

(105) Maezono T, Tokumura M, Sekine M, Kawase Y. Hydroxyl radical concentration profile in photo-Fenton oxidation process: Generation and consumption of hydroxyl radicals during the discoloration of azo-dye Orange II. Chemosphere 2011;82(10):1422-1430.

(106) Eremia SAV, Chevalier-Lucia D, Radu G, Marty J. Optimization of hydroxyl radical formation using TiO_2 as photocatalyst by response surface methodology. Talanta 2008;77(2):858-862.

(107) Ku J, Zimowski E. United States Department of Labor, Occupational Safety and Health Administration. 3M Formaldehyde Monitor (Model 3721). Product evaluation (PE-10) 1989;205(February 21).

(108) Sahni M, Locke BR. Quantification of Hydroxyl Radicals Produced in Aqueous Phase Pulsed Electrical Discharge Reactors. Ind Eng Chem Res 2006;45(17):5819-5825.

(109) Steiner MG, Babbs CF. Quantitation of the hydroxyl radical by reaction with dimethyl sulfoxide. Arch Biochem Biophys 1990;278(2):478-481.

(110) Sun B, Sato M, Sid Clements J. Optical study of active species produced by a pulsed streamer corona discharge in water. J Electrostatics 1997;39(3):189-202.

(111) Sunka P, Babický V, Clupek M, Lukes P, Simek M, Schmidt J, Cern M. Generation of chemically active species by electrical discharges in water. Plasma Sources Sci Technol 1999;8(2):258-265.

(112) Hoeben W, van Veldhuizen E, Rutgers W, Kroesen G. Gas phase corona discharges for oxidation of phenol in an aqueous solution. J Phys D: Appl Phys 1999;32(24):133-137.

(113) Ono R, Oda T. Measurement of hydroxyl radicals in pulsed corona discharge. J Electrostatics 2002;55(3–4):333-342.

(114) Czili H, Horváth A. Applicability of coumarin for detecting and measuring hydroxyl radicals generated by photoexcitation of TiO_2 nanoparticles. Appl Catal B 2008;81(3–4):295-302.

(115) Sato,M, Ohgiyama,T and Clements,JS. Formation of chemical species and their effects on microorganisms using a pulsed high voltage discharge in water. Industry Applications Society Annual Meeting, 1994., Conference Record of the 1994 IEEE; 1994.

(116) Zhang J, Nosaka Y. Quantitative Detection of OH Radicals for Investigating the Reaction Mechanism of Various Visible-Light TiO_2 Photocatalysts in Aqueous Suspension. J Phys Chem C 2013;117(3):1383-1391.

(117) Louit G, Foley S, Cabillic J, Coffigny H, Taran F, Valleix A, Renault JP, Pin S. The reaction of coumarin with the OH radical revisited: hydroxylation product analysis determined by fluorescence and chromatography. Radiat Phys Chem 2005;72(2–3):119-124.

(118) Chong MN, Jin B, Chow CWK, Saint C. Recent developments in photocatalytic water treatment technology: A review. Water Res 2010;44(10):2997-3027.

(119) Leblebici ME, Stefanidis GD, Van Gerven T. Comparison of photocatalytic space-time yields of 12 reactor designs for wastewater treatment. Chem Eng Process 2015;97:106-111.

(120) Shon HK, Vigneswaran S, Ngo HH, Kim JH. Chemical coupling of photocatalysis with flocculation and adsorption in the removal of organic matter. Water Res 2005;39(12):2549-2558.

(121) Chong MN, Jin B, Zhu HY, Chow CWK, Saint C. Application of H-titanate nanofibers for degradation of Congo Red in an annular slurry photoreactor. Chem Eng J 2009;150(1):49-54.

(122) McMurray TA, Byrne JA, Dunlop PSM, Winkelman JGM, Eggins BR, McAdams ET. Intrinsic kinetics of photocatalytic oxidation of formic and oxalic acid on immobilised TiO_2 films. Appl Catal A 2004;262(1):105-110.

(123) Peill NJ, Hoffmann MR. Development and Optimization of a TiO_2-Coated Fiber-Optic Cable Reactor: Photocatalytic Degradation of 4-Chlorophenol. Environ Sci Technol 1995;29(12):2974-2981.

(124) Jiang J, Zhou Z, Sharma VK. Occurrence, transportation, monitoring and treatment of emerging micro-pollutants in waste water — A review from global views. Microchem J 2013;110(0):292-300.

(125) Li M, Cao H, Han D, Li X, He M. Kinetics and mechanism of the reactions of OH radicals with p-nitroaniline in gas-phase and aqueous solution. Comp Theor Chem 2015;1055(0):68-77.

(126) Hashimoto K, Hiroshi I, Fujishima A. TiO_2 Photocatalysis: A Historical Overview and Future Prospects. Jpn J Appl Phys 2005;44(12):8269.

(127) Fan H, Li G, Yang F, Yang L, Zhang S. Photodegradation of cellulose under UV light catalysed by TiO_2. J Chem Technol Biotechnol 2011;86(8):1107-1112.

(128) Kawai T, Sakata T. Conversion of carbohydrate into hydrogen fuel by a photocatalytic process. Nature 1980;286(5772):474-476.

(129) Bahnemann DW, Lawton LA, Robertson PKJ. The Application of Semiconductor Photocatalysis for the Removal of Cyanotoxins from Water and Design Concepts for Solar Photocatalytic Reactors for Large Scale Water Treatment. In: Suib SL, editor. New and Future Developments in Catalysis. 1st ed. Amsterdam: Elsevier; 2013. p. 395-415.

(130) Robertson PKJ, Robertson JMC, Bahnemann DW. Removal of microorganisms and their chemical metabolites from water using semiconductor photocatalysis. J Hazard Mater 2012;211–212(0):161-171.

(131) Kominami H, Murakami S, Kohno M, Kera Y, Okada K, Ohtani B. Stoichiometric decomposition of water by titanium(IV) oxide photocatalyst synthesized in organic media: Effect of synthesis and irradiation conditions on photocatalytic activity. Phys Chem Chem Phys 2001;3(18):4102-4106.

(132) McCullagh C, Robertson PKJ, Adams M, Pollard PM, Mohammed A. Development of a slurry continuous flow reactor for photocatalytic treatment of industrial waste water. J Photochem Photobiol A 2010;211(1):42-46.

(133) Zazo JA, Casas JA, Mohedano AF, Gilarranz MA, Rodríguez JJ. Chemical Pathway and Kinetics of Phenol Oxidation by Fenton's Reagent. Environ Sci Technol 2005;39(23):9295-9302.

(134) Szabó-Bárdos E, Somogyi K, Törő N, Kiss G, Horváth A. Photocatalytic decomposition of l-phenylalanine over TiO_2: Identification of intermediates and the mechanism of photodegradation. Appl Catal B 2011;101(3–4):471-478.

(135) Hirakawa T, Yawata K, Nosaka Y. Photocatalytic reactivity for $O_2^{\cdot -}$ and OH radical formation in anatase and rutile TiO_2 suspension as the effect of H_2O_2 addition. Appl Catal A 2007;325(1):105-111.

(136) Nosaka Y, Daimon T, Nosaka AY, Murakami Y. Singlet oxygen formation in photocatalytic TiO_2 aqueous suspension. Phys Chem Chem Phys 2004;6(11):2917-2918.

(137) Yan X, Ohno T, Nishijima K, Abe R, Ohtani B. Is methylene blue an appropriate substrate for a photocatalytic activity test? A study with visible-light responsive titania. Chem Phys Lett 2006;429(4–6):606-610.

(138) Ohtani B. Preparing Articles on Photocatalysis—Beyond the Illusions, Misconceptions, and Speculation. Chem Lett 2008;37(3):216-229.

(139) Mills A. An overview of the methylene blue ISO test for assessing the activities of photocatalytic films. Appl Catal B 2012;128:144-149.

(140) Kim J, Lee CW, Choi W. Platinized WO3 as an Environmental Photocatalyst that Generates OH Radicals under Visible Light. Environ Sci Technol 2010;44(17):6849-6854.

(141) Li Z, Liang T, Lv S, Zhuang Q, Liu Z. A Rationally Designed Upconversion Nanoprobe for in Vivo Detection of Hydroxyl Radical. J Am Chem Soc 2015;137(34):11179-11185.

(142) Lindsey ME, Tarr MA. Quantitation of hydroxyl radical during Fenton oxidation following a single addition of iron and peroxide. Chemosphere 2000;41(3):409-417.

(143) Zhang J, Nosaka Y. Generation of OH radicals and oxidation mechanism in photocatalysis of WO_3 and $BiVO_4$ powders. J Photochem Photobiol A 2015;303–304:53-58.

(144) Randorn C, Irvine JTS, Robertson P. Synthesis of Visible-Light-Activated Yellow Amorphous Photocatalyst. Int J Photoenergy 2008;2008:1-6.

(145) Suttiponparnit K, Jiang J, Sahu M, Suvachittanont S, Charinpanitkul T, Biswas P. Role of Surface Area, Primary Particle Size, and Crystal Phase on Titanium Dioxide Nanoparticle Dispersion Properties. Nanoscale Research Letters 2010;6(1):27-27.

(146) Liang S, Xia Y, Zhu S, Zheng S, He Y, Bi J, Liu M, Wu L. Au and Pt co-loaded g-C_3N_4 nanosheets for enhanced photocatalytic hydrogen production under visible light irradiation. Appl Surf Sci 2015;358,(Part A):304-312.

(147) Vamvasakis I, Georgaki I, Vernardou D, Kenanakis G, Katsarakis N. Synthesis of WO_3 catalytic powders: evaluation of photocatalytic activity under NUV/visible light irradiation and alkaline reaction pH. J Sol Gel Sci Technol 2015;76(1):120-128.

(148) Bi Y, Ehsan MF, Huang Y, Jin J, He T. Synthesis of Cr-doped $SrTiO_3$ photocatalyst and its application in visible-light-driven transformation of CO_2 into CH_4. J CO2 Utilization 2015;12:43-48.

(149) Legrini O, Oliveros E, Braun AM. Photochemical processes for water treatment. Chem Rev 1993;93(2):671-698.

(150) Kamalakkannan J, Chandraboss VL, Prabha S, Senthilvelan S. Advanced construction of heterostructured $InCrO_4$-TiO_2 and its dual properties of greater UV-photocatalytic and antibacterial activity. RSC Adv 2015;5(94):77000-77013.

(151) Wojtoniszak M, Zielinska B, Kalenczuk RJ, Mijowska E. Photocatalytic performance of titania nanospheres deposited on graphene in coumarin oxidation reaction. Mater Sci-Poland 2012;30(1):32-38.

(152) Li G, Wong KH, Zhang X, Hu C, Yu JC, Chan RCY, Wong PK. Degradation of Acid Orange 7 using magnetic AgBr under visible light: The roles of oxidizing species. Chemosphere 2009;76(9):1185-1191.

(153) Zhang J, Nosaka Y. Mechanism of the OH Radical Generation in Photocatalysis with TiO_2 of Different Crystalline Types. J Phys Chem C 2014;118(20):10824-10832.

(154) Guan H, Zhu L, Zhou H, Tang H. Rapid probing of photocatalytic activity on titania-based self-cleaning materials using 7-hydroxycoumarin fluorescent probe. Anal Chim Acta 2008;608(1):73-78.

(155) Huang Z, Sun Q, Lv K, Zhang Z, Li M, Li B. Effect of contact interface between TiO_2 and g-C_3N_4 on the photoreactivity of g-C_3N_4/TiO_2 photocatalyst: (0 0 1) vs (1 0 1) facets of TiO_2. Appl Catal B 2015;164:420-427.

(156) Wood PM. The potential diagram for oxygen at pH 7. Biochem J 1988;253(1):287-289.

(157) Zhang G, Lan Z, Lin L, Lin S, Wang X. Overall water splitting by Pt/g-C_3N_4 photocatalysts without using sacrificial agents. Chem Sci 2016;7(5):3062-3066.

(158) Medronho B, Lindman B. Brief overview on cellulose dissolution/regeneration interactions and mechanisms. Adv Colloid Interface Sci 2015;222:502-508.

(159) Yamane C, Aoyagi T, Ago M, Sato K, Okajima K, Takahashi T. Two Different Surface Properties of Regenerated Cellulose due to Structural Anisotropy. Polym J 2006;38(8):819-826.

(160) Biermann O, Hädicke E, Koltzenburg S, Müller-Plathe F. Hydrophilicity and Lipophilicity of Cellulose Crystal Surfaces. Angew Chem Int Ed 2001;40(20):3822-3825.

(161) Glasser WG, Atalla RH, Blackwell J, Malcolm Brown R, Burchard W, French AD, Klemm DO, Nishiyama Y. About the structure of cellulose: debating the Lindman hypothesis. Cellulose 2012;19(3):589-598.

(162) Medronho B, Lindman B. Competing forces during cellulose dissolution: From solvents to mechanisms. Curr Opin Colloid Interface Sci 2014;19(1):32-40.

(163) Medronho B, Duarte H, Alves L, Antunes FE, Romano A, Valente AJM. The role of cyclodextrin-tetrabutylammonium complexation on the cellulose dissolution. Carbohydr Polym 2016;140:136-143.

(164) Wada M, Ike M, Tokuyasu K. Enzymatic hydrolysis of cellulose I is greatly accelerated via its conversion to the cellulose II hydrate form. Polym Degrad Stab 2010;95(4):543-548.

(165) Sakurada I, Hutino K. Über die intramizellare Quellung der Zellulose durch Wasser. Kolloid Z 1936;77(3):346-351.

(166) Dadi AP, Varanasi S, Schall CA. Enhancement of cellulose saccharification kinetics using an ionic liquid pretreatment step. Biotechnol Bioeng 2006;95(5):904-910.

(167) Kljun A, Benians TAS, Goubet F, Meulewaeter F, Knox JP, Blackburn RS. Comparative Analysis of Crystallinity Changes in Cellulose I Polymers Using ATR-FTIR, X-ray Diffraction, and Carbohydrate-Binding Module Probes. Biomacromolecules 2011;12(11):4121-4126.

(168) Zhao H, Holladay EJ, Kwak JH, Zhang ZC. A New Route to Improved Glucose Yields in Cellulose Hydrolysis. J Biobased Mater Bio 2007;1:210.

(169) Alves L, Medronho BF, Antunes FE, Romano A, Miguel MG, Lindman B. On the role of hydrophobic interactions in cellulose dissolution and regeneration: Colloidal aggregates and molecular solutions. Colloids Surf Physicochem Eng Aspects 2015;483:257-263.

(170) Mittal A, Katahira R, Himmel ME, Johnson DK. Effects of alkaline or liquid-ammonia treatment on crystalline cellulose: changes in crystalline structure and effects on enzymatic digestibility. Biotechnol Biofuels 2011;4(1):1-16.

(171) Ma H, Zhang B, Zhang P, Li S, Gao Y, Hu X. An efficient process for lignin extraction and enzymatic hydrolysis of corn stalk by pyrrolidonium ionic liquids. Fuel Process Technol 2016;148:138-145.

(172) Shafiei M, Zilouei H, Zamani A, Taherzadeh MJ, Karimi K. Enhancement of ethanol production from spruce wood chips by ionic liquid pretreatment. Appl Energy 2013;102:163-169.

(173) Zhang G, Ni C, Huang X, Welgamage A, Lawton LA, Robertson PKJ, Irvine JTS. Simultaneous cellulose conversion and hydrogen production assisted by cellulose decomposition under UV-light photocatalysis. Chem Commun 2016;52:1673-1676.

(174) Zhao H, Jones CL, Baker GA, Xia S, Olubajo O, Person VN. Regenerating cellulose from ionic liquids for an accelerated enzymatic hydrolysis. J Biotechnol 2009;139(1):47-54.

(175) Dadi AP, Schall CA, Varanasi S. Mitigation of cellulose recalcitrance to enzymatic hydrolysis by ionic liquid pretreatment. Appl Biochem Biotechnol 2007;137(1):407-421.

(176) Liu L, Chen H. Enzymatic hydrolysis of cellulose materials treated with ionic liquid BMIM]Cl. Chinese Sci Bull 2006;51(20):2432-2436.

(177) Zhang Z, Zhao ZK. Solid acid and microwave-assisted hydrolysis of cellulose in ionic liquid. Carbohydr Res 2009;344(15):2069-2072.

(178) Morales-delaRosa S, Campos-Martin JM, Fierro JLG. High glucose yields from the hydrolysis of cellulose dissolved in ionic liquids. Chem Eng J 2012;181–182:538-541.

(179) Široký J, Blackburn RS, Bechtold T, Taylor J, White P. Attenuated total reflectance Fourier-transform Infrared spectroscopy analysis of crystallinity changes in lyocell following continuous treatment with sodium hydroxide. Cellulose 2010;17(1):103-115.

(180) Hatchard CG, Parker CA. A New Sensitive Chemical Actinometer. II. Potassium Ferrioxalate as a Standard Chemical Actinometer. Proc R Soc Lond A Math Phys Sci 1956;235(1203):518.

(181) Han J, Zhou C, French AD, Han G, Wu Q. Characterization of cellulose II nanoparticles regenerated from 1-butyl-3-methylimidazolium chloride. Carbohydr Polym 2013;94(2):773-781.

(182) Hinterstoisser B, Åkerholm M, Salmén L. Effect of fiber orientation in dynamic FTIR study on native cellulose. Carbohydr Res 2001;334(1):27-37.

(183) Carrillo F, Colom X, Suñol JJ, Saurina J. Structural FTIR analysis and thermal characterisation of lyocell and viscose-type fibres. Eur Polym J 2004;40(9):2229-2234.

(184) Pang J, Liu X, Wu M, Wu Y, Zhang X, Sun R. Fabrication and Characterization of Regenerated Cellulose Films Using Different Ionic Liquids. J Spectrosc 2014;2014:8.

(185) Morgado DL, Frollini E. Thermal decomposition of mercerized linter cellulose and its acetates obtained from a homogeneous reaction. Polímeros 2011;21:111.

(186) Serpone N. Relative photonic efficiencies and quantum yields in heterogeneous photocatalysis. Journal of Photochemistry and Photobiology A: Chemistry 1997;104(1):1-12.

(187) Thoorens G, Krier F, Leclercq B, Carlin B, Evrard B. Microcrystalline cellulose, a direct compression binder in a quality by design environment—A review. Int J Pharm 2014;473(1–2):64-72.

(188) De Lasa HI, Serrano B, Salaices M. Photocatalytic reaction engineering. 1st Edition ed. New York: Springer; 2005.

(189) Patel P, Vaidya P, Singh G. An Overview of Impellers, Velocity Profile and Reactor Design. Proceedings of the 2014 COMSOL Conference 2014.

(190) Serajuddin M, Anand Rao K, Sreenivas T. Modelling and simulation of vacuum filtration of ore slurry: a case study on limestone-hosted Indian uranium ore. Can Metall Q 2016:1-9.

(191) Li W, Liu J, He L, Liu J, Sun S, Huang Z, Liang XM, Gao D, Ding W. Simulation and experimental study on the effect of channeling flows on the transport of toxins in hemodialyzers. J Membr Sci 2016;501:123-133.

(192) Dong Y, Keil FJ, Korup O, Rosowski F, Horn R. Effect of the catalyst pore structure on fixed-bed reactor performance of partial oxidation of n-butane: A simulation study. Chem Eng Sci 2016;142:299-309.

(193) Vialle S, Druhan JL, Maher K. Multi-phase flow simulation of CO_2 leakage through a fractured caprock in response to mitigation strategies. Int J Greenhouse gas control 2016;44:11-25.

(194) Rana H. Comparison of Industrial Agitation for Simulated Batch Reactor Vessel Mixing in Bioethanol Fermentation. Proceedings of the 2015 COMSOL Conference 2015.

(195) Alcamo R, Micale G, Grisafi F, Brucato A, Ciofalo M. Large-eddy simulation of turbulent flow in an unbaffled stirred tank driven by a Rushton turbine. Chem Eng Sci 2005;60(8–9):2303-2316.

(196) Sun C. True density of microcrystalline cellulose. J Pharm Sci 2005;94(10):2132-2134.

(197) Karuppa Raj T, Singh A, Tare S, Varma S. Study of fluid flow around impeller blades in Rushton turbine in a baffled vessel using computational fluid dyanmics. ARPN-JEAS 2014;9(5):659.

(198) Avinash K, Joella A, Rubio-Atoche C, Catherine X, Le SN, Joel B, Ranade Vivek V. Flow Generated by Radial Flow Impellers: PIV Measurements and CFD Simulations. Int J Chem React Eng 2004;2:1542.

(199) Tsui Y, Chou J, Hu YH. Blade Angle Effects on the Flow in a Tank Agitated by the Pitched-Blade Turbine. J Fluids Eng 2006;128(4):774-782.

(200) Cabrera MI, Alfano OM, Cassano AE. Absorption and Scattering Coefficients of Titanium Dioxide Particulate Suspensions in Water. J Phys Chem 1996;100(51):20043-20050.

(201) Egerton TA, Tooley IR. UV absorption and scattering properties of inorganic-based sunscreens. Int J Cosmetic Sci 2012;34(2):117-122.

(202) Hon DNS. Weathering and photochemistry of wood. In: Hon DNS, Shiraishi N, editors. Wood and Cellulosic Chemistry, Second Edition, Revised, and Expanded: Taylor & Francis; 2000. p. 513.

(203) Tokode OI, Prabhu R, Lawton LA, Robertson PKJ. Effect of controlled periodic-based illumination on the photonic efficiency of photocatalytic degradation of methyl orange. J Catal 2012;290:138-142.

(204) Ho GW, Chua KJ, Siow DR. Metal loaded WO_3 particles for comparative studies of photocatalysis and electrolysis solar hydrogen production. Chem Eng J 2012;181–182:661-666.

(205) Rochetto UL, Tomaz E. Degradation of volatile organic compounds in the gas phase by heterogeneous photocatalysis with titanium dioxide/ultraviolet light. J Air Waste Manage Assoc 2015;65(7):810-817.

(206) Zou L, Luo Y, Hooper M, Hu E. Removal of VOCs by photocatalysis process using adsorption enhanced TiO_2–SiO_2 catalyst. Chem Eng Process 2006;45(11):959-964.

(207) Alrousan DMA, Dunlop PSM, McMurray TA, Byrne JA. Photocatalytic inactivation of E. coli in surface water using immobilised nanoparticle TiO_2 films. Water Res 2009;43(1):47-54.

(208) Kondarides DI, Daskalaki VM, Patsoura A, Verykios XE. Hydrogen Production by Photo-Induced Reforming of Biomass Components and Derivatives at Ambient Conditions. Catal Lett 2008;122(1):26-32.

(209) Kaneko M, Saito R, Ueno H, Nemoto J, Izuoka A. Efficient Photocatalytic Decomposition of Glucose, Starch, and Cellulose to CO_2 Using a Mesoporous Semiconductor Thin Film. Catal Lett 2011;141(8):1199-1206.

(210) Speltini A, Sturini M, Dondi D, Annovazzi E, Maraschi F, Caratto V, Profumo A, Buttafava A. Sunlight-promoted photocatalytic hydrogen gas evolution from water-suspended cellulose: a systematic study. Photochem Photobiol Sci 2014;13(10):1410-1419.

(211) Caravaca A, Jones W, Hardacre C, Bowker M. H_2 production by the photocatalytic reforming of cellulose and raw biomass using Ni, Pd, Pt and Au on titania. Proc R Soc A 2016;472(2191).

(212) Neyens E, Baeyens J. A review of classic Fenton's peroxidation as an advanced oxidation technique. J Hazard Mater 2003;98(1–3):33-50.

(213) Clement D. The Blistering of Paper during Hydrogen Peroxide Bleaching. J Am Inst Conserv 1983;23(1):47-62.

(214) Mussatto SI, Rocha GJM, Roberto IC. Hydrogen peroxide bleaching of cellulose pulps obtained from brewer's spent grain. Cellulose 2008;15(4):641-649.

(215) Daneshvar N, Salari D, Khataee AR. Photocatalytic degradation of azo dye acid red 14 in water: investigation of the effect of operational parameters. J Photochem Photobiol A 2003;157(1):111-116.

(216) Lousada CM, Johansson AJ, Brinck T, Jonsson M. Mechanism of H_2O_2 Decomposition on Transition Metal Oxide Surfaces. J Phys Chem C 2012;116(17):9533-9543.

(217) Doong R, Chang W. Photodegradation of parathion in aqueous titanium dioxide and zero valent iron solutions in the presence of hydrogen peroxide. J Photochem Photobiol A 1998;116(3):221-228.

(218) Ilisz I, Föglein K, Dombi A. The photochemical behavior of hydrogen peroxide in near UV-irradiated aqueous TiO_2 suspensions. J Mol Catal A: Chem 1998;135(1):55-61.

(219) Strlič M, Kolar J, Šelih V, Kočar D, Pihlar B. A comparative study of several transition metals in Fenton-like reaction systems at circum-neutral pH. Acta Chim Slov 2003;50:619-632.

(220) Marianou AA, Michailof CM, Pineda A, Iliopoulou EF, Triantafyllidis KS, Lappas AA. Glucose to Fructose Isomerization in Aqueous Media over Homogeneous and Heterogeneous Catalysts. ChemCatChem 2016;8(6):1100-1110.

(221) Topper YJ, Stetten D. The biological transformation of galactose into glucose. Journal of Biological Chemistry 1951;193(1):149-155.

(222) Kim G, Lee S, Choi W. Glucose–TiO_2 charge transfer complex-mediated photocatalysis under visible light. Applied Catalysis B: Environmental 2015;162:463-469.

(223) Watanabe M, Aizawa Y, Iida T, Nishimura R, Inomata H. Catalytic glucose and fructose conversions with TiO_2 and ZrO_2 in water at 473 K: Relationship between reactivity and acid–base property determined by TPD measurement. Applied Catalysis A: General 2005;295(2):150-156.

(224) Muralidharan M, Anbarasu V, Elaya Perumal A, Sivakumar K. Carrier mediated ferromagnetism in Cr doped $SrTiO_3$ compounds. J Mater Sci : Mater Electron 2015;26(9):6352-6365.

(225) Guo J, Li Y, Zhu S, Chen Z, Liu Q, Zhang D, Moon W, Song D. Synthesis of WO_3@Graphene composite for enhanced photocatalytic oxygen evolution from water. RSC Adv 2012;2(4):1356-1363.

(226) van Benthem K, Elsässer C, French RH. Bulk electronic structure of $SrTiO_3$: Experiment and theory. J Appl Phys 2001;90(12):6156-6164.

Appendix A: Characterisation of photocatalysts

Methodology

Characterisation of photocatalysts was performed by our collaborators at University of St. Andrews, Fife, UK. WO_3, LaCr-$SrTiO_3$ and Cr-$SrTiO_3$ were characterised by X-Ray diffraction (XRD) and UV-Visible absorption. XRD analysis of powders was examined on a SToe STADI/P powder diffractometer. Incident radiation was generated using a Cu k_α source (λ=1.54056 Å). Diffuse reflectance spectra were collected on a JASCO-V550 UV-visible spectrophotometer. The characterisation of Pt-C_3N_4 and yellow TiO_2 has been reported elsewhere in literature (65,144).

Results

XRD patterns of WO_3, Cr-$SrTiO_3$ and LaCr-$SrTiO_3$ samples were determined as shown in Figure A 1. The commercial WO_3 nanoparticles exhibited a typical crystallized monoclinic phase structure, and the Cr-doped and La,Cr-co-doped $SrTiO_3$ samples possessed homogeneous crystallized cubic perovskite structures, with no impurity phase found for either of the doped samples and these results were consistent with literature (224,225). In the co-doped samples, since La and Cr substitute the Sr and Ti, respectively, and the radius of La is similar with that of Sr while the radius of Cr was similar to that of Ti, the peak positions of the Cr-$SrTiO_3$ and LaCr-$SrTiO_3$ samples are not shifted compared to those of pure $SrTiO_3$.

In the UV−visible absorption spectra of WO_3, Cr-$SrTiO_3$ and LaCr-$SrTiO_3$ shown in Figure A 2, WO_3 exhibited visible light absorption up to 470 nm, which corresponds to the band-gap energy of ca. 2.64 eV. $SrTiO_3$, however, has no absorption in the visible light region (band gap of 3.75 eV) and metal-doping has been shown to be a feasible method for extending the light absorption of $SrTiO_3$ into the visible region (226). Doping of Cr into the A-site of $SrTiO_3$ induces an absorption band in the visible region centred at around 450 nm. The visible light absorption is ascribed to the electron excitation from the Cr doping levels formed above the valence band of $SrTiO_3$ to the conduction band of $SrTiO_3$ (66). It was reported that La, Cr- co-doped $SrTiO_3$ showed enhanced photocatalytic performance compared to the single Cr-doped $SrTiO_3$ due to the inhibition of the formation of Cr^{6+} species in the B site (66). Therefore, a co-doped sample, LaCr-$SrTiO_3$ was prepared by the same method. The visible light absorption of LaCr-$SrTiO_3$ was significantly enhanced compared to the Cr-$SrTiO_3$, with two strong absorption peaks centred at around 450 nm and 650 nm in the visible light region. In the case of co-doping, more intermittent doping levels are formed within the band-gap of $SrTiO_3$ compared to the single Cr doped $SrTiO_3$, which results in the visible light absorption.

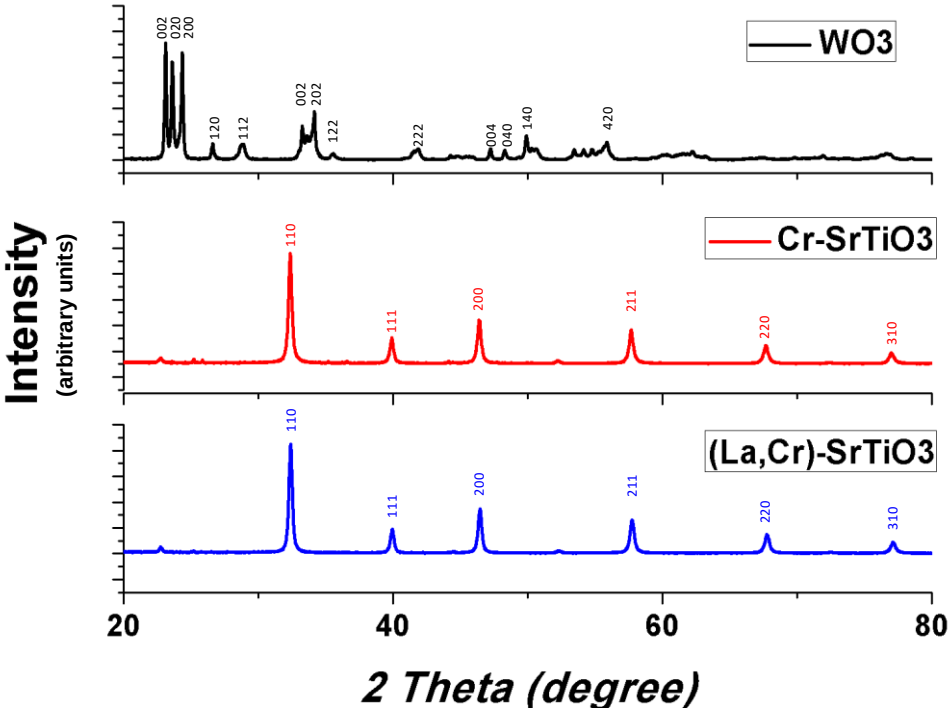

Figure A 1: XRD profiles of photocatalysts representing the plane indices (224,225)

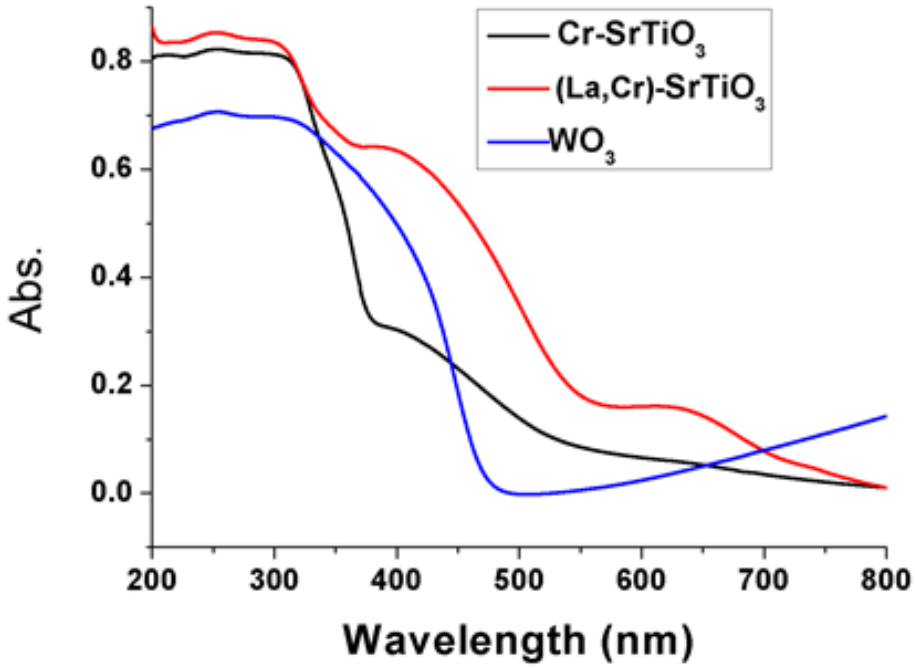

Figure A 2: UV-Visible absorption spectra of photocatalysts

Appendix B: Actinometry experiments and raw data of accumulated products quantified with the HPLC

Actinometry experiments were performed using a method proposed by Hatchard and Parker (180).

Materials

Sodium acetate, iron (II) sulphate heptahydrate, 1,10-phenanthroline monohydrate and concentrated sulphuric acid were purchased from Sigma-aldrich, UK. Potassium ferrioxalate was purchased from Alfa-aesar, UK. All chemicals were used as received without further purification.

Calibration of Fe^{2+} concentration

Sodium acetate buffer solution was prepared by mixing 49.2 g of CH_3COONa in 600 ml DI water and 360 ml of 1N H_2SO_4 and diluting to a final volume of 1 L by DI water. A solution of $0.4x10^{-6}$ M iron(II) sulphate in 0.1 N H_2SO_4 was also prepared. 110 mg of 1,10-phenanthroline monohydrate, a complexing agent was dissolved in 100 ml of water to make a solution of 0.1 wt% 1,10-phenanthroline monohydrate and stored in the dark. 0, 1.25, 2.5, 3.75, 5.0 and 6.25 ml of $0.4x10^{-6}$ M $FeSO_4$ in 0.1 N H_2SO_4 were added to 6 dark bottles. 1.25 ml of 1 N H_2SO_4 and 6.25 ml of sodium acetate buffer solution were then added to each bottle. Finally, 2.5 ml of the prepared 1,10-phenanthroline monohydrate was added each bottle to prepare Fe^{2+} concentrations from 0 to 0.182 µM. These solutions were let to react in dark for 45-55 minutes to allow the Fe^{2+}-phenanthroline complex to develop. 1 ml

of sample was drawn from each bottle and analysed in a CARY 300 UV-vis spectrophotometer at 510 nm. From the absorbance values obtained, a calibration graph was plotted (Figure B 1).

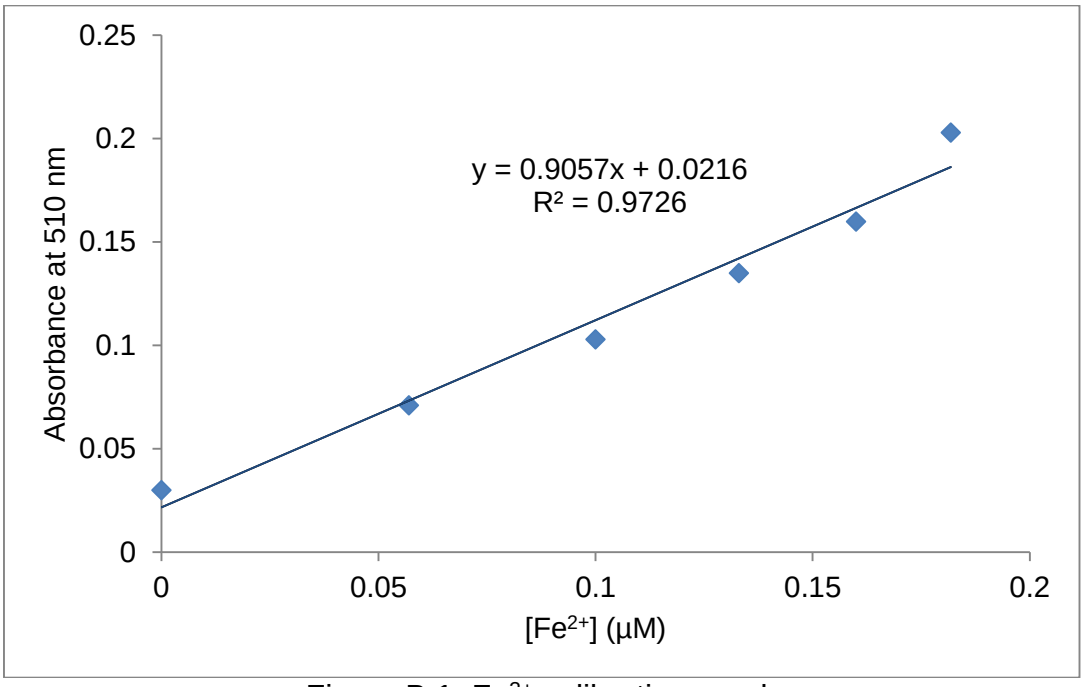

Figure B 1: Fe^{2+} calibration graph

Actinometry procedure

Ferrioxalate solution was prepared by dissolving 2.948 g of potassium ferrioxalate in 10 ml of 1N H_2SO_4 and diluting the solution to a final volume of 100 ml with water in dark. 10 ml of 1N H_2SO_4 and 90 ml of DI water was then to this solution which was placed in the same 250 ml beaker used for photocatalytic fermentable sugar production experiments. This beaker was placed 11 cm away from the illumination source. Upon illumination, 1 ml sample was taken from the beaker at 1, 5 and 10 minutes of irradiation. The sample was then mixed with 0.5 ml sodium acetate buffer solution and 2 ml of 0.1 wt% 1,10-phenanthroline monohydrate and diluted to 50 ml with water in a dark bottle. Upon allowing a 45-55 minutes' reaction time in the dark, 1 ml

of sample from each dark bottle was then withdrawn and its absorbance was measured using a CARY 300 UV-vis spectrophotometer at 510 nm.

Calculations

To calculate the photon flux, the number of moles of Fe2+ has to be first calculated using equation B1.

$$Moles\ of\ Fe^{2+} = \frac{V_1 V_3 A}{V_2 \epsilon L} \quad \text{..... Equation B1}$$

where, V_1 is the total volume of the irradiated solution (L), V_2 is the volume of the sample taken (L), V_3 is the final volume of the diluted sample (L), ϵ is the molar absorptivity of Fe^{2+} calculated from the slope of the calibration curve. (mol/L), L is the cell path length (1 cm) and A is the absorbance value of the sample at 10 minutes.

Photon flux could then be calculated using equation B2.

$$(Photon\ flux) = \frac{Moles\ of\ Fe^{2+}}{\sigma_{Fe^{2+}} t} \quad \text{..... Equation B2}$$

where, t is the illumination time (10 minutes) and $\sigma_{Fe^{2+}}$ is 0.97.

Raw data from HPLC

Concentration of accumulated products as quantified with the HPLC and the calculated actual concentration of the products are shown in the following tables (Table C1, Table C2, Table C3 and Table C4).

Replicate	**1**	**2**	**3**
Volume of accumulated sample		**18 ml**	
Concentration of glucose from HPLC (g/L)	8.46E-04	-	6.08E-04
Concentration of Fructose from HPLC (g/L)	-	4.04E-04	-
Concentration of Acetic acid from HPLC (g/L)	2.17E-03	1.89E-03	5.59E-03
Concentration of anhydroglucose from HPLC (g/L)	4.38E-04	1.72E-03	2.17E-03
Concentration of DMF from HPLC (g/L)	1.86E-03	-	-
Concentration of Formic acid from HPLC (g/L)	-	1.87E-02	3.50E-02
Concentration of Formaldehyde from HPLC (g/L)	-	-	3.12E-03
Concentration of Dihydroxyacetone from HPLC (g/L)	-	-	9.99E-04
Glucose (uM)	0.17	-	0.12
Fructose (uM)	-	0.08	-
Acetic acid (uM)	1.30	1.14	3.35
Anhydroglucose (uM)	0.10	0.38	0.48
DMF(uM)	0.70	-	-
Formic acid (uM)	-	14.60	27.37
Formaldehyde (uM)	-	-	3.74
Dihydroxyacetone (uM)	-	-	0.40

Table C1: Raw data of accumulated products formed during cellulose I photocatalysis (green rows) and their calculated respective concentration (blue rows).

Replicate	1	2	3
Volume of accumulated sample	18 ml		
Concentration of glucose from HPLC (g/L)	-	3.78E-03	2.86E-03
Concentration of cellobiose from HPLC (g/L)	-	2.20E-03	3.09E-03
Concentration of Fructose from HPLC (g/L)	9.17E-03	6.26E-03	4.96E-03
Concentration of Acetic acid from HPLC (g/L)	3.77E-02	5.84E-02	4.42E-02
Concentration of anhydroglucose from HPLC (g/L)	-	4.90E-04	-
Concentration of DMF from HPLC (g/L)	4.21E-03	1.48E-03	
Concentration of Formic acid from HPLC (g/L)	1.05E+00	1.12E+00	9.26E-01
Concentration of Glycolaldehyde from HPLC (g/L)	-	8.30E-03	6.46E-03
Concentration of Arabinose from HPLC (g/L)	-	9.60E-04	4.81E-04
Concentration of Galactose from HPLC (g/L)	-	6.49E-04	4.68E-04
Concentration of Erythrose from HPLC (g/L)	-	-	2.31E-03
Concentration of dihydroxyacetone from HPLC (g/L)	-	1.18E-02	1.08E-02
Glucose (uM)	-	0.76	0.57
Cellobiose (uM)	-	0.23	0.33
Fructose (uM)	1.83	1.25	0.99
Acetic acid (uM)	22.64	35.04	26.51
Anhydroglucose (uM)	-	0.11	-
DMF(uM)	1.58	0.55	-
Formic acid (uM)	820.70	875.29	724.69
Glycolaldehyde (uM)	-	4.98	3.87
Arabinose (uM)	-	0.23	0.12
Galactose (uM)	-	0.13	0.09
Erythrose (uM)	-	-	0.69
dihydroxyacetone (uM)	-	4.73	4.32

Table C2: Raw data of accumulated products formed during cellulose II photocatalysis (green rows) and their calculated respective concentration (blue rows).

Replicate	1	2	3
Volume of accumulated sample	18 ml		
Concentration of glucose from HPLC (g/L)	2.99E-03	2.46E-03	2.58E-03
Concentration of cellobiose from HPLC (g/L)	3.15E-04	-	3.23E-04
Concentration of Fructose from HPLC (g/L)	8.40E-03	1.48E-03	2.73E-03
Concentration of Acetic acid from HPLC (g/L)	-	5.77E-03	3.13E-03
Concentration of anhydroglucose from HPLC (g/L)	8.01E-03	1.63E-02	2.46E-02
Concentration of DMF from HPLC (g/L)	9.30E-03	3.20E-03	7.13E-03
Concentration of Formic acid from HPLC (g/L)	-	2.52E-02	1.84E-02
Concentration of Galactose from HPLC (g/L)	-	-	7.08E-04
Concentration of sorbitol from HPLC (g/L)	-	-	2.87E-04
Glucose (uM)	0.60	0.49	0.52
Cellobiose (uM)	0.03	-	0.03
Fructose (uM)	1.68	0.30	0.55
Acetic acid (uM)	-	3.46	1.88
Anhydroglucose (uM)	1.78	3.63	5.47
DMF(uM)	3.49	1.20	2.68
Formic acid (uM)	-	19.72	14.42
Galactose (uM)	-	-	0.14
Sorbitol (uM)	-	-	0.06

Table C3: Raw data of accumulated products formed during cellulose I photocatalysis with dialysis membrane bags (green rows) and their calculated respective concentration (blue rows).

Replicate	1	2	3
Volume of accumulated sample	18 ml		
Concentration of glucose from HPLC (g/L)	4.38E-03	4.45E-03	-
Concentration of Fructose from HPLC (g/L)	4.14E-03	1.68E-03	2.44E-03
Concentration of Acetic acid from HPLC (g/L)	5.72E-03	4.46E-03	8.88E-03
Concentration of anhydroglucose from HPLC (g/L)	3.62E-02	2.90E-02	3.61E-02
Concentration of DMF from HPLC (g/L)	-	-	4.39E-03
Concentration of Formic acid from HPLC (g/L)	1.34E-01	1.17E-01	2.29E-01
Glucose (uM)	0.88	0.89	-
Fructose (uM)	0.83	0.34	0.49
Acetic acid (uM)	3.43	2.68	5.33
Anhydroglucose (uM)	8.04	6.44	8.02
DMF(uM)	-	-	1.65
Formic acid (uM)	105.25	91.76	178.98

Table C4: Raw data of accumulated products formed during cellulose II photocatalysis with dialysis membrane bags (green rows) and their calculated respective concentration (blue rows).

Appendix C: Mixing profile streamline slice plots, XY plots and YZ plots of other stirrer bars and impeller configurations

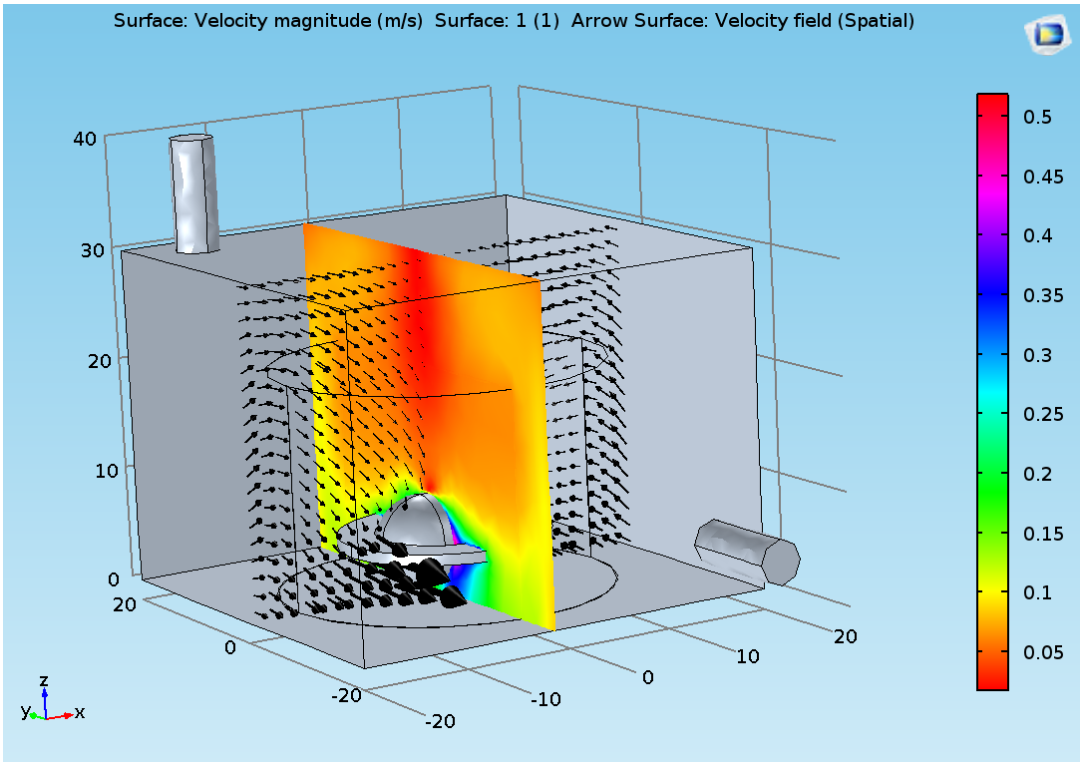

Figure C 1:Streamline slice plot – Spin ring

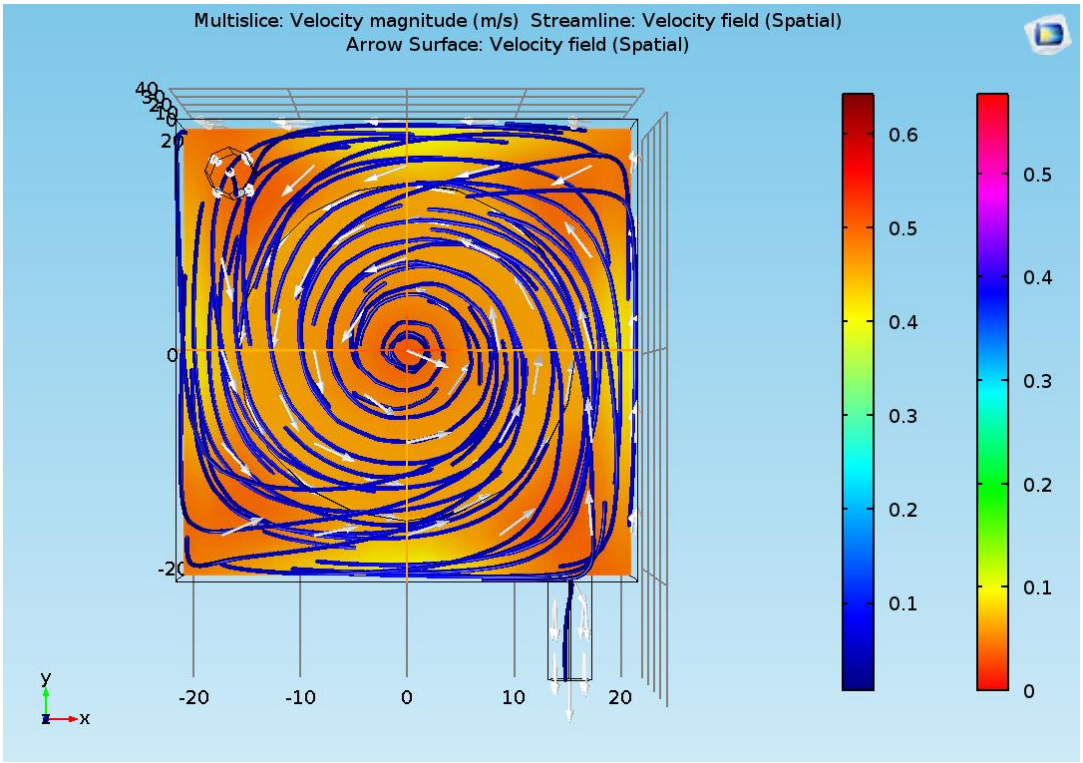

Figure C 2: XY plot – Spin ring

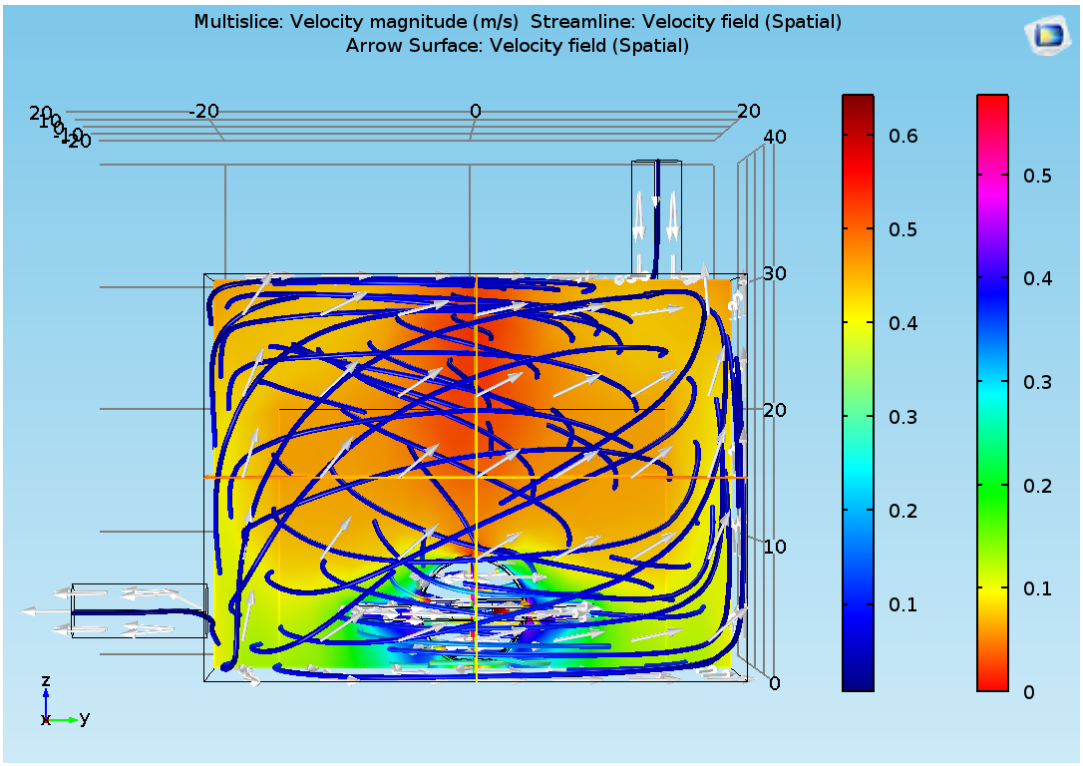

Figure C 3: YZ plot – Spin ring

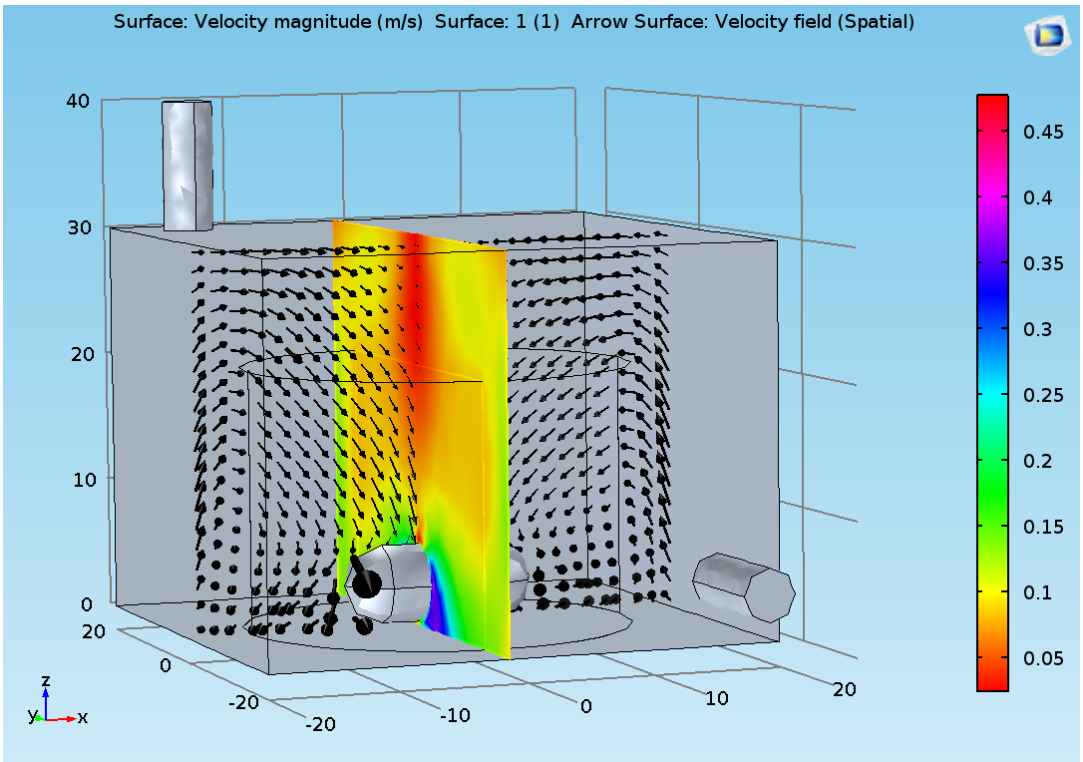

Figure C 4: Streamline slice plot – Cylindrical

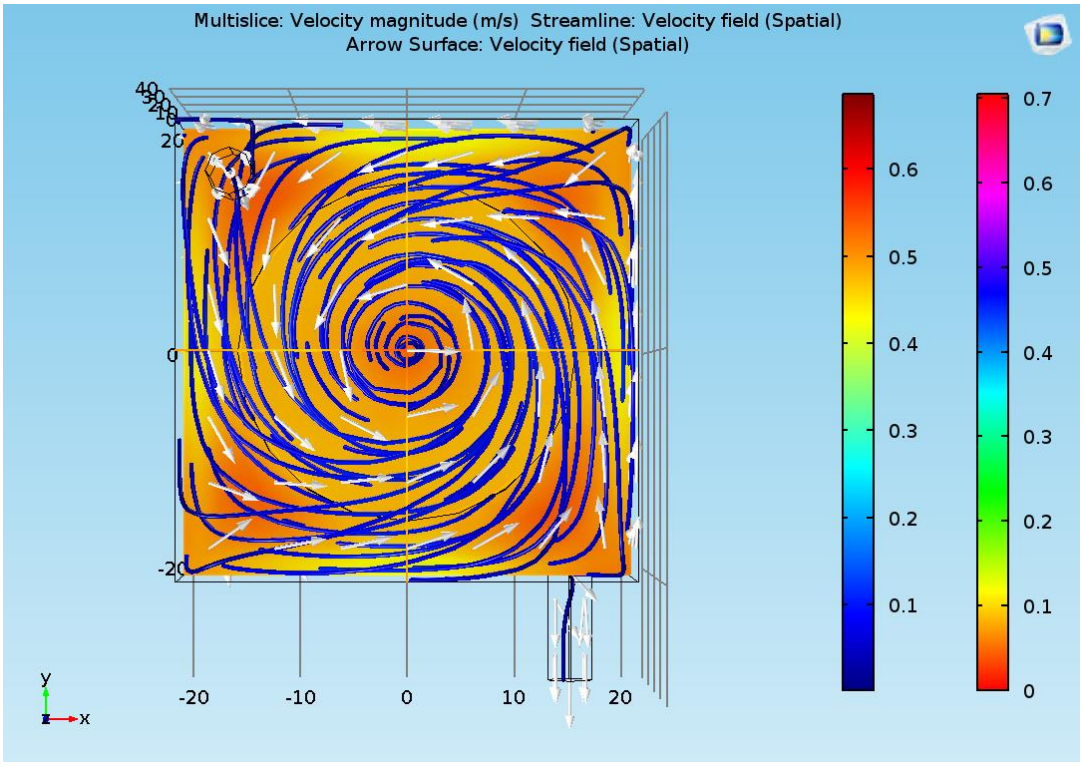

Figure C 5: XY plot – Cylindrical

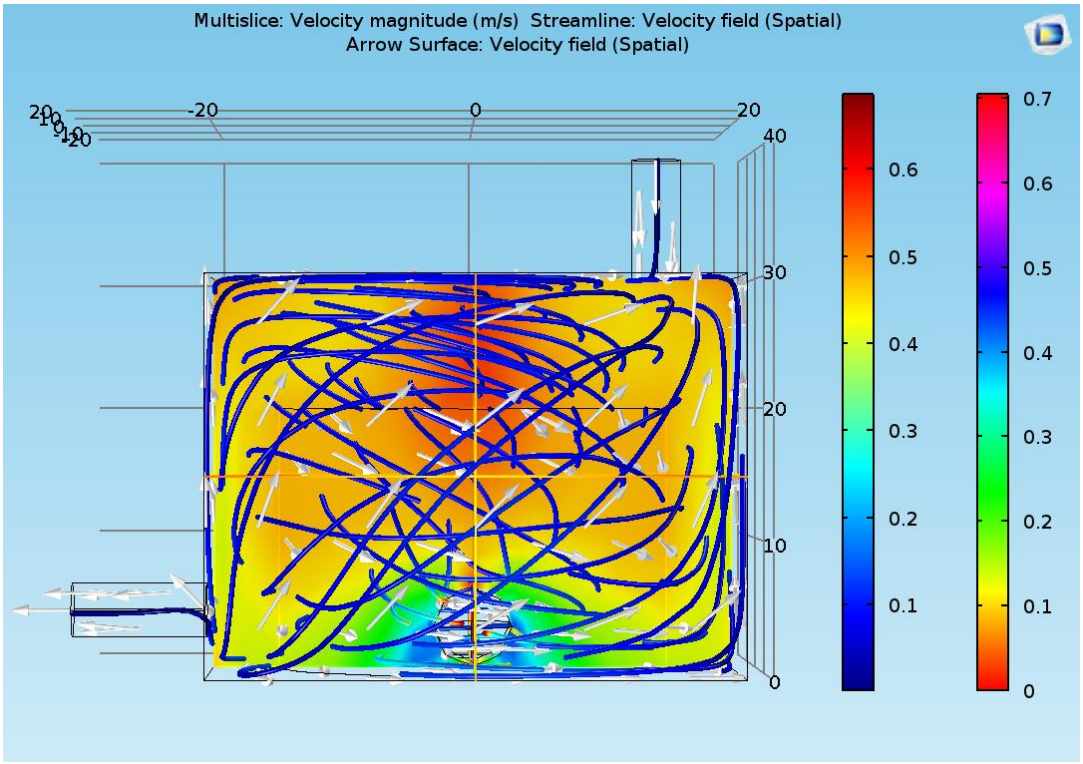

Figure C 6: YZ plot – Cylindrical

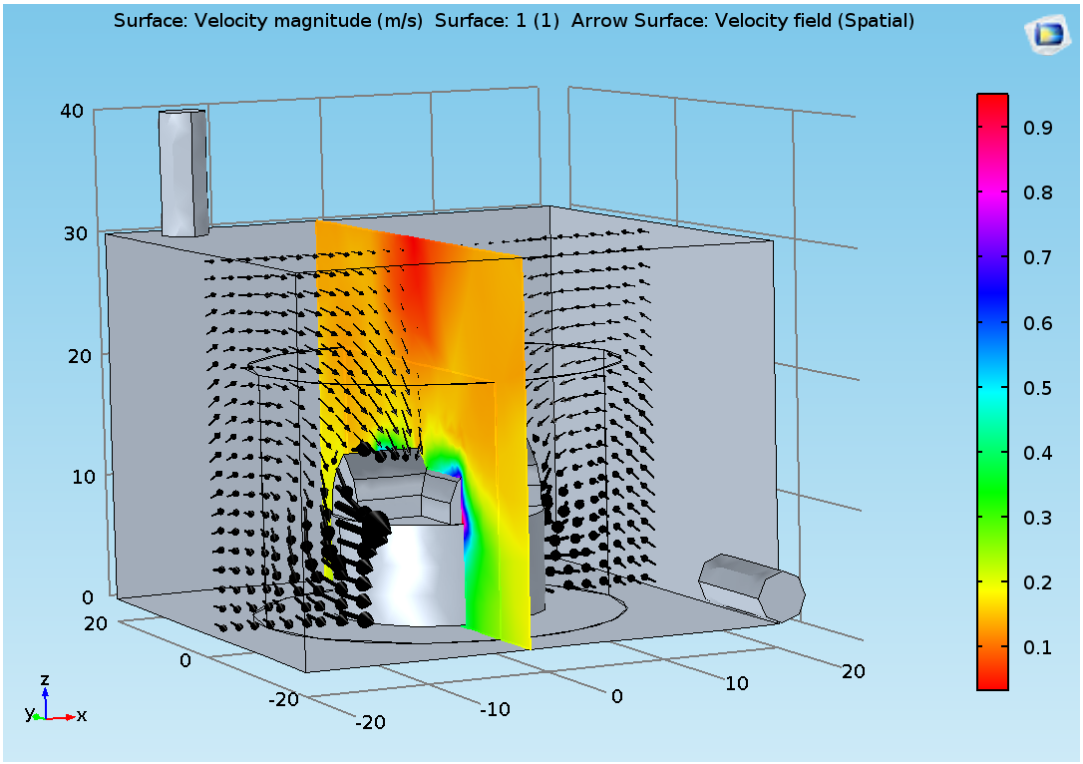

Figure C 7: Streamline slice plot – Single sided plus

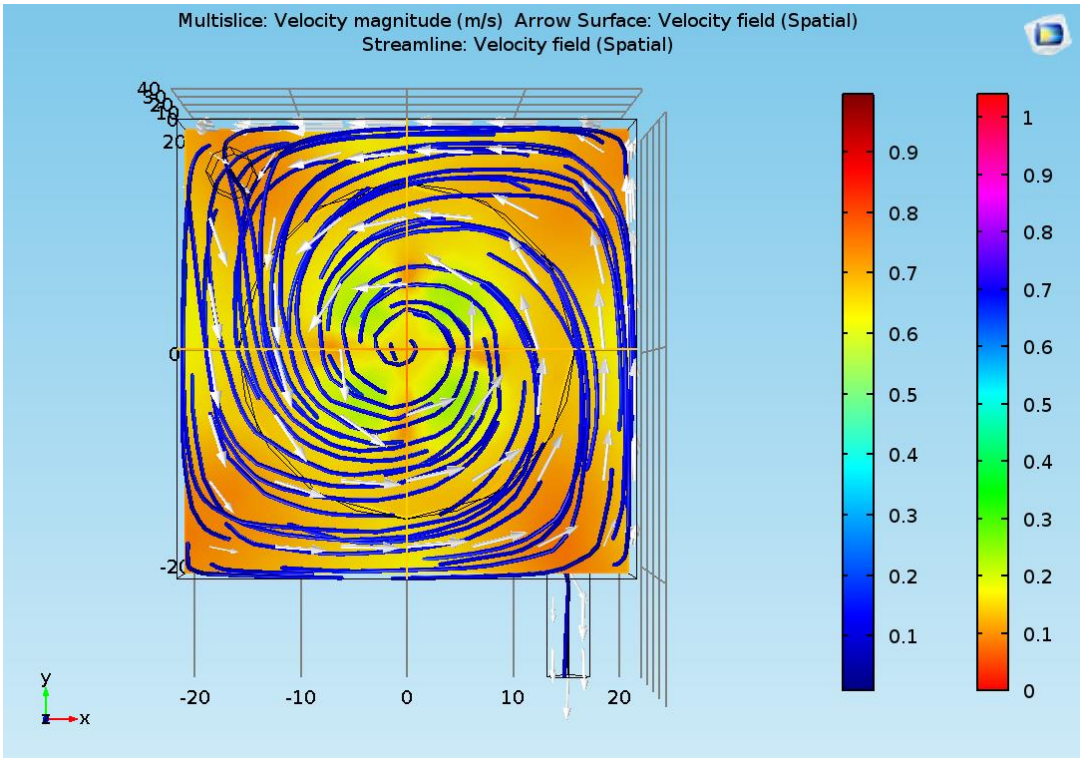

Figure C 8: XY plot- Single sided plus

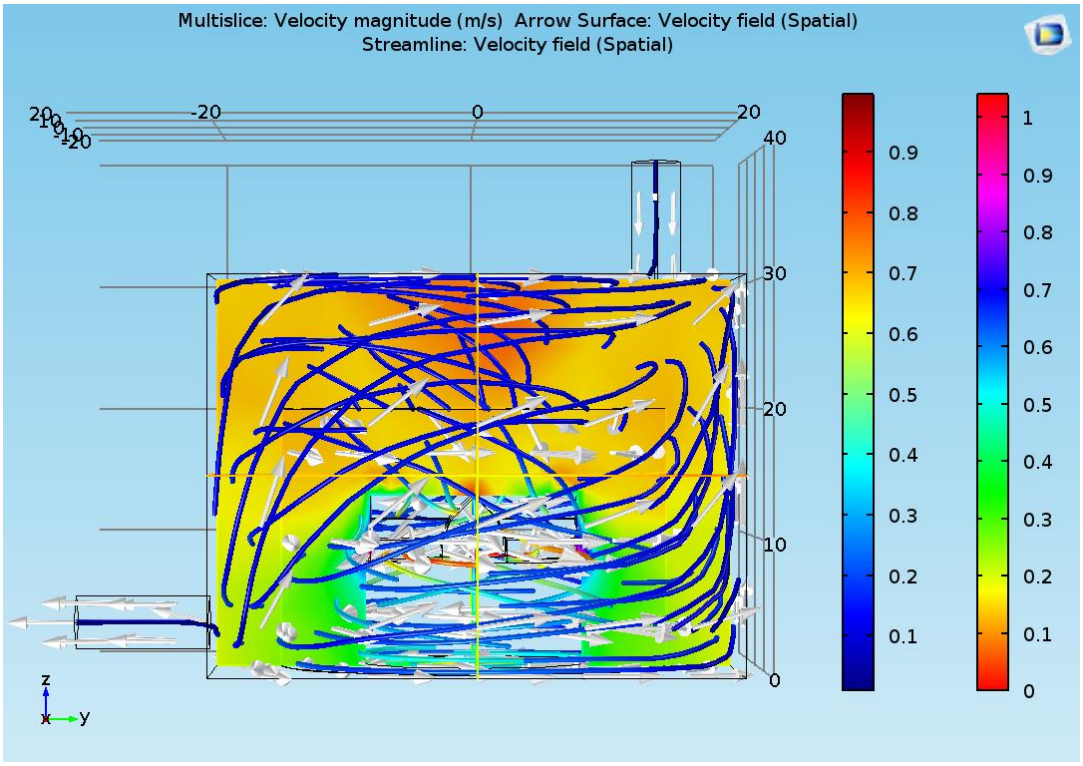

Figure C 9: YZ plot - Single sided plus

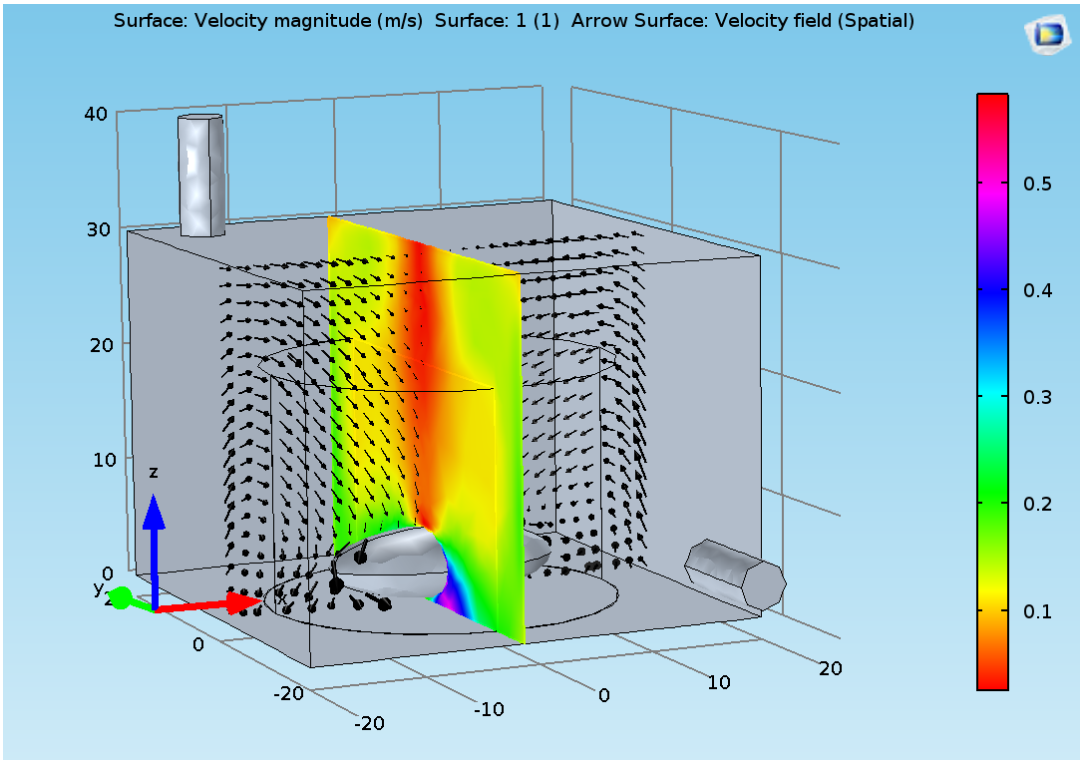

Figure C 10: Streamline slice plot – Capsule

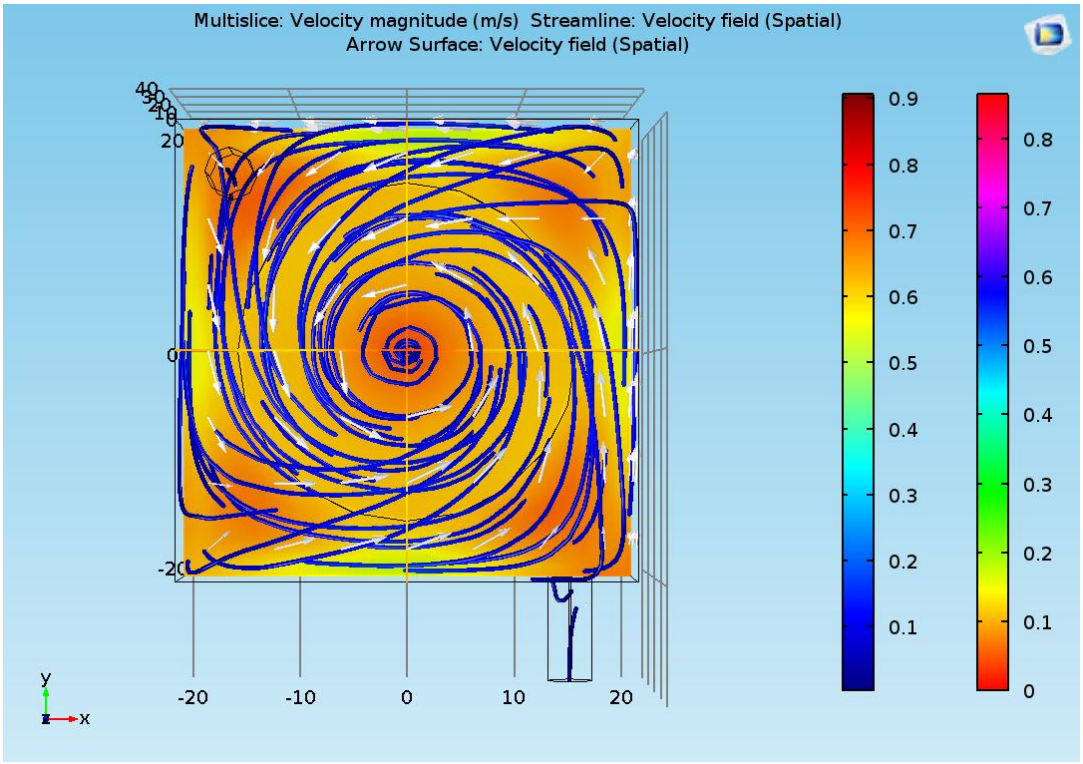

Figure C 11: XY plot – Capsule

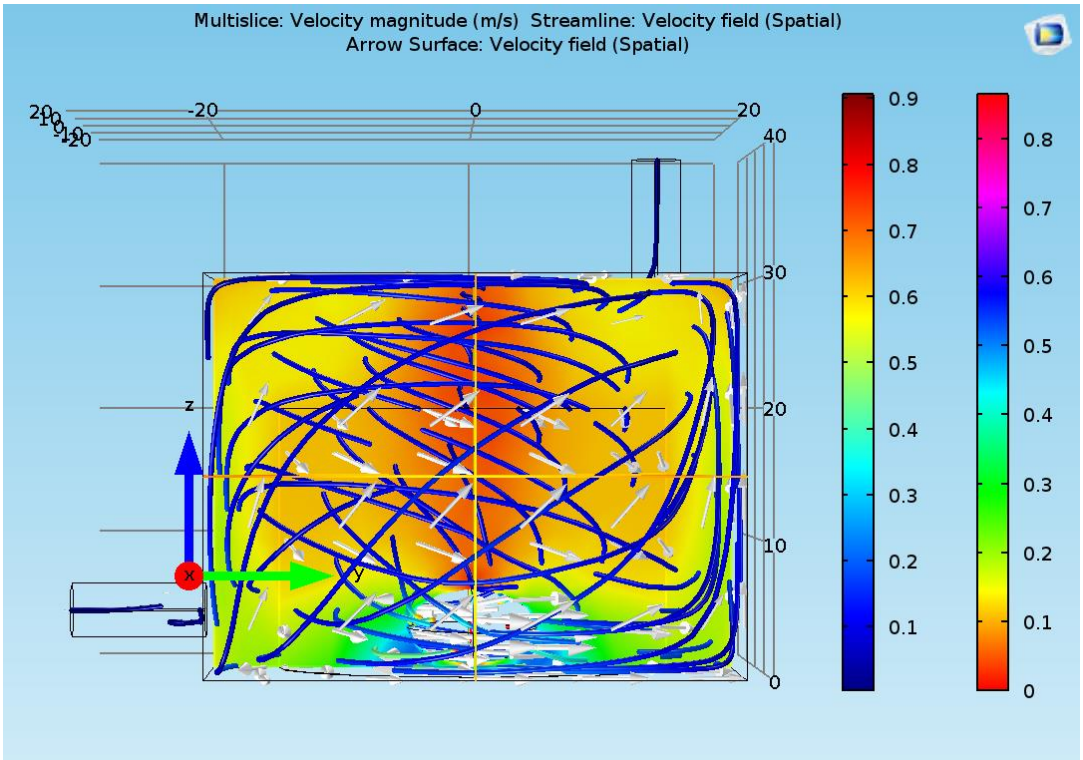

Figure C 12: YZ plot – Capsule

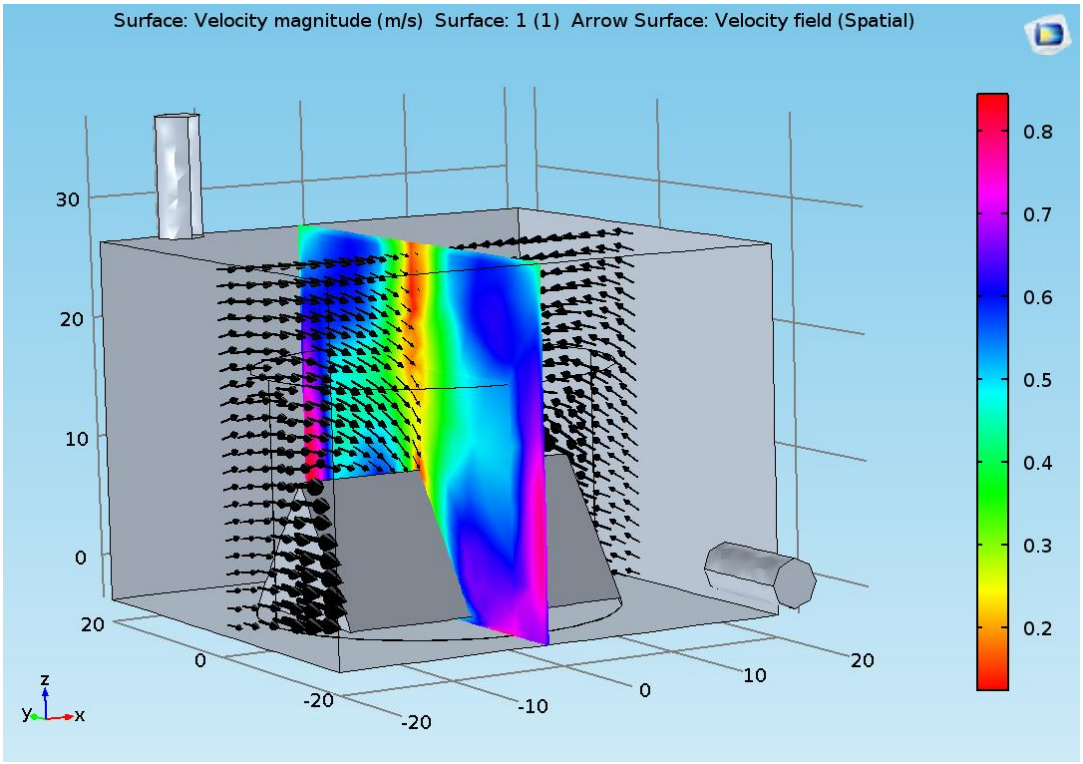

Figure C 13: Streamline slice plot - Triangular wedge

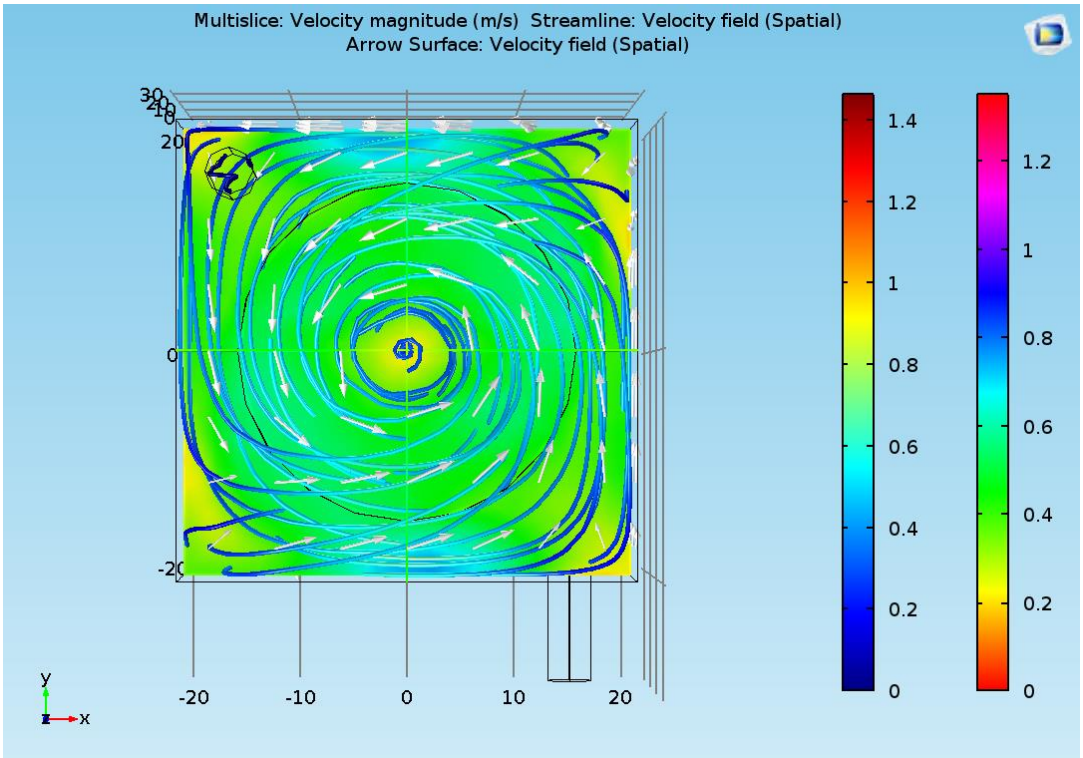

Figure C 14: XY plot - Triangular wedge

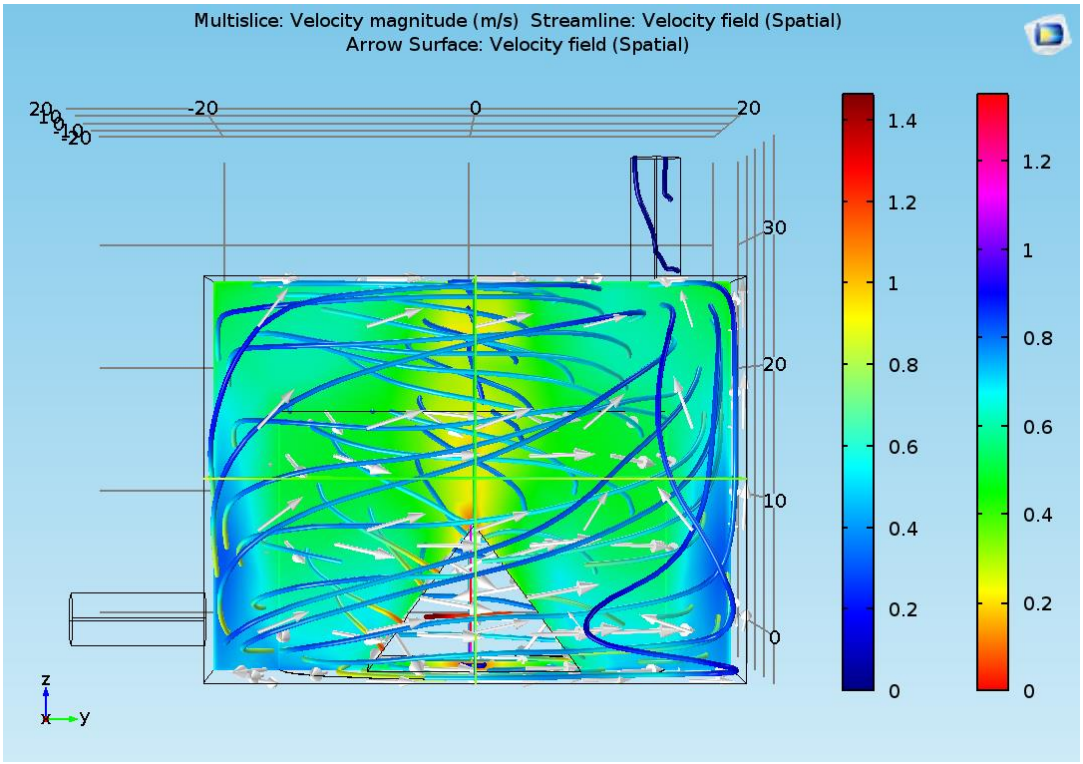

Figure C 15: YZ plot - Triangular wedge

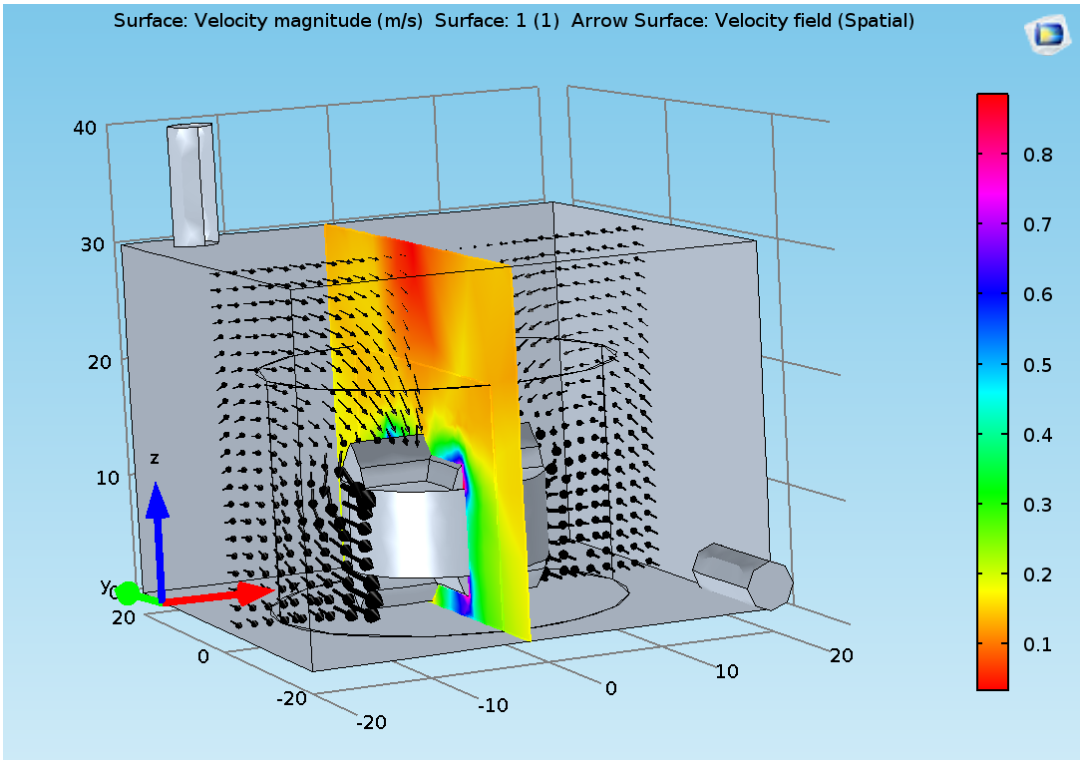

Figure C 16: Streamline slice plot - Cross head plus

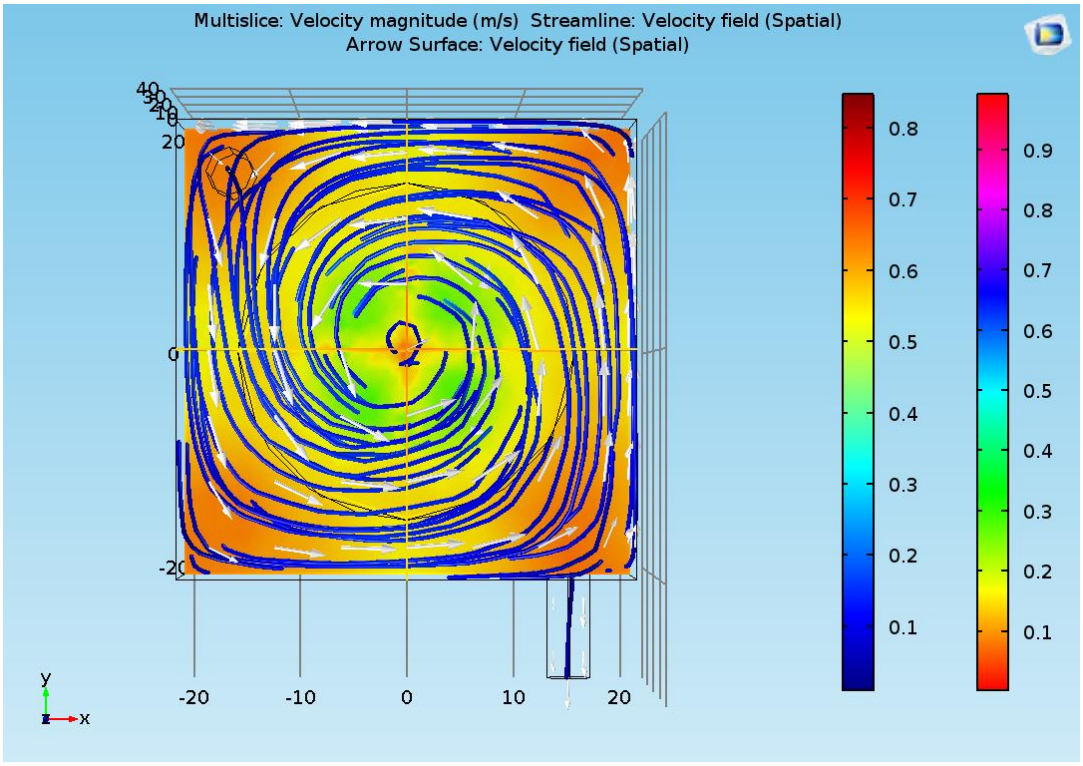

Figure C 17: XY plot - Cross head plus

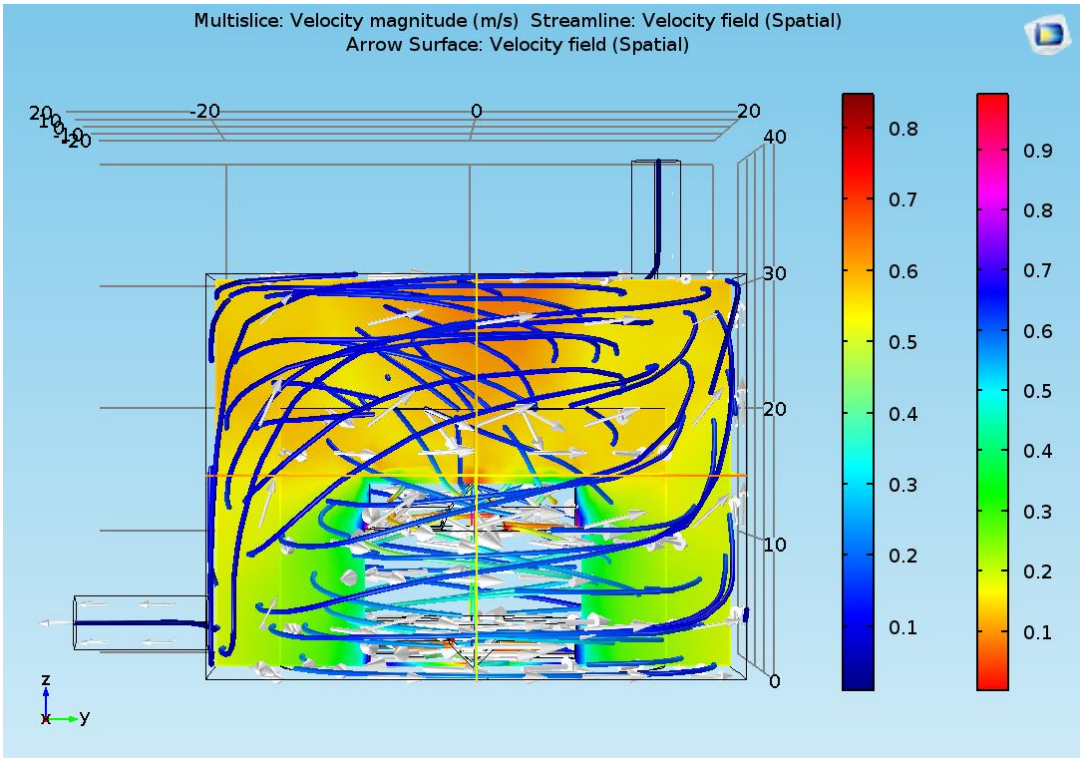

Figure C 18: YZ plot - Cross head plus

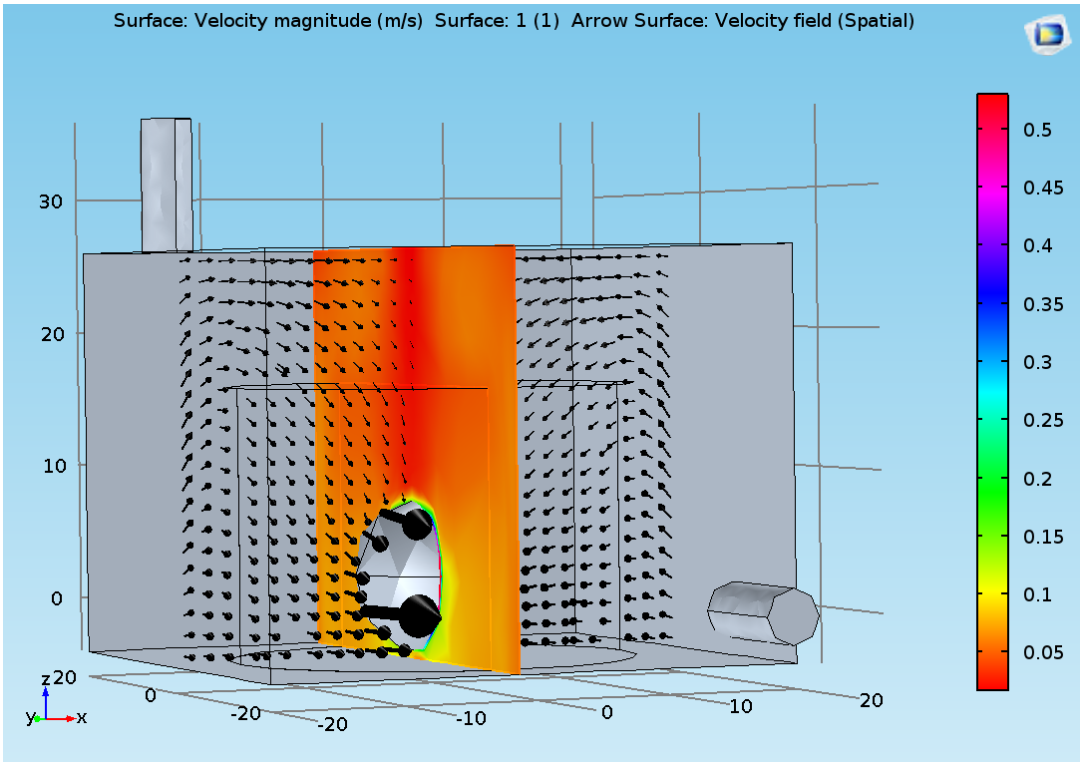

Figure C 19: Streamline slice plot – Sphere

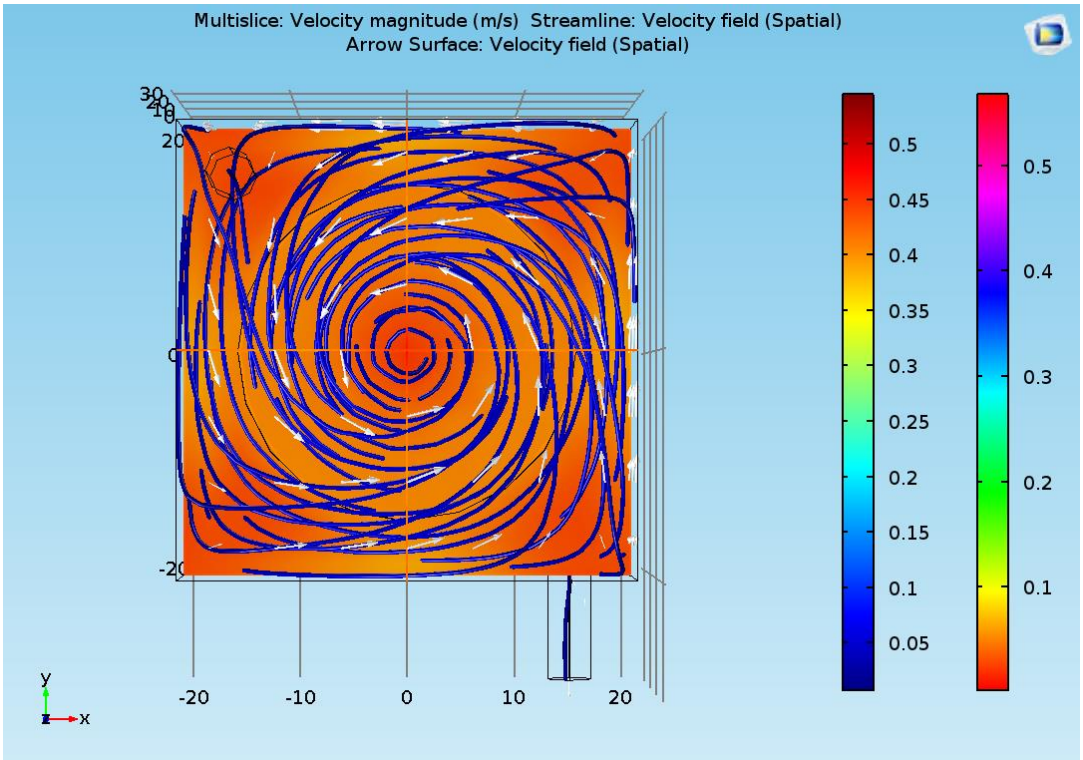

Figure C 20: XY plot – Sphere

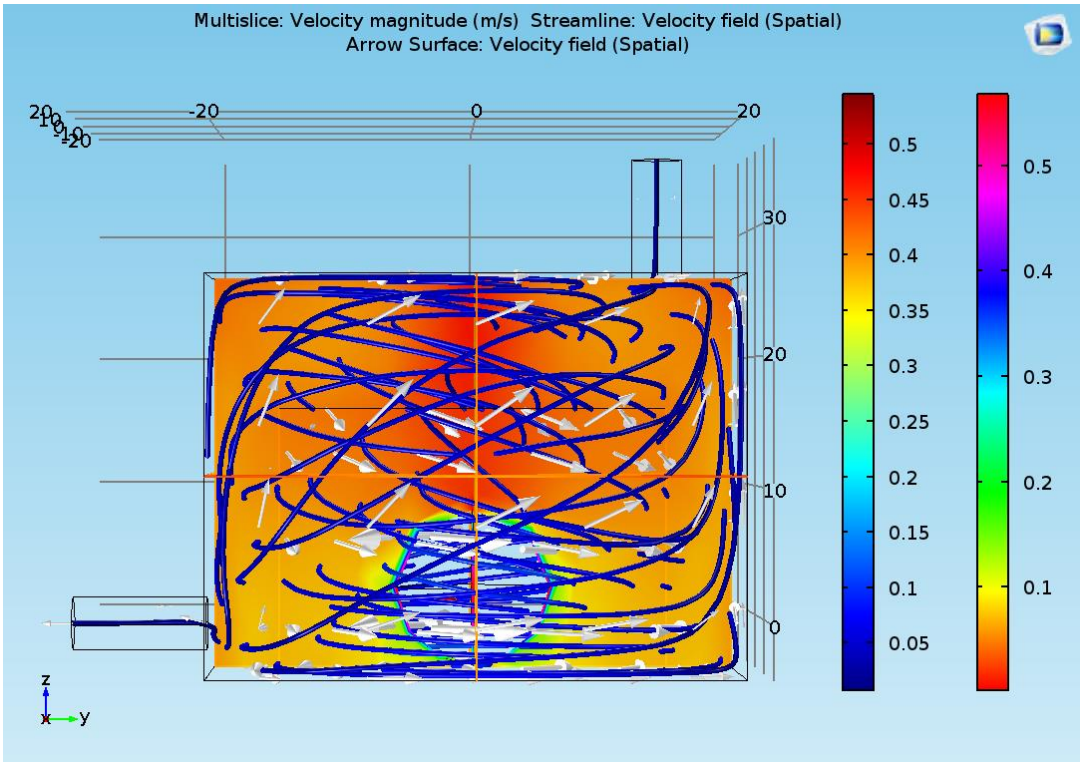

Figure C 21: YZ plot – Sphere

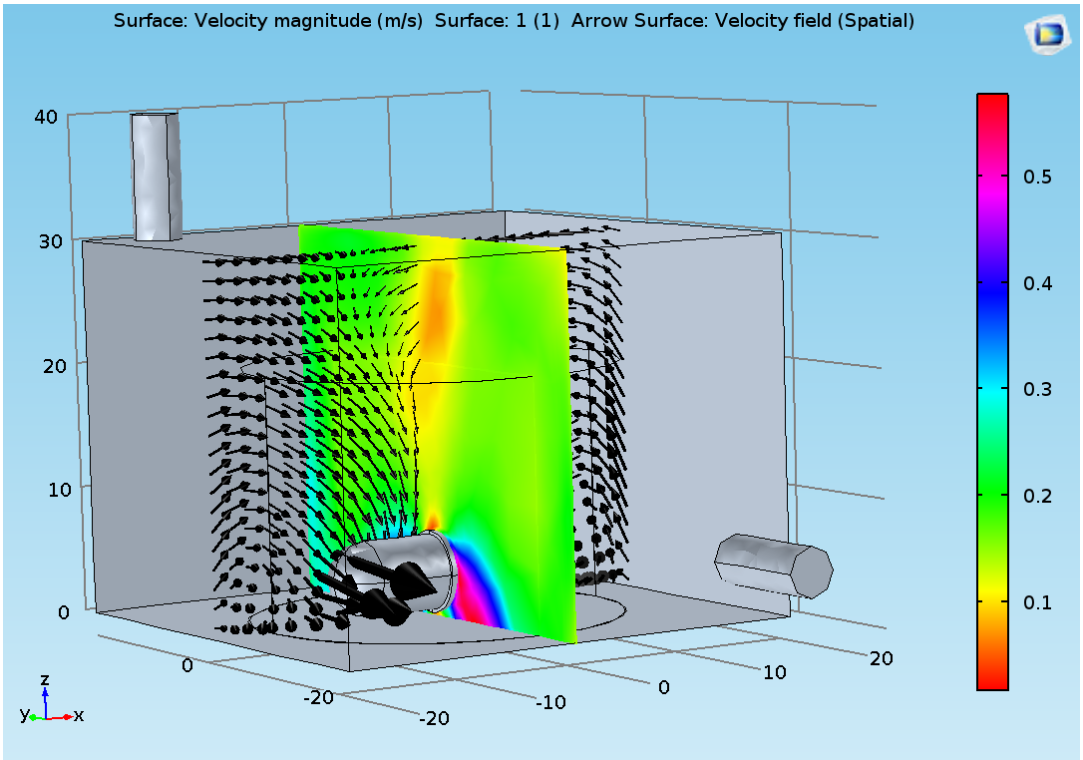

Figure C 22: Streamline slice plot - Pivot cylindrical

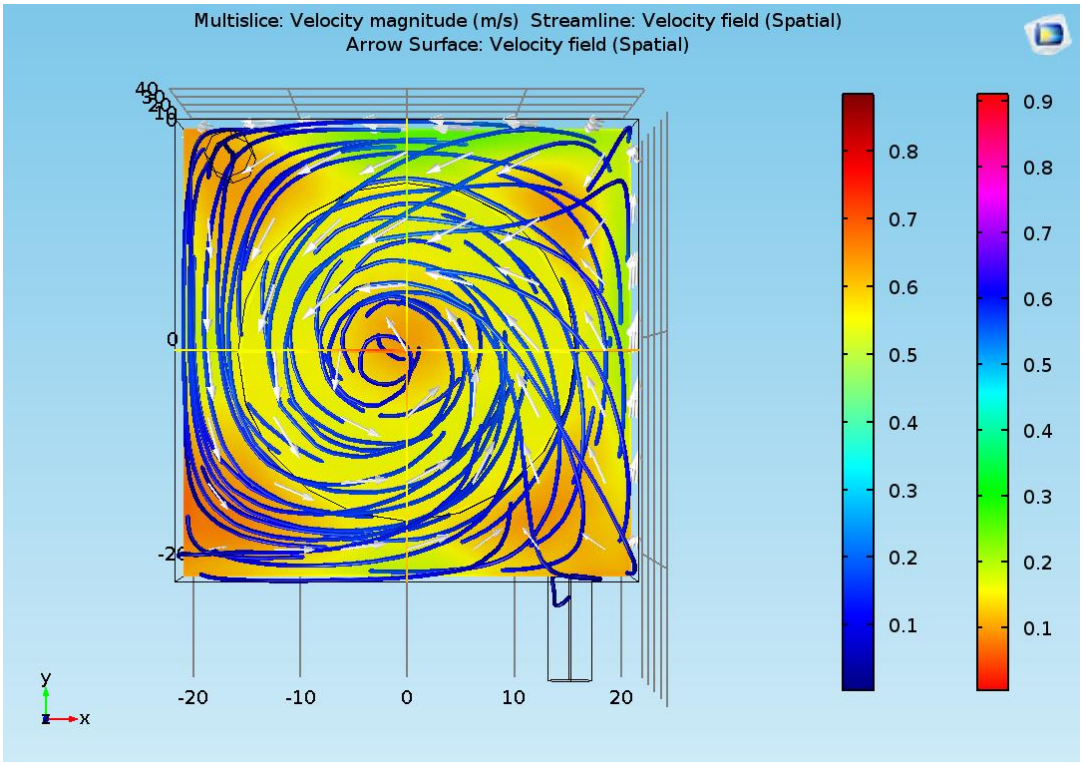

Figure C 23: XY plot - Pivot cylindrical

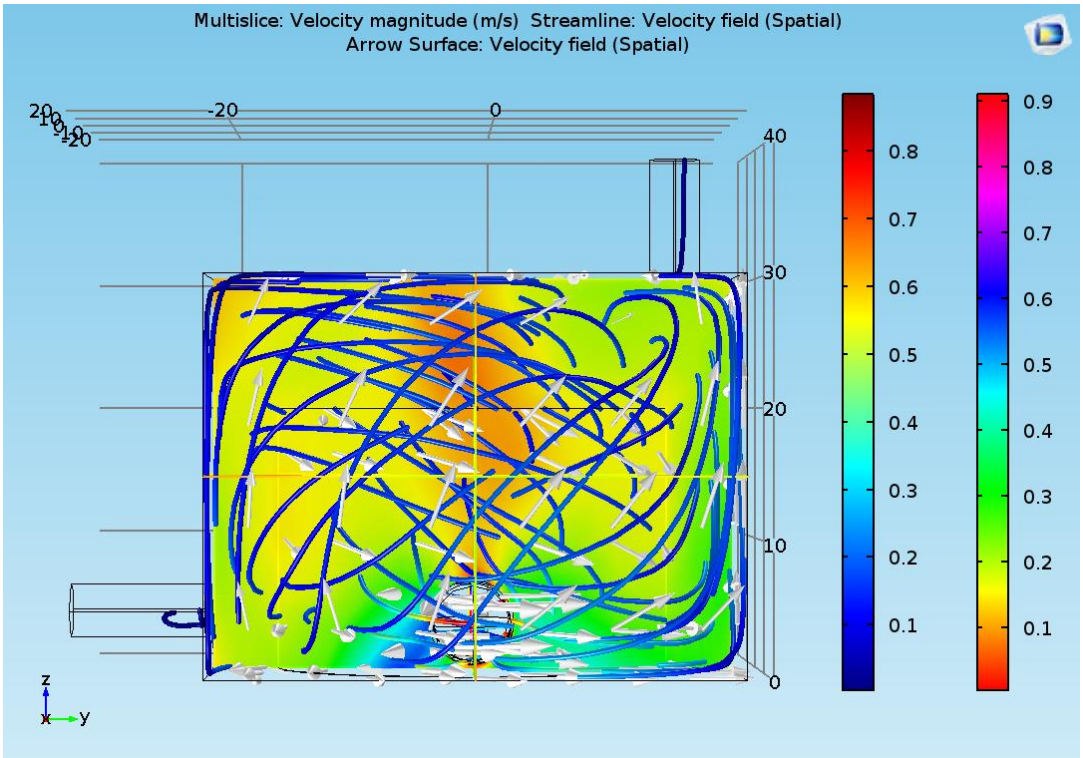

Figure C 24: YZ plot - Pivot cylindrical

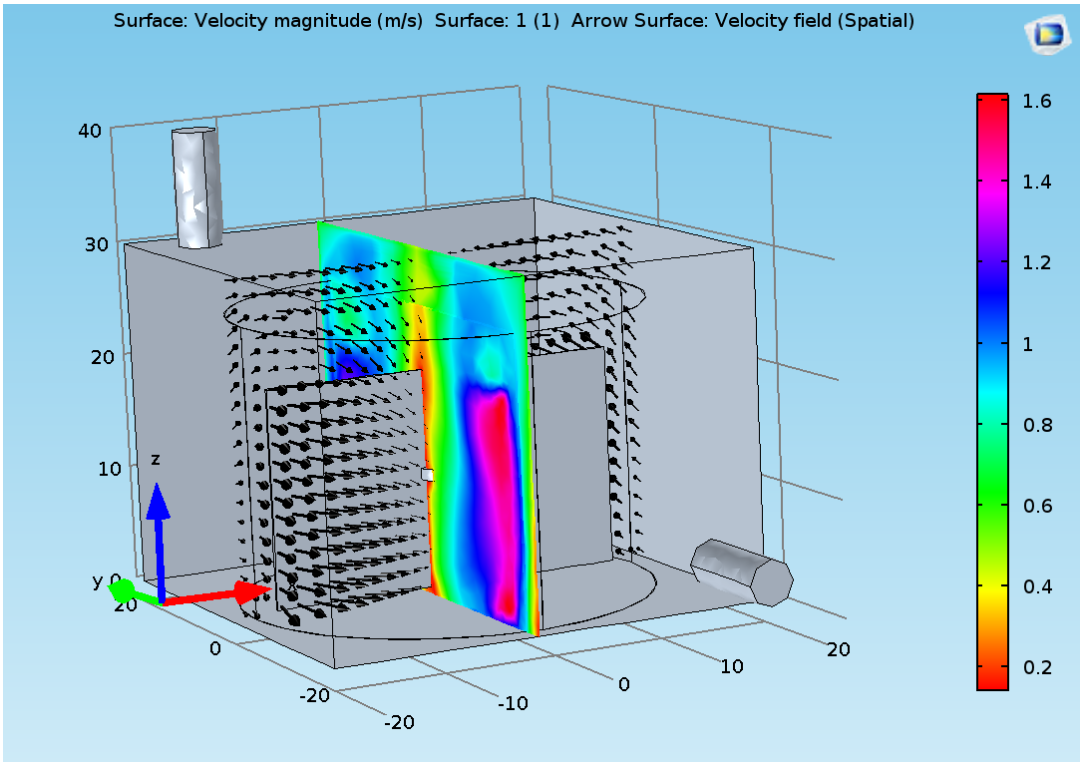

Figure C 25: Streamline slice plot - 4 broad blade impeller

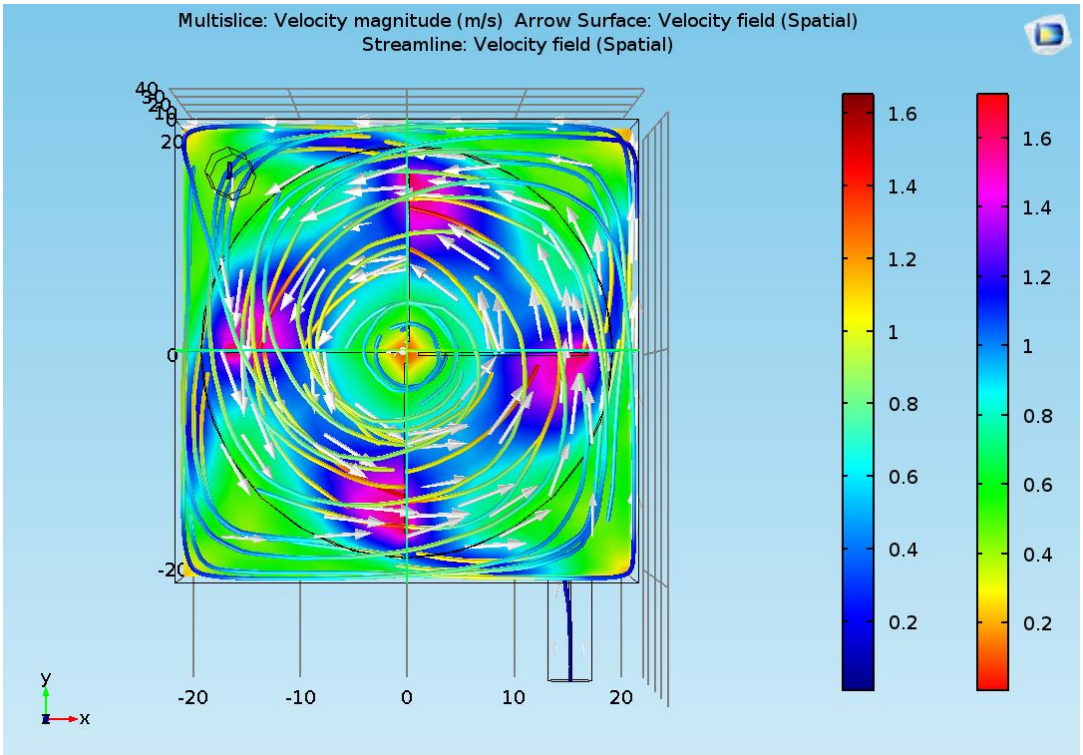

Figure C 26: XY plot - 4 broad blade impeller

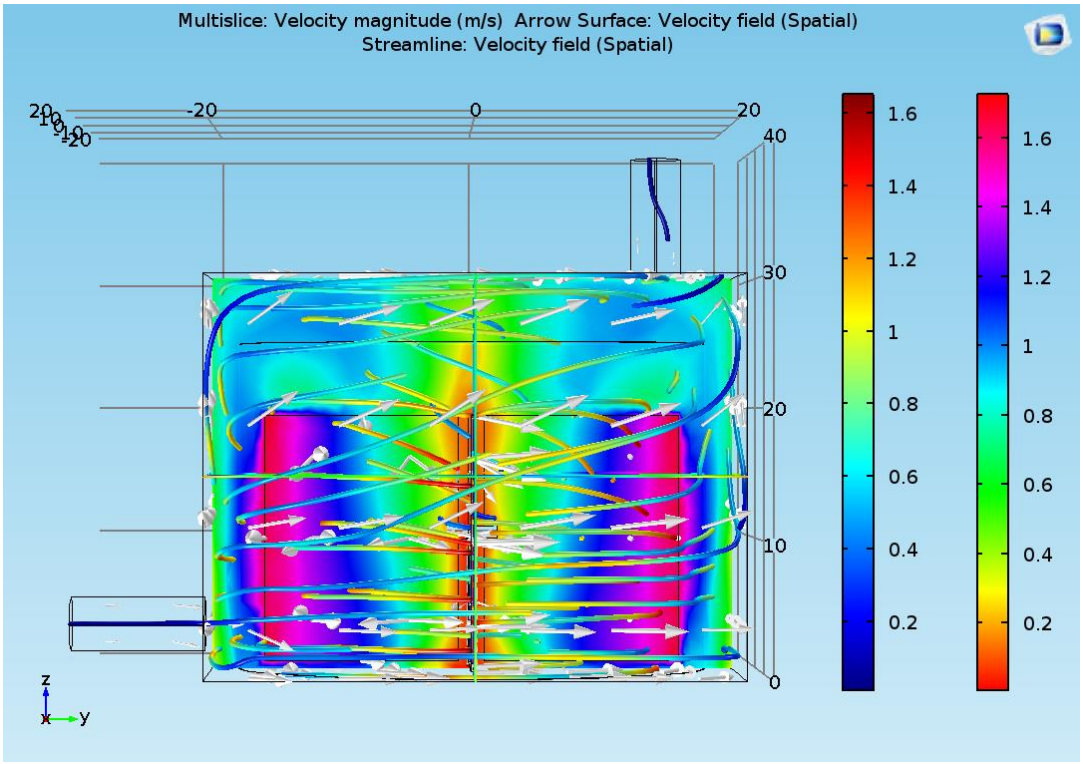

Figure C 27: YZ plot – 4 broad blade impeller

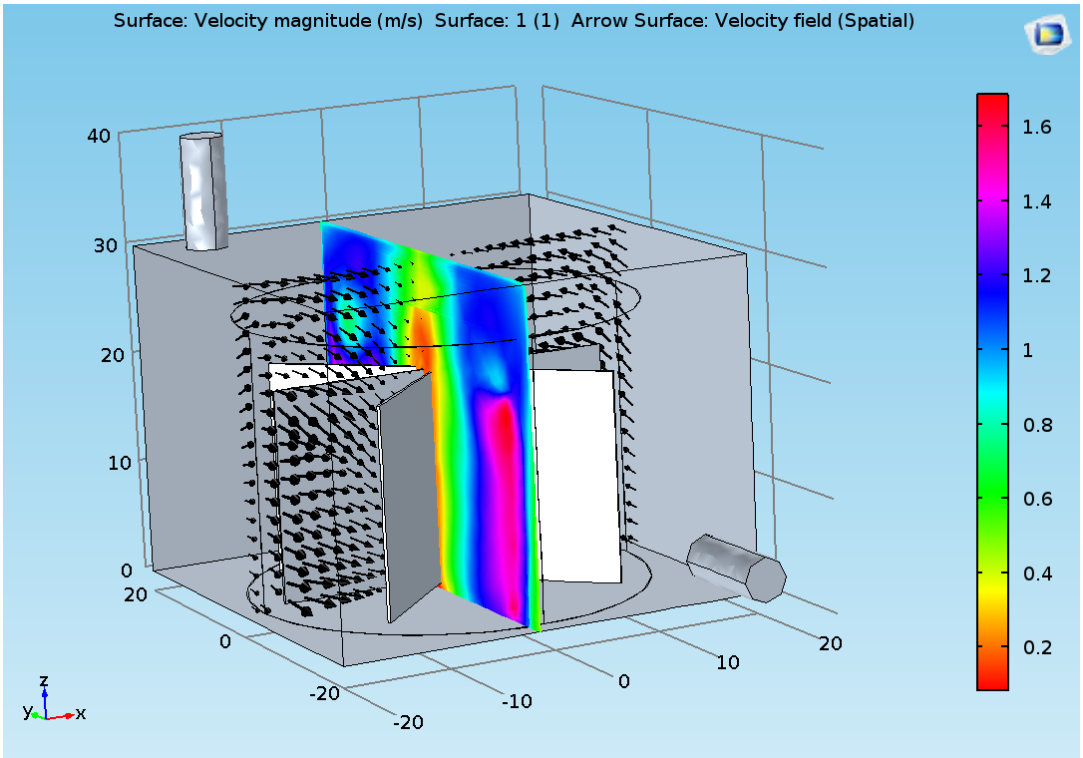

Figure C 28: Streamline slice plot - 8 broad blade impeller

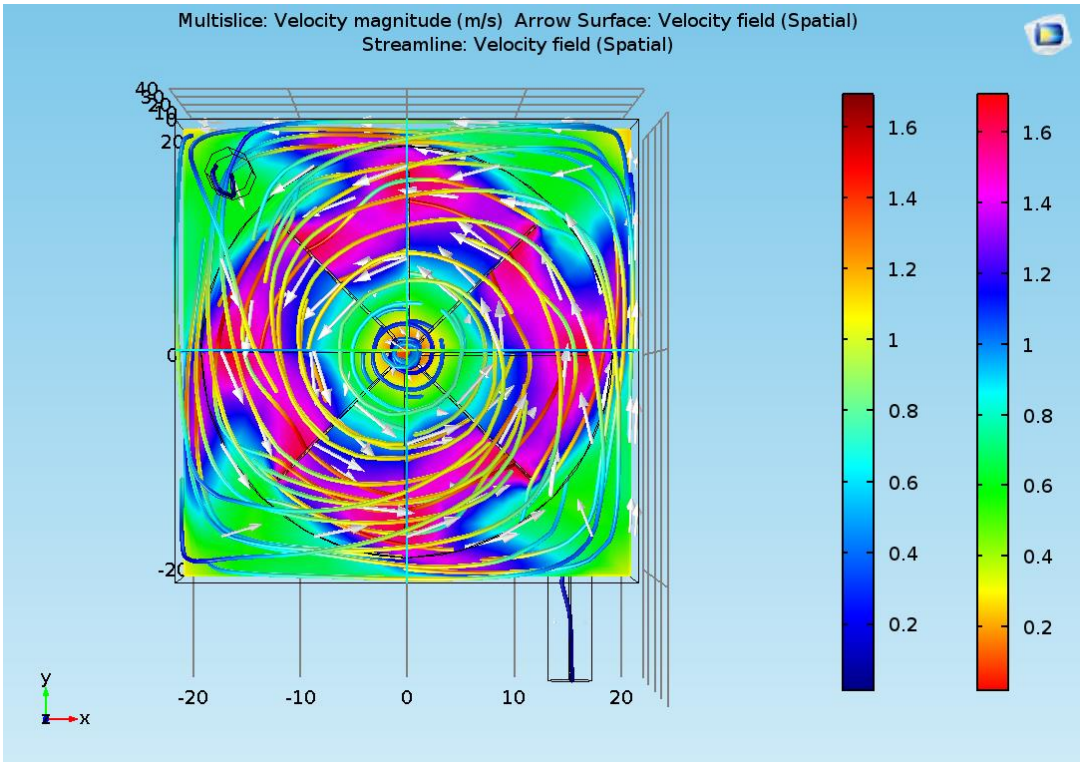

Figure C 29: XY plot - 8 broad blade impeller

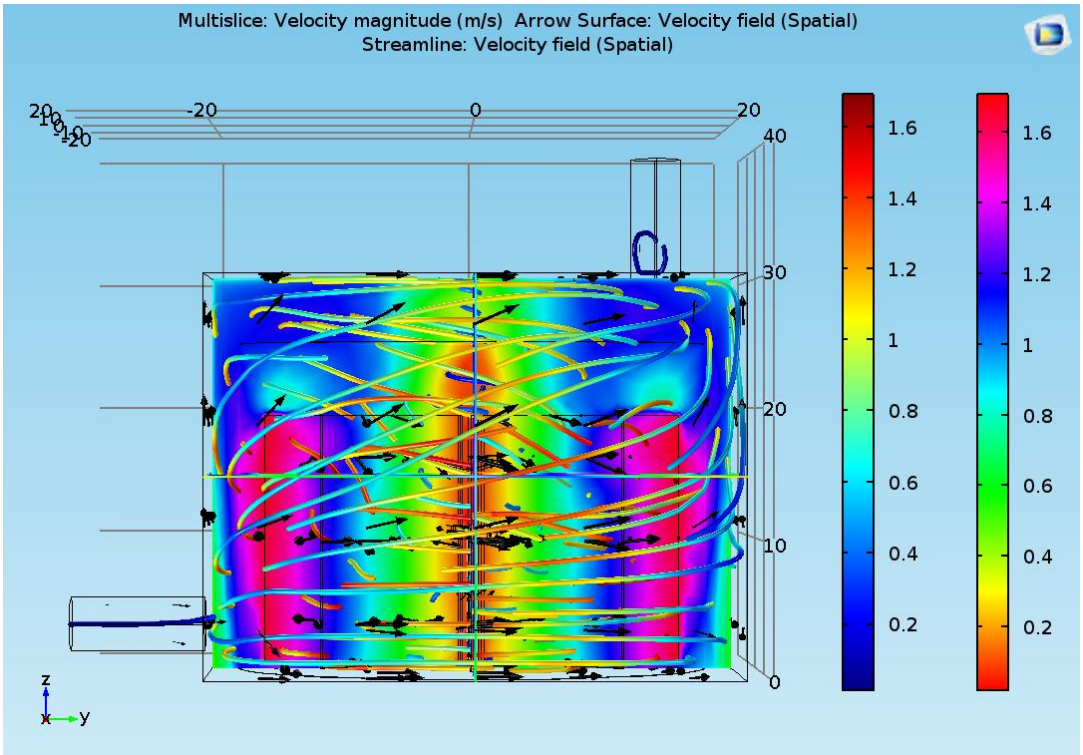

Figure C 30: YZ plot - 8 broad blade impeller

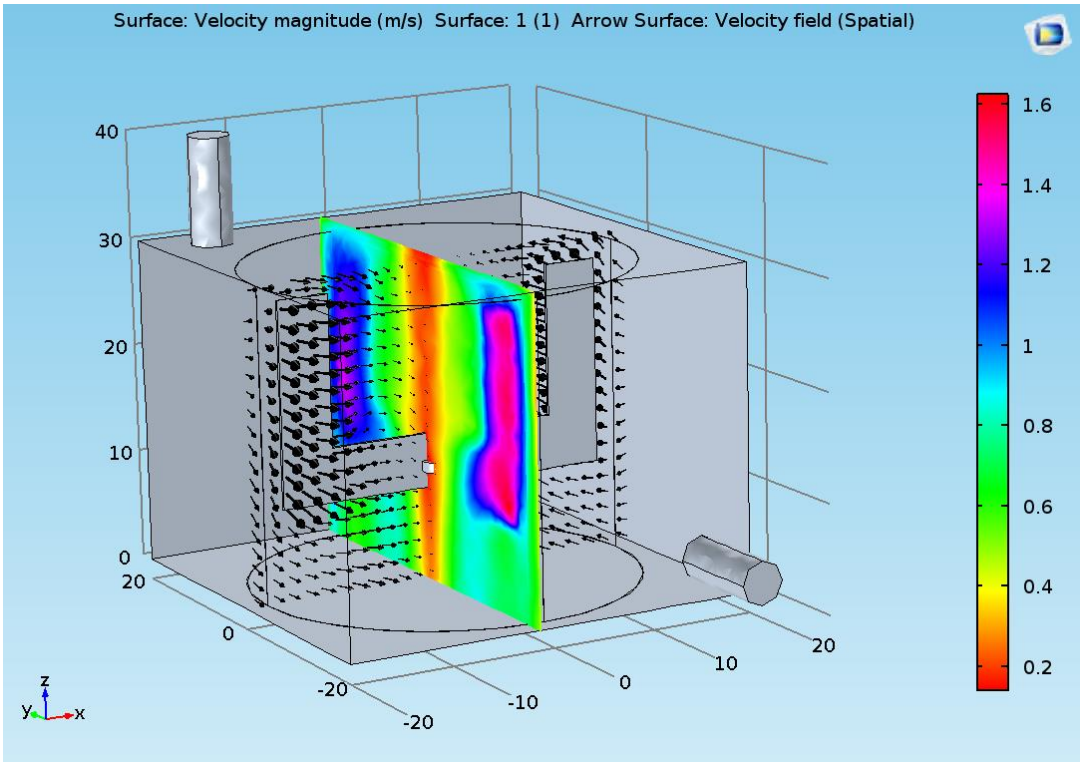

Figure C 31: Streamline slice plot – 2 anchors

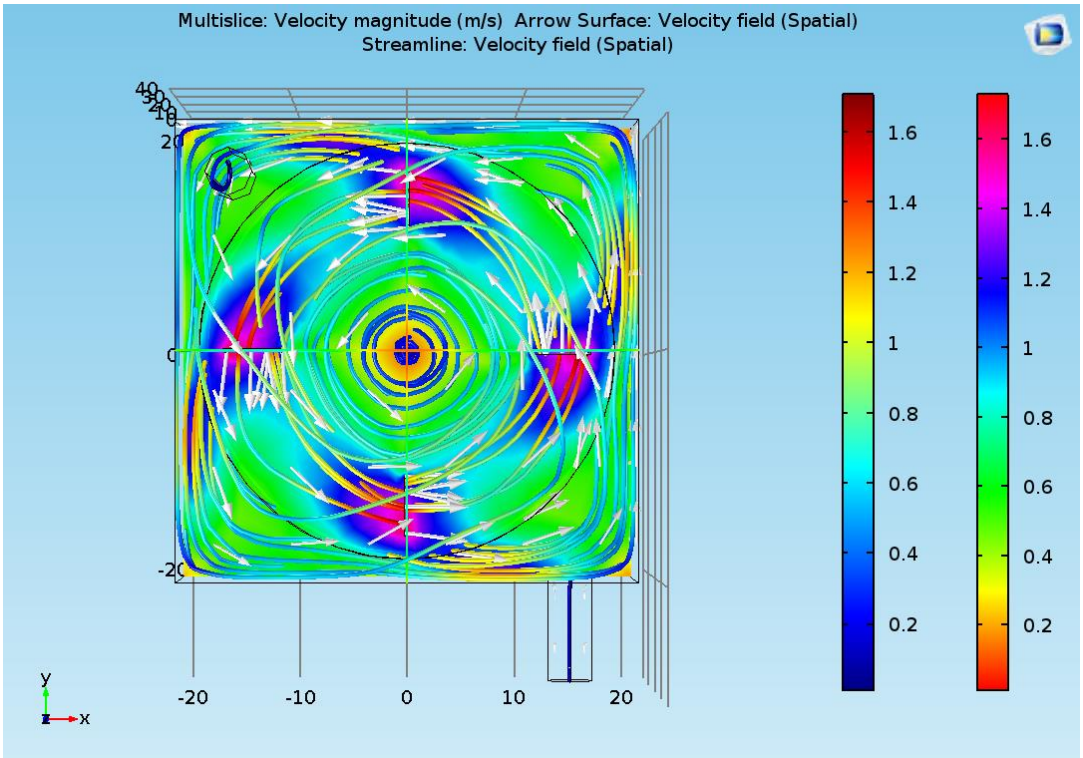

Figure C 32: XY plot - 2 anchors

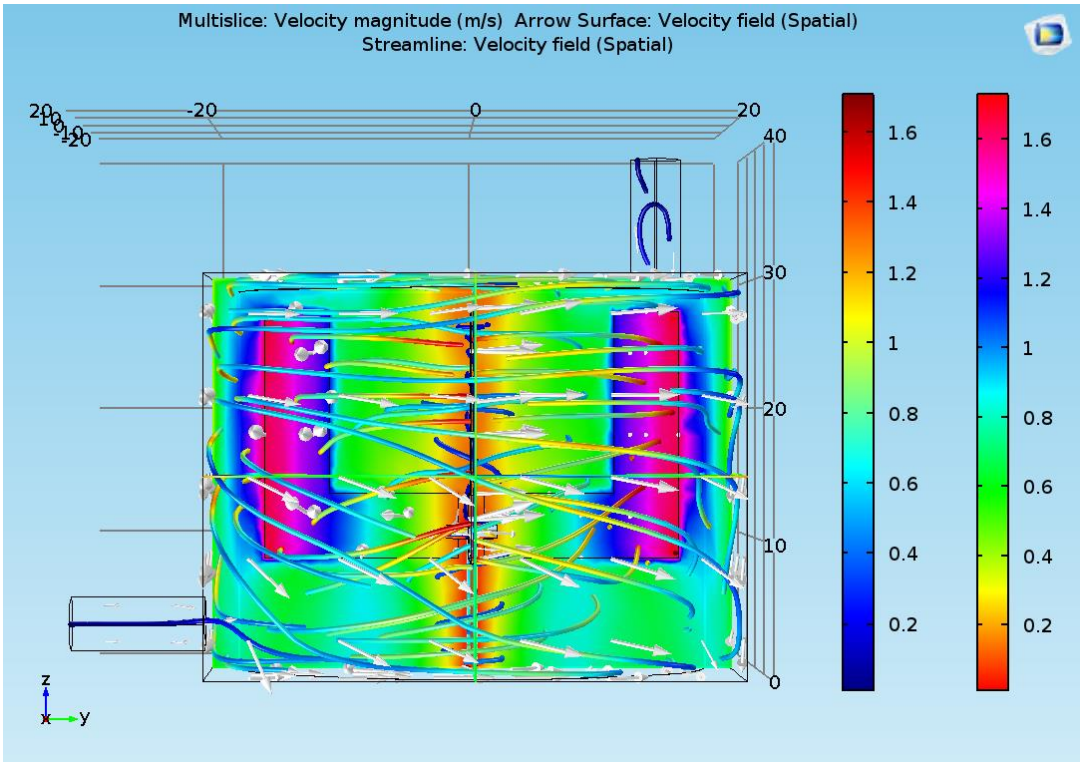

Figure C 33: YZ plot - 2 anchors

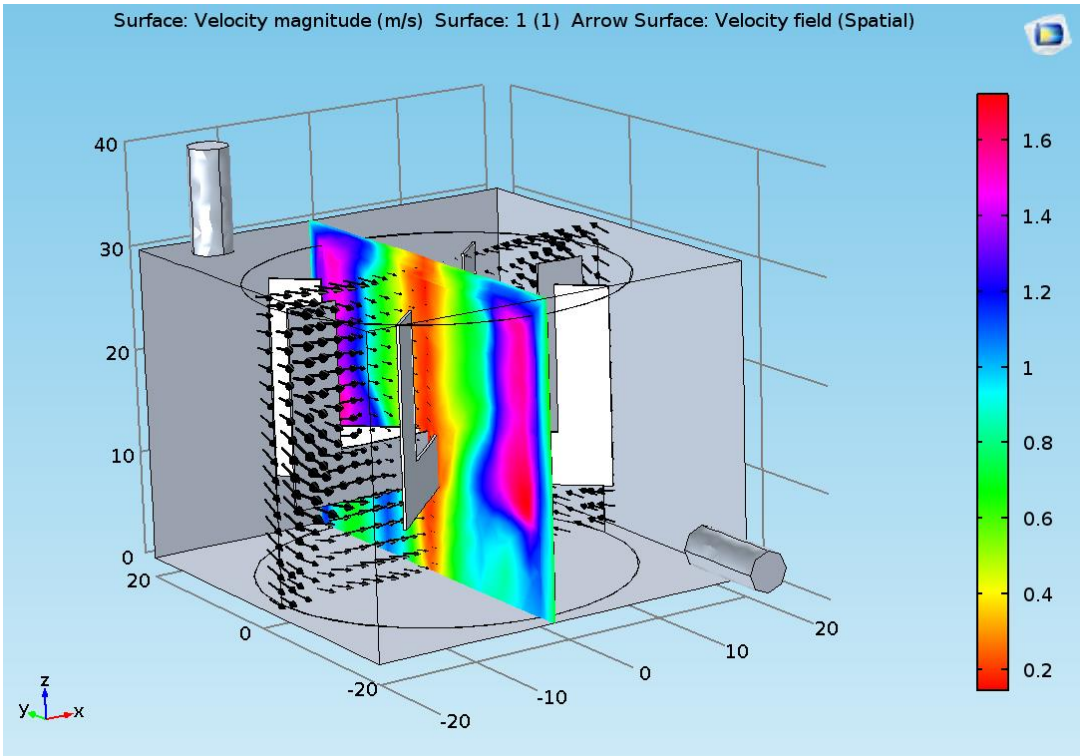

Figure C 34: Streamline slice plot – 4 anchors

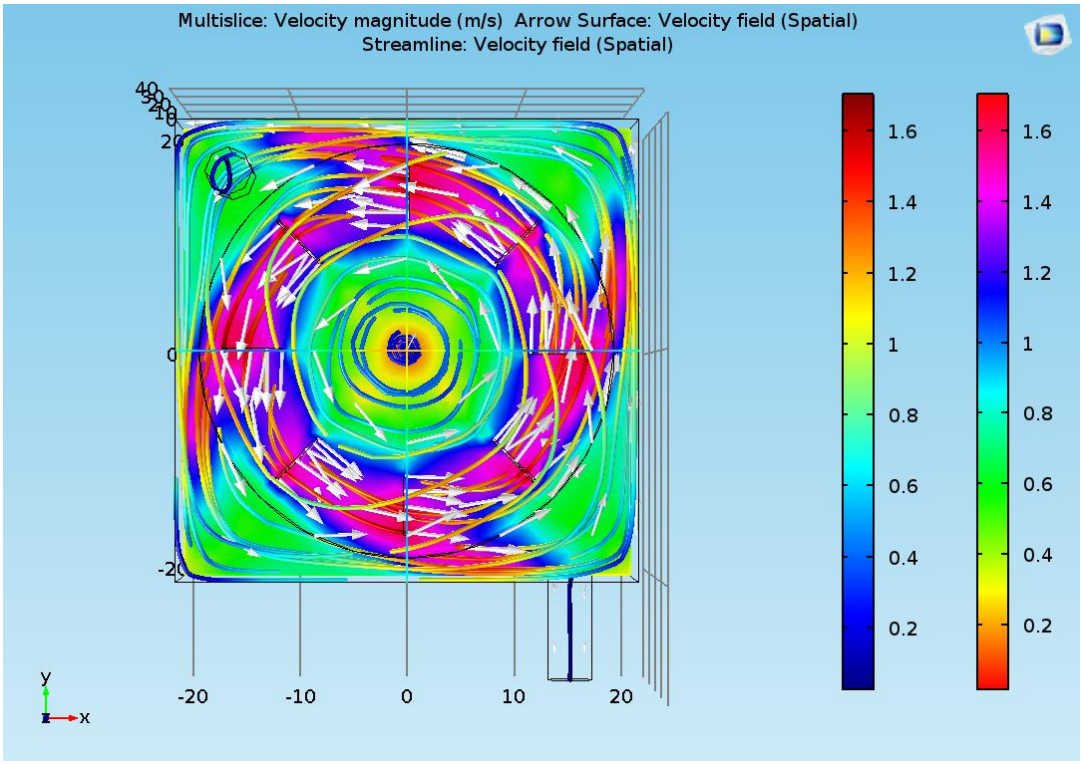

Figure C 35: XY plot - 4 anchors

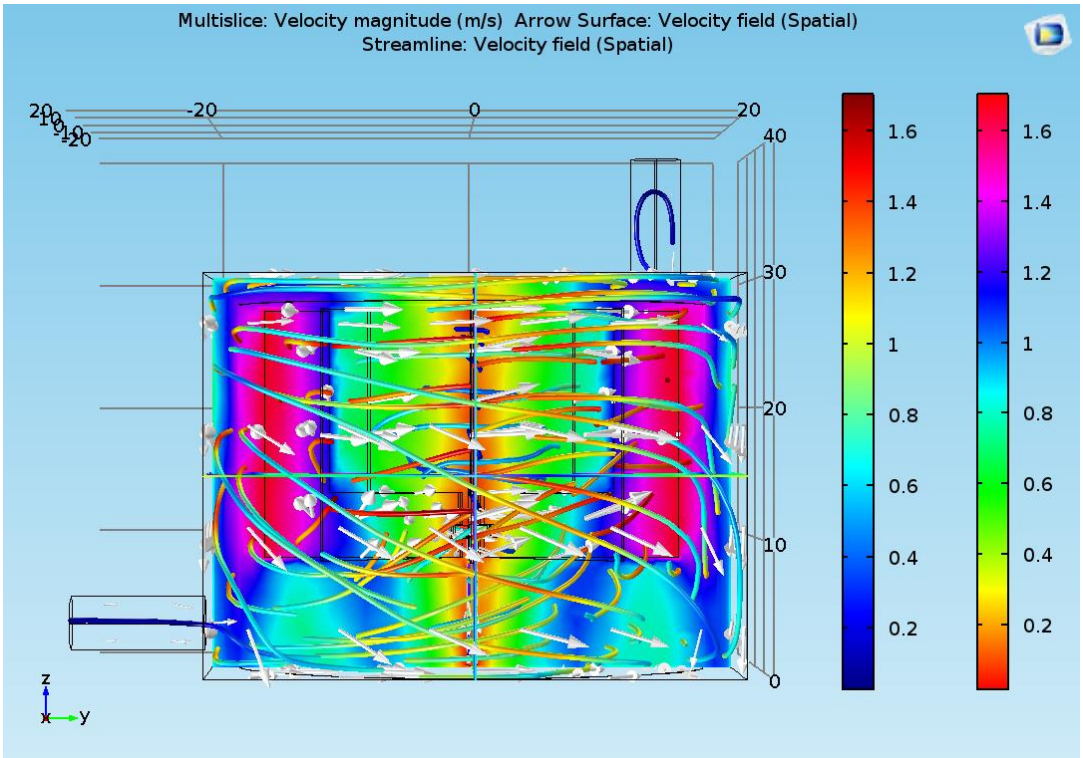

Figure C 36: YZ plot - 4 anchors

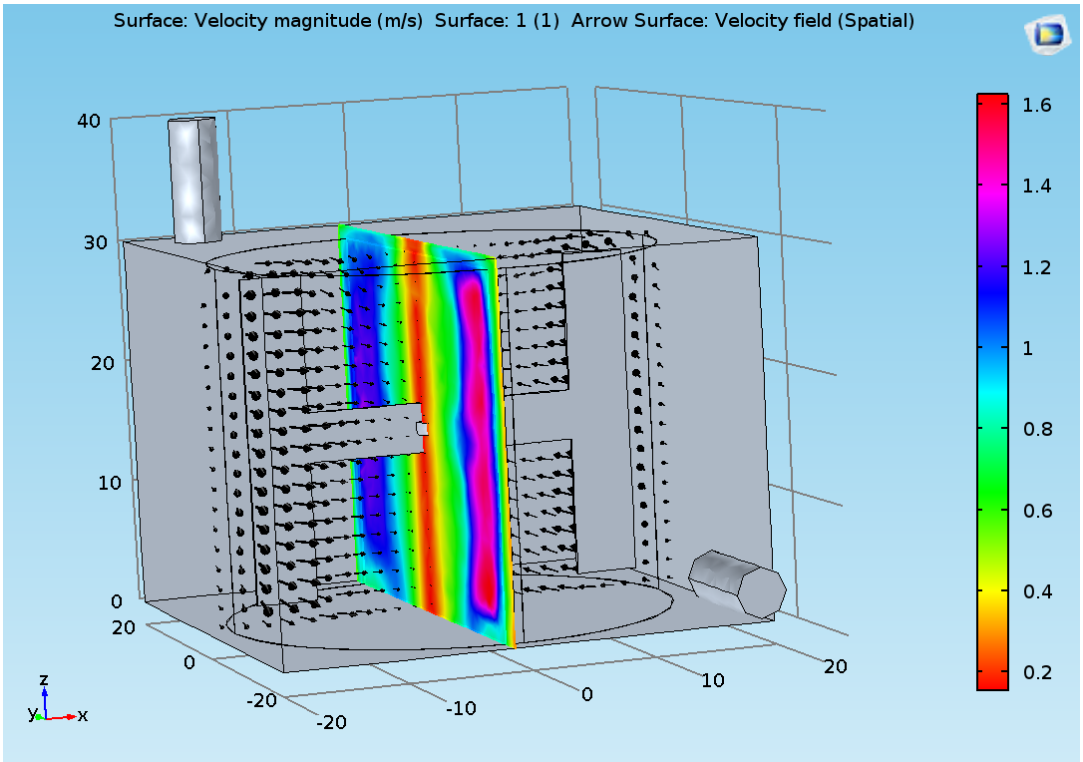

Figure C 37: Streamline slice plot – 2 H shaped

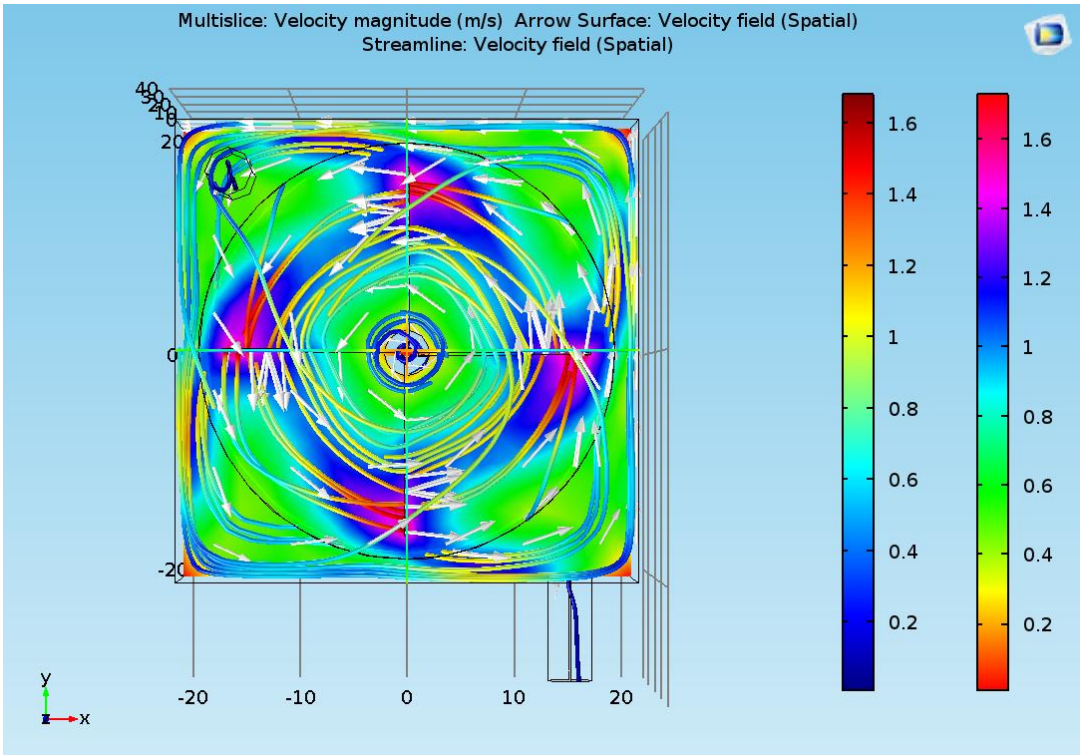

Figure C 38: XY plot - 2 H shaped

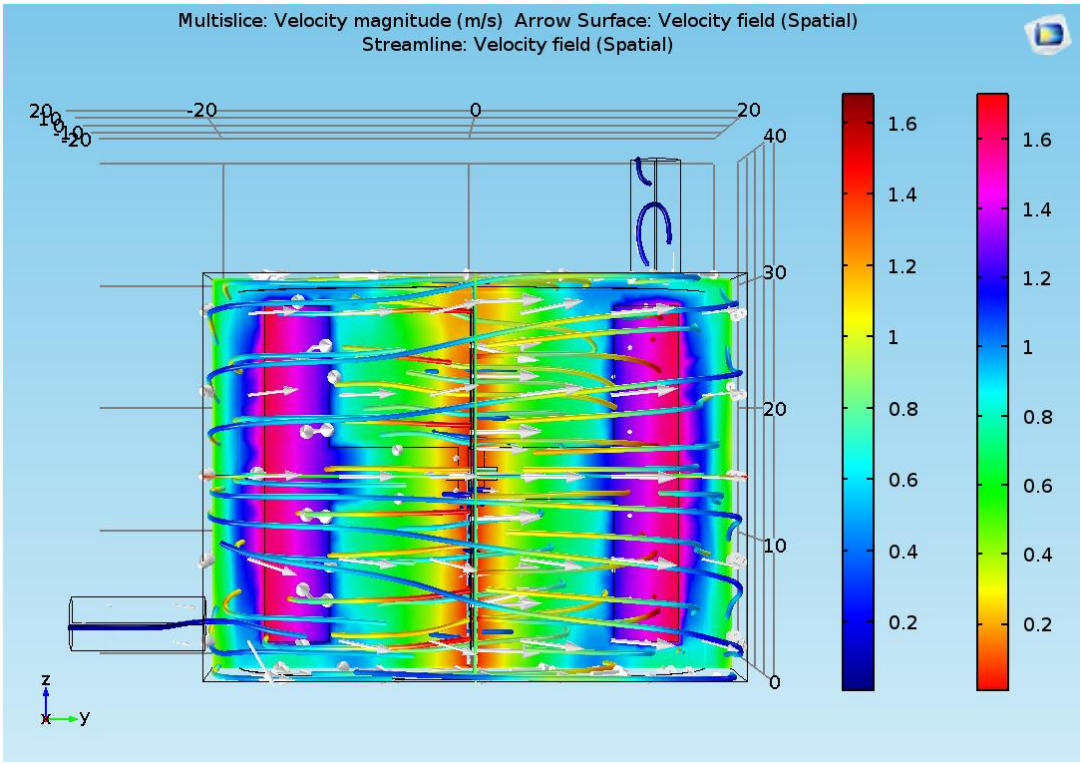

Figure C 39: YZ plot - 2 H shaped

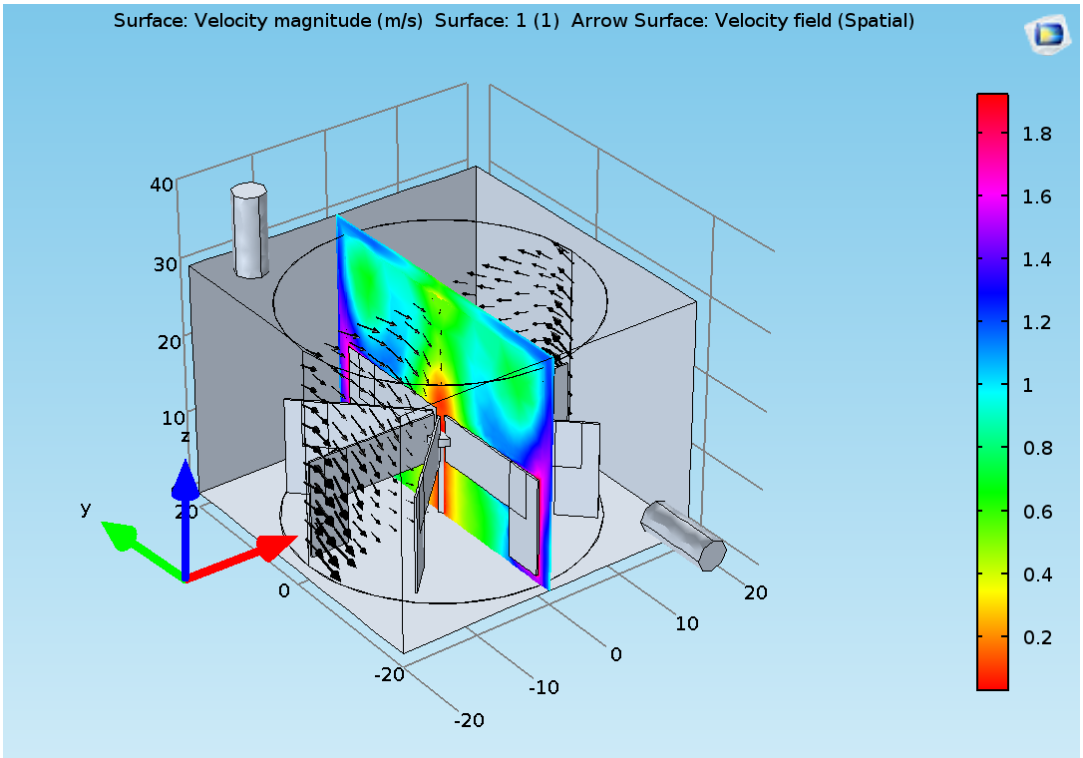

Figure C 40: Streamline slice plot – 4 inverted anchors

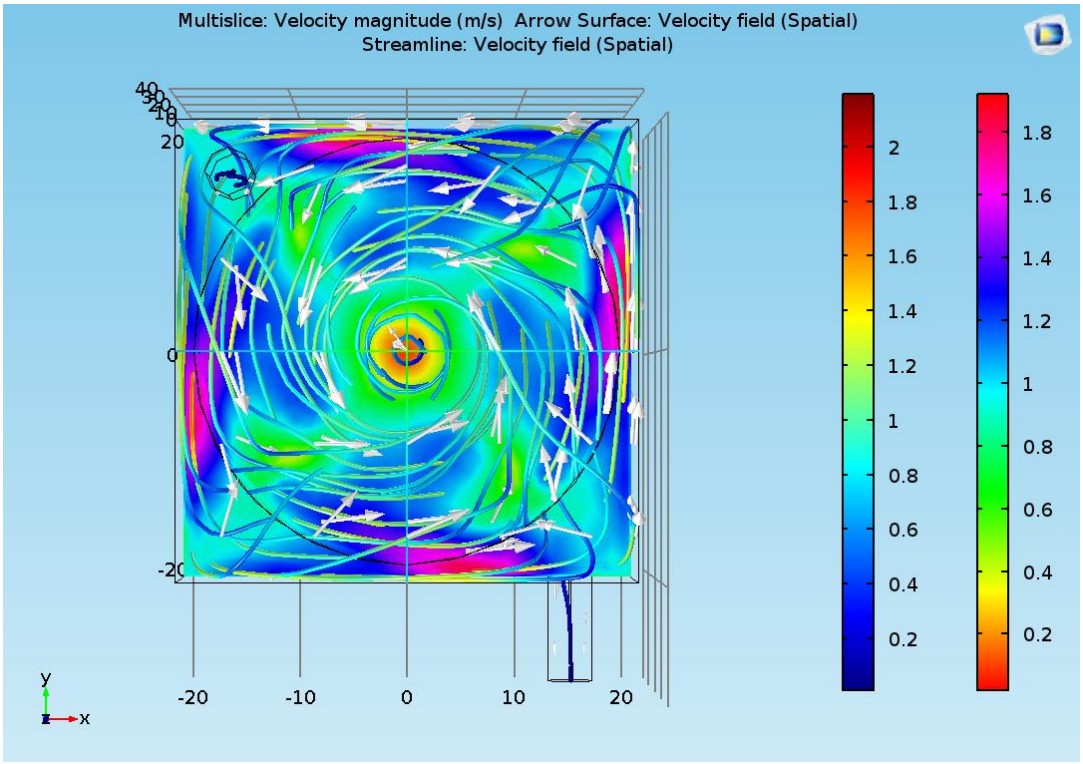

Figure C 41: XY plot - 4 inverted anchors

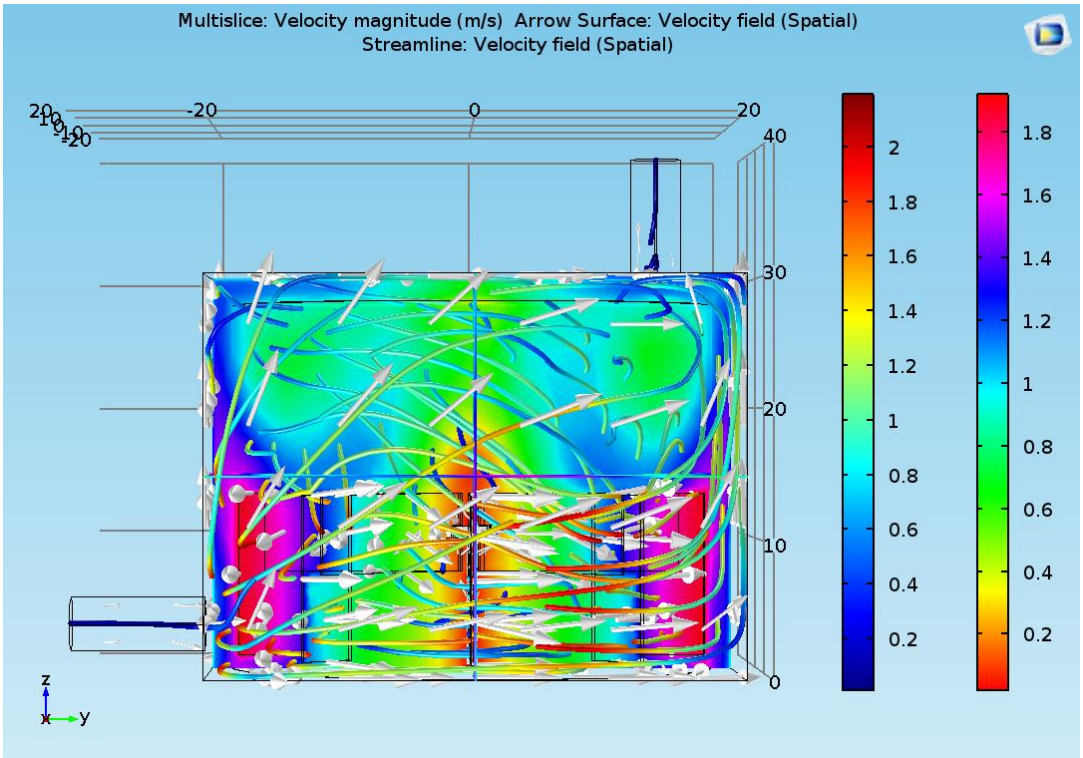

Figure C 42: YZ plot - 4 inverted anchors

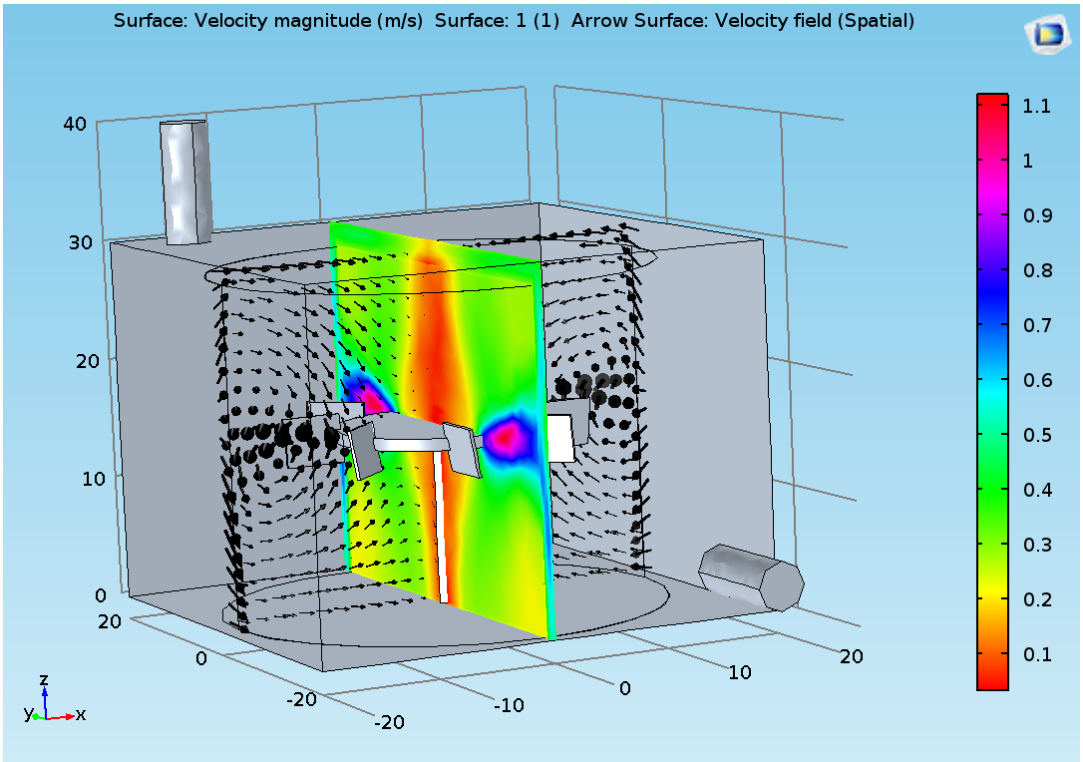

Figure C 43: Streamline slice plot - Angled 8-blade Rushton

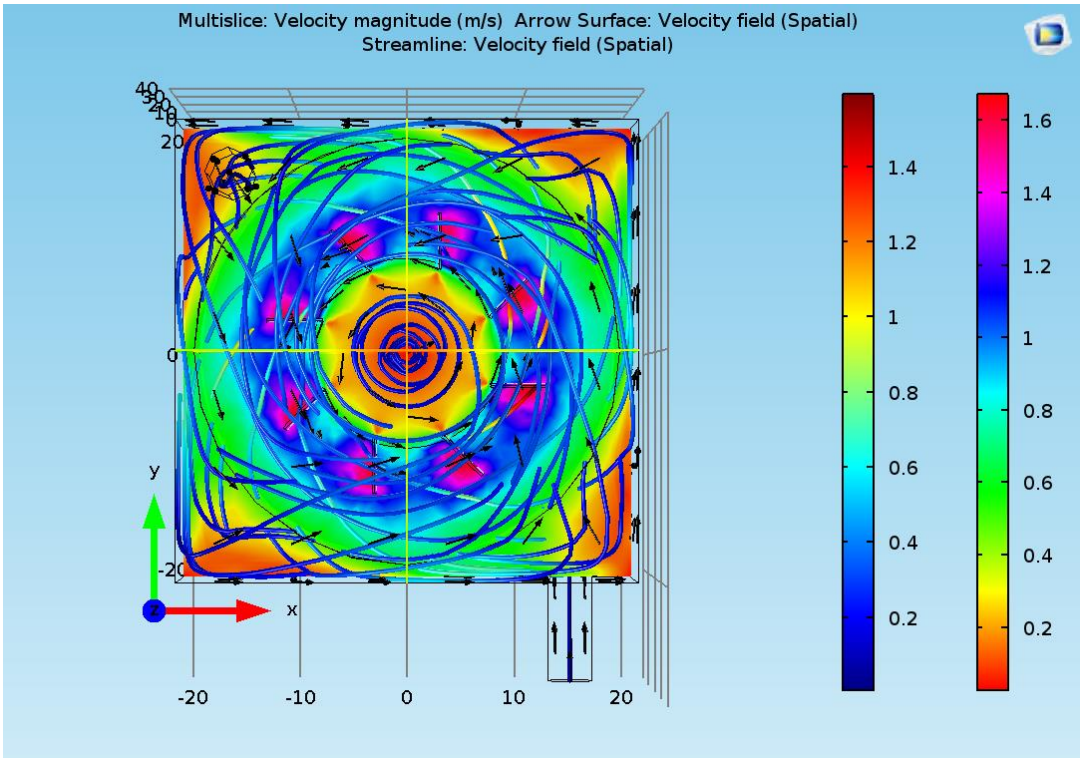

Figure C 44: XY plot- Angled 8-blade Rushton

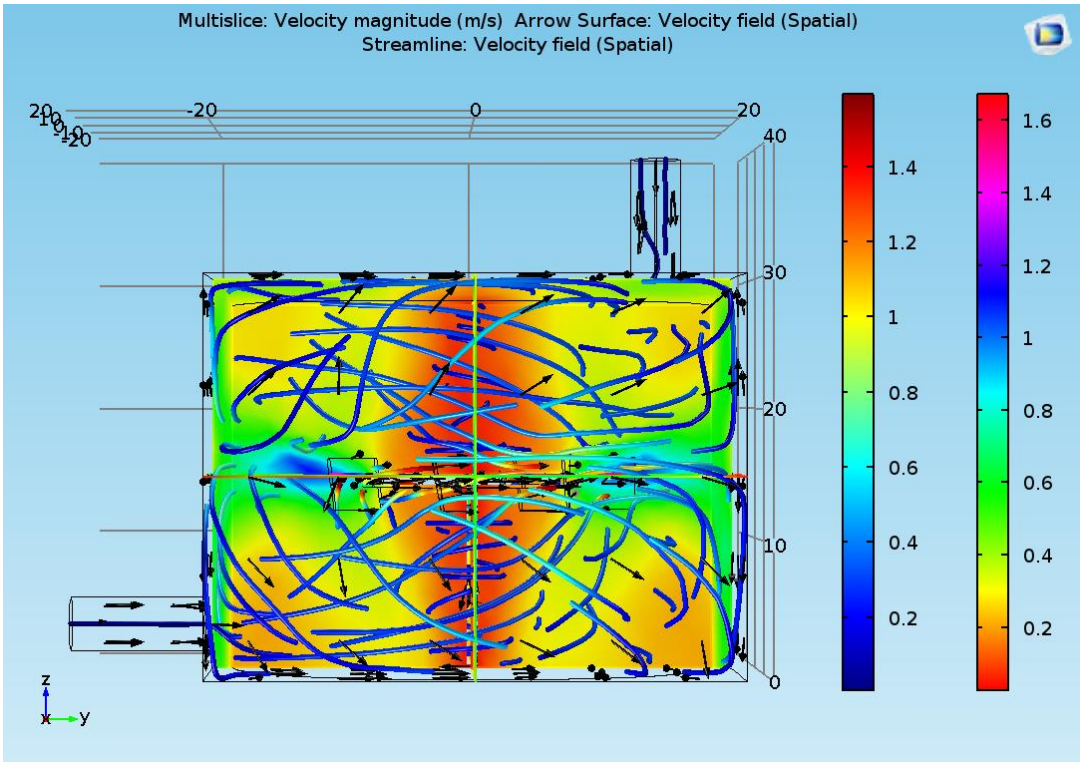

Figure C 45: YZ plot - Angled 8-blade Rushton

Appendix D: Actinometry in the SFPR and raw data of various products quantified with the HPLC

The procedure for preparing all the solutions required for actinometry was the same as mentioned in Appendix B, except that the required volumes were different as mentioned below.

Actinometry procedure

Ferrioxalate solution was prepared by dissolving 2.948 g of potassium ferrioxalate in 10 ml of 1N H_2SO_4 and diluting the solution to a final volume of 100 ml with water in dark. 5.5 ml of this ferrioxalate solution was mixed with 0.55 ml of 1N H_2SO_4 and 4.95 ml of DI water and transferred to one frame of the SFPR sandwiched between two Pyrex end plates. This frame was then placed 3 cm away from the illumination source. Upon illumination, 1 ml sample was taken from the SFPR at 1, 5 and 10 minutes of irradiation. The sample was then mixed with 0.5 ml sodium acetate buffer solution and 2 ml of 0.1 wt% 1,10-phenanthroline monohydrate and diluted to 50 ml with water in a dark bottle. Upon allowing a 45-55 minutes' reaction time in the dark, 1 ml of sample from each dark bottle was then withdrawn and its absorbance was measured using a CARY 300 UV-vis spectrophotometer at 510 nm.

Calculation

To calculate the photon flux, the number of moles of Fe^{2+} has to be first calculated using equation B1. A, the absorbance value of the sample used in

equation B1 was at 5 minutes. Photon flux could then be calculated using equation B2, where the illumination time, t was taken as 5 minutes.

Raw data of various products quantified with the HPLC

Concentration of various products at different sample times as quantified with the HPLC and the calculated actual concentration of the respective products are shown in the following tables (Table D1, Table D2, Table D3 and Table D4). The values given in these tables are the average values obtained from triplicates. It has to be noted that the volume of sample collected during each sample time was 20 ml, which was concentrated down to 1 ml and then analysed in the HPLC.

Time (minutes)	1	2	5	10	15	20	25	30	45	60	75	90	105	120	135	150	165	180
Concentration of glucose from HPLC (g/L)	8.92E-04	-	-	-	7.29E-04	-	8.36E-04	5.00E-04	-	-	-	1.88E-04	-	5.06E-04	-	-	-	-
Concentration of cellobiose from HPLC (g/L)	8.95E-04	-	1.74E-04	-	-	-	3.17E-04	7.32E-04	-	-	1.76E-04	2.64E-04	1.99E-04	4.71E-04	1.57E-04	-	-	-
Concentration of Fructose from HPLC (g/L)	1.14E-03	2.49E-04	-	-	-	4.79E-04	4.52E-04	6.57E-04	3.71E-04	3.24E-04	-	7.09E-04	2.95E-04	4.95E-04	2.65E-04	-	-	-
Concentration of anhydroglucose from HPLC (g/L)	1.31E-03	6.96E-04	5.05E-04	3.53E-04	3.91E-04	2.20E-04	-	1.98E-03	2.43E-04	1.32E-04	1.96E-04	4.73E-04	3.08E-04	1.53E-03	2.23E-04	6.56E-04	3.51E-04	8.81E-04
Concentration of D-Galactose from HPLC (g/L)	-	-	-	-	-	-	-	1.06E-04	-	-	1.90E-04	-	-	-	-	2.68E-04	-	-
Concentration of Acetic acid from HPLC (g/L)	-	9.63E-04	-	-	5.50E-04	-	-	5.52E-04	1.18E-03	8.06E-04	2.74E-04	2.96E-04	2.71E-04	7.94E-04	1.09E-03	1.01E-03	4.67E-04	2.04E-04
Concentration of Formic acid from HPLC (g/L)	7.37E-03	5.57E-03	1.97E-02	-	4.59E-03	1.56E-02	-	5.41E-03	7.08E-03	1.42E-02	3.27E-03	3.21E-03	6.14E-03	3.62E-03	7.31E-03	5.48E-03	5.76E-03	1.49E-02
Concentration of dihydroxyacetone from HPLC (g/L)	4.36E-04	1.79E-04	3.75E-04	3.16E-04	3.39E-04	2.59E-04	9.83E-04	2.54E-04	6.20E-04	-	-	-	3.26E-04	2.04E-04	4.44E-04	2.75E-04	-	-
Concentration of DMF from HPLC (g/L)	1.29E-04	-	-	-	-	-	-	4.71E-04	-	-	-	-	-	-	-	-	-	-
Concentration of Formaldehyde from HPLC (g/L)	7.27E-04	5.43E-04	1.01E-03	1.37E-03	6.81E-04	7.42E-04	4.35E-04	1.25E-03	6.47E-04	7.57E-04	7.76E-04	1.29E-03	6.63E-04	1.42E-03	1.10E-03	1.08E-03	6.26E-04	1.59E-03
Concentration of Sorbitol from HPLC (g/L)	-	-	-	-	2.34E-04	-	3.01E-04	-	-	-	3.49E-04	-	-	-	-	-	-	-
Concentration of Glycolaldehyde from HPLC (g/L)	-	-	2.93E-04	-	-	-	-	-	-	-	-	-	-	-	3.84E-04	2.31E-04	-	2.73E-04
Concentration of HMF from HPLC (g/L)	-	-	-	-	-	-	-	-	-	-	-	1.15E-03	-	1.99E-03	-	-	-	7.46E-04

Concentration of Xylose from HPLC (g/L)	-	-	-	-	-	-	-	-	-	-	-	-	-	-	-	8.73E-05	-	-
Concentration of Arabinose from HPLC (g/L)	-	-	-	-	-	-	-	-	-	-	-	-	-	-	-	1.18E-04	-	-
Glucose (uM)	0.20	-	-	-	0.16	-	0.19	0.11	-	-	-	0.04	-	0.11	-	-	-	-
Cellobiose (uM)	0.10	-	0.02	-	-	-	0.04	0.09	-	-	0.02	0.03	0.02	0.06	0.02	-	-	-
Fructose (uM)	0.25	0.06	-	-	-	0.11	0.10	0.15	0.08	0.07	-	0.16	0.07	0.11	0.06	-	-	-
Anhydroglucose (uM)	0.32	0.17	0.12	0.09	0.10	0.05	-	0.49	0.06	0.03	0.05	0.12	0.08	0.38	0.06	0.16	0.09	0.22
D-Galactose (uM)	-	-	-	-	-	-	-	0.02	-	-	0.04	-	-	-	-	0.06	-	-
Acetic acid (uM)	-	0.64	-	-	0.37	-	-	0.37	0.79	0.54	0.18	0.20	0.18	0.53	0.73	0.67	0.31	0.14
Formic acid (uM)	6.40	4.85	17.13	-	3.99	13.59	-	4.70	6.16	12.32	2.84	2.79	5.34	3.15	6.35	4.76	5.01	12.95
Dihydroxyacetone (uM)	0.19	0.08	0.17	0.14	0.15	0.12	0.44	0.11	0.28	-	-	-	0.14	0.09	0.20	0.12	-	-
DMF (uM)	0.05	-	-	-	-	-	-	0.20	-	-	-	-	-	-	-	-	-	-
Formaldehyde (uM)	0.97	0.72	1.35	1.83	0.91	0.99	0.58	1.66	0.86	1.01	1.03	1.72	0.88	1.89	1.46	1.44	0.84	2.11
Sorbitol (uM)	-	-	-	-	0.05	-	0.07	-	-	-	0.08	-	-	-	-	-	-	-
Glycolaldehyde (uM)	-	-	0.20	-	-	-	-	-	-	-	-	-	-	-	0.26	0.15	-	0.18
HMF (uM)	-	-	-	-	-	-	-	-	-	-	-	0.36	-	0.63	-	-	-	0.24
Xylose (uM)	-	-	-	-	-	-	-	-	-	-	-	-	-	-	-	0.02	-	-
Arabinose (uM)	-	-	-	-	-	-	-	-	-	-	-	-	-	-	-	0.03	-	-

Table D1: Raw data of various products formed during cellulose I photocatalysis in the SFPR with the plus shaped magnetic stirrer bar (green rows) and their calculated respective concentration (blue rows).

Time (minutes)	1	2	5	10	15	20	25	30	45	60	75	90	105	120	135	150	165	180
Concentration of glucose from HPLC (g/L)	5.88 E-04	2.64 E-04	6.94 E-04	-	2.03 E-03	4.14 E-04	2.19 E-04	4.67 E-04	1.04 E-03	4.79 E-04	2.55 E-04	6.42 E-04	2.95 E-04	2.74 E-04	5.40 E-04	8.42 E-04	-	1.81 E-04
Concentration of cellobiose from HPLC (g/L)	3.05 E-04	1.77 E-04	-	-	5.54 E-04	-	-	-	1.41 E-04	-	5.47 E-04	2.86 E-04	-	3.03 E-04	7.49 E-04	2.14 E-04	-	-
Concentration of Fructose from HPLC (g/L)	7.33 E-04	3.81 E-04	2.45 E-04	1.27 E-04	1.17 E-03	3.54 E-04	-	3.44 E-04	3.01 E-04	-	-	5.38 E-04	3.84 E-04	-	5.18 E-04	3.48 E-04	-	-
Concentration of anhydroglucose from HPLC (g/L)	1.10 E-03	8.81 E-04	1.26 E-03	6.30 E-04	1.54 E-03	4.47 E-04	5.04 E-04	3.64 E-04	1.09 E-03	6.60 E-04	9.22 E-04	1.45 E-03	8.36 E-04	1.49 E-03	1.55 E-03	4.36 E-04	8.91 E-04	9.66 E-04
Concentration of D-Galactose from HPLC (g/L)	-	-	-	-	-	-	-	-	-	-	-	-	-	-	-	-	1.26 E-04	1.56 E-04
Concentration of Erythrose from HPLC (g/L)	-	-	-	-	-	-	-	4.59 E-04	-	-	-	-	-	-	-	-	-	-
Concentration of Acetic acid from HPLC (g/L)	1.55 E-03	8.22 E-04	1.01 E-03	1.64 E-03	2.07 E-03	1.25 E-03	1.29 E-03	1.07 E-03	2.62 E-03	1.19 E-03	1.07 E-03	1.55 E-03	2.04 E-03	1.73 E-03	2.14 E-03	1.78 E-03	1.79 E-03	2.68 E-03
Concentration of Formic acid from HPLC (g/L)	1.82 E-02	1.37 E-02	1.58 E-02	2.09 E-02	2.03 E-02	7.94 E-03	1.10 E-02	1.35 E-02	1.10 E-02	2.30 E-02	1.78 E-02	1.37 E-02	1.31 E-02	2.54 E-02	1.87 E-02	2.13 E-02	1.76 E-02	1.00 E-02
Concentration of dihydroxyacetone from HPLC (g/L)	-	-	-	-	2.34 E-04	3.37 E-04	-	-	-	4.88 E-04	-	7.64 E-04	-	-	-	-	1.70 E-04	2.18 E-03
Concentration of DMF from HPLC (g/L)	-	-	-	-	-	-	-	-	-	-	-	-	-	-	2.60 E-04	-	-	-
Concentration of L-Sorbitol from HPLC (g/L)	1.64 E-04	-	-	-	-	-	9.65 E-05	1.36 E-04	-	-	1.53 E-04	-	-	1.72 E-04	1.94 E-04	-	-	2.70 E-04
Concentration of Glycolaldehyde from HPLC (g/L)	-	-	-	-	-	-	-	-	-	-	-	3.56 E-04	-	-	-	5.99 E-04	-	3.13 E-04
Concentration of Arabinose from HPLC (g/L)	-	-	-	-	-	-	-	1.49 E-04	-	-	-	-	-	-	-	-	-	-
Glucose (uM)	0.13	0.06	0.15	-	0.45	0.09	0.05	0.10	0.23	0.11	0.06	0.14	0.07	0.06	0.12	0.19	-	0.04
Cellobiose (uM)	0.04	0.02	-	-	0.06	-	-	-	0.02	-	0.06	0.03	-	0.04	0.09	0.03	-	-
Fructose (uM)	0.16	0.08	0.05	0.03	0.26	0.08	-	0.08	0.07	-	-	0.12	0.09	-	0.12	0.08	-	-
Anhydroglucose (uM)	0.27	0.22	0.31	0.16	0.38	0.11	0.12	0.09	0.27	0.16	0.23	0.36	0.21	0.37	0.38	0.11	0.22	0.24
D-Galactose (uM)	-	-	-	-	-	-	-	-	-	-	-	-	-	-	-	-	0.03	0.03

Erythrose (uM)	-	-	-	-	-	-	-	0.15	-	-	-	-	-	-	-	-	-	-
Acetic acid (uM)	1.04	0.55	0.67	1.09	1.38	0.84	0.86	0.71	1.74	0.79	0.72	1.03	1.36	1.15	1.43	1.19	1.20	1.79
Formic acid (uM)	15.82	11.92	13.72	18.19	17.62	6.91	9.52	11.72	9.58	19.98	15.51	11.95	11.38	22.08	16.29	18.53	15.34	8.71
Dihydroxyacetone (uM)	-	-	-	-	0.10	0.15	-	-	-	0.22	-	0.34	-	-	-	-	0.08	0.97
DMF (uM)	-	-	-	-	-	-	-	-	-	-	-	-	-	-	0.11	-	-	-
L-Sorbitol (uM)	0.04	-	-	-	-	-	0.02	0.03	-	-	0.03	-	-	0.04	0.04	-	-	0.06
Glycolaldehyde (uM)	-	-	-	-	-	-	-	-	-	-	-	0.24	-	-	-	0.40	-	0.21
Arabinose (uM)	-	-	-	-	-	-	-	0.04	-	-	-	-	-	-	-	-	-	-

Table D2: Raw data of various products formed during cellulose II photocatalysis in the SFPR with the plus shaped magnetic stirrer bar (green rows) and their calculated respective concentration (blue rows).

Time (minutes)	1	2	5	10	15	20	25	30	45	60	75	90	105	120	135	150	165	180
Concentration of glucose from HPLC (g/L)	5.41 E-04	1.43 E-03	-	-	-	-	-	-	-	1.96 E-04	-	-	-	-	-	1.62 E-04	-	-
Concentration of cellobiose from HPLC (g/L)	-	2.54 E-04	-	-	-	-	-	-	-	-	-	-	-	-	-	-	-	-
Concentration of Fructose from HPLC (g/L)	2.03 E-04	1.11 E-03	-	3.00 E-04	-	1.61 E-04	9.73 E-04	3.50 E-04	9.02 E-04	2.28 E-04	-	-	2.00 E-04	3.43 E-04	-	4.57 E-04	2.27 E-04	-
Concentration of anhydroglucose from HPLC (g/L)	3.18 E-04	1.89 E-03	4.43 E-04	5.74 E-04	9.20 E-04	3.98 E-04	4.81 E-04	7.69 E-04	2.87 E-03	5.40 E-04	3.50 E-04	-	5.25 E-04	5.37 E-04	4.43 E-04	3.62 E-03	7.62 E-04	1.55 E-03
Concentration of D-Galactose from HPLC (g/L)	-	5.52 E-04	-	-	-	-	-	-	-	-	-	-	-	-	-	-	-	8.31 E-04
Concentration of Erythrose from HPLC (g/L)	-	-	-	-	-	-	-	-	-	-	-	-	-	-	-	-	-	-
Concentration of Acetic acid from HPLC (g/L)	2.65 E-04	1.27 E-03	1.87 E-03	4.07 E-04	1.39 E-03	3.49 E-04	2.30 E-03	5.93 E-04	6.10 E-04	7.20 E-04	9.47 E-04	1.85 E-03	1.40 E-03	5.70 E-04	3.31 E-03	8.11 E-04	1.23 E-03	1.74 E-03
Concentration of Formic acid from HPLC (g/L)	5.30 E-03	1.43 E-02	7.59 E-03	-	3.00 E-03	1.26 E-02	9.17 E-03	-	-	2.84 E-02	1.14 E-02	1.44 E-02	1.40 E-02	5.81 E-03	9.40 E-03	1.13 E-02	1.03 E-02	8.29 E-03
Concentration of dihydroxyacetone from HPLC (g/L)	2.14 E-04	1.06 E-03	2.32 E-04	8.08 E-04	8.06 E-04	-	6.94 E-04	1.30 E-03	1.14 E-03	2.13 E-03	6.06 E-04	7.62 E-04	3.66 E-04	1.20 E-03	1.45 E-04	3.75 E-04	2.20 E-04	6.24 E-04
Concentration of Pyruvaldehyde from HPLC (g/L)	-	-	-	-	-	-	-	-	-	-	-	-	1.11 E-04	-	-	-	-	-
Concentration of DMF from HPLC (g/L)	-	-	-	-	-	-	-	-	-	-	-	-	-	-	-	2.21 E-04	-	-
Concentration of Formaldehyde from HPLC (g/L)	6.01 E-04	-	5.60 E-04	-	-	-	4.93 E-04	1.98 E-03	2.23 E-04	-	-	-	2.44 E-03	4.03 E-04	9.80 E-04	1.65 E-03	9.79 E-04	1.29 E-03
Concentration of L-sorbitol from HPLC (g/L)	-	-	-	1.29 E-04	-	-	-	-	-	-	-	-	-	-	-	-	-	-
Concentration of Glycolaldehyde from HPLC (g/L)	-	-	-	-	-	-	-	-	-	-	-	-	-	4.02 E-04	-	2.65 E-04	-	-
Glucose (uM)	0.12	0.32	-	-	-	-	-	-	-	0.04	-	-	-	-	-	0.04	-	-
Cellobiose (uM)	-	0.03	-	-	-	-	-	-	-	-	-	-	-	-	-	-	-	-
Fructose (uM)	0.05	0.25	-	0.07	-	0.04	0.22	0.08	0.20	0.05	-	-	0.04	0.08	-	0.10	0.05	-
Anhydroglucose (uM)	0.08	0.47	0.11	0.14	0.23	0.10	0.12	0.19	0.71	0.13	0.09	-	0.13	0.13	0.11	0.89	0.19	0.38

D-Galactose (uM)	-	0.12	-	-	-	-	-	-	-	-	-	-	-	-	-	-	-	0.18
Erythrose (uM)	-	-	-	-	-	-	-	-	-	-	-	-	-	-	-	-	-	-
Acetic acid (uM)	0.18	0.84	1.25	0.27	0.93	0.23	1.53	0.40	0.41	0.48	0.63	1.23	0.93	0.38	2.21	0.54	0.82	1.16
Formic acid (uM)	4.61	12.42	6.60	-	2.61	10.97	7.98	-	-	24.67	9.90	12.53	12.20	5.05	8.18	9.85	8.96	7.21
Dihydroxyacetone (uM)	0.10	0.47	0.10	0.36	0.36	-	0.31	0.58	0.51	0.94	0.27	0.34	0.16	0.53	0.06	0.17	0.10	0.28
Pyruvaldehyde (uM)	-	-	-	-	-	-	-	-	-	-	-	-	0.06	-	-	-	-	-
DMF (uM)	-	-	-	-	-	-	-	-	-	-	-	-	-	-	-	0.09	-	-
Formaldehyde (uM)	0.80	-	0.75	-	-	-	0.66	2.64	0.30	-	-	-	3.26	0.54	1.31	2.21	1.31	1.72
L-sorbitol (uM)	-	-	-	0.03	-	-	-	-	-	-	-	-	-	-	-	-	-	-
Glycolaldehyde (uM)	-	-	-	-	-	-	-	-	-	-	-	-	-	0.27	-	0.18	-	-

Table D3: Raw data of various products formed during cellulose I photocatalysis in the SFPR with the Rushton impeller (green rows) and their calculated respective concentration (blue rows).

Time (minutes)	1	2	5	10	15	20	25	30	45	60	75	90	105	120	135	150	165	180
Concentration of glucose from HPLC (g/L)	8.30 E-04	-	6.78 E-04	-	-	-	-	3.52 E-04	-	-	-	-	-	-	-	-	6.69 E-04	-
Concentration of cellobiose from HPLC (g/L)	-	-	-	-	-	-	-	-	-	-	-	-	-	-	-	-	-	-
Concentration of Fructose from HPLC (g/L)	9.54 E-04	1.39 E-03	4.26 E-04	-	3.16 E-04	2.37 E-04	1.98 E-04	-	-	3.73 E-04	-	5.62 E-04	1.78 E-04	3.05 E-04	5.31 E-04	5.97 E-04	1.84 E-03	4.42 E-04
Concentration of anhydroglucose from HPLC (g/L)	3.06 E-03	3.88 E-03	2.38 E-03	2.12 E-04	3.21 E-03	3.71 E-04	2.99 E-04	5.91 E-04	4.92 E-04	4.11 E-04	2.32 E-04	1.17 E-03	1.31 E-03	9.90 E-04	2.02 E-03	9.57 E-04	2.00 E-03	6.73 E-04
Concentration of D-Galactose from HPLC (g/L)	-	-	-	-	2.02 E-04	-	-	-	-	-	-	-	1.84 E-04	-	-	6.11 E-04	-	-
Concentration of Erythrose from HPLC (g/L)	3.71 E-04	-	-	4.51 E-04	-	-	-	-	-	-	-	-	-	-	-	-	-	-
Concentration of Acetic acid from HPLC (g/L)	3.73 E-03	2.14 E-03	7.31 E-04	2.52 E-03	9.33 E-04	2.13 E-04	2.15 E-03	7.26 E-04	7.71 E-04	2.62 E-03	1.48 E-03	3.47 E-03	1.74 E-03	2.61 E-03	3.86 E-03	5.92 E-03	4.74 E-03	5.36 E-03
Concentration of Formic acid from HPLC (g/L)	3.86 E-02	1.22 E-02	6.27 E-03	1.18 E-02	8.92 E-03	-	1.77 E-02	1.23 E-02	7.04 E-03	2.52 E-02	8.89 E-03	8.25 E-03	3.90 E-03	1.74 E-02	1.41 E-02	3.17 E-02	2.05 E-02	2.81 E-02
Concentration of dihydroxyacetone from HPLC (g/L)	2.19 E-04	-	-	4.04 E-04	-	1.25 E-04	-	6.73 E-04	-	-	3.66 E-04	6.67 E-04	4.01 E-04	-	4.99 E-04	9.35 E-04	2.23 E-04	-
Concentration of Pyruvaldehyde from HPLC (g/L)	-	-	-	-	-	-	-	-	-	-	-	2.91 E-04	-	-	-	-	-	-
Concentration of DMF from HPLC (g/L)	-	-	-	-	-	-	-	-	-	-	-	-	-	-	-	1.45 E-04	-	-
Concentration of Formaldehyde from HPLC (g/L)	6.51 E-04	8.89 E-04	-	8.60 E-04	-	1.16 E-04	4.13 E-04	-	-	7.04 E-04	7.22 E-04	-	-	8.83 E-04	3.22 E-04	1.61 E-03	1.36 E-03	1.25 E-03
Concentration of L-sorbitol from HPLC (g/L)	-	-	-	-	-	-	-	1.11 E-04	-	-	-	-	-	-	-	-	-	-
Concentration of Glycolaldehyde from HPLC (g/L)	-	-	-	-	-	-	-	-	-	-	-	-	-	-	-	2.41 E-04	-	-
Glucose (uM)	0.18	-	0.15	-	-	-	-	0.08	-	-	-	-	-	-	-	-	0.15	-
Cellobiose (uM)	-	-	-	-	-	-	-	-	-	-	-	-	-	-	-	-	-	-
Fructose (uM)	0.21	0.31	0.09	-	0.07	0.05	0.04	-	-	0.08	-	0.12	0.04	0.07	0.12	0.13	0.41	0.10
Anhydroglucose (uM)	0.76	0.96	0.59	0.05	0.79	0.09	0.07	0.15	0.12	0.10	0.06	0.29	0.32	0.24	0.50	0.24	0.49	0.17

D-Galactose (uM)	-	-	-	-	0.04	-	-	-	-	-	-	-	0.04	-	-	0.14	-	-
Erythrose (uM)	0.12	-	-	0.15	-	-	-	-	-	-	-	-	-	-	-	-	-	-
Acetic acid (uM)	2.48	1.43	0.49	1.68	0.62	0.14	1.43	0.48	0.51	1.75	0.99	2.31	1.16	1.74	2.57	3.94	3.16	3.57
Formic acid (uM)	33.55	10.65	5.46	10.29	7.75	-	15.43	10.71	6.12	21.92	7.73	7.17	3.39	15.09	12.30	27.55	17.81	24.47
Dihydroxyacetone (uM)	0.10	-	-	0.18	-	0.06	-	0.30	-	-	0.16	0.30	0.18	-	0.22	0.42	0.10	-
Pyruvaldehyde (uM)	-	-	-	-	-	-	-	-	-	-	-	0.16	-	-	-	-	-	-
DMF (uM)	-	-	-	-	-	-	-	-	-	-	-	-	-	-	-	0.06	-	-
Formaldehyde (uM)	0.87	1.19	-	1.15	-	0.15	0.55	-	-	0.94	0.96	-	-	1.18	0.43	2.15	1.81	1.66
L-sorbitol (uM)	-	-	-	-	-	-	-	0.02	-	-	-	-	-	-	-	-	-	-
Glycolaldehyde (uM)	-	-	-	-	-	-	-	-	-	-	-	-	-	-	-	0.16	-	-

Table D4: Raw data of various products formed during cellulose II photocatalysis in the SFPR with the Rushton impeller (green rows) and their calculated respective concentration (blue rows).

Appendix E: Full text of papers published or accepted for publication.

Journal of Photochemistry and Photobiology A: Chemistry 334 (2017) 13–19

Contents lists available at ScienceDirect

Journal of Photochemistry and Photobiology A: Chemistry

journal homepage: www.elsevier.com/locate/jphotochem

Comparative assessment of visible light and UV active photocatalysts by hydroxyl radical quantification

Sanjay Nagarajan[a,*], Nathan C. Skillen[a], Federica Fina[b], Guan Zhang[b], Chamnan Randorn[b], Linda A. Lawton[c], John T.S. Irvine[b], Peter K.J. Robertson[a,*]

[a] Centre for the Theory and Application of Catalysis (CenTACat), School of Chemistry and Chemical Engineering, Queen's University Belfast, David Keir Building, Stranmillis Road, Belfast BT9 5AG, United Kingdom
[b] JTSI Group, University of St. Andrews, School of Chemistry, Purdie Building, North Haugh, St Andrews, KY16 9ST, United Kingdom
[c] School of Pharmacy and Life Sciences, Sir Ian Wood Building Robert Gordon University, Garthdee Road, Aberdeen AB10 7GJ, United Kingdom

ARTICLE INFO

Article history:
Received 28 September 2016
Received in revised form 25 October 2016
Accepted 27 October 2016
Available online 3 November 2016

Keywords:
Photocatalyst
Visible light photocatalysts
OH radical
Coumarin
P25

ABSTRACT

A simple method for determining hydroxyl radical yields on semiconductor photocatalysts is highly desirable, especially when comparing different photocatalyst materials. This paper reports the screening of a selection of visible light active photocatalysts such as Pt-C_3N_4, 5% LaCr doped $SrTiO_3$, $Sr_{0.95}Cr_{0.05}TiO_3$ and Yellow TiO_2 and compares them against WO_3 and ultra violet (UV) light activated TiO_2 P25 (standard commercial catalysts) based on their oxidative strengths (OH radical producing capability) using a well-studied chemical probe–coumarin. 7-hydroxycoumarin, the only fluorescent hydroxylation product of this reaction can then be measured to indirectly quantify the OH radicals produced. P25 under UV light produced the highest concentration of OH radicals (16.9 μM), followed by WO_3 (0.56 μM) and Pt-C_3N_4 (0.25 μM). The maximum OH radical production rate for P25, WO_3 and Pt-C_3N_4 were also determined and found to be 35.6 μM/hr, 0.28 μM/h and 0.88 μM/h respectively. The other visible light activated photocatalysts did not produce any OH radicals primarily as a result of their electronic structure. Furthermore, it was concluded that, if any visible light absorbing photocatalysts are to be fabricated in future for the purpose of photocatalytic oxidation, their OH radical producing rates (and quantities) should be determined and compared to P25.

1. Introduction

Photocatalysis has gained significant interest since the early publication by Fujishima and Honda in 1972, demonstrating the potential of splitting water over TiO_2 [1]. Since this publication, photocatalysis has been applied to a broad range of fields including waste water treatment, microbe destruction, toxin removal, energy production and air treatment. [2–8]. The mechanism of photocatalysis has been well documented and can be generally represented by the equations shown in reactions 1–9 [9,10]. The formation of surface radical species such as superoxide ($O_2^{\cdot-}$) and hydroxyl radicals ($OH^{\cdot}$) play a key role in a number of photocatalytic pathways and as such their identification and quantification is a key consideration. As shown in reaction 2, OH radicals are primarily generated from the reaction between valence band holes (h_{vb+}) and hydroxyl ions on the catalyst surface. An indirect pathway, *via* $O_2^{\cdot-}$, also results in OH radical formation, as shown in reactions 3–6. The efficiency of OH radicals in photocatalytic reactions is predominantly based on their strong oxidising potential of 2.8 V (vs NHE) [11]. The non-selective nature of these reactive oxygen species also aids rapid degradation of various pollutants and organic contaminants [3,7,11–16].

$$Photocatalyst + h\nu \rightarrow h_{vb^+} + e_{cb^-} \quad (1)$$

$$h_{vb^+} + OH^- (or H_2O) \rightarrow OH^{\cdot} \quad (2)$$

$$e_{cb^-} + O_2 \rightarrow O_2^{\cdot-} \quad (3)$$

$$O_2^{\cdot-} + H^+ \rightarrow HO_2^{\cdot} \quad (4)$$

* Corresponding authors.
E-mail addresses: snagarajan01@qub.ac.uk (S. Nagarajan), p.robertson@qub.ac.uk (P.K.J. Robertson).

http://dx.doi.org/10.1016/j.jphotochem.2016.10.034
1010-6030/

$$HO_2 + HO_2 \rightarrow H_2O_2 + O_2 \quad (5)$$

$$H_2O_2 + e_{cb^-} \rightarrow OH^{\cdot} + OH^- \quad (6)$$

$$O_2^{\cdot-} + reactants \rightarrow products \quad (7)$$

$$substrates + {\cdot}OH \rightarrow products \quad (8)$$

$$e_{cb^-} + OH^{\cdot} \rightarrow OH^- \quad (9)$$

where, h_{vb}^+ represents VB holes and e_{cb}^- means CB electrons.

Newly developed photocatalytic technologies and materials have often utilised model compounds and screening methods to assess their performance [17–20]. Common evaluation methods reported in the literature include the decomposition of dyes such as methylene blue (ISO test 10678:2010), or degradation of organic pollutants such as 4-chlorophenol or toluene [17–20]. These procedures are often coupled with the corresponding calculated photonic efficiencies and quantum yields to evaluate overall efficiency. While these methods can be effective in identifying the specific photocatalytic performance of a material in relation to a fingerprint compound, they provide little information regarding the production of OH radicals involved within the mechanism. Therefore, the requirement for a simple and robust method of radical quantification for screening the oxidative potential of catalysts has significantly increased. The challenge in OH radical quantification lies in both the non-selective nature and short lifetime (~1 ns) of the radical, which restricts the possibility of direct quantification [21]. Consequently, a range of methods have been developed such as emission spectroscopy, laser induced fluorescence, electron spin resonance, spin trap and chemical probes or quencher based methods to quantify OH radicals [21–37].

The use of a chemical probe to capture OH radicals presents a potentially efficient way to measure the radical due to the low cost, rapid analysis time and reproducibility of the method. Monitoring a probe compound through spectroscopy allows the concentration of OH radicals to be calculated based on stoichiometric ratios of products formed. A recently reported *in vivo* technique utilised a nanoprobe comprising of a nanoparticle and azo dye in order to quantify OH radicals in the femtomolar range [37]. Here the nanoparticle was used as an energy donor and the modified orange was used as an OH radical capturing ligand molecule (and the energy acceptor).

Dimethyl sulfoxide (DMSO) based methods for OH radical capture have also been utilised in the past to quantify these species *via* the formation of formaldehyde [28,29,31]. The formation of CH_4 in a closed system coupled with O_2 bubbling however reduces the suitability of utilising DMSO as a probe molecule.

In the past, OH radical quantification has been carried out for various commercially available photocatalysts, photo-Fenton's reaction and other modified TiO_2 based visible light photocatalysts with either coumarin or terepthalic acid as probe molecules [21,23,31–36,38,39]. Both compounds are capable of acting as OH radical traps by forming fluorescent products as result of reacting with the radical species. Terepthalic acid has been investigated in a study by Ishibashi et al. who achieved an OH radical concentration of 7×10^{-5} M based on the measurement of 2-hydroxyterepthalic acid [35]. In addition to the use of terepthalic acid as a probe molecule, coumarin has been used in a number of studies to determine the concentration of OH radicals produced from TiO_2 at relatively high loadings of 1 to 5 g/L [21,23,40]. For instance, Czili et al. used 100 μM coumarin as the probe molecule to capture OH radicals under a 40 W UV lamp. They determined a maximum OH radical production rate of 23.39 μM/g/h (calculated from their reported 7-hydroxycoumarin rates) with 1 g/L TiO_2 P25 photocatalyst.

This paper utilises coumarin as a hydroxyl radical trap and reports the screening of a selection of visible light responsive photocatalysts under low power illumination based on their OH radical producing capability. In contrast to previous reports, which concentrated on quantifying the OH radicals produced from TiO_2, other commercially available and a few synthesised photocatalysts [21,23,31,40], this work focusses on assessing the oxidative strength of visible light photocatalytsts Pt-C_3N_4, 5% LaCr doped $SrTiO_3$, $Sr_{0.95}Cr_{0.05}TiO_3$ (referred to as Cr-$SrTiO_3$ from here on) and yellow TiO_2 and compares them against commercial TiO_2 P25 and WO_3 for evaluation. In addition, a low catalyst loading was used to highlight efficient OH radical formation can be achieved without requiring large quantities of powdered catalyst.

2. Experimental procedure

2.1. Materials

Coumarin and 7-hydroxycoumarin were purchased from Tokyo Chemical Industry UK Ltd, while TiO_2 P25 was purchased from Degussa (now Evonik industries) and WO_3 nano powders were purchased from Sigma Aldrich. All commercial chemicals were used as received. The catalysts Pt-C_3N_4 [41], 5% LaCr doped $SrTiO_3$, Cr-$SrTiO_3$ and yellow TiO_2 [42] were synthesised at the school of chemistry, University of St. Andrews, using methods cited in the literature [41–43].

2.2. Characterisation of photocatalysts

WO_3, LaCr-$SrTiO_3$ and Cr-$SrTiO_3$ were characterised by X-Ray diffraction (XRD) and UV–vis absorption. XRD analysis of powders was examined on a STOe STADI/P powder diffractometer. Incident radiation was generated using a Cu k_α source (λ = 1.54056 Å). Diffuse reflectance spectra were collected on a JASCO-V550 UV–vis spectrophotometer. The characterisation of Pt-C_3N_4 and yellow TiO_2 has been reported elsewhere in literature [41,42].

2.3. Photocatalytic experiments

All photocatalytic experiments were performed in closed screw cap bottles. The reaction solution was composed of 100 ml of 100 μM coumarin along with 10 mg of photocatalyst (0.1 g/L). A magnetic stirrer bar was placed inside the bottle and the bottle was then placed on a magnetic stirrer at a distance of 11 cm from a 36 W compact fluorescent non-integrated visible lamp (Philips, colour code 830) or a 36 W UV lamp (Philips, Cleo lamps). The spectral outputs of the lamps were measured by a StellaNet spectrometer and the spectra are shown in the Supplementary material (Fig. S1). Prior to illumination, the reaction solution was stirred in the dark to allow a state of equilibrium to be reached. The length of time required in the dark was calculated from the control experiments conducted in the absence of light. During irradiation, samples (3 ml) were taken at dedicated time intervals for a maximum of 120 mins. Samples were filtered through a 0.22 μm Millex syringe filter prior to analysis. Coumarin absorbance was monitored using a Cary 300 Scan, UV–vis Spectrophotometer at 277 nm, with a scan rate of 400 nm/min. 7-hydroxycoumarin fluorescence was measured in a PerkinElmer LS 50 B luminescence spectrophotometer,

using an excitation wavelength of 332 nm and emission wavelength at 456 nm [21]. The excitation and emission slit width was 4 mm and the scan rate was 200 nm/min. A sample UV/Visible and fluorimeter spectra, with peaks at 277 nm and 456 nm respectively, are shown in the Supplementary material Fig. S2 and Fig. S3. All experiments were performed in triplicate.

2.4. OH radical quantification

OH radicals were quantified based on a modified method described by Zhang *et al.* [38] and according to Eq. (1). The concentration of OH radicals was calculated by assuming that 6.1% of total OH radicals were captured as 7-hydroxycoumarin. The stoichiometric ratio of one mole of OH radical consumed for the production of one mole of 7-hydroxycoumarin was used [23]. The total number of OH radicals produced over time during this photocatalytic process was calculated using the following equation.

$$X = \left\{ \frac{A}{6.1\%} - B \right\} \quad (1)$$

Where, X is the total OH radical concentration (μM) produced during photocatalysis, A is the mean 7-hydroxycoumarin concentration (μM) and B is the amount of OH radicals (μM) produced during the light control experiments. The concentration of coumarin and 7-hydroxycoumarin was calculated using a standard curve of known concentrations as shown in the Supplementary material (Fig. S4, Fig. S5 and Fig. S6).

3. Results and discussion

3.1. Characterisation of photocatalysts

XRD patterns of WO_3, Cr-$SrTiO_3$ and LaCr-$SrTiO_3$ samples were determined as shown (Fig. 1). The commercial WO_3 nanoparticles exhibited a typical crystallized monoclinic phase structure, and the Cr-doped and La,Cr-co-doped $SrTiO_3$ samples possessed homogeneous crystallized cubic perovskite structures, with no impurity phase found for either of the doped samples and these results were consistent with literature [44,45]. In the co-doped samples, since La and Cr substitute the Sr and Ti, respectively, and the radius of La is similar with that of Sr while the radius of Cr was similar to that of Ti, the peak positions of the Cr-$SrTiO_3$ and LaCr-$SrTiO_3$ samples are not shifted compared to those of pure $SrTiO_3$.

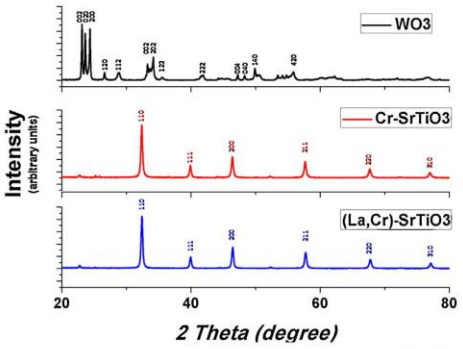

Fig. 1. XRD profiles of photocatalysts representing the plane indices [44,45].

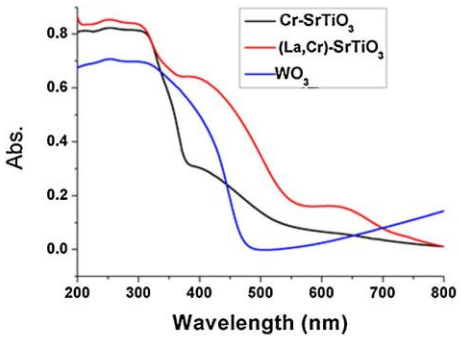

Fig. 2. UV–vis absorption spectra of photocatalysts.

In the UV–vis absorption spectra of WO_3, Cr-$SrTiO_3$ and LaCr-$SrTiO_3$ (Fig. 2), WO_3 exhibited visible light absorption up to 470 nm, which corresponds to the band-gap energy of ca. 2.64 eV. $SrTiO_3$, however, has no absorption in the visible light region (bandgap of 3.75 eV) and metal-doping has been shown to be a feasible method for extending the light absorption of $SrTiO_3$ into the visible region [46]. Doping of Cr into the A-site of $SrTiO_3$ induces an absorption band in the visible region centred at around 450 nm (Fig. 2). The visible light absorption is ascribed to the electron excitation from the Cr doping levels formed above the valence band of $SrTiO_3$ to the conduction band of $SrTiO_3$ [43]. It was reported that La, Cr-co-doped $SrTiO_3$ showed enhanced photocatalytic performance compared to the single Cr-doped $SrTiO_3$ due to the inhibition of the formation of Cr^{6+} species in the B site [43]. Therefore, a co-doped sample, LaCr-$SrTiO_3$ was prepared by the same method. The visible light absorption of LaCr-$SrTiO_3$ was significantly enhanced compared to the Cr-$SrTiO_3$, with two strong absorption peaks centred at around 450 nm and 650 nm in the visible light region. In the case of co-doping, more intermittent doping levels are formed within the band-gap of $SrTiO_3$ compared to the single Cr doped $SrTiO_3$, which results in the visible light absorption.

3.2. Photocatalytic OH radical production

3.2.1. UV light photocatalysis on P25

P25 has been one of the most extensively investigated and most active commercially available photocatalysts under UV irradiation and therefore was used as a benchmark for comparison in this study. Although, recent studies have reported that nano-spherical $InCrO_4$-loaded TiO_2 and TiO_2 nanospheres deposited on graphene performed better than P25 for OH radical production and dye degradation upon UV irradiation [47,48], to date P25 is still regarded as the benchmark. The photocatalytic hydroxylation of coumarin over P25 under UV light and subsequent formation of 7-hydroxycoumarin is shown in Fig. 3. The production of 7-hydroxycoumarin under these conditions equates to a peak OH radical concentration of 16.9 μM after 45 mins.

As shown in the figure, near complete degradation (97%) of coumarin was achieved after 120 mins irradiation. This level of degradation was likely to result from the increased adsorption of coumarin onto the catalyst, which facilitated the reaction with surface bound OH radicals. The role of surface bound radicals and those that are present in bulk has been highlighted in a previous publication by Li et al. [49], who investigated acid orange oxidation over TiO_2 P25 and AgBr. This group investigated the quenching of

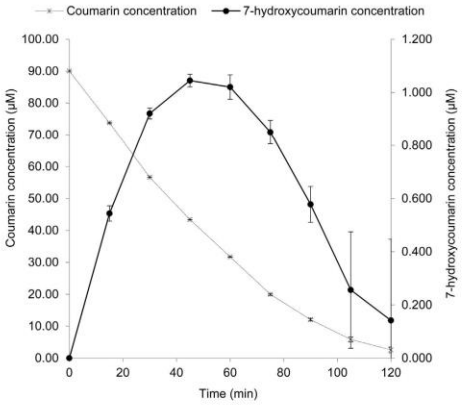

Fig. 3. Coumarin and 7-hydroxycoumarin profiles of 100 ml of 100 μM coumarin with 0.1 g/L P25 under 36 W UV light.

OH radicals at the catalyst surface and in bulk in order to demonstrate that surface bound species were the predominant radicals in the oxidation pathway. This observation confirmed that increased adsorption of the substrate on the catalyst surface can significantly increase the degradation efficiency.

Fig. 3 also shows the profile of 7-hydroxycoumarin production and decomposition which indirectly indicates the quantity of OH radicals generated. 7-hydroxycoumarin concentration peaked at 45 min, with a maximum concentration of 1.045 μM, which was equivalent to 16.9 μM OH radicals (as calculated from Eq. (1)). It was observed that an average production rate of 1.8 μM/h was achieved during the first 45 mins, followed by an average degradation rate of 0.46 μM/h during the latter stages of irradiation. The decrease in concentration of 7-hydroxycoumarin could also be attributed to the presence of superoxide radicals as reported by Czili and Horvath [23].

Several reports have suggested the kinetics for 7-hydroxycoumarin generation from coumarin with P25 under UV irradiation are zero order [21,23,38,50–52], however, a number of these investigations also used a high concentration of both catalyst and coumarin. Furthermore, it has been suggested that at higher concentrations of coumarin (>100 μM), more UV light is absorbed by this probe and not the catalyst, which results in a low 7-hydroxycoumarin and OH radical production rate [23]. In the present study, K_{app} which is the rate constant for the formation of 7-hydroxycoumarin was calculated to be 0.0234 μM/min whereas K_{dis}, the rate constant for the disappearance of 7-hydroxycoumarin was calculated to be 0.0135 μM/min. In this study we have established that both, production and degradation of 7-hydroxycoumarin followed zero order kinetics, which is agreement with previous studies.

3.2.2. Visible light photocatalysis

A number of visible light catalysts were also selected for comparison against P25 TiO_2. While the synthesised catalysts all possessed energy band gaps that supported visible light activation, only WO_3 and Pt-C_3N_4 had energy band potentials (valence band at 3.2 V and 1.4 V respectively and conduction band at 0.2 V and −1.3 V respectively) that would facilitate OH radical formation either directly or indirectly as mentioned in reactions 2–6. Catalysts LaCr-$SrTiO_3$, Cr-$SrTiO_3$ and yellow TiO_2 (valence bands at 2.7 V, 2.7 V and 2.6 V respectively and conduction bands at −0.1 V for all the three photocatalysts) were selected to monitor if 7-hydroxycoumarin was formed even when the electronic structure of the catalyst was not suited to the redox potential of the reaction.

The photocatalytic hydroxylation of coumarin to 7-hydroxycoumarin over WO_3 and Pt-C_3N_4 under visible light is shown in Fig. 4. As can be seen, minimal conversion of coumarin was observed over both Pt-C_3N_4 and WO_3, which was also supported by the low formation of 7-hydroxycoumarin (Fig. 5). Pt-C_3N_4 displayed a slow yet steady conversion rate, reaching a 0.91% drop in coumarin after 120 mins of irradiation whereas, a varying coumarin concentration pattern was seen over time on WO_3. It is interesting to note that there was an initial decrease in coumarin concentration followed by an increase which may be attributed to coumarin desorption from the surface of WO_3. This desorption could be a result of the alteration in equilibrium in the closed system due to the possible evolution of O_2 from water on WO_3 under visible light.

While the decrease in coumarin concentration is low, production of OH radicals over Pt-C_3N_4 and WO_3 was supported by the detection of 7-hydroxycoumarin upon photocatalysis (Fig. 5).

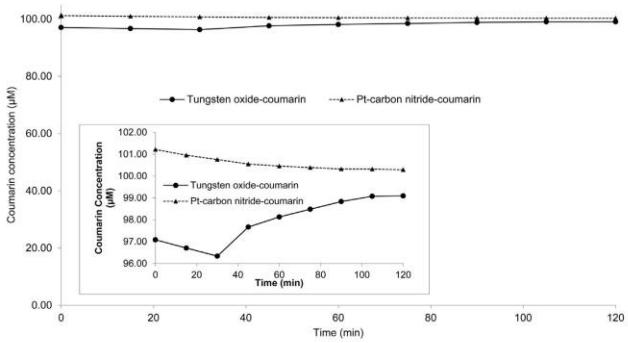

Fig. 4. Coumarin profiles of 100 ml of 100 μM coumarin with 0.1 g/L visible light photocatalysts; Inset: coumarin profiles of WO_3 and Pt-C_3N_4.

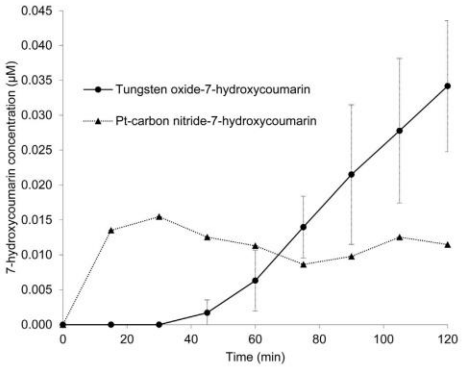

Fig. 5. 7-hydroxycoumarin production profiles of 100 ml of 100 μM coumarin with 0.1 g/L visible light photocatalysts.

When WO_3 was used as the photocatalyst, there was no 7-hydroxycoumarin production until 30 min of irradiation which could be due to the rapid recombination of the electrons and the photo generated holes. After 30 min, OH radical production was steady with a gradual generation of 7-hydroxycoumarin being observed. In the case of Pt-C_3N_4 however, 7-hydroxycoumarin production was seen from 15 min. The initial increase in the 7-hydroxycoumarin concentration correlates to a rapid degradation of coumarin during the first 60 mins of irradiation.

In contrast to Pt-C_3N_4 and WO_3, the catalysts LaCr-$SrTiO_3$, Cr-$SrTiO_3$ and yellow TiO_2 displayed no activity towards coumarin conversion to 7-hydroxycoumarin, which indicates no OH radical formation. Furthermore, under prolonged visible light irradiation no detectable 7-hydroxycoumarin was recorded.

3.2.3. Influence of photocatalysts' electronic structure and particle size on OH radical formation

In order to evaluate and discuss the performance of the catalysts, it is essential to consider the primary contributing factors; electronic structure and particle size. The electronic structure of the catalysts dictates the initial photo-excitation of electrons to higher energy levels, while the particle size dictates the concentration of photons absorbed and surface reactions between coumarin and OH radicals. As shown in reactions (2)–(6), OH radicals can occur *via* two routes in photocatalysis. The direct formation at the valence band requires a redox potential of 2.8 V vs NHE, while the indirect method occurs *via* the intermediate radical, $O_2^{\cdot-}$ and requires a redox potential of −0.33 V vs NHE [53]. The electronic structure of the catalysts tested in this study, in relation to the redox potentials required for radical formation, are shown in Fig. 6.

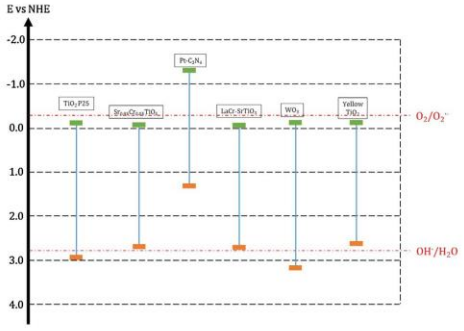

Fig. 6. Electronic structure of the photocatalysts used.

As Fig. 6 shows, catalysts TiO_2 P25, Pt-C_3N_4 and WO_3 possess an electronic structure which corresponds to the redox potential of OH radical formation *via* either direct or indirect mechanisms. The favourable electronic structure of TiO_2 for OH radical formation has been well documented and is evident from the results highlighted here. The performance of Pt-C_3N_4 and WO_3 for OH radical formation, however, has not been as well reported. The structure of WO_3 with a more positive valence band suggests it is capable of generating surface OH radicals, however, the results obtained indicate minimal 7-hydroxycoumarin production within 2 h. Based on the structure, it was likely an increased rate of recombination preventing OH radical formation *via* the valence band hole, due to insufficient energy to initiate a reduction reaction at the conduction band [21]. To prevent recombination and to increase the OH radical production, Kim et al. synthesised Pt-doped WO_3 and found that the OH radical production from Pt-WO_3 was significantly higher than un-doped WO_3 [20]. Furthermore, the large particle size of approximately 100 nm for WO_3 indicates a smaller surface area, which leads to minimum absorption of light.

The electronic structure of Pt-C_3N_4 as seen from Fig. 6 clearly indicates a reducing catalyst, which is also supported by its application in water reduction investigations [54]. Therefore, the hydroxylation of coumarin and subsequent formation of 7-hydroxycoumarin, as indicated by the earlier results, is likely *via* the indirect $O_2^{\cdot-}$ pathway. Based upon this observation, it is likely the low yield of OH radicals is a result of competition for the conduction band electron between superoxide formation and H^+ reduction to form H_2 (0 V vs NHE). In addition, since all these experiments were performed in a closed system with limited O_2, a reducing catalyst such as Pt-C_3N_4 is expected to produce less OH radicals than an open system. Furthermore, despite a favourable particle size of 20–40 nm, Pt-C_3N_4 was observed to agglomerate to form larger aggregates leading to a decrease in surface area and in turn light absorption.

In the case of LaCr-$SrTiO_3$, Cr-$SrTiO_3$ and yellow TiO_2, the electronic structures showed both the valence band and conduction band of all these catalysts to be lower than the redox potentials to facilitate radical formation as seen in Fig. 6. These catalysts were primarily used as a control parameter to ensure no 7-hydroxycoumarin formation was observed.

The calculated OH radical concentrations and production rates produced over all catalysts screened are summarised in Table 1. The results show that the activity of the visible light activated photocatalysts studied were significantly lower than commercial P25 under UV light. This further emphasises that although there are numerous visible light absorbing photocatalysts, their ability to produce OH radicals is significantly lower than P25. In future, if any visible light absorbing photocatalysts are to be fabricated for the purpose of photocatalytic oxidation, their OH radical producing rates (and quantities) should be determined and compared to P25 as demonstrated here.

4. Conclusion

The aim of screening UV and visible light absorbing photocatalysts to assess their oxidative strength was accomplished successfully by trapping OH radicals produced by the photocatalysts in 7-hydroxycoumarin. The OH radical production

Table 1
Pseudo maximum OH radical production rates and quantities.

Photocatalyst	Light Source	Maximum OH radical concentration (μM)	Time at which maximum concentration of OH radical was produced (min)	Maximum OH radical production rate (μM/h)
P25	UV	16.9	45	35.654
WO_3	visible	0.560	120	0.280
Pt-C_3N_4	visible	0.254	30	0.886

capabilities of various photocatalysts covering a range of band gaps and particle sizes were assessed by comparing and discussing their differences with the commercial UV light activated P25. To conclude, visible light activated photocatalysts such as LaCr-$SrTiO_3$, Cr-$SrTiO_3$ and yellow TiO_2 did not produce any OH radicals and this could be attributed to their electronic structure. Whereas, the (pseudo) maximum OH radical production rates of other visible light activated photocatalysts namely, WO_3 (0.28 μM/h) and Pt-C_3N_4 (0.886 μM/h) were found to be significantly lower when compared to the commercial UV light activated P25 photocatalyst (35.654 μM/h). This method could be further exploited as novel photocatalysts are developed and to compare a range of P25 concentrations for OH radical production. This study further emphasises the challenges faced by the visible light photocatalysts for photocatalytic oxidation.

Acknowledgements

This work was supported by the Engineering and Physical Sciences Research Council (Project number EP/K036769/1), Robert Gordon University's IDEAS PhD studentship and Queen's University Belfast's PhD studentship. The author would also like to thank Professor A Prasanna de Silva, School of Chemistry and Chemical Engineering, Queen's University Belfast, for his valuable contribution during the progress meetings. Supporting data are openly available on Queen's University, Belfast Research Portal, http://pure.qub.ac.uk/portal/en/datasets/search.html.

References

[1] A. Fujishima, K. Honda, Electrochemical photolysis of water at a semiconductor electrode, Nature 238 (1972) 37–38.
[2] D.W. Bahnemann, L.A. Lawton, P.K.J. Robertson, The application of semiconductor photocatalysis for the removal of cyanotoxins from water and design concepts for solar photocatalytic reactors for large scale water treatment, in: S.L. Suib (Ed.), New and Future Developments in Catalysis, 1st ed., Elsevier, Amsterdam, 2013, pp. 395–415.
[3] M.R. Hoffmann, S.T. Martin, W. Choi, D.W. Bahnemann, Environmental applications of semiconductor photocatalysis, Chem. Rev. 95 (1995) 69–96.
[4] P.K.J. Robertson, J.M.C. Robertson, D.W. Bahnemann, Removal of microorganisms and their chemical metabolites from water using semiconductor photocatalysis, J. Hazard. Mater. 211–212 (2012) 161–171.
[5] H. Kominami, S. Murakami, M. Kohno, Y. Kera, K. Okada, B. Ohtani, Stoichiometric decomposition of water by titanium(IV) oxide photocatalyst synthesized in organic media: effect of synthesis and irradiation conditions on photocatalytic activity, Phys. Chem. Chem. Phys. 3 (2001) 4102–4106.
[6] C. McCullagh, P.K.J. Robertson, M. Adams, P.M. Pollard, A. Mohammed, Development of a slurry continuous flow reactor for photocatalytic treatment of industrial waste water, J. Photochem. Photobiol. A 211 (2010) 42–46.
[7] P.K.J. Robertson, Semiconductor photocatalysis: an environmentally acceptable alternative production technique and effluent treatment process, J. Clean. Prod. 4 (1996) 203–212.
[8] M. Adams, I. Campbell, C. McCullagh, D. Russell, D.W. Bahnemann, P.K.J. Robertson, From ideal reactor concepts to reality: the novel drum reactor for photocatalytic wastewater treatment, Int. J. Chem. React. Eng. 11 (2013) 621–632.
[9] O. Carp, C.L. Huisman, A. Reller, Photoinduced reactivity of titanium dioxide, Prog. Solid State Chem. 32 (2004) 33–177.
[10] C. McCullagh, N. Skillen, M. Adams, P.K.J. Robertson, Photocatalytic reactors for environmental remediation: a review, J. Chem. Technol. Biotechnol. 86 (2011) 1002–1017.
[11] J. Jiang, Z. Zhou, V.K. Sharma, Occurrence transportation, monitoring and treatment of emerging micro-pollutants in waste water–a review from global views, Microchem. J. 110 (2013) 292–300.
[12] A. Asghar, A.A. Abdul Raman, W.M.A. Wan Daud, Advanced oxidation processes for in-situ production of hydrogen peroxide/hydroxyl radical for textile wastewater treatment: a review, J. Clean. Prod. 87 (2015) 826–838.
[13] H. Fan, G. Li, F. Yang, L. Yang, S. Zhang, Photodegradation of cellulose under UV light catalysed by TiO2, J. Chem. Technol. Biotechnol. 86 (2011) 1107–1112.
[14] E. Szabó-Bárdos, K. Somogyi, N. Törő, G. Kiss, A. Horváth, Photocatalytic decomposition of l-phenylalanine over TiO2: Identification of intermediates and the mechanism of photodegradation, Appl. Catal. B Environ. 101 (2011) 471–478.
[15] T. Hirakawa, K. Yawata, Y. Nosaka, Photocatalytic reactivity for O2- and OH radical formation in anatase and rutile TiO2 suspension as the effect of H2O2 addition, Appl. Catal. A Gen. 325 (2007) 105–111.
[16] Y. Nosaka, T. Daimon, A.Y. Nosaka, Y. Murakami, Singlet oxygen formation in photocatalytic TiO2 aqueous suspension, Phys. Chem. Chem. Phys. 6 (2004) 2917–2918.
[17] X. Yan, T. Ohno, K. Nishijima, R. Abe, B. Ohtani, Is methylene blue an appropriate substrate for a photocatalytic activity test? A study with visible-light responsive titania, Chem. Phys. Lett. 429 (2006) 606–610.
[18] B. Ohtani, Preparing articles on photocatalysis–beyond the illusions misconceptions, and speculation, Chem. Lett. 37 (2008) 216–229.
[19] A. Mills, An overview of the methylene blue ISO test for assessing the activities of photocatalytic films, Appl. Catal. B Environ. 128 (2012) 144–149.
[20] J. Kim, C.W. Lee, W. Choi, Platinized WO3 as an environmental photocatalyst that generates OH radicals under visible light, Environ. Sci. Technol. 44 (2010) 6849–6854.
[21] Q. Xiang, J. Yu, P.K. Wong, Quantitative characterization of hydroxyl radicals produced by various photocatalysts, J. Colloid Interface Sci. 357 (2011) 163–167.
[22] M. Sato, T. Ohgiyama, J.S. Clements, Formation of chemical species and their effects on microorganisms using a pulsed high voltage discharge in water, Ind. Appl. Soc. Annu. Meet. 2 (1994) 1455–1461.
[23] H. Czili, A. Horváth, Applicability of coumarin for detecting and measuring hydroxyl radicals generated by photoexcitation of TiO2 nanoparticles, Appl. Catal. B Environ. 81 (2008) 295–302.
[24] R. Ono, T. Oda, Measurement of hydroxyl radicals in pulsed corona discharge, J. Electrost. 55 (2002) 333–342.
[25] W. Hoeben, E. van Veldhuizen, W. Rutgers, G. Kroesen, Gas phase corona discharges for oxidation of phenol in an aqueous solution, J. Phys. D Appl. Phys. 32 (1999) 133–137.
[26] P. Sunka, V. Babický, M. Clupek, P. Lukes, M. Simek, J. Schmidt, M. Cern, Generation of chemically active species by electrical discharges in water, Plasma Sources Sci. Technol. 8 (1999) 258–265.
[27] B. Sun, M. Sato, J. Sid Clements, Optical study of active species produced by a pulsed streamer corona discharge in water, J. Electrost. 39 (1997) 189–202.
[28] M.G. Steiner, C.F. Babbs, Quantitation of the hydroxyl radical by reaction with dimethyl sulfoxide, Arch. Biochem. Biophys. 278 (1990) 478–481.
[29] M. Sahni, B.R. Locke, Quantification of hydroxyl radicals produced in aqueous phase pulsed electrical discharge reactors, Ind. Eng. Chem. Res. 45 (2006) 5819–5825.
[30] J. Ku, E. Zimowski, United States department of labor occupational safety and health administration. 3 M formaldehyde monitor (Model 3721), Prod. Eval. (PE-10) 205 (1989).
[31] S.A.V. Eremia, D. Chevalier-Lucia, G. Radu, J. Marty, Optimization of hydroxyl radical formation using TiO2 as photocatalyst by response surface methodology, Talanta 77 (2008) 858–862.
[32] T. Maezono, M. Tokumura, M. Sekine, Y. Kawase, Hydroxyl radical concentration profile in photo-fenton oxidation process: generation and consumption of hydroxyl radicals during the discoloration of azo-dye orange II, Chemosphere 82 (2011) 1422–1430.
[33] M. Tokumura, R. Morito, R. Hatayama, Y. Kawase, Iron redox cycling in hydroxyl radical generation during the photo-fenton oxidative degradation: dynamic change of hydroxyl radical concentration, Appl. Catal. B Environ. 106 (2011) 565–576.
[34] S. Kanazawa, T. Furuki, T. Nakaji, S. Akamine, R. Ichiki, Measurement of OH radicals in aqueous solution produced by atmospheric-pressure LF plasma jet, Int. J. PEST 6 (2012) 166–171.
[35] K. Ishibashi, A. Fujishima, T. Watanabe, K. Hashimoto, Quantum yields of active oxidative species formed on TiO2 photocatalyst, J. Photochem. Photobiol. A 134 (2000) 139–142.
[36] T. Hirakawa, Y. Nosaka, Properties of O2.- and OH. formed in TiO2 aqueous suspensions by photocatalytic reaction and the influence of H2O2 and some ions, Langmuir 18 (2002) 3247–3254.

[37] Z. Li, T. Liang, S. Lv, Q. Zhuang, Z. Liu, A rationally designed upconversion nanoprobe for in vivo detection of hydroxyl radical, J. Am. Chem. Soc. 137 (2015) 11179–11185.
[38] J. Zhang, Y. Nosaka, Quantitative detection of OH radicals for investigating the reaction mechanism of various visible-light TiO2 photocatalysts in aqueous suspension, J. Phys. Chem. C 117 (2013) 1383–1391.
[39] M.E. Lindsey, M.A. Tarr, Quantitation of hydroxyl radical during Fenton oxidation following a single addition of iron and peroxide, Chemosphere 41 (2000) 409–417.
[40] J. Zhang, Y. Nosaka, Generation of OH radicals and oxidation mechanism in photocatalysis of WO3 and BiVO4 powders, J. Photochem. Photobiol. A 303–304 (303) (2015) 53––.
[41] F. Fina, H. Menard, J.T.S. Irvine, The effect of Pt NPs crystallinity and distribution on the photocatalytic activity of Pt-g-C3N4, Phys. Chem. Chem. Phys. 17 (2015) 13929–13936.
[42] C. Randorn, J.T.S. Irvine, P. Robertson, Synthesis of visible-light-activated yellow amorphous photocatalyst, Int. J. Photoenergy 2008 (2008) 1–6.
[43] S. Ouyang, H. Tong, N. Umezawa, J. Cao, P. Li, Y. Bi, Y. Zhang, J. Ye, Surface-alkalinization-Induced enhancement of photocatalytic H2 evolution over srTiO3-based photocatalysts, J. Am. Chem. Soc. 134 (2012) 1974–1977.
[44] M. Muralidharan, V. Anbarasu, A. Elaya Perumal, K. Sivakumar, Carrier mediated ferromagnetism in Cr doped SrTiO3 compounds, J. Mater. Sci. Mater. Electron. 26 (2015) 6352–6365.
[45] J. Guo, Y. Li, S. Zhu, Z. Chen, Q. Liu, D. Zhang, W. Moon, D. Song, Synthesis of WO3@Graphene composite for enhanced photocatalytic oxygen evolution from water, RSC Adv. 2 (2012) 1356–1363.
[46] K. van Benthem, C. Elsässer, R.H. French, Bulk electronic structure of SrTiO3: Experiment and theory, J. Appl. Phys. 90 (2001) 6156–6164.
[47] J. Kamalakkannan, V.L. Chandraboss, S. Prabha, S. Senthilvelan, Advanced construction of heterostructured InCrO4-TiO2 and its dual properties of greater UV-photocatalytic and antibacterial activity, RSC Adv. 5 (2015) 77000–77013.
[48] M. Wojtoniszak, B. Zielinska, R.J. Kalenczuk, E. Mijowska, Photocatalytic performance of titania nanospheres deposited on graphene in coumarin oxidation reaction, Mater. Sci. Pol. 30 (2012) 32–38.
[49] G. Li, K.H. Wong, X. Zhang, C. Hu, J.C. Yu, R.C.Y. Chan, P.K. Wong, Degradation of acid orange 7 using magnetic AgBr under visible light: the roles of oxidizing species, Chemosphere 76 (2009) 1185–1191.
[50] J. Zhang, Y. Nosaka, Mechanism of the OH radical generation in photocatalysis with TiO2 of different crystalline types, J. Phys. Chem. C 118 (2014) 10824–10832.
[51] H. Guan, L. Zhu, H. Zhou, H. Tang, Rapid probing of photocatalytic activity on titania-based self-cleaning materials using 7-hydroxycoumarin fluorescent probe, Anal. Chim. Acta 608 (2008) 73–78.
[52] Z. Huang, Q. Sun, K. Lv, Z. Zhang, M. Li, B. Li, Effect of contact interface between TiO2 and g-C3N4 on the photoreactivity of g-C3N4/TiO2 photocatalyst: (0 1) vs (1 0 1) facets of TiO2, Appl. Catal. B Environ. 164 (2015) 420–427.
[53] P.M. Wood, The potential diagram for oxygen at pH 7, Biochem. J. 253 (1988) 287–289.
[54] G. Zhang, Z. Lan, L. Lin, S. Lin, X. Wang, Overall water splitting by Pt/g-C3N4 photocatalysts without using sacrificial agents, Chem. Sci. 7 (2016) 3062–3066.

Chemical Engineering Journal 313 (2017) 301–308

Contents lists available at ScienceDirect

Chemical Engineering Journal

journal homepage: www.elsevier.com/locate/cej

Mixing regime simulation and cellulose particle tracing in a stacked frame photocatalytic reactor

Sanjay Nagarajan [a,*], Lorenzo Stella [a,b], Linda A. Lawton [c], John T.S. Irvine [d], Peter K.J. Robertson [a,*]

[a] Centre for the Theory and Application of Catalysis (CenTACat), School of Chemistry and Chemical Engineering, Queen's University Belfast, David Keir Building, Stranmillis Road, Belfast BT9 5AG, United Kingdom
[b] Atomistic Simulation Centre (ASC), School of Mathematics and Physics, Queen's University Belfast, University Road, Belfast BT7 1NN, United Kingdom
[c] School of Pharmacy and Life Sciences, Sir Ian Wood Building Robert Gordon University, Garthdee Road, Aberdeen AB10 7GJ, United Kingdom
[d] JTSI Group, University of St. Andrews, School of Chemistry, Purdie Building, North Haugh, St Andrews KY16 9ST, United Kingdom

HIGHLIGHTS

- A novel reactor for photocatalytic cellulose breakdown was designed.
- Eight blade Rushton impeller was compared against a stirrer bar.
- Mixing regime and particle tracing simulations were performed using COMSOL.
- Particle tracing simulations confirmed the superiority of the Rushton impeller.

GRAPHICAL ABSTRACT

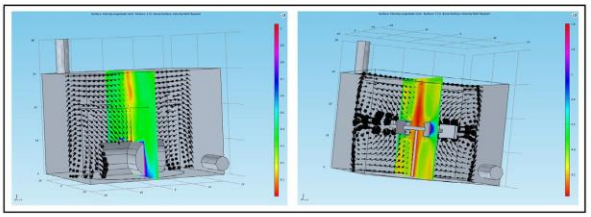

ARTICLE INFO

Article history:
Received 20 July 2016
Received in revised form 1 December 2016
Accepted 4 December 2016
Available online 7 December 2016

Keywords:
Photocatalysis
COMSOL
Fermentable sugars
Mixing
Simulation

ABSTRACT

To sustainably meet the global energy demand, unconventional methods to produce renewable energy must emerge. Biofuels from cellulose (via fermentable sugar production) mediated via photocatalysis provides an alternative to conventional fossil fuels. In order to effectively drive photocatalytic processes an effective reactor design is required, the design of which is influenced by a number of key factors such as the catalyst to reactant ratio and residence time, catalyst illumination time, light penetration and distribution for the system, mass transfer limitations (mixing) and product recovery. In this study we use COMSOL Multiphysics® to simulate and assess one of the mentioned parameters – mixing regime of cellulose particles in a Stacked Frame Photocatalysis Reactor (SFPR). In the reactor design, we compare two mixers: a 'plus' shaped magnetic stirrer bar and an 8 blade Rushton impeller. The simulations reveal that the Rushton impeller offers a radial mixing pattern with a higher fluid velocity of 1.2 m/s when compared to the stirrer bar that offers a fluid velocity of 0.9 m/s. Cellulose particle tracing simulations confirm that the particle dispersion is superior in the case of the Rushton impeller as the vorticity generated during the mixing push the particles to the reactor's walls. Since the particles are forced towards the walls, there is a probability of more particles being illuminated than in the case of no or improper mixing.

1. Introduction

Fossil fuel depletion and raising greenhouse gas emissions have increased the need for alternative renewable energy technologies. Along with solar energy, wind energy and tidal energy, biofuels

* Corresponding authors.
E-mail addresses: snagarajan01@qub.ac.uk (S. Nagarajan), p.robertson@qub.ac.uk (P.K.J. Robertson).

http://dx.doi.org/10.1016/j.cej.2016.12.016
1385-8947/

could also contribute to the global clean energy production. Biofuel production could be brought about from various sources such as waste vegetable oil, food waste, animal fats, algae and cellulose. Among these sources, cellulose is the most attractive raw material as it is the world's most abundant organic material [1]. However, cellulose as such cannot be used directly as a fuel and has to be converted to fermentable sugars which can then lead to the production of bio alcohols via fermentation. Conventionally, cellulose hydrolysis has been achieved through environmentally unfavourable, high energy consuming physico-chemical methods such as steam explosion, pyrolysis or acid/alkali hydrolysis [2]. A potential new route for cellulose breakdown using photocatalysis could be an alternative, more sustainable method to breakdown the cellulose molecule to smaller carbohydrate species [3]. Photocatalysis is a light driven chemical reaction. When light of a specific wavelength with energy greater than or equal to band gap energy illuminates a photocatalyst, an electron from the valence band (VB) gets promoted to the conduction band (CB) leaving behind a positive hole in the VB. These positive holes react with water or OH^- to form hydroxyl radicals which can carry out oxidation reactions such as break down of cellulose.

Conventional reactors for chemical engineering are well established and classified, whereas photocatalytic reactor designs are relatively new [4]. In addition to the conventional reactor design parameters such as reactor geometry, mixer configuration, mode of operation (continuous or batch), separation efficiency, residence time, reaction selectivity, materials of construction and cost, the following parameters with respect to illumination need to be considered while designing a photocatalytic reactor [5],

(i) Type of illumination source
(ii) Output power of the light source
(iii) Spectral distribution
(iv) Maintenance
(v) Inclusion of reflectors, mirrors and windows
(vi) Construction materials to facilitate light transmission

Furthermore, the illumination source also influences the choice of materials for reactor construction. When external ultraviolet (UV) light sources are used for photocatalysis, expensive fused silica (quartz) is the primary choice of material for the reactor vessel as standard glass is not fully transparent to UV radiation, especially at wavelengths less than 400 nm. Pyrex glass, which is a cheaper alternative may, however, be used under near UV illumination (350–400 nm) or for visible light photocatalysis. When illumination sources are deployed within the reactor, the unit is made of materials such as aluminium or stainless steel (for reflection and light distribution), however Pyrex or quartz lamp housing units will still be required. A range of light sources that could be used to illuminate the TiO_2 photocatalytic system is summarised in Table 1. In addition, sample spectra of two commonly used UV lamps (500 W Xenon lamp and 36 W fluorescent UV lamps) are shown in Fig. 1.

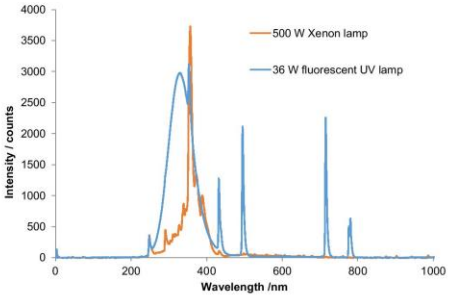

Fig. 1. Lamp spectra of a 500 W Xenon lamp and a 36 W fluorescent UV lamp.

As previously reported in the literature, photocatalytic reactor designs can potentially fulfil the following objectives: [6–8]

(i) Improve the catalyst to reactant ratio and residence time,
(ii) Increase the catalyst illumination time,
(iii) Improve light penetration and distribution for the system,
(iv) Eliminate mass transfer limitations and
(v) Increase the product production and recovery.

Photocatalytic reactors can be broadly grouped under either suspended or immobilised photoreactors based on the mode of photocatalyst deployment. It is not feasible to compare the current reactor designs on a common scale as they have their own advantages and disadvantages based on their area of application [4]. Recently, however, 12 different photocatalytic reactors for wastewater treatment were compared using a benchmark ratio proposed as the photocatalytic space time yield (PSTY) [6]. According to Leblebici et al. PSTY is defined as "the volume of water treated for each kW lamp power per volume of reactor per unit of time" [6]. After normalising various designs using PSTY, they concluded that the pilot scale slurry reactor with a suspended photocatalyst system outperformed the other designs. This was as a result of issues such as high light distribution, decreased mass transfer limitation and high photocatalyst surface area available for illumination and hence is also the most commonly used reactor design in the field of photocatalysis [9,10].

Simulation is a useful tool to compare various reactor configurations or to compare different modifications done to the same reactor design without having to fabricate the actual unit thereby making it a useful tool in engineering design to reduce the time and costs. There are numerous software packages available for such simulations including MATLAB®, ANSYS®, COMSOL Multiphysics®, and SOLIDWORKS®. The rotating machinery turbulent flow k-ε model in COMSOL Multiphysics® 5.1 was used in this

Table 1
Potential illumination sources.

Type of illumination source	Spectral range	Power	Reference
Mercury arc lamp	UV and visible (265–580 nm)	300 W	[28]
Medium pressure mercury arc lamp	UV (peak at 365 nm)	700 W	[29]
Incandescent lamps	UV and visible (200–600 nm)	200 W	[30]
Mercury vapour fluorescent lamp	UV (peak at 254 nm)	6–10 W	[31–33]
PL-L-40 Philips UV lamps	UV (peak at 365 nm)	40 W	[34]
Blacklight blue Panasonic Fluorescent lamps	UV (300–400 nm)	4 W	[35]
Light emitting diodes (FoxUV™)	UV (peak at 360 nm)	454 μW	[36,37]
InGaN Light emitting diodes	UV (390–410 nm)	10–20 mW	[38]
TG Purple Hi LED E1L5M-4P0A2-01 Light emitting diodes	UV (peak at 383 nm)	20 mW	[39]

study [11]. The reason for choosing k-ε model for the simulations are as follows,

(i). This model uses minimal computational resources,
(ii). Offers a good trade-off between accuracy and the computational resource requirement,
(iii). Performs well when the pressure drop in the system is expected to be negligible,
(iv). Provides an approximation of the flow patterns for a new design, such as the SFPR.

Simulation and modelling have been reported earlier for chemical reactions, multi-phase fluid flow, mixing, filtration, dialysis and other processes, [11–16] but only for a limited number of applications in photocatalytic reactors. Simulations focussing especially on mixing regimes in a reactor using COMSOL Multiphysics® have been performed in the past for reactor design verification and bioethanol fermentation purposes [11,16]. Patel *et al.* performed COMSOL Multiphysics® simulations to determine the best possible mixing profiles to understand the mass transfer for a combination of either ellipsoidal or flat base vessel with five different impeller blade configurations [11]. Similarly, Rana performed simulations to determine the mixing profiles of marine impeller and Rushton impeller for bioethanol fermentation [16]. Furthermore, Rana reported that marine impellers were superior in performance and cost efficient over Rushton impellers for bioethanol fermentation in a stirred tank reactor. This paper describes the design of a novel SFPR (slurry reactor design) along with its mixing regime simulations of a commercially available 'plus shaped' stirrer bar and an 8 blade Rushton impeller configuration for the SFPR.

2. Methodology

2.1. Stacked frame photocatalysis reactor (SFPR) design

A novel SFPR was designed using FreeCAD 15.0. The SFPR design consists of the following parts,

(i). Perspex frames (with and without inlet/outlet ports)
(ii). Pyrex end plates
(iii). Acrylic inlet and outlet port tubes
(iv). Silicone rubber gaskets
(v). Nylon threaded rods, nuts and washers
(vi). 'Plus' shaped magnetic stirrer bar or a stainless steel 316 grade impeller (8 blade Rushton impeller)

Fig. 2. shows the front view of the SFPR frames displaying the dimensions, M6 slots for inserting the threaded rods and the slots for holding the reaction mixture (cellulose + water + TiO_2). The thickness of each frame is 10 mm and the liquid holding volume of each frame is 12 ml. All the silicone gaskets were of the same dimensions as the Perspex frames, except that the thickness was 1.5 mm. Similarly, the Pyrex end plates were also of the same dimensions as the Perspex frames, except that the thickness was 3.8 mm and there was no slot for the liquid holding volume.

Two Perspex frames were also designed to have inlet and outlet ports as shown in Fig. 3. Multiple frames were stacked together with alternating gaskets and sandwiched between Pyrex end plates on either side to form the SFPR.

Threaded ports (Fig. 4) made of acrylic tubes were further fixed to the inlet and the outlet ports of the frames to facilitate inflow and outflow of the reaction mixture. A light source would be positioned in such a way so that it faces the end plate adjacent to the frame with the inlet port.

To facilitate mixing in the reactor, a commercially available 'plus shaped' magnetic stirrer bar configuration and an 8 blade Rushton impeller was designed to fit the liquid holding volume of the SFPR (Fig. 5). The dimensions of the stirrer bar are 19.1 mm × 9.5 mm × 2 mm (width × height × thickness) and that of the Rushton impeller are 20 mm × 15 mm (total width × total height), 4 mm × 5 mm (blade height × blade width) and a shaft diameter of 1 mm.

Despite the extensive use of baffles in conventional chemical reactors, no baffles were installed in this assembled photocatalytic reactor. The reasons for this being that the baffles might block the

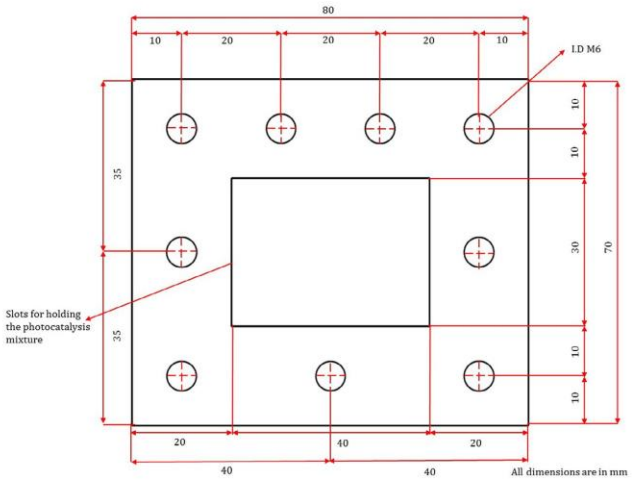

Fig. 2. Front view of SFPR frames.

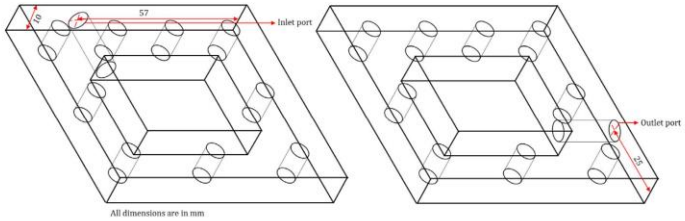

Fig. 3. Isometric view of a frame with ports.

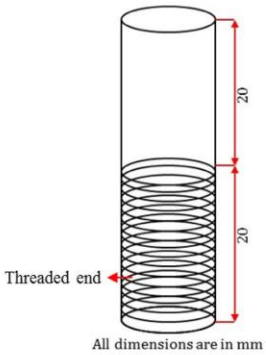

Fig. 4. Ports for inlet and outlet with an outer diameter of M6.

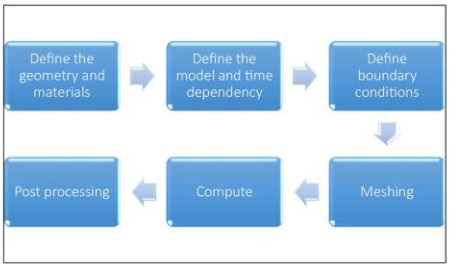

Fig. 6. COMSOL simulation procedure.

light reaching the photocatalyst, avoid vortex formation thereby diminishing chances of forcing the reaction mixture towards the walls (and the illumination source), hence creating "dead layers" and decreasing the fluid-particle mass transfer [17].

2.2. Mixing simulation

A flow chart on the simulation procedure is given in Fig. 6. Firstly, the geometry of the fluid domain (liquid holding domain) of the SFPR was created in the COMSOL Multiphysics® 5.1 workspace assuming that 4 frames were stacked together. When 4 frames are stacked together, the liquid holding domain measures 40 mm × 40 mm × 30 mm (thickness × width × height) and has a volume of 48 ml. The inlets and the outlet ports were also created. Secondly, the mixer (either the stirrer bar or the impeller) was created.

Once the geometry of the system was defined, rotating machinery turbulent flow k-ε model with a frozen rotor study (stationary with respect to the reactor) was selected in COMSOL Multiphysics®. This model uses incompressible fluid flow and assumes Reynolds-Averaged-Navier-Stokes (RANS) equation for the fluid flow [11]. Next, the material in the fluid domain was defined as water. Its fluid properties were defined with the density being 1000 kg/m^3 and the dynamic viscosity being 1.002×10^{-3} Pa.s. Then the rotating domains were allotted and the speed of rotation of the mixer was set at 1000 rpm. Subsequently, the inlet was

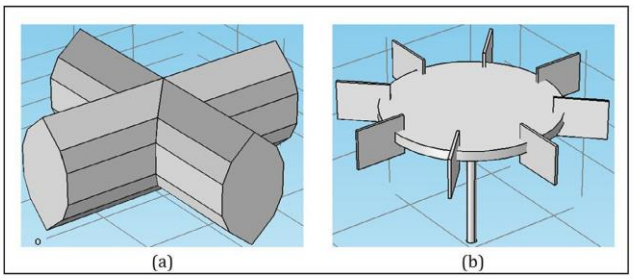

Fig. 5. (a) 'plus shaped' magnetic stirrer bar and (b) 8 blade Rushton impeller.

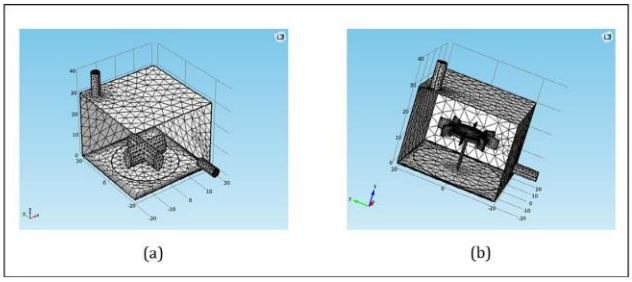

Fig. 7. Meshing of the SFPR fluid domain hosting (a) plus shaped stirrer bar and (b) 8 blade Rushton impeller.

assigned and the normal inflow velocity of the system was set at 0.01 m/s. The outlet for the system was then defined with the backflow suppressed. Finally, flow continuity was set up for the rotating and the fluid domains. All domains were meshed using the "physics controlled mesh" option provided by COMSOL Multiphysics® model builder and hence automatic (Fig. 7).

2.3. Particle tracing

Once mixing simulation was completed, particle tracing module was added to the model to simulate the motion of cellulose particles in the SFPR. Then a new time dependent study was included in the model for particle tracing. A drag force node was introduced to the module where the fluid domain defined in the mixing simulation was chosen as the domain where the particles will be present. The velocity field and the dynamic viscosity from the mixing simulation results were used to compute the drag force on the cellulose particles. The inlet and the outlet for the cellulose particles were then defined. The number of particles per release was set as 3000. From the mixing simulation results, the velocity field was chosen and defined as the initial velocity of the particles for particle tracing. In the particle properties section, the density of the cellulose particles was set as 1500 kg/m^3 (an average value obtained from literature) [18] and the particle diameter was set as 55 μm (obtained as an average diameter for cellulose particle from various suppliers). Furthermore, to use the results from the mixing simulation for the velocity field and to reduce the computation time for particle tracing, in the time dependent solver settings, the mixing simulation study was selected and included. The time range to compute the motion of the cellulose particles was chosen from 0 s to 1 s, with a step time of 0.1 s to visualise the mixing at the initial stages. It has to be noted that this SFPR was originally designed for the purpose of photocatalytic cellulose breakdown and hence cellulose particles were used as model particles to simulate particle tracing, however this reactor could also be used for other generic photocatalytic applications such as wastewater treatment.

3. Results and discussion

3.1. Mixing simulation

Mixing simulation for the SFPR with the 'plus shaped' stirrer bar and an 8 blade Rushton impeller configurations were performed and results in the form of slice plots, XY streamline plots and YZ streamline plots were generated and summarised in Figs. 8 and 9 respectively. As seen from Fig. 8, the arrows indicate the direction of fluid flow as a result of mixing where the size of the arrows is proportional to the fluid velocity at that point. It can be observed that the fluid velocity is higher (as seen from the proportional arrows) close to the blades of the Rushton impeller when compared to the walls of the stirrer bar. This observation is explained by the flat blade impeller exerting a relatively stronger force on the fluid than the convex walls of the stirrer bar. This explanation is further supported by the specific velocity magnitudes where the maximum fluid velocity close to the walls of the impeller blade and the stirrer bar is 1.2 m/s and 0.9 m/s respectively.

Fig. 9 shows the XY and YZ streamline plots of the mixing profiles respectively in the SFPR with a plus shaped stirrer bar and the 8 blade Rushton impeller. As can be seen from the XY plot, a prominent circular flow is developed with the stirrer bar, however it is not the case with the Rushton impeller. The arrows indicate the

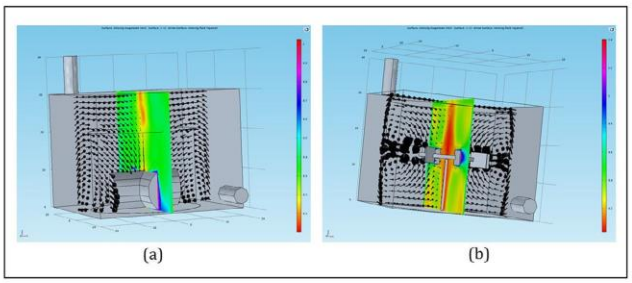

Fig. 8. Mixing profile – Slice plot of SFPR with (a) plus shaped stirrer bar and (b) 8 blade Rushton impeller.

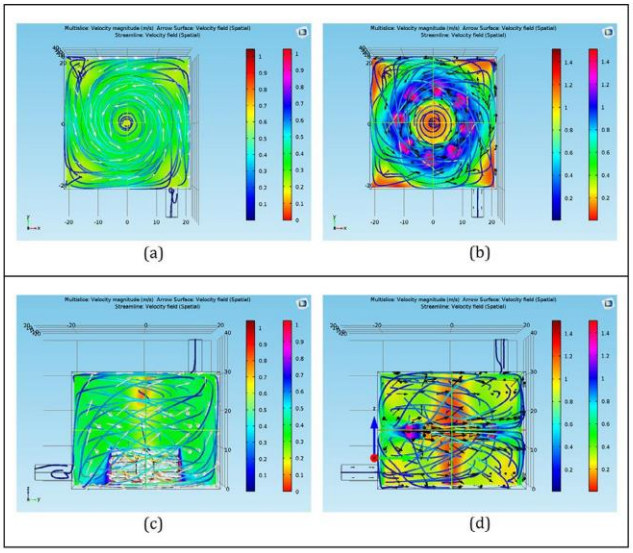

Fig. 9. Mixing profiles – XY streamline plot for SFPR with (a) plus shaped stirrer bar and (b) 8 blade Rushton impeller and YZ streamline plot for SFPR with (c) plus shaped stirrer bar and (d) 8 blade Rushton impeller.

direction of fluid flow during mixing. The velocity magnitude spread across the XY plane for the stirrer bar is in the range of 0.2–0.4 m/s and that for the impeller is in the range of 0.1–1.2 m/s as seen from the streamlines and the spatial velocity fields.

Furthermore, Fig. 9 also shows that there are no obvious "dead layers" in both the cases, which is an indication that when particles are introduced in the SFPR, they will stay in suspension. The maximum fluid velocity in both the cases is observed close to the walls of the impeller blades and the stirrer bar. Once the fluid is pushed away from the stirrer bar, the fluid velocity drops to 0.4 m/s along the walls of the SFPR. Whereas in the case of the impeller, a fully developed radial mixing pattern is observed. This observation is consistent with the existing literature [19–21]. The fluid velocity close to the top centre of the SFPR is small, indicating that a tiny vorticity is generated when the stirrer bar is used. This conclusion is also supported by the XY streamline plot. In the case of the impeller, a well-developed vorticity is seen in the middle thereby pushing the fluid towards the walls. In the case of a photocatalytic reactor (SFPR), when the liquid is forced towards the walls of the reactor, it will help in illuminating the reaction mixture evenly thereby fulfilling the need for light penetration.

3.2. Particle tracing simulation

Once the mixing simulation was completed, particle tracing simulations for cellulose in the SFPR were performed. The particle tracing simulations revealed that the motion of the cellulose particles in both the cases followed the fluid flow patterns initiated by the mixing. As a result of mixing, in both the cases, cellulose particles were well dispersed in the suspension. In the case of the impeller, as a result of a prominent vorticity developed due to agitation, the particles enter the vortex first along with the fluid flow and with the constant rotation of the impeller they are pulled closer to the blades and instantaneously pushed towards the walls.

TiO_2 photocatalyst particles are water insoluble white odourless transition metal oxide powders that have a bandgap of 3.2 eV which corresponds to an excitation wavelength of 387 nm [22]. One of the most commonly used forms of TiO_2 is the Evonik P25 form which is a mixture of 70% anatase and 30% rutile crystal phases of TiO_2. This combination is commercially preferred to avoid photocatalytic losses due to recombination [23]. The average size of TiO_2 particles are in the range of 25–65 nm [24], which could aggregate to form particles in the size range of microns or could adsorb on to the cellulose surface thereby considerably increasing the combined particle size. In addition, since the motion of particles in the fluid domain are proportional to the fluid motion, these photocatalyst particles are expected to have a similar motion such as that of cellulose in the fluid domain. Since the particles are forced towards the walls, the chances of more photocatalyst particles being illuminated are higher than a system which offers no mixing. This mechanism also decreases the mass transfer limitations and will help to improve the cellulose-TiO_2 particle interaction, thereby producing desired products. The videos of the cellulose particle tracing in a SFPR with the stirrer bar and the impeller can be found in the Supplements as video 1 and video 2 respectively.

From literature, the scattering and absorption coefficients of P25 could be obtained which correspond to 54,208 $cm^2\ g^{-1}$ and 887 $cm^2\ g^{-1}$ at 365 nm respectively [25]. It should be noted that the scattering coefficient is multiple folds (60 times) higher than the absorption coefficient which means that the majority of the light extinction depends on scattering. This was also supported by Egerton and Tooley, who reported that when illuminated at 360 nm, TiO_2 particles of a mean size 50 nm contributed only a meagre 22% for extinction [26]. They also reported that with the increase in particle size, scattering coefficient would increase. This increase could be possible in the case of cellulose-TiO_2 mix in a SFPR. With cellulose being poor light absorbers [27] and with the

possibility of TiO_2-cellulose aggregate formation, the scattering coefficient for these particles (and aggregates) would tend to increase in the SFPR and would contribute to a uniform light distribution within the reactor. In addition, from the numbers reported in literature it is evident that minimal light absorption by TiO_2 particles occurs and therefore would have an effect on photocatalysis. Hence to avoid a negative effect of minimal absorption on photocatalysis, proper mixing has to be established as reported in this study. It should be noted that more insight on the motion of particles and radiation scattering could be revealed when particle-particle interaction and the particle-radiation interaction studies are undertaken in the future.

4. Conclusion

Mixing profiles in the SFPR with various impeller and stirrer bar configurations were determined using the rotating machinery turbulent flow k-ε model in COMSOL Multiphysics® 5.1. Simulations were performed with water present in the fluid domain. The mixers were set to be operated at 1000 rpm. The results reveal that the plus shaped stirrer bar had a circular flow with the highest average fluid flow velocity around 0.9 m/s whereas, the 8 blade Rushton impeller had a superior performance than the stirrer bar and produced a radial mixing profile in addition to having higher fluid flow velocity of 1.2 m/s.

Further to the mixing profiles, particle tracing simulations were also performed in the SFPR using cellulose as the model particle. The drag force of the cellulose particles in the particle tracing were proportional to the fluid velocity obtained from the mixing simulations. In the cases with both the stirrer bar and the Rushton impeller, the particles were well dispersed, however the particle dispersion was superior in the case of the Rushton impeller where the vorticity generated during mixing pushed the particles towards the walls. A similar particle motion is expected with the TiO_2 P25 photocatalyst due to the mixing regime generated by the Rushton impeller, thereby facilitating better illumination of the photocatalyst.

Acknowledgements

This work was supported by the Engineering and Physical Sciences Research Council (Project number EP/K036769/1), Robert Gordon University's IDEAS PhD studentship and Queen's University Belfast's PhD studentship. The authors would also like to thank COMSOL Ltd for support and guidance provided through their training workshop in Belfast in October 2015 and the associated trial licence access to COMSOL Multiphysics 5.1. The authors would also like to thank Professor A Prasanna de Silva, School of Chemistry and Chemical Engineering, Queen's University Belfast, for his valuable contribution during progress meetings. Supporting data are openly available on Queen's University, Belfast Research Portal, http:// pure.qub.ac.uk/portal/en/datasets/search.html.

Appendix A. Supplementary data

Supplementary data associated with this article can be found, in the online version, at http://dx.doi.org/10.1016/j.cej.2016.12.016.

References

[1] G. Thoorens, F. Krier, B. Leclercq, B. Carlin, B. Evrard, Microcrystalline cellulose, a direct compression binder in a quality by design environment—A review, Int. J. Pharm. 473 (2014) 64–72.
[2] Y. Sun, J. Cheng, Hydrolysis of lignocellulosic materials for ethanol production: a review, Bioresour. Technol. 83 (2002) 1–11.
[3] G. Zhang, C. Ni, X. Huang, A. Welgamage, L.A. Lawton, P.K.J. Robertson, J.T.S. Irvine, Simultaneous cellulose conversion and hydrogen production assisted by cellulose decomposition under UV-light photocatalysis, Chem. Commun. (2016).
[4] C. McCullagh, N. Skillen, M. Adams, P.K.J. Robertson, Photocatalytic reactors for environmental remediation: a review, J. Chem. Technol. Biotechnol. 86 (2011) 1002–1017.
[5] H.I. De Lasa, B. Serrano, M. Salaices, Photocatalytic Reaction Engineering, 1st ed., Springer, New York, 2005.
[6] M.E. Leblebici, G.D. Stefanidis, T. Van Gerven, Comparison of photocatalytic space-time yields of 12 reactor designs for wastewater treatment, Chem. Eng. Process. 97 (2015) 106–111.
[7] V. Pareek, S. Chong, M. Tadé, A.A. Adesina, Light intensity distribution in heterogenous photocatalytic reactors, Asia-Pac. J. Chem. Eng. 3 (2008) 171–201.
[8] M.N. Chong, B. Jin, C.W.K. Chow, C. Saint, Recent developments in photocatalytic water treatment technology: a review, Water Res. 44 (2010) 2997–3027.
[9] C. McCullagh, P.K.J. Robertson, M. Adams, P.M. Pollard, A. Mohammed, Development of a slurry continuous flow reactor for photocatalytic treatment of industrial waste water, J. Photochem. Photobiol., A 211 (2010) 42–46.
[10] A.E. Cassano, O.M. Alfano, Reaction engineering of suspended solid heterogeneous photocatalytic reactors, Catal. Today 58 (2000) 167–197.
[11] P. Patel, P. Vaidya, G. Singh, An overview of impellers, velocity profile and reactor design, in: Proceedings of the 2014 COMSOL Conference, 2014.
[12] M. Serajuddin, K. Anand Rao, T. Sreenivas, Modelling and simulation of vacuum filtration of ore slurry: a case study on limestone-hosted Indian uranium ore, Can. Metall. Q. 1–9 (2016).
[13] W. Li, J. Liu, L. He, J. Liu, S. Sun, Z. Huang, X.M. Liang, D. Gao, W. Ding, Simulation and experimental study on the effect of channeling flows on the transport of toxins in hemodialyzers, J. Membr. Sci. 501 (2016) 123–133.
[14] Y. Dong, F.J. Keil, O. Korup, F. Rosowski, R. Horn, Effect of the catalyst pore structure on fixed-bed reactor performance of partial oxidation of n-butane: a simulation study, Chem. Eng. Sci. 142 (2016) 299–309.
[15] S. Vialle, J.L. Druhan, K. Maher, Multi-phase flow simulation of CO_2 leakage through a fractured caprock in response to mitigation strategies, Int. J. Greenhouse Gas Control 44 (2016) 11–25.
[16] H. Rana, Comparison of industrial agitation for simulated batch reactor vessel mixing in bioethanol fermentation, in: Proceedings of the 2015 COMSOL Conference, 2015.
[17] R. Alcamo, G. Micale, F. Grisafi, A. Brucato, M. Ciofalo, Large-eddy simulation of turbulent flow in an unbaffled stirred tank driven by a Rushton turbine, Chem. Eng. Sci. 60 (2005) 2303–2316.
[18] C. Sun, True density of microcrystalline cellulose, J. Pharm. Sci. 94 (2005) 2132–2134.
[19] T. Karuppa Raj, A. Singh, S. Tare, S. Varma, Study of fluid flow around impeller blades in Rushton turbine in a baffled vessel using computational fluid dynamics, ARPN-JEAS 9 (5) (2014) 659.
[20] K. Avinash, A. Joella, C. Rubio-Atoche, X. Catherine, S.N. Le, B. Joel, V. Ranade Vivek, Flow generated by radial flow impellers: PIV measurements and CFD simulations, Int. J. Chem. React. Eng. 2 (2004) 1542.
[21] Y. Tsui, J. Chou, Y.H. Hu, Blade angle effects on the flow in a tank agitated by the pitched-blade turbine, J. Fluids Eng. 128 (4) (2006) 774–782.
[22] N. Serpone, A.V. Emeline, Semiconductor photocatalysis – past, present, and future outlook, J. Phys. Chem. Lett. 3 (2012) 673–677.
[23] Q. Xiang, J. Yu, P.K. Wong, Quantitative characterization of hydroxyl radicals produced by various photocatalysts, J. Colloid Interface Sci. 357 (2011) 163–167.
[24] A.A. Gribb, J.F. Banfield, Particle size effects on transformation kinetics and phase stability in nanocrystalline TiO_2, Am. Mineral. 82 (2015) 717.
[25] M.I. Cabrera, O.M. Alfano, A.E. Cassano, Absorption and scattering coefficients of titanium dioxide particulate suspensions in water, J. Phys. Chem. 100 (1996) 20043–20050.
[26] T.A. Egerton, I.R. Tooley, UV absorption and scattering properties of inorganic-based sunscreens, Int. J. Cosmet. Sci. 34 (2012) 117–122.
[27] D.N.S. Hon, D.N.S. Hon, Weathering and photochemistry of wood, in: D.N.S. Hon, N. Shiraishi (Eds.), Wood and Cellulosic Chemistry, Second ed., Taylor & Francis, 2000, p. 513, Revised, and Expanded.
[28] J. Tian, X. Hu, H. Yang, Y. Zhou, H. Cui, H. Liu, High yield production of reduced TiO_2 with enhanced photocatalytic activity, Appl. Surf. Sci. 360 (2016) 738–743, Part B.
[29] C. Raillard, V. Hêquet, P. Le Cloirec, J. Legrand, Kinetic study of ketones photocatalytic oxidation in gas phase using TiO_2-containing paper: effect of water vapor, J. Photochem. Photobiol., A 163 (2004) 425–431.
[30] H.M. Yadav, T.V. Kolekar, A.S. Barge, N.D. Thorat, S.D. Delekar, B.M. Kim, B.J. Kim, J.S. Kim, Enhanced visible light photocatalytic activity of Cr3+-doped anatase TiO_2 nanoparticles synthesized by sol–gel method, J. Mater. Sci.: Mater. Electron. 27 (2015) 526–534.
[31] G. Zuo, Z. Cheng, H. Chen, G. Li, T. Miao, Study on photocatalytic degradation of several volatile organic compounds, J. Hazard. Mater. 128 (2006) 158–163.
[32] J. Zhong, J. Wang, L. Tao, M. Gong, L. Zhimin, Y. Chen, Photocatalytic degradation of gaseous benzene over TiO_2/Sr_2CeO_4: kinetic model and degradation mechanisms, J. Hazard. Mater. 139 (2007) 323–331.
[33] S.B. Kim, H.T. Hwang, S.C. Hong, Photocatalytic degradation of volatile organic compounds at the gas–solid interface of a TiO_2 photocatalyst, Chemosphere 48 (2002) 437–444.

[34] H. Ourrad, F. Thevenet, V. Gaudion, V. Riffault, Limonene photocatalytic oxidation at ppb levels: assessment of gas phase reaction intermediates and secondary organic aerosol heterogeneous formation, Appl. Catal. B 168–169 (2015) 183–194.
[35] A. Miyawaki, S. Taira, F. Shiraishi, Performance of continuous stirred-tank reactors connected in series as a photocatalytic reactor system, Chem. Eng. J. 286 (2016) 594–601.
[36] O.I. Tokode, R. Prabhu, L.A. Lawton, P.K.J. Robertson, Effect of controlled periodic-based illumination on the photonic efficiency of photocatalytic degradation of methyl orange, J. Catal. 290 (2012) 138–142.
[37] O. Tokode, R. Prabhu, L.A. Lawton, P.K.J. Robertson, The effect of pH on the photonic efficiency of the destruction of methyl orange under controlled periodic illumination with UV-LED sources, Chem. Eng. J. 246 (2014) 337–342.
[38] K. Natarajan, T.S. Natarajan, H.C. Bajaj, R.J. Tayade, Photocatalytic reactor based on UV-LED/TiO2 coated quartz tube for degradation of dyes, Chem. Eng. J. 178 (2011) 40–49.
[39] J. Shie, C. Pai, Photodegradation kinetics of toluene in indoor air at different humidities using UVA, UVC and UVLED light sources in the presence of silver titanium dioxide, Indoor Built Environ. 19 (2010) 503–512.

Renewable and Sustainable Energy Reviews 77 (2017) 182–192

Contents lists available at ScienceDirect

Renewable and Sustainable Energy Reviews

journal homepage: www.elsevier.com/locate/rser

Cellulose II as bioethanol feedstock and its advantages over native cellulose

Sanjay Nagarajan[a,*], Nathan C. Skillen[a], John T.S. Irvine[b], Linda A. Lawton[c], Peter K.J. Robertson[a,*]

[a] School of Chemistry and Chemical Engineering, Queen's University Belfast, David Keir Building, Stranmillis Road, Belfast BT9 5AG, United Kingdom
[b] JTSI Group, University of St. Andrews, School of Chemistry, Purdie Building, North Haugh, St Andrews KY16 9ST, United Kingdom
[c] School of Pharmacy and Life sciences, Sir Ian Wood Building Robert Gordon University, Garthdee Road, Aberdeen AB10 7GJ, United Kingdom

ARTICLE INFO

Keywords:
Cellulose II
Lignocellulosic biomass
Fermentable sugars
Bioethanol
Amphiphilic

ABSTRACT

Alternative renewable energy must emerge to sustainably meet the energy demands of the present and future. Current alternatives to fossil fuels are electricity from solar, wind and tidal energies and biofuels. Biofuels, especially bioethanol could be produced from lignocellulosic feedstock via pre-treatment and fermentation. The cellulose I content of most lignocellulosic feedstock is significant, yet its highly crystalline amphiphilic structure interlinked with the lignin network makes it difficult to process for bioethanol production. Processing lignocellulosic biomass via a range of physico-chemical, mechanical and biological pre-treatment methods have been well established, however a relatively new area on the use of cellulose II (a polymorph of native cellulose obtained via mercerisation or regeneration) for the production of bioethanol is still in its early stages. Hence, this review discusses in detail the advantages of using cellulose II over cellulose I as feedstock for bioethanol production. Furthermore, current green and sustainable methods for cellulose II production and the advantages and disadvantages of each method are discussed. In addition, examples from literature reporting higher fermentable sugar and bioethanol yields using cellulose II as feedstock are reviewed, thereby highlighting its importance in the field of bioethanol production. The conclusion from this review suggests that, in all the cases studied, fermentable sugar and/or bioethanol production was found to be higher when cellulose II was used as feedstock instead of native cellulose/lignocellulosic biomass. This higher yield could be attributed to the modified structural and lattice arrangement of cellulose II, its porous volume and degree of polymerisation.

1. Introduction

Enhanced global utilisation of fossil fuels with the associated increase in greenhouse gas (GHG) emissions from growing anthropogenic activities is continuously debated. Global politics also influences the movement of fossil fuel stock across boundaries. It was predicted that serious fossil fuel depletion will be experienced by 2030 [1]. The International Energy Agency (IEA) estimated that global fossil fuel dependence would drop from 82% to 76% by 2035 with up to 18% of total energy consumed from renewable energy resources [2]. This emphasises the need to increase renewable energy production and accordingly investments are underway globally to expand renewable energy production (Fig. 1).

There are a range of alternate energy resources available to supplement fossil fuels, including bioenergy (e.g. biogas, biodiesel, biomass and bioethanol), solar, geothermal, ocean/marine and wind. Amongst the alternatives mentioned above, bioenergy has the potential to replace current transportation fuels. Bioenergy for transportation includes, biodiesel and bioethanol. Feedstocks essential to produce biodiesel include algae, waste vegetable oils, animal fats, palm oil and non-edible oils [3]. Whereas, the feedstock required to produce bioethanol could be classified into first generation feedstocks – food crops such sugarcane and corn and second generation feedstocks – lignocellulosic materials and cellulosic wastes [4,5].

Second generation bioethanol production entirely utilises cellulose I and its wastes as feedstock for the fact that cellulose I is the most abundant naturally available organic material on earth. Shown below in Table 1 are the cellulose I contents of various lignocellulosic biomass. All the feedstock mentioned in Table 1 have varying amounts of lignin in them. Lignin is an aromatic hydrophobic compound which forms interlinking complexes with cellulose I and reduces freely available cellulose I, hence giving plants their structural stability [6]. It is expensive, both from an energy and cost perspective to breakdown the lignin network in lignocelluloses to release cellulose I followed by cellulose I degradation to release fermentable sugars for bioethanol production. In order to utilise cellulose to the fullest, it is better to use

* Corresponding authors.
E-mail addresses: snagarajan01@qub.ac.uk (S. Nagarajan), p.robertson@qub.ac.uk (P.K.J. Robertson).

http://dx.doi.org/10.1016/j.rser.2017.03.118
Received 29 November 2016; Received in revised form 12 January 2017; Accepted 25 March 2017

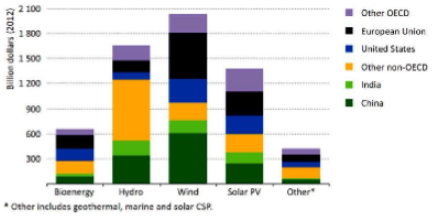

Fig. 1. Cumulative investment in renewables-based power generation, 2013–2035, where OECD stands for Organisation for Economic Co-operation and Development [2], (Reprinted with permission from "IEA Publishing. OECD/IEA© 2013").

Table 1
Cellulose I content of various bioethanol feedstocks [82–86].

Material	% cellulose I content (wt/wt)
Green algae	20–40
Cotton, flax, etc.	80–95
Grasses	25–40
Hardwoods	45 ± 2
Hardwood barks	22–40
Softwoods	18–38
Softwood barks	42 ± 2
Corn stalks	39–47
Wheat straw	37–41
Newspapers	40–55
Chemical pulps	60–80
Rice straw	46.5 ± 1.5
Wheat straw	35–37
Rice husk	25–35
Bagasse	32–43

freely available cellulose in the form of processed cellulose waste rather than lignocelluloses.

Bioethanol production from native cellulose or lignocellulosic biomass have been extensively studied and reviewed in the past [7–13]. All the published reviews have emphasised the use of cellulose I for biofuel production, however, the review presented here highlights the importance of cellulose II as feedstock for biofuel production over cellulose I. Even though cellulose II production has been in practice since 1850's, green, clean and sustainable methods for the production of cellulose II has been introduced only recently [14]. It was well established in the past decade that cellulose II was the most easily digestible polymorph of cellulose with its modified lattice arrangement, higher porous volume, higher surface wettability and lower crystallinity compared to cellulose I, however its use as feedstock for bioethanol production was not extensively studied.

The aim of this review is to emphasise the importance of cellulose II as a superior feedstock than cellulose I for bioethanol production. This was achieved by subdividing the review into three subsections. The first section explains the structural differences between cellulose I and cellulose II comparing its advantages and disadvantages. The subsequent section details modern, green and renewable methods for cellulose II production and the final section discusses recent examples from literature on the superiority of cellulose II over cellulose I as feedstock for biofuel production thereby highlighting its importance in the area of renewable energy. This review was prepared to serve as a resource for researchers working in the field of lignocellulosic biofuels to acquire knowledge on the advantages of cellulose II over cellulose I for biofuel production.

2. Structure of Cellulose

Cellulose I is an amphiphilic homopolysaccharide compound [15]. Individual β-D-glucose units joined by a (1–4)-glycosidic bond as well as intermolecular and intramolecular hydrogen bonds and hydrophobic interactions give rise to a rigid cellulose structure [15,16]. Cellulose I molecules have both disordered amorphous and highly ordered crystalline regions along its chain [17]. The structure of cellulose I with chair confirmation and equatorial orientation of the glucose molecules, the β (1–4) glycosidic bond and the intramolecular and intermolecular hydrogen bonds represented by the green dotted lines are shown in Fig. 2.

In addition to the characteristic hydrogen bonds of cellulose I, van der Waals interactions (hydrophobic interactions) also play a major role in stabilising the structure of cellulose I. The intermolecular and intramolecular hydrogen bonds along with the van der Waals interactions make cellulose I an amphiphilic compound. Cellulose I was proposed to be an amphiphilic compound because all three hydroxyl groups of the anhydroglucose units have an equatorial orientation making it hydrophilic and the H atoms of its C–H bonds have an axial orientation making it hydrophobic [15,18–24] (Fig. 3). Clear understanding of the amphiphilic property of cellulose I is necessary to choose appropriate amphiphilic solvents to dissolve cellulose I for the purpose of cellulose II production or for further chemical processing of native cellulose. The most common solvent, water which is non-amphiphilic would not dissolve cellulose I because of this reason.

Different polymorphs of cellulose could be produced from its native form as seen in Fig. 4 [25]. Physico-chemical treatments of native microcrystalline cellulose (cellulose I) yields these different polymorphs. Native cellulose Iα is produced by microbes whereas the most abundant cellulose Iβ is found in higher plants. Although cellulose Iα and Iβ have parallel strands of cellulose, they differ in their lattice arrangement with the former being triclinic and the latter having a monoclinic structure.

Cellulose II could be produced from both cellulose Iα or Iβ via alkali treatment (mercerisation) or solubilising and recrystallising (regeneration) respectively. In a few rare instances, naturally occurring cellulose II has been isolated [25–27]. This naturally occurring cellulose II was isolated from a mutant *Acetobacter xylinum* strain, whereas it's wild strain generally produces cellulose Iα. Unlike cellulose I, cellulose II has an antiparallel strand arrangement and monoclinic lattice arrangement. Other polymorphs of cellulose such as cellulose III_I and cellulose III_{II} could be reversibly produced from cellulose I and cellulose II via NH_3 treatment respectively. The degree of conversion of cellulose III polymorph and the reversibility back to the parent polymorph depends on the process in which ammonia is removed from the reaction mixture [28]. This polymorph was reported to exhibit a monoclinic crystal structure similar to cellulose II [29]. Another similarity that was observed among cellulose III_I, cellulose III_{II} and cellulose II structure was the orientation of the $-CH_2OH$ group. It was found to be in gauche-trans (gt) conformation in cellulose III_I (and cellulose III_{II}) unlike its parent polymorph, cellulose I which has the hydroxymethyl group in trans-gauche (tg) conformation [29]. When these cellulose III_I and cellulose III_{II} materials are heat treated, cellulose IV_I and cellulose IV_{II} are formed. It was reported that although cellulose IV_I and cellulose IV_{II} have similar unit cell size they have different polarity, with the former having a parallel arrangement and the latter having an antiparallel arrangement following its parent polymorphs, cellulose I and cellulose II respectively [30].

An in-depth understanding of the polymorph's characteristics is necessary for determining its end use. Cellulose I is the naturally abundant cellulose whereas, cellulose II is the most commonly used man made cellulose and for this reason there is abundant information in literature regarding the production and characterisation of these polymorphs [16,17,25,31]. It is evident from published literature that the hydrogen bonding interactions play a governing role in stabilising

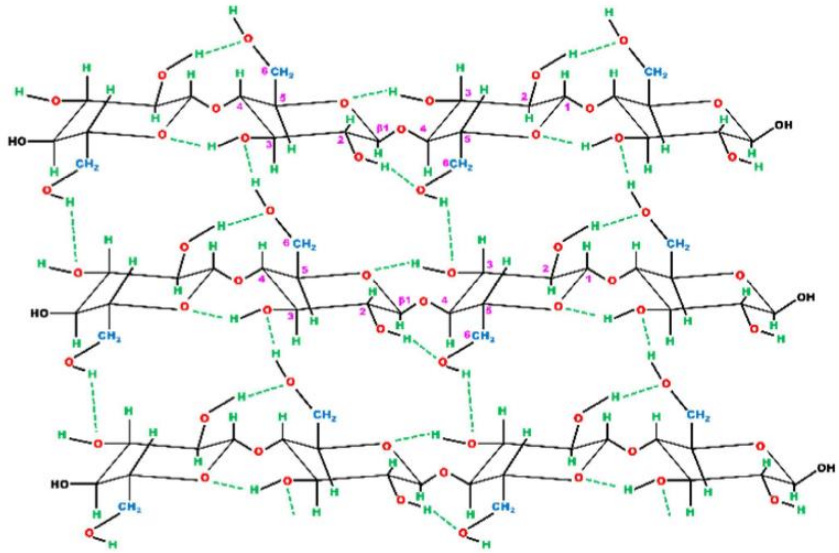

Fig. 2. Structure of cellulose I.

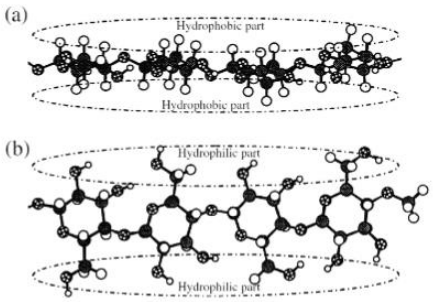

Fig. 3. Hydrophilic and hydrophobic sides of Cellulose I: (a) top view of glucopyranose ring plane; (b), front view of glucopyranose ring plane [20], (Reprinted with permission from "Macmillan Publishers Ltd: Polymer Journal, copyright 2006").

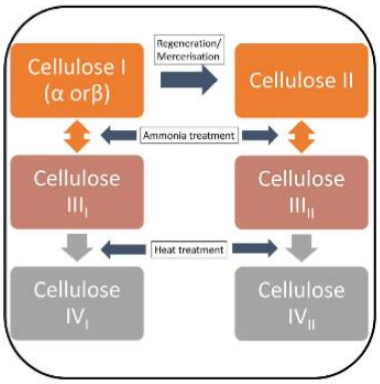

Fig. 4. Cellulose polymorphs.

the molecular structure of these polymorphs. The hydrogen bonding networks for cellulose I and cellulose II are shown along the a-c axis in Fig. 5. As can be seen, there are differences in hydrogen bonding between the two polymorphs which were induced due to the irreversible transformation of cellulose I to cellulose II during mercerisation or regeneration. As a result of the transformation, the latter exists as anti-parallel chains while the former hosts a parallel chain strand arrangement.

The intermolecular hydrogen bonding is more complicated in cellulose II when compared to cellulose I due to its antiparallel chain arrangement. For instance, in cellulose I, the O6-H-O3 (indicated within a red circle in Fig. 5.) intermolecular hydrogen bond is formed parallel to the a-axis as a result of tg conformation of the $-CH_2OH$ group. Whereas in cellulose II, the $-CH_2OH$ group occurs in the gt conformation due to the anti-parallel chain arrangement and hence forms the O6-H-O2 (indicated within a green circle in Fig 5.) intermolecular hydrogen bond [31]. The gt and tg conformations of the $-CH_2OH$ group not only determine the hydrogen bonding in cellulose polymorphs but also determine the fate of chemical reactivity with various radical species and chemical compounds. Apart from

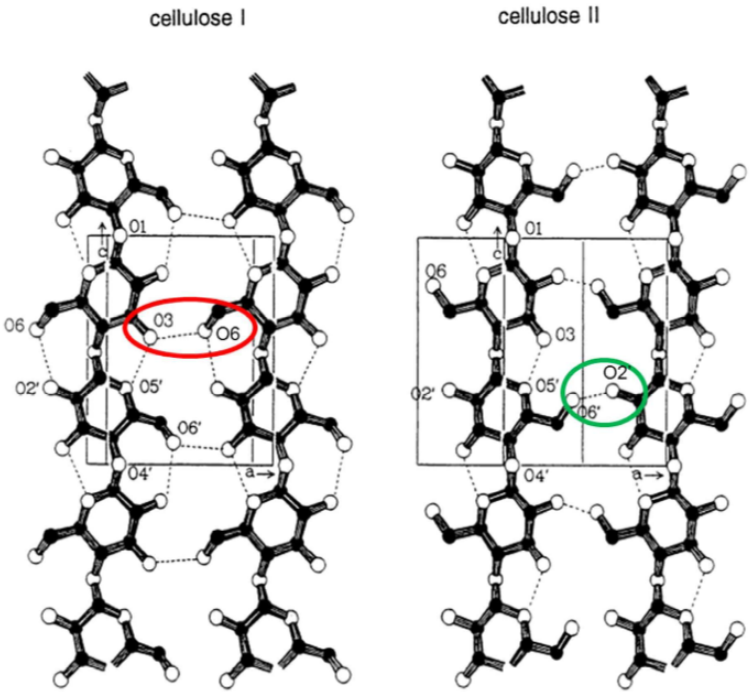

Fig. 5. Intermolecular and intramolecular hydrogen bonding in cellulose I and cellulose II [31], (Reprinted with permission from "John Wiley and Sons, copyright 1998").

hydrogen bonds, glycosidic bonds are formed between the C1 of a glucose monomer and C4 of the subsequent monomer. During the transformation from cellulose I to cellulose II, it is the hydrogen bonding network that is reorganised whereas the glycosidic linkages are not affected. Furthermore, cellulose II in its hydrate (non-dried) form has superior digestibility than dried cellulose II and cellulose I [32,33]. This is because of the increased inter-planar spacing (d-spacing) created due the presence of two water molecules per two chain unit cell of cellulose II hydrate [32,33]. The increased d-spacing is also due to the weakening of the hydrophobic bonds (van der Waals interaction) thereby increasing the hydrophilicity [20,32,34]. In contrast to cellulose I, cellulose II has its glucopyranose rings stacked with each other by hydrophobic interactions along the (1 −1 0) plane, thereby resulting in an increased density of hydroxyl groups on the surface leading to increased hydrophilicity [20]. This increased density of hydroxyl groups gives cellulose II a wetting angle of 12° which is significantly lower than many polymers such as polyvinyl alcohol, polymethyl methacrylate, starch and polyethylene [20]. Furthermore, crystallinity index (CrI) results of cellulose I and cellulose II suggests that the latter is less crystalline than the former [35]. Additionally, from literature it can also be seen that the surface area and the porous volume of cellulose II is higher than that of cellulose I [34,36]. The characterisation of both cellulose I and II clearly indicates the latter to be a far more suitable starting material for the efficient release of fermentable sugars and subsequently, biofuel production [32,34,37].

3. Cellulose II synthesis for fermentable sugar and biofuel production

Cellulose I is difficult to process without pre-treatment, whereas cellulose II is the most commonly used man-made form which is relatively easier to process. Hence, to gain better accessibility to the cellulose structure for chemical processing, cellulose II has to be derived from cellulose I via an efficient pre-treatment process. Due to its amphiphilicity, cellulose I cannot be dissolved in water, however it can be dissolved in various other solvents such as trifluoroacetic acid, ionic liquids, onium hydroxides, molten salts and cold alkalis [15,38–41] (Table 2).

In contrast to conventional alkali dissolution, ionic liquids and onium hydroxides are considered as green amphiphilic non-derivatising cellulose I solvents having negligible volatility and greater stability at higher temperatures [39,41]. Once dissolved, the irreversibly produced cellulose II can be precipitated out by the addition of anti-solvents such as water, ethanol, acetone, dilute acids or methanol. The nature of anti-solvents used, influence the structure and reactivity of cellulose II [18].

3.1. Conventional cellulose II production method – alkali treatment

Alkali treatment of cellulose I is one of the oldest known industrial processes. In the field of fibre production, it is known as the viscose

Table 2
Cellulose II production methods.

Treatment type	Solvent used	Temperature (°C)	Method synopsis	Reference
Alkali	Aqueous NaOH solution	–	Cellulose xanthogenate prepared from pulp is dissolved in aqueous NaOH and precipitated out of solution (viscose process).	[42–44]
	0–30% aqueous NaOH solution	70 °C/85 °C	Cellulose I was dissolved in NaOH aqueous solution followed by precipitation and purification (mercerisation). 9–15% NaOH aqueous solution was found to produce better cellulose II yields than other concentrations at 85 °C.	[46,54]
	6% aqueous NaOH solution	−8 °C to −20 °C	Cellulose I was dissolved at sub-zero temperatures and after 10 min of dissolution at −15 °C cellulose II started to appear.	[50]
Ionic liquid	1-ethyl-3-methylimidazolium acetate (EMIM-Ac)	120 °C/160 °C	Avicel, switchgrass, eucalyptus and pine samples were dissolved in EMIM-Ac at the 120 °C/160 °C and upon dissolution, cellulose II was precipitated out using hot water. Higher rate of cellulose II formation was observed with higher temperature.	[65]
	21 different ionic liquids	50 °C/80 °C	Avicel, α-cellulose, spruce wood, silver fir, common beech and chestnut wood of 1–5 wt% was dissolved in 21 different ionic liquids at 50 °C and upon dissolution cellulose II was precipitated. EMIM-Ac was found to dissolve standard cellulose I samples and 1-allyl-3-methylimidazolium-chloride (AMIM-Cl) dissolved the wood samples.	[69]
	imidazolium based ionic liquids containing odd or even numbered alkyl side chains in combination with a range of anions	100 °C	8 wt% of Avicel PH 101 was dissolved in ionic liquids at 100 °C. Upon dissolution, excess methanol was used to precipitate cellulose II. It was determined that ionic liquids with shorter even numbered side chains (2 or 4) combined with chloride anions showed good cellulose I dissolving properties.	[70]
Onium hydroxide	Aqueous solutions of tetrabutylammonium hydroxide (TBAH) and tertabutylphosphonium hydroxide (TBPH).	25 °C	Cellulose I was dissolved in 40–70 wt% aqueous TBAH and TBPH solution. Hot ethanol was added to the solution to precipitate cellulose II. It was determined that a concentration range of 50–60% TBAH and 50–70% TBPH in water was required for complete cellulose I dissolution at room temperature	[40]
	TBAH	16–28 °C	Cellulose I was dissolved in 40 and 60 wt% TBAH at different temperatures. Precipitation and regeneration of cellulose II was performed by the addition of hot water. It was determined that cellulose I dissolved better at 16 °C due to the stable ionic structure of TBAH at lower temperatures.	[75]
	TBPH, tetraethylphosphonium hydroxide (TEPH), tri-n-hexylphosphine tetramethylammonium hydroxide (THTMAH), tetraethylammonium hydroxide (TEAH), TBAH, tri-n-butylmethylphosphonium hydroxide and tetra-n-hexylammonium hydroxide	25 °C	Cellulose I was dissolved in various 40 wt% onium hydroxide aqueous solutions. A concentration of 15 wt% cellulose I was found to be dissolved in all the onium hydroxides, whereas TBPH and TBAH dissolved 20 wt% cellulose I. THTMAH and TEAH did not dissolve any cellulose I.	[73]
Phosphoric acid	77–85 wt% phosphoric acid	5–75 °C	0.5–3% wt./v cellulose I was dissolved in 77–85 wt% phosphoric acid in the temperature range of 5–75 °C. Regeneration was performed with the addition of water. They determined that a higher concentration of phosphoric acid (≥83 wt %) was required to completely dissolve cellulose I.	[76]
Trifluoroacetic acid	99% Trifluoroacetic acid (TFA)	0–65 °C	Cotton linters were mixed in 99% TFA in mass ratios of 1:15 at different temperatures ranging from 0 °C to 65 °C for 3 h. The swollen samples were washed with water to recover cellulose II. Complete conversion to cellulose II was only observed at 0 °C.	[77]
Supercritical water solubilisation	Supercritical water	320–400 °C	A 10 wt% cellulose I was mixed with water in a microreactor and rapidly heated for 0.02–0.6 s at 320–400 °C and 25–33 MPa pressure to obtain cellulose II. It was determined that at temperatures higher than 380 °C, cellulose I conversion was constant and was independent of pressure.	[78]

process [42–44]. In viscose process, cellulose from pulp is converted to cellulose xanthogenate. This cellulose derivative is then dissolved in aqueous NaOH. Upon dissolution, the cellulose II derivative formed is precipitated out from solution followed by purification of cellulose II with removal of the substituent [42]. Viscose process is still being used for the production of cellophane, a packaging material.

Unlike the viscose process, mercerisation is another method to produce cellulose II from cellulose I without derivatisation. Mercerisation was introduced by J. Mercer in the 1850's where cellulose I was allowed to swell in a concentrated NaOH aqueous solution followed by dissolution and precipitation [45,46]. Ever since mercerisation was introduced, it has been used to produce cellulose II frequently [47–55].

Yu et al. tested the effect of a range of NaOH concentrations and temperatures on the mercerisation of cellulose I [54]. The feedstock material used in their experiments was ground jute fibres with an approximate particle size of 1 mm which were dispersed in aqueous NaOH solutions in the concentration range of 0–30% at 70 °C and 85 °C. It was determined that the highest cellulose II content was obtained with a 20% aqueous NaOH solution at 85 °C and 25% aqueous NaOH solution at 70 °C upon mercerisation (Fig. 6). It was further determined that the crystallinity index increased in the concentration range of 5–9% NaOH which is due to the increased reactivity of the amorphous regions in the jute fibres. Due to the increase in concentration of Na^+ and OH^- ions present beyond 9% concentration, penetration of the cellulose I lattice became easier thereby producing cellulose II with the lowest crystallinity until 15% NaOH concentration. When the concentration of NaOH was further increased until 30%, viscosity of the solution increased and hence the crystallinity of the resulting cellulose II sample was higher. It was also determined that the crystallinity index of the precipitated cellulose II was lower with a higher temperature (85 °C).

In contrast to determining the effect of high temperatures on mercerisation, Wang and Deng tested the effect of cellulose I dissolution at sub-zero temperatures [50]. They dissolved cotton linters in 6% NaOH solution at temperatures ranging from −8 °C to −20 °C. The percentage solubility of the samples were calculated and it was found that 25–32% solubility was reached (and plateaued) at temperatures of −15 °C and −20 °C. It was also determined that cellulose II started to appear after 10 min of dissolution time at −15 °C.

3.2. New methods for cellulose II production

3.2.1. Ionic liquid treatment

Ionic liquids are molten salts with melting temperatures lower than 100 °C. Most common ionic liquids to date are air and moisture stable

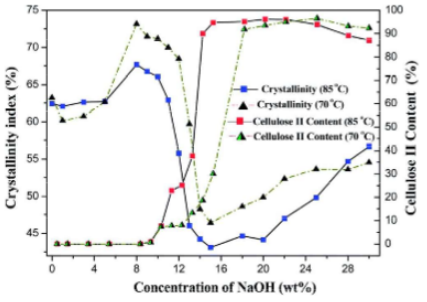

Fig. 6. Crystallinity index and cellulose II content of mercerised jute fibres by aqueous NaOH for 4 h [54] (Reprinted with permission from "The Royal Society of Chemistry").

imidazolium based salts [56]. Currently, ionic liquids are of prime interest due to their versatility as solvents in various applications [57,58]. They are highly flexible, as a number of cation and anion combinations could be fabricated based on its end use. Methylimidazolium and methylpyridinium based cations, and chloride, acetate and formate anions are the most commonly used species for designing cellulose I dissolving ionic liquids [39], however, other anions such as Br^-, SCN^-, BF_4^- and PF_6^-, have also been used [14,39,56]. It is believed that the OH groups of the neighbouring C6 and C3 cellulose chains form an electron donor-acceptor complex with ionic liquids to result in the dissolution of cellulose I [39].

Ever since Swatloski et al. [14] demonstrated the use of ionic liquids as cellulose I dissolving solvents for the irreversible production of cellulose II, numerous researchers have opted for the use of various ionic liquids for the production of regenerated cellulose [36,49,59–68]. For instance, Cheng et al. reported the use of an ionic liquid 1-ethyl-3-methylimidazolium acetate (EMIM-Ac) to produce cellulose II from Avicel, switchgrass, eucalyptus and pine [65]. The biomass samples were milled to 40 mesh prior to EMIM-Ac treatment. The samples were heated to 120 °C for 1, 3, 6 or 12 h. Upon dissolution, hot water was added to precipitate cellulose II out of the solution. X-ray diffraction (XRD) profiles of the dried samples revealed that after treatment with EMIM-Ac, all the samples were converted to cellulose II as seen in Fig. 7, however switch grass samples showed residual cellulose I after an hour's treatment [65,66]. This group performed further experiments at a higher temperature of 160 °C and found that the rate of cellulose II formation was higher at higher temperatures, however there are chances of cellulose I depolymerisation when dissolved at higher temperatures.

Zavrel et al. performed a high throughput screening to compare and determine the best ionic liquid for producing cellulose II from Avicel and lignocellulose [69]. Apart from Avicel and α-cellulose as the standard cellulose I samples, lignocellulosic materials such as spruce wood, silver fir, common beech and chestnut wood of size 1–2 mm were dissolved in a range of ionic liquids. They screened 21 different ionic liquids for their ability to dissolve cellulose I (and lignocellulose) of 1–5 wt% for 8–12 h at 50 °C and precipitated cellulose II. Amongst the screened ionic liquids, EMIM-Ac was found to be effective for dissolving cellulose I whereas 1-allyl-3-methylimidazolium-chloride (AMIM-Cl) was found to be effective for dissolving wood chips as observed from their light scattering measurements. In addition, it was also observed that at a higher temperature of 80 °C, the dissolution of cellulose I was quicker when compared to lower temperatures ranging from 40 °C to 60 °C (Fig. 8). It was elucidated that viscosity of the ionic liquids is affected at higher temperatures enabling better dissolution. Furthermore, at higher temperatures the hydrogen bonds present in cellulose I structure were destabilised thereby enhancing the rate of cellulose I dissolution.

Vitz et al. performed cellulose I dissolution studies using various imidazolium based ionic liquids containing odd or even numbered alkyl side chains in combination with a range of anions [70]. Few ionic liquids used in their study were commercially available whereas the remaining were synthesised before the dissolution experiments. A concentration of 8 wt% of cellulose I (Avicel PH 101) was dissolved in the ionic liquids at 100 °C. In some cases, microwave irradiation was used to dissolve cellulose I in ionic liquids. Upon dissolution for 1 h, cellulose II was precipitated with the addition of excess methanol. From their experiments it was primarily concluded that moisture free ionic liquids were needed to achieve high dissolution of cellulose I. Furthermore, they deduced that the moisture uptake by ionic liquids with various anions followed the resulting order $CH_3COO^- \approx (CH_3)_2PO_4^- > (CN_2)N^-$ > triflate > BF_4^- > PF_6^-. Secondly, they established that imidazolium based ionic liquids with shorter even numbered side chains (two or four) combined with chloride anions showed good cellulose I dissolving properties. In addition to chloride anions, acetate and phosphate anions were shown to have good cellulose I dissolution properties. Results upon microwave

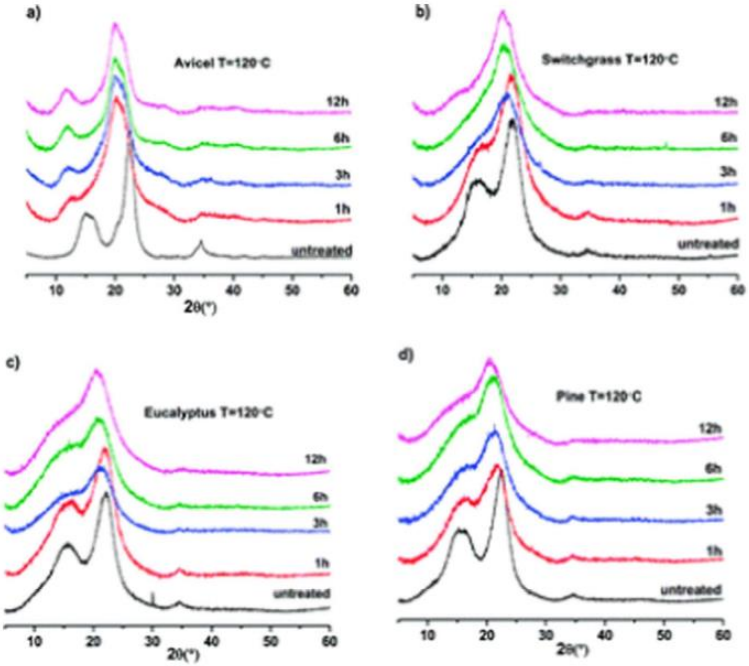

Fig. 7. XRD profiles for cellulose samples treated at 120 °C [65] (Reprinted with permission from "American Chemical Society, Biomacromolecules, Copyright 2011").

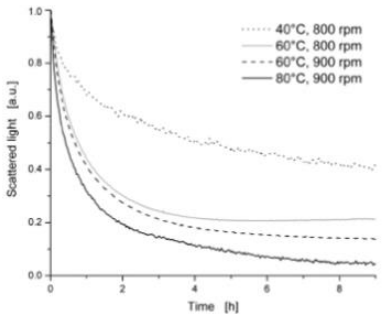

Fig. 8. Influence of temperature and shaking on the dissolution of 4 wt% Avicel in EMIM-Ac [69] (Reprinted with permission from "Elsevier, Bioresource Technology, Copyright 2009").

irradiation revealed that the yield of cellulose II was 86% for 1-ethyl-3-methylimidazolium chloride whereas the yield from ionic liquid, 1-ethyl-3-methylimidazolium diethyl phosphate was 96%. This was attributed to the degradation of cellulose I in chloride containing ionic liquid under microwave irradiation.

Zhang et al. performed nuclear magnetic resonance (NMR) spectroscopic studies on the dissolution of cellobiose (a disaccharide containing two anhydroglucose units) in EMIM-Ac to understand the mechanism of cellulose I dissolution in ionic liquids [71]. They provided evidence that the acetate ion in EMIM-Ac forms a hydrogen bond with the hydrogen atoms of the cellobiose hydroxyl group whereas the imidazolium ion bonds with the oxygen atoms of the cellobiose hydroxyl group thereby dissolving it.

It can be seen from literature that ionic liquids for cellulose II production is ever expanding. Despite the high versatility for fabrication of ionic liquids and negligible vapour pressure, its high viscosity at room temperature, instability in the presence of water and the requirement of temperatures higher than room temperature to dissolve cellulose I does not make it completely "environmental friendly" for the production of cellulose II.

3.2.2. Onium hydroxide treatment

Solvents containing onium and hydroxide ions are termed as onium hydroxides. Examples of onium hydroxides are tetrabutylammonium hydroxide (TBAH), tetramethylammonium hydroxide (TMAH) or tertabutylphosphonium hydroxide (TBPH). Onium hydroxides, unlike ionic liquids, are usually found as aqueous solutions and have the capability to dissolve wet cellulose I samples. Solvents of this class also have the added advantage of lower viscosity when compared to their ionic liquid counterparts. They are also liquid at room temperature and they do not require heating to dissolve cellulose I. Additionally, Toth et al. demonstrated that an aqueous onium hydroxide, TMAH was a better Mercerising agent than aqueous NaOH [72].

Abe et al. demonstrated the use of onium hydroxides, TBAH and TBPH for the production of cellulose II from cellulose I [40]. They dissolved cellulose I in various concentrations of aqueous TBAH and TBPH ranging from 40 to 70 wt% at room temperature (25 °C). It was determined that a concentration range of 50–60% TBAH and 50–70% TBPH in water was required for complete cellulose I dissolution at room temperature. Cellulose I was insoluble in all the other concentrations of onium hydroxides used. Upon dissolution, hot ethanol was added to precipitate cellulose II. H NMR studies were further conducted to study the mechanism of cellulose dissolution in onium hydroxides. It was established from these studies that the hydroxide ion of the onium hydroxides formed hydrogen bonds with the hydroxyl groups of cellulose. This mechanism of cellulose dissolution observed is similar to that in ionic liquids as mentioned earlier. This provides further evidence that an amphiphilic compound such as cellulose could only be dissolved in amphiphilic solvents.

Furthermore, Abe et al. published a follow up paper to their above mentioned work (in 2012) to examine the effect of different onium cations on their cellulose I dissolution capability [73]. They used a range of commercially available and tailor made onium hydroxides such as TBPH, tetraethylphosphonium hydroxide (TEPH), tri-n-hexylphosphine tetramethylammonium hydroxide (THTMAH), tetraethylammonium hydroxide (TEAH), TBAH, tri-n-butylmethylphosphonium hydroxide and tetra-n-hexylammonium hydroxide and determined the effect of temperature and cellulose I loading on cellulose I solubility. All the onium hydroxides used, dissolved a concentration of 15 wt% cellulose I, whereas TBPH and TBAH dissolved 20 wt% cellulose I. THTMAH and TEAH did not dissolve any cellulose I. The non-dissolving ability of TEAH was attributed to the low hydrophobicity of the cation which was determined via C NMR studies. Furthermore, they also observed that a similar onium hydroxide, TEPH dissolved up to 15 wt% cellulose I because the phosphonium cation had a higher hydrophobicity than the ammonium cation in TEAH. This established the amphiphilic nature of both the onium hydroxides and cellulose I. When an amphiphilic solvent such as aqueous TBAH or TBPH was employed for cellulose I dissolution, an optimum amount of water was required in solution to form hydrogen bonds between the hydroxyl groups of cellulose I (hydrophilic regions) and water. Addition of cellulose I to such an amphiphilic solvent disrupts the inter and intramolecular hydrogen bonds within the cellulose I structure forming new hydrogen bonds with the surrounding water molecule. Furthermore, hydrophobic cations in these amphiphilic solvents interact with the respective hydrophobic regions in cellulose I causing complete dissolution of cellulose I. Further details on the characteristics of amphiphilic solvents used for cellulose I dissolution could be found elsewhere [15,18,23,41,74].

Wei et al. performed cellulose I dissolution experiments in aqueous TBAH at different temperatures to determine the effect of temperature on the production of cellulose II [75]. They dissolved 376 mg cellulose I in 5 ml aqueous TBAH (40 and 60 wt%) in a temperature range of 16–28 °C for 60 min. It was determined that better solubility of cellulose I was achieved with 40 wt% TBAH at 16 °C. Although, cellulose I dissolved at 16 °C showed superior solubility, upon regeneration using hot water, all the samples showed a peak shift in the XRD spectra thereby suggesting the conversion to cellulose II. Since the ionic structure of TBAH was stable at a lower temperature, it was suggested that a strong hydrogen bond network was formed between the onium hydroxide and cellulose I enabling higher solubility.

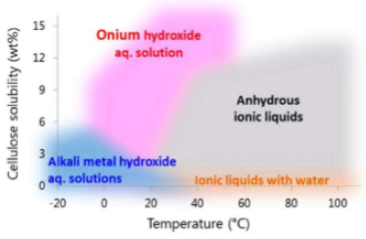

Fig. 9. Cellulose I solubility in various solvents [73] (Reprinted with permission from "American Chemical Society, Sustainable Chemistry and Engineering, Copyright 2015").

To emphasise the amphiphilicity of cellulose I and TBAH, Alves et al. compared the dissolution of cellulose I in aqueous TBAH and NaOH [41]. A concentration of 1 wt% cellulose I was dispersed in 8 wt % aqueous NaOH and frozen at −20 °C for 24 h, followed by thawing at room temperature with gentle mixing. Similarly, 1 wt% cellulose I was mixed with 40 wt% aqueous TBAH at room temperature for 30 min. After dissolution, dilute H_2SO_4 was added to the mixture to precipitate and regenerate cellulose II. A clear cellulose I solution was obtained when both TBAH and NaOH were used as solvents indicating complete dissolution when observed with the naked eye. When viewed under a polarised light microscope, however, cellulose I fragments were seen in the aqueous NaOH solution but not in the case of aqueous TBAH solution. Furthermore, SEM images revealed that needle-like crystallite structures were observed in NaOH solution and a wrinkled film like morphology was observed in the TBAH solution indicating that complete cellulose I dissolution occurred in the latter but not the former. Dynamic light scattering measurements revealed that the average particle size in the TBAH system was between 10 and 20 nm whereas in the case of the NaOH system it was 200 nm. Additionally, the lower crystallinity index of the TBAH extracted cellulose II when compared to cellulose I and NaOH extracted cellulose II supported their results. Thus it can be seen that near molecular level dissolution was achieved when TBAH was used as a solvent. The authors attributed this to the amphiphilic nature of cellulose I and TBAH emphasising the superiority of onium hydroxides over alkalis as solvents for dissolving cellulose I. The advantage of using onium hydroxides over alkali metal hydroxides and (aqueous) ionic liquids for cellulose I dissolution was established by Abe et al. and is shown in Fig. 9 [73].

3.2.3. Phosphoric acid treatment

Jia et al. dissolved cellulose I in phosphoric acid and produced cellulose II via regeneration with the addition of water [76]. They prepared a range of cellulose I – phosphoric acid concentrations with 0.5–3% wt./v cellulose I and 77–85 wt% phosphoric acid in the temperature range of 5–75 °C. An esterification reaction occurred when cellulose I was mixed with phosphoric acid forming a cellulose I - phosphoric acid ester. Upon dissolution, when water was added to regenerate cellulose II, phosphoric acid in the complex was displaced by the water molecules. The transformation of cellulose I to cellulose II was confirmed with the XRD and FTIR (Fourier Transform Infrared spectroscopy) spectra. Furthermore, they determined that a higher concentration of phosphoric acid (≥83 wt%) was required to completely dissolve cellulose I whereas in any other lower concentration, only swelling occurs. In addition, they also established that up to 3% wt./v cellulose I could be dissolved in phosphoric acid and any concentration above that would cause the dispersion of cellulose I but not dissolution in phosphoric acid. When dissolution experiments were performed under different temperatures, it was determined that complete dissolution was favoured at lower temperatures as monitored by an UV–visible spectrometer.

3.2.4. Trifluoroacetic acid treatment

Zhao et al. introduced a new non-derivatising method to produce cellulose II from cotton linters using trifluoroacetic acid (TFA) at low temperatures [77]. Cotton linters was mixed in 99% TFA in mass ratios of 1:15 at different temperatures ranging from 0 °C to 65 °C for 3 h. The swollen samples were washed with water to remove traces of TFA

and recover cellulose II. The production of cellulose II was confirmed using XRD measurements. They observed an inverse temperature effect for the production of cellulose II using TFA as the solvent. At 0 °C, cellulose I was completely converted to cellulose II whereas with an increase in temperature only partial conversion was observed. The reason for this partial conversion was attributed to the lack of TFA cyclic dimer formation at higher temperatures. As proposed, TFA tend to form cyclic dimers at lower temperatures but not at higher temperatures. Weak interactions were suggested to be formed between the C=O of the TFA dimers and cellulose I at 0 °C. These interactions could disrupt the hydrogen bonding network thereby facilitating cellulose I decrystallisation, but the TFA monomers formed at higher temperatures were not able to disrupt the hydrogen bonds favouring only partial conversion. In addition, SEM analysis showed that the supramolecular structure of cellulose was undisturbed before and after TFA treatment which confirms that treatment with TFA would only partially produce cellulose II. Although the inverse temperature effect for cellulose II production was established, risks involved in the handling and use of TFA makes it a less preferred solvent for cellulose II production.

3.2.5. Supercritical water solubilisation

Sasaki et al. proposed a new method for cellulose II production from native cellulose (cellulose I) using near and supercritical water as a solvent [78]. A concentration of 10 wt% cellulose I was mixed with water in a microreactor and rapidly heated for 0.02–0.6 s at 320–400 °C and 25–33 MPa pressure. It was determined that at 320 °C and 25 MPa, cellulose II was not produced instead, soluble saccharides of cellulose were formed. In the range of 360–380 °C, partial cellulose I dissolution occurred and in the range of 375–380 °C, 50% cellulose I conversion was achieved accounting for both cellulose II and soluble saccharides of cellulose. At 400 °C cellulose I disappeared within 0.02 s and both cellulose II and soluble saccharides of cellulose were obtained. It was further established that at temperatures higher than 380 °C, cellulose I conversion was constant and was independent of the pressure.

At the near and supercritical water temperatures, the intermolecular and intramolecular hydrogen bonds become weaker in cellulose I thereby facilitating bond cleavage. Also, at higher temperatures, the density and dielectric constant of water decreases with the increase in hydrophobicity and diffusion coefficient which favours the partial dissolution and hydrolysis of cellulose I. Although advantages such as the use of environment friendly solvent (water) and one pot cellulose II production was emphasised by the authors, the disadvantages such as non-selectivity, decomposition of desired products at high temperatures and high energy input overshadow its advantages.

4. Fermentable sugar and biofuel production with cellulose II

With a view towards biofuel production, Mittal et al. dissolved four types of cellulose I obtained from various sources (Avicel PH-101, α-cellulose, cotton linters and cellulose extracted from corn stover) in 16.5 wt% aqueous NaOH at 25 °C under a nitrogen atmosphere [47]. Upon dissolution and precipitation, the cellulose I samples were found to be converted to cellulose II. In addition to the conversion, they tested the enzymatic digestibility of these cellulose I and cellulose II samples using Genencor GC220 cellulase enzyme preparation. They determined that the enzymatic digestibility of cellulose II was superior to that of cellulose I from their experiments. The initial enzymatic hydrolysis rate of cellulose II was found to be two times faster than cellulose I. The superior digestibility was attributed towards the increased non-crystalline regions present in cellulose II as a result of mercerisation.

Ma et al. used pyrrolidonium based ionic liquids to extract regenerated cellulose from corn stalk for fermentable sugar production via enzymatic hydrolysis [79]. Ionic liquids such as N-methyl-2-pyrrolidonium hydrogen sulfate (MPHS), N-methyl-2-pyrrolidonium dihydrogen phosphate (MPDP), N-methyl-2-pyrrolidonium chloride (MPC) and N-methyl-2-pyrrolidonium methanesulfonate (MPMS) and their respective aqueous solutions were synthesised for dissolving the lignocellulosic feedstock. A concentration of 0.05 wt% corn stalk was added to the ionic liquids and the mixture was heated to 90 °C and stirred for 30 min. Then 20 ml of 1:1 acetone/deionised water solution was added to the mixture to precipitate regenerated cellulose. Reduced crystallinity of the regenerated cellulose samples was confirmed using the FTIR spectra obtained. These regenerated cellulose samples (1 g/ml) were subjected to enzymatic hydrolysis for the production of fermentable sugars. Commercial *Aspergillus niger* cellulase (0.02 g) was used for enzymatic hydrolysis. The enzymatic hydrolysis experiments were performed at 50 °C for 72 h at a pH 4.8, maintained using 0.1 M sodium citrate buffer. Highest yield of fermentable sugars of 91.81% followed by 73.59% and 70.18% were produced from regenerated cellulose obtained with aqueous MPC, MPMS and MPC treatment respectively. These high sugar yields were attributed to the hydrogen bonding capability and the acidity of the ionic liquids which effectively removed the bound hemicelluloses and lignin in the corn stalk in addition to the reduced crystallinity of the obtained regenerated cellulose.

Shafiei et al. dissolved either spruce wood chips or powder in ionic liquids EMIM-Ac, and 1-butyl-3-methylimidazolium acetate (BMIM-Ac) and an organic solvent N-methylmorpholine-N-oxide (NMMO) [68]. Wood chips or powder (5%) was mixed with the ionic liquids at 120 °C in an oil bath for varied experiment times. Upon dissolution, 20 ml of boiling water was added to the solution to precipitate cellulose II from the mixture. The precipitated cellulose II was filtered through a filter paper and washed with excess water to remove any bound ionic liquids. As a result of ionic liquid pre-treatment, cellulose II was formed with lower crystallinity than the untreated wood samples. Furthermore, enzymatic hydrolysis of cellulose II and cellulose I (wood chips and powder) samples was carried out at 45 °C for 72 h in citrate buffer with a mixture of cellulase and β-glucosidase enzymes. The fermentable sugar yield from EMIM-Ac (66%) and BMIM-Ac (57%) treated wood chips samples were found to be significantly higher than the NMMO (38%) treated and untreated samples (2%). After hydrolysis, the hydrolysates were separated and subjected to ethanol fermentation using *Saccharomyces cerevisiae* CCUG53310 at 32 °C for 24 h. A higher yield of ethanol production for EMIM-Ac (67%) and BMIM-Ac (52%) in comparison to NMMO (36%) treated and untreated (3%) samples upon fermentation was observed. The reason for a higher yield of fermentable sugars and bioethanol production was attributed towards the lower crystallinity of the raw material, cellulose II.

In addition to the example mentioned above and various well documented evidences mentioned earlier on the use of ionic liquids for cellulose II production, there has also been a techno-economic study published by Klein-Marcuschamer et al. in 2011 on the feasibility of ionic liquids for ligno-cellulosic biorefineries [80]. Based on their study it can be inferred that the key barrier to scale-up is the cost of ionic liquids needed for cellulose I dissolution which dominates the proportion of total costs involved followed by the cost of ionic liquid loading and the rate of ionic liquid recycling. In order to compensate for the ionic liquid loading, aqueous ionic liquid mixtures have been used by Fu and Mazza [63]. They dissolved triticale straw in 5%, 25%, 50% and pure EMIM-Ac to obtain cellulose II for enzymatic hydrolysis. As can be seen from their results in Fig. 10, when pure EMIM-Ac was used to dissolve straw, almost complete cellulose II hydrolysis was seen after approximately 8 h, with decreasing the ionic liquid loading to 50%, cellulose II hydrolysis fell from 100% to 80% at 8 h. With a further decrease in the EMIM-Ac loading to 25% and 5%, an even lower cellulose II amount was hydrolysed. According to the feasibility study conducted by Klein-Marcuschamer et al., there has to be an optimum trade-off between the ionic liquid loading and the hydrolysate pro-

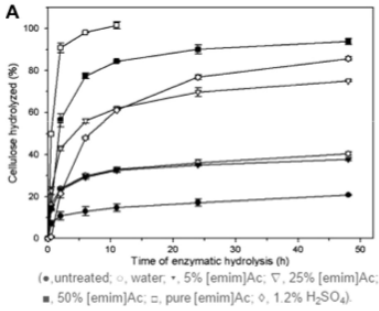

Fig. 10. Cellulose hydrolysis [63] (Reprinted with permission from "Elsevier, Bioresource Technology, Copyright 2011").

duced. Furthermore, their economic analysis also revealed that the revenue generated by the lignin by-products could offset a part of the investment costs.

5. Conclusion

Current global energy scenario demands an increase in the use of renewable energy to mitigate emissions, particularly in the transportation sector. The use of biofuels for transportation would help to achieve the emission targets. To make biofuels attractive, the price of it must however match the current oil price. This would be feasible when biofuel industries turn into biorefineries and offset the costs by

(i) improving the biofuel yields and
(ii) producing value added by-products.

To improve the yield of biofuels, especially bioethanol, a more easily accessible cellulose feedstock has to be input. It is evident from this review that cellulose II has distinct advantages over cellulose I (and lignocellulosic biomass) as feedstock for biofuel production. When lignocellulosic materials are used in biorefineries, interfering lignin network hinders the complete utilisation of cellulose. Even though when cellulose I is separated from lignin using appropriate pre-treatment methods such as steam explosion, ammonia explosion or acid/alkali hydrolysis [81], the crystalline structure of native cellulose combined with the hydrophobic interactions and the intra and inter-molecular hydrogen bond network makes it difficult to process further via microbiological, enzymatic or chemical routes.

To overcome this problem, lignocellulose pre-treatment focussing on delignification combined with simultaneous production of cellulose II have been used. Cellulose II could be produced by simply dissolving cellulose I or lignocellulosic feedstock in an appropriate amphiphilic solvent followed by regeneration using an anti-solvent such as water, ethanol, methanol, dilute acids or acetone. Cellulose II has been well established to have a lower crystallinity than cellulose I. The former is also said to have the highest wettability, porous volume and surface area than cellulose I [20,34,36]. These advantages make cellulose II an easily digestible polymorph of cellulose, however it has not been used extensively for biofuel production purposes. Though the use of cellulose II as biofuel feedstock has not been comprehensively studied, the limited results reported have strongly established the fact that cellulose II is a better feedstock than native cellulose (and lignocellulosic wastes) for biofuel production.

A range of solvents have been used for the production of cellulose II. With mercerisation dating back to 1850's, until today, there has been significant developments in the field of dissolution and regeneration of cellulose. Of all the solvents used, molecular level dissolution could be achieved only when ionic liquids or onium hydroxides are used as solvents. This is because of the amphiphilic nature of both the cellulose I and the solvents, however an optimum solvent loading is required to make biorefineries profitable. Ionic liquids' cellulose I dissolving ability is affected when they come in contact with water and hence aqueous onium hydroxide solution can be used as a substitute for ionic liquids. Also from an energy perspective, onium hydroxides offer an advantage over ionic liquids as preferred solvents for cellulose I dissolution due to their high cellulose I dissolving capacity at room temperature. Although there are room temperature ionic liquids available for cellulose dissolution, their high viscosity limits its use.

The prospect of using cellulose II as feedstock for biofuel production has been experimented but requires more research considering the advantages it offers. Literature evidence available suggests that the potential of cellulose II for biofuel production is higher than cellulose I as discussed in this review. These initial results from most researchers are promising but several research gaps such as the scalability, selectivity, recyclability of cellulose I solvents, use of wet biomass for integrated biofuel production and economic viability needs to be addressed to proceed further. Hence cellulose II needs to be seriously considered as an alternative feedstock option if cellulosic biorefineries are to become a feasible reality.

Acknowledgements

The authors would like to acknowledge the funding support from Engineering and Physical Sciences Research Council (Project no. EP/K036769/1) and Queen's University Belfast's Ph.D. studentship. The authors would also like to thank Professor A. Prasanna de Silva, School of Chemistry and Chemical Engineering, Queen's University Belfast, for his valuable contribution during the progress meetings.

References

[1] Wigley TML, Richels R, Edmonds JA. Economic and environmental choices in the stabilization of atmospheric CO_2 concentrations. Nature 1996;379:240–3.
[2] van der Hoeven M. World energy outlook report; 2013.
[3] Gui MM, Lee KT, Bhatia S. Feasibility of edible oil vs. non-edible oil vs. waste edible oil as biodiesel feedstock. Energy 2008;33:1646–53.
[4] Nagarajan S, Chou SK, Cao S, Wu C, Zhou Z. An updated comprehensive techno-economic analysis of algae biodiesel. Bioresour Technol 2013;145:150–6.
[5] Linoj KN, Prabha D, Anandajit G, Sameer M. Liquid Biofuels in South Asia: resources and Technologies. Asian Biotechnol Dev Rev 2006;8:31.
[6] Betts WB, Dart RK, Ball AS, Pedlar SL. Betts WB, editor. Biosynthesis and structure of lignocellulose. London: Springer; 1991. p. 139–55.
[7] Brown TR, Brown RC. A review of cellulosic biofuel commercial-scale projects in the United States. Biofuels Bioprod Bioref 2013;7:235–45.
[8] Carroll A, Somerville C. Cellulosic biofuels. Annu Rev Plant Biol 2009;60:165–82.
[9] Sticklen MB. Plant genetic engineering for biofuel production: towards affordable cellulosic ethanol. Nat Rev Genet 2008;9:433.
[10] Sannigrahi P, Ragauskas AJ, Tuskan GA. Poplar as a feedstock for biofuels: a review of compositional characteristics. Biofuels Bioprod Bioref 2010;4:209–26.
[11] Naik SN, Goud VV, Rout PK, Dalai AK. Production of first and second generation biofuels: a comprehensive review. Renew Sust Energ Rev 2010;14:578–97.
[12] David K, Ragauskas AJ. Switchgrass as an energy crop for biofuel production: a review of its ligno-cellulosic chemical properties. Energy Environ Sci 2010;3:1182–90.
[13] Weng J, Li X, Bonawitz ND, Chapple C. Emerging strategies of lignin engineering and degradation for cellulosic biofuel production. Curr Opin Biotechnol 2008;19:166–72.
[14] Swatloski RP, Spear SK, Holbrey JD, Rogers RD. Dissolution of cellose with ionic liquids. J Am Chem Soc 2002;124:4974–5.
[15] Lindman B, Karlström G, Stigsson L. On the mechanism of dissolution of cellulose. J Mol Liq 2010;156:76–81.
[16] Silverstein RA. A comparison of chemical pretreatment methods for converting cotton stalks to ethanol; 2005.
[17] Sjöström E. Wood chemistry. San Diego: Fundamentals and Applications Academic Press; 1993.
[18] Medronho B, Lindman B. Brief overview on cellulose dissolution/regeneration

interactions and mechanisms. Adv Colloid Interface Sci 2015;222:502–8.
[19] Xi J, Du W, Zhong L. Probing the interaction between cellulose and cellulase with a nanomechanical sensor. In: Van de Ven T, Godbout L, (eds). Cellulose – medical, pharmaceutical and electronic applications, InTech; 2013. p. 125.
[20] Yamane C, Aoyagi T, Ago M, Sato K, Okajima K, Takahashi T. Two different surface properties of regenerated cellulose due to structural anisotropy. Polym J 2006;38:819–26.
[21] Biermann O, Hädicke E, Koltzenburg S, Müller-Plathe F. Hydrophilicity and lipophilicity of cellulose crystal surfaces. Angew Chem Int Ed 2001;40:3822–5.
[22] Glasser WG, Atalla RH, Blackwell J, Malcolm Brown R, Burchard W, French AD, Klemm DO, Nishiyama Y. About the structure of cellulose: debating the Lindman hypothesis. Cellulose 2012;19:589–98.
[23] Medronho B, Lindman B. Competing forces during cellulose dissolution: from solvents to mechanisms. Curr Opin Colloid Interface Sci 2014;19:32–40.
[24] Medronho B, Duarte H, Alves L, Antunes FE, Romano A, Valente AJM. The role of cyclodextrin-tetrabutylammonium complexation on the cellulose dissolution. Carbohydr Polym 2016;140:136–43.
[25] O'Sullivan A. Cellulose: the structure slowly unravels. Cellulose 1997;4:173–207.
[26] Shibazaki H, Saito M, Kuga S, Okano T. Native cellulose II production by acetobacter xylinum under physical constraints. Cellulose 1998;5:165–73.
[27] Kuga S, Takagi S, Brown RM. Native folded-chain cellulose II. Polymer 1993;34:3293–7.
[28] Yatsu LY, Calamari TA, Benerito RR. Conversion of cellulose i to stable cellulose III. Text Res J 1986;56:419–24.
[29] Wada M, Chanzy H, Nishiyama Y, Langan P. Cellulose IIII crystal structure and hydrogen bonding by synchrotron X-ray and neutron fiber diffraction. Macromolecules 2004;37:8548–55.
[30] Isogai A, Usuda M, Kato T, Uryu T, Atalla RH. Solid-state CP/MAS carbon-13 NMR study of cellulose polymorphs. Macromolecules 1989;22:3168–72.
[31] Klemm D, Philipp B, Heinze T, Heinze U, Wagenknecht W. General considerations on structure and reactivity of cellulose: Section 2.1–2.1.4. In: Anonymous , editor. Comprehensive cellulose chemistry. Weinheim: Wiley-VCH Verlag GmbH & Co. KGaA; 1998. p. 9–29.
[32] Wada M, Ike M, Tokuyasu K. Enzymatic hydrolysis of cellulose I is greatly accelerated via its conversion to the cellulose II hydrate form. Polym Degrad Stab 2010;95:543–8.
[33] Sakurada I, Hutino K. Über die intramizellare Quellung der Zellulose durch Wasser. Kolloid Z 1936;77:346–51.
[34] Boissou F, Muhlbauer A, De OV, Leclercq L, Kunz W, Marinkovic S, Estrine B, Nardello-Rataj V, Jerome F. Transition of cellulose crystalline structure in biodegradable mixtures of renewably-sourced levulinate alkyl ammonium ionic liquids, gamma]-valerolactone and water. Green Chem 2014;16:2463–71.
[35] Kljun A, Benians TAS, Goubet F, Meulewaeter F, Knox JP, Blackburn RS. Comparative analysis of crystallinity changes in cellulose I polymers using ATR-FTIR, X-ray diffraction, and carbohydrate-binding module probes. Biomacromolecules 2011;12:4121–6.
[36] Dadi AP, Varanasi S, Schall CA. Enhancement of cellulose saccharification kinetics using an ionic liquid pretreatment step. Biotechnol Bioeng 2006;95:904–10.
[37] Wahlstrom RM, Suurnakki A. Enzymatic hydrolysis of lignocellulosic polysaccharides in the presence of ionic liquids. Green Chem 2015;17:694–714.
[38] Zhao H, Holladay EJ, Kwak JH, Zhang ZC. A new route to improved glucose yields in cellulose hydrolysis. J Biobased Mater Bio 2007;1:210.
[39] Pinkert A, Marsh KN, Pang S, Staiger MP. Ionic liquids and their interaction with cellulose. Chem Rev 2009;109:6712–28.
[40] Abe M, Fukaya Y, Ohno H. Fast and facile dissolution of cellulose with tetrabutylphosphonium hydroxide containing 40 wt% water. Chem Commun 2012;48:1808–10.
[41] Alves L, Medronho BF, Antunes FE, Romano A, Miguel MG, Lindman B. On the role of hydrophobic interactions in cellulose dissolution and regeneration: colloidal aggregates and molecular solutions. Colloids Surf Physicochem Eng Asp 2015;483:257–63.
[42] Klemm D, Heublein B, Fink H, Bohn A. Cellulose: fascinating biopolymer and sustainable raw material. Angew Chem Int Ed 2005;44:3358–93.
[43] Cross CF, Bevan EJ, Beadle C. Die chemie der pflanzenfasern. Cellulosen, oxycellulosen, lignocellulosen. Ber Dtsch Chem Ges 1893;26:2520–33.
[44] Cross CF, Bevan ET, Beadle C. Thiokohlensäureester der Cellulose. Ber Dtsch Chem Ges 1893;26:1090–7.
[45] Guenet J. Chapter 5 – cellulose. In: Guenet J, editor. Polymer-solvent molecular compounds. London: Elsevier; 2008. p. 57–69.
[46] Mercer J. Improvements in the preparation of cotton and other fabrics and other fibrous materials. British Patent; 1850. p. 13296.
[47] Mittal A, Katahira R, Himmel ME, Johnson DK. Effects of alkaline or liquid-ammonia treatment on crystalline cellulose: changes in crystalline structure and effects on enzymatic digestibility. Biotechnol Biofuels 2011;4:1–16.
[48] Dinand E, Vignon M, Chanzy H, Heux L. Mercerization of primary wall cellulose and its implication for the conversion of cellulose I→cellulose II. Cellulose 2002;9:7–18.
[49] Liu W, Zhao S, Li L, Xin XZ. Enhancement of cellulose reactivity using an ionic liquid pretreatment step. Cell Chem Technol 2015;49:397–403.
[50] Wang Y, Deng Y. The kinetics of cellulose dissolution in sodium hydroxide solution at low temperatures. Biotechnol Bioeng 2009;102:1398–405.
[51] Sharma S, Nair SS, Zhang Z, Ragauskas AJ, Deng Y. Characterization of micro fibrillation process of cellulose and mercerized cellulose pulp. RSC Adv 2015;5:63111–22.
[52] Halonen H, Larsson PT, Iversen T. Mercerized cellulose biocomposites: a study of influence of mercerization on cellulose supramolecular structure, water retention value and tensile properties. Cellulose 2012;20:57–65.
[53] Revol JF, Dietrich A, Goring DAI. Effect of mercerization on the crystallite size and crystallinity index in cellulose from different sources. Can J Chem 1987;65:1724–5.
[54] Yu L, Lin J, Tian F, Li X, Bian F, Wang J. Cellulose nanofibrils generated from jute fibers with tunable polymorphs and crystallinity. J Mater Chem A 2014;2:6402–11.
[55] Jin E, Guo J, Yang F, Zhu Y, Song J, Jin Y, Rojas OJ. On the polymorphic and morphological changes of cellulose nanocrystals (CNC-I) upon mercerization and conversion to CNC-II. Carbohydr Polym 2016;143:327–35.
[56] Wilkes JS, Zaworotko MJ. Air and water stable 1-ethyl-3-methylimidazolium based ionic liquids. J Chem Soc Chem Commun 1992;13:965–7.
[57] Plechkova NV, Seddon KR. Applications of ionic liquids in the chemical industry. Chem Soc Rev 2008;37:123–50.
[58] Earle MJ, Seddon KR. Ionic liquids: green solvents for the future. In: Abraham MA, Moens L, editors. Clean solvents: alternative media for chemical reactions and processing. Washington DC: American Chemical Society; 2002. p. 10–25.
[59] Dutta S, De S, Alam MI, Abu-Omar MM, Saha B. Direct conversion of cellulose and lignocellulosic biomass into chemicals and biofuel with metal chloride catalysts. J Catal 2012;288:8–15.
[60] Hou X, Smith TJ, Li N, Zong M. Novel renewable ionic liquids as highly effective solvents for pretreatment of rice straw biomass by selective removal of lignin. Biotechnol Bioeng 2012;109:2484–93.
[61] Xiao S, Liu B, Wang Y, Fang Z, Zhang Z. Efficient conversion of cellulose into biofuel precursor 5-hydroxymethylfurfural in dimethyl sulfoxide–ionic liquid mixtures. Bioresour Technol 2014;151:361–6.
[62] Park JI, Steen EJ, Burd H, Evans SS, Redding-Johnson A, Batth T, Benke PI, D'haeseleer P, Sun N, Sale KL, Keasling JD, Lee TS, Petzold CJ, Mukhopadhyay A, Singer SW, Simmons BA, Gladden JM. A Thermophilic ionic liquid-tolerant cellulase cocktail for the production of cellulosic biofuels. PLoS One 2012;7:e37010.
[63] Fu D, Mazza G. Aqueous ionic liquid pretreatment of straw. Bioresour Technol 2011;102:7008–11.
[64] Bokinsky G, Peralta-Yahya PP, George A, Holmes BM, Steen EJ, Dietrich J, Soon Lee T, Tullman-Ercek D, Voigt CA, Simmons BA, Keasling JD. Synthesis of three advanced biofuels from ionic liquid-pretreated switchgrass using engineered Escherichia coli. Proc Natl Acad Sci USA 2011;108:19949–54.
[65] Cheng G, Varanasi P, Li C, Liu H, Melnichenko YB, Simmons BA, Kent MS, Singh S. Transition of cellulose crystalline structure and surface morphology of biomass as a function of ionic liquid pretreatment and its relation to enzymatic hydrolysis. Biomacromolecules 2011;12:933–41.
[66] Samayam IP, Hanson BL, Langan P, Schall CA. Ionic-liquid induced changes in cellulose structure associated with enhanced biomass hydrolysis. Biomacromolecules 2011;12:3091–8.
[67] Dadi AP, Schall CA, Varanasi S. Mitigation of cellulose recalcitrance to enzymatic hydrolysis by ionic liquid pretreatment. Appl Biochem Biotechnol 2007;137:407–21.
[68] Shafiei M, Zilouei H, Zamani A, Taherzadeh MJ, Karimi K. Enhancement of ethanol production from spruce wood chips by ionic liquid pretreatment. Appl Energy 2013;102:163–9.
[69] Zavrel M, Bross D, Funke M, Büchs J, Spiess AC. High-throughput screening for ionic liquids dissolving (ligno-)cellulose. Bioresour Technol 2009;100:2580–7.
[70] Vitz J, Erdmenger T, Haensch C, Schubert US. Extended dissolution studies of cellulose in imidazolium based ionic liquids. Green Chem 2009;11:417–24.
[71] Zhang J, Zhang H, Wu J, Zhang J, He J, Xiang J. NMR spectroscopic studies of cellobiose solvation in EmimAc aimed to understand the dissolution mechanism of cellulose in ionic liquids. Phys Chem Chem Phys 2010;12:1941–7.
[72] Toth T, Borsa J, Reicher J, Sallay P, Sajo I, Tanczos I. Mercerization of cotton with tetramethylammonium hydroxide. Text Res J 2003;73:273–8.
[73] Abe M, Kuroda K, Ohno H. Maintenance-free cellulose solvents based on onium hydroxides. ACS Sustain Chem Eng 2015;3:1771–6.
[74] Behrens MA, Holdaway JA, Nosrati P, Olsson U. On the dissolution state of cellulose in aqueous tetrabutylammonium hydroxide solutions. RSC Adv 2016;6:30199–204.
[75] Wei W, Wei X, Gou G, Jiang M, Xu X, Wang Y, Hui D, Zhou Z. Improved dissolution of cellulose in quaternary ammonium hydroxide by adjusting temperature. RSC Adv 2015;5:39080–3.
[76] Jia X, Chen Y, Shi C, Ye Y, Wang P, Zeng X, Wu T. Preparation and characterization of cellulose regenerated from phosphoric acid. J Agric Food Chem 2013;61:12405–14.
[77] Zhao H, Holladay JE, Kwak JH, Zhang ZC. Inverse temperature-dependent pathway of cellulose decrystallization in trifluoroacetic acid. J Phys Chem B 2007;111:5295–300.
[78] Sasaki M, Adschiri T, Arai K. Production of cellulose II from native cellulose by near- and supercritical water solubilization. J Agric Food Chem 2003;51:5376–81.
[79] Ma H, Zhang B, Zhang P, Li S, Gao Y, Hu X. An efficient process for lignin extraction and enzymatic hydrolysis of corn stalk by pyrrolidonium ionic liquids. Fuel Process Technol 2016;148:138–45.
[80] Klein-Marcuschamer D, Simmons BA, Blanch HW. Techno-economic analysis of a lignocellulosic ethanol biorefinery with ionic liquid pre-treatment. Biofuels, Bioprod Bioref 2011;5:562–9.
[81] Sun Y, Cheng J. Hydrolysis of lignocellulosic materials for ethanol production: a review. Bioresour Technol 2002;83:1–11.
[82] Demirbas A. Bioethanol from cellulosic materials: a renewable motor fuel from biomass. Energy Sources 2005;27:327–37.
[83] Nasri-Nasrabadi B, Behzad T, Bagheri R. Extraction and characterization of rice straw cellulose nanofibers by an optimized chemomechanical method. J Appl Polym Sci 2014:131.
[84] Lindedam J, Bruun S, Jørgensen H, Felby C, Magid J. Cellulosic ethanol: interactions between cultivar and enzyme loading in wheat straw processing. Biotechnol Biofuels 2010;3:1–10.
[85] Mansaray KG, Ghaly AE. Thermal degradation of rice husks in nitrogen atmosphere. Bioresour Technol 1998;65:13–20.
[86] Jústiz-Smith NG, Virgo GJ, Buchanan VE. Potential of Jamaican banana, coconut coir and bagasse fibres as composite materials. Mater Charact 2008;59:1273–8.